Influence of microstructure on debonding at the fiber/matrix interface in fiber-reinforced polymers under tensile loading

Luca Di Stasio

▶ **To cite this version:**

Luca Di Stasio. Influence of microstructure on debonding at the fiber/matrix interface in fiber-reinforced polymers under tensile loading. Materials. Université de Lorraine; Université de technologie de Luleå (Suède), 2019. English. NNT : 2019LORR0229 . tel-02552524

HAL Id: tel-02552524
https://hal.univ-lorraine.fr/tel-02552524

Submitted on 23 Apr 2020

HAL is a multi-disciplinary open access archive for the deposit and dissemination of scientific research documents, whether they are published or not. The documents may come from teaching and research institutions in France or abroad, or from public or private research centers.

L'archive ouverte pluridisciplinaire **HAL**, est destinée au dépôt et à la diffusion de documents scientifiques de niveau recherche, publiés ou non, émanant des établissements d'enseignement et de recherche français ou étrangers, des laboratoires publics ou privés.

AVERTISSEMENT

Ce document est le fruit d'un long travail approuvé par le jury de soutenance et mis à disposition de l'ensemble de la communauté universitaire élargie.

Il est soumis à la propriété intellectuelle de l'auteur. Ceci implique une obligation de citation et de référencement lors de l'utilisation de ce document.

D'autre part, toute contrefaçon, plagiat, reproduction illicite encourt une poursuite pénale.

Contact : ddoc-theses-contact@univ-lorraine.fr

LIENS

Code de la Propriété Intellectuelle. articles L 122. 4
Code de la Propriété Intellectuelle. articles L 335.2- L 335.10
http://www.cfcopies.com/V2/leg/leg_droi.php
http://www.culture.gouv.fr/culture/infos-pratiques/droits/protection.htm

UNIVERSITÉ DE LORRAINE

École doctorale C2MP

Effet de la microstructure sur le décollement à l'interface fibre/matrice dans les stratifiés à matrice polymère avec renfort en fibre soumis à traction

THÈSE

présentée et soutenue publiquement le 13 décembre 2019 à Luleå (Suède)

pour l'obtention du

Doctorat de l'Université de Lorraine

Mention Sciences des Matériaux

par

Luca Di Stasio

Composition du jury

Federica DAGHIA	Maître de Conférences – Département de Génie Mécanique (DGM) et Laboratoire de Mécanique et Technologie (LMT), École Normale Supérieure de Cachan, France	**Rapporteur**
Yves BERTHAUD	Professeur – Institut Jean le Rond d'Alembert, Université Pierre et Marie Curie, France	**Rapporteur**
Kristofer GAMSTEDT	Professeur – Division of Applied Mechanics, Department of Engineering Sciences, Uppsala University, Suède	**Examinateur**
Zoubir AYADI	Professeur – Département Science et Ingénierie des Matériaux et Métallurgie, Institut Jean Lamour (IJL), Université de Lorraine, France	**Directeur de thèse**
Janis VARNA	Professeur – Division of Materials Science, Department of Engineering Sciences and Mathematics, Luleå University of Technology, Suède	**Directeur de thèse**

Institut Jean Lamour – UMR 7198 – Département SI2M – Equipe 304
Université de Lorraine – Pôle M4 : Matière, Matériaux, Métallurgie, Mécanique

Influence of microstructure on debonding at the fiber/matrix interface in fiber-reinforced polymers under tensile loading

Luca Di Stasio

Division of Materials Science
Department of Engineering Sciences and Mathematics
Luleå University of Technology
Luleå, Sweden

&

Institut Jean Lamour
École Européenne d'Ingénieurs en Génie des Matériaux
Université de Lorraine
Nancy, France

The work presented in this thesis is the result of the collaboration between Luleå University of Technology and Université de Lorraine aimed at a double degree as part of the DocMASE Programme

A mio figlio, Levante Libero Antonio:
abbi sempre il coraggio di tentare!

Never give up on a dream just because of the time it will take to accomplish it. The time will pass anyway.

Earl Nightingale

. . . e intanto si allarga la nebbia e avresti potuto vivere al mare

---

Luciano Ligabue

Preface

I bought my first and current car, *La Melanza*, in August 2015, just a few weeks before starting my doctoral studies at Luleå University of Technology and Université de Lorraine. Today, October 2019, *La Melanza* has traveled 127′712 kilometers. It has been, indeed, a long journey. One that has brought me to live in two different countries, France and Sweden, and to visit five more, Germany, Greece, Russia, Italy and Spain, for conferences, summer schools and exchanges. A journey in which I have learned a lot, made new friends and built a family. And, apparently, even managed to write a Ph.D. thesis! No such journey could be ventured alone, and here I would like to thank everyone who helped and supported me in these years.

It is common use to place supervisors at the top of the acknowledgements list, and I will not be any different. It is however not in adherence to custom, but with sincere gratitude that I place them here in the first place. Thus, many thanks to Prof. Janis Varna for accepting me as his Ph.D. student, sharing his knowledge, correcting my mistakes, pointing my efforts in the right direction, always being curious and passionate about research. Thanks to Prof. Zoubir Ayadi, for welcoming me in France and supporting me all along.
I then wish to thank all the members of the Polymeric Composite Group at LTU for welcoming me in Luleå, for showing me how to survive at $-30°$, for the interesting discussions over a coffee and for their help to solve the problems in the lab: Johanna, Roberts, Patrik, Lennart, Zainab, Nawres, Hiba, Liva, Andrejs, Stephanie, Linqi.
I wish to thank also all the people that have helped me extricate myself in all the administrative needs that an international project requires, and have always answered with patience and a smile to my (at times many) questions: Birgitta, Fredrik, Marie-Louise, Christine, Martine, Nadine and Flavio.
And finally, my thoughts go to my family. To Scarlett, for "the purest love in the world is between a grumpy dad and the pet he said he never wanted", and I guess I'm just another proof of it. To Levante, for forcing me to work in order to stay awake late at night guarding him, and for bringing already so much joy in my life. To Valentina, for following me in two different countries, for bringing so many beautiful things in my life and, every now and then, reminding me that there are worse things in life than a deadline for a paper (or a thesis!).

Luleå, October 2019
Luca Di Stasio

Résumé

L'objectif principal de cette thèse est d'étudier l'effet de la microstructure sur l'amorçage et propagation de décollements entre fibre et matrice. Dans ce but, des modèles de Volume Elémentaire Représentatif (VER) des composites unidirectionnels et des stratifiés croisés sont développés, caractérisés par différentes configurations des fibres et degré d'endommagement. L'amorçage du décollement est analysé par rapport à la distribution des contraintes à l'interface entre fibre et matrice. En revanche, la propagation du décollement est étudiée avec l'approche de la Mécanique Linéaire Elastique de la Rupture (MLER), et plus spécifiquement avec l'évaluation du taux de restitution d'énergie en Mode I et Mode II. Les champs de déplacement et contrainte sont calculés avec la Méthode des éléments finis (MEF) dans le logiciel Abaqus. La détermination des composants du taux de restitution d'énergie est effectuée avec la technique de fermeture virtuelle de fissure implémentée par l'auteur en langage Python.
La solution élastique du problème de décollement entre fibre et matrice est caractérisée par la présence de deux régimes : celui de fissure ouverte et celui de fissure fermée. Dans le deuxième cas, il existe une zone proche de la pointe de fissure où les lèvres du décollement sont en contact. Dans le premier cas, le décollement est ouvert et il n'existe aucun contact entre les lèvres du décollement. Dans le régime de fissure ouverte, les champs des déplacements et contraintes présentent une singularité oscillatoire. Un 'étude de convergence de la technique de fermeture virtuelle de fissure est donc requis et constitue le premier élément du travail de cette thèse. Il est constaté que le taux de restitution d'énergie total ne dépend pas de la taille des éléments proches de la pointe de fissure, alors que le taux en Mode I et Mode II présent une dépendance significative de la taille des éléments dans le cas de fissure ouverte. Il est montré que le taux de restitution d'énergie en Mode I et Mode II ne converge pas, ce à dire que le comportement asymptotique n'est pas limité. Par conséquence, il n'est pas possible d'utiliser l'erreur entre itérations successives comme mesure de la convergence de la solution et une comparaison est donc nécessaire avec des résultats obtenus avec une autre méthode. Le taux de restitution d'énergie calculé avec la méthode d'éléments de frontière, disponible dans la littérature, est choisi comme référence. Ensuite, la propagation de décollement entre fibre et matrice est étudiée dans Volume Elémentaire Représentative de : composites unidirectionnels avec épaisseur variable, mesuré par le nombre des rangées des fibres, de ceux extrêmement minces (une rangée des fibres) au plus épais ; stratifié croisé avec un pli central à 90° d'épaisseur variable, mesuré par le nombre des rangées des fibres, de ceux extrêmement minces (une rangée des fibres) au plus épais ; composites unidirectionnels épais, modélisés comme infinis à travers l'épaisseur. Configurations multiples

de l'endommagement sont aussi examinées, qui correspondent à différentes étapes du processus d'amorçage des fissures transverses : décollements isolés ; décollements interagissant distribués dans la direction d'application de la charge mécanique ; décollements localisés sur fibres consécutives à travers l'épaisseur. Entre les résultats plus importants, il est constaté que ni l'épaisseur du pli à 90° ni l'épaisseur du pli à 0° influence le taux de restitution d'énergie du décollement, différemment de ce qu'a été observé pour les fissures transverses. En revanche, il est montré que le taux de restitution d'énergie est affecté de manière significative par l'interaction mutuelle entre décollements dans la direction d'application de la charge et qu'il existe une distance caractéristique (mesuré par le nombre des fibres sans endommagement) déterminant la région d'influence entre décollements.
Enfin, la taille du décollement juste après l'amorçage et la taille ultime du décollement sont estimées à partir de l'analyse de la distribution des contraintes à l'interface entre fibre et matrice (pour l'amorçage) et sur la base du critère de Griffith de la MLER. La taille maximale d'un décollement dans un stratifié croisé est estimé dans l'intervalle 40° - 60°, résultat qui est en très bon accord avec précédentes observations microscopiques disponibles dans la littérature.

Abstract

The main objective of the present work is to investigate the influence of the microstructure on debond growth along the fiber arc direction. To this end, models of 2-dimensional Representative Volume Elements (RVEs) of Uni-Directional (UD) composites and cross-ply laminates are developed. The Representative Volume Elements are characterized by different configurations of fibers and different damage states. Debond initiation is studied through the analysis of the distribution of stresses at the fiber/matrix interface in the absence of damage. Debond growth on the other hand is characterized using the approach of Linear Elastic Fracture Mechanics (LEFM), specifically through the evaluation of the Mode I, Mode II and total Energy Release Rate (ERR). Displacement and stress fields are evaluated by means of the Finite Element Method (FEM) using the commercial solver Abaqus. The components of the Energy Release Rate are then evaluated using the Virtual Crack Closure Technique (VCCT), implemented in a custom Python routine.
The elastic solution of the debonding problem presents two different regimes: the *open crack* and the *closed crack* behaviour. In the latter, debond faces are in contact in a region of finite size at the debond tip; in the latter, the debond is everywhere open and no contact exists between the faces. In the *open crack* regime, it is known that stress and displacement fields at the debond tip present an oscillating singularity. A convergence analysis of the VCCT in the context of the FEM solution is thus required to guarantee the validity of results and represents the first step of the work presented in this thesis. It is found that the total ERR does not depend on the size of elements at the debond tip, while the values of Mode I and Mode II ERR depend on element size in the *open crack* or *mixed mode* case. It is furthermore shown that Mode I and Mode II ERR do not converge, i.e. their asymptotic behavior for decreasing element size is not bounded. Thus, error reduction between successive iterations cannot be used to validate the solution and comparison with another method is required. Results obtained with the Boundary Element Method (BEM), available in the literature, are selected to this end.
Debond growth under remote tensile loading is then studied in Representative Volume Elements of: UD composites of varying thickness, measured in terms of number of rows of fibers, from extremely thin (one fiber row) to thick ones; cross-ply laminates with a central 90° ply of varying thickness, measured as well in terms of number of rows of fibers, from extremely thin (one fiber row) to thick ones; thick UD composites (modelled as infinite along the through-the-thickness direction). Different damage configurations are also considered, corresponding to different stages of transverse crack onset: non-interacting isolated debonds; interacting debonds distributed along the loading direction; debonds on consecutive fibers along the through-the-thickness direction. Among the most relevant

results, it is found that neither the 90° ply thickness nor the 0° ply thickness influences debond ERR in cross-ply laminates, differently from what is observed for transverse cracks with the so-called ply-thickness and ply-block effects. On the other hand, debond interaction along the loading direction is shown to influence significantly the Energy Release Rate, but this interaction possesses a characteristic distance (in terms of number of undamaged fibers) that defines the region of influence between debonds.
Finally, an estimation of debond size at initiation and of debond maximum size is proposed based on arguments from stress analysis (for initiation) and on Griffith's criterion from LEFM (for propagation). For a debond in a cross-ply laminate, its maximum size is estimated to lie in the range $40° - 60°$, which is in strong agreement with previous results from microscopic observations available in the literature.

Abrégé

A la fin de la deuxième décennie du XXI siècle, l'industrie du transport fait face de nombreux défis qui détermineront son évolution dans la prochaine décennie et au-delà. Le premier défi est la sensibilisation croissante du grand public aux problèmes environnementaux et, en conséquence, l'intensification de l'action gouvernementale à regard du changement climatique, fait qui détermine une montée en pression sur tous les secteurs industriels qui sont grands émetteurs et dont lesquels le transport fait partie. Le deuxième défi est représenté en revanche par la course à la réduction des prix, dû à une majeure concurrence (comme, par exemple, dans les secteurs des vecteurs spatiales avec l'entrée des acteurs privés dans le marché) et à nouveaux modèles commerciaux (comme le covoiturage dans l'industrie automobile ou les compagnies à bas prix dans le transport aérien).

Une stratégie simple mais efficace pour répondre à ces défis est la réduction du poids des structures du véhicule, en maintenant constantes la capacité payante. Le premier effet de cette stratégie est de réduire la consommation de carburant, fait qu'en revanche conduit à une réduction des émissions dans les véhicules à carburants fossiles et à l'augmentation de l'autonomie des véhicules électriques. En outre, la réduction de la quantité des matériaux utilisée dans les structures se traduit souvent en une réduction des coûts de fabrications et donc du prix pour l'utilisateur. D'autre côté le transport est un secteur dont l'attention à la sécurité est prioritaire, avec des processus de certifications extrêmement rigoureux. Cette exigence pose des contraintes considérables sur l'ampleur des interventions de réduction du poids des structures.

Le développement dans les dernières vingt ans d'un nouvel type de stratifié en polymère avec renfort en fibre, les stratifiés thin-ply, propose une solution à ce problème en offrant des stratifies considérablement plus légères avec, au même temps, des meilleures propriétés mécaniques. Nombreux essais ont en fait montré la capacité de ces stratifiés de retarder et aussi empêcher l'amorçage et la propagation des fissures transverses. Les fissures transverses représentent un mécanisme de rupture à l'échelle des plis qui a lieu plutôt tôt dans le processus d'endommagement du stratifié et qui conduit à la dégradation des propriétés mécaniques du composite et favorise l'apparition des autres formes d'endommagement (délaminage, rupture des fibres) souvent plus critique pour l'intégrité de la structure. Dans les années 1970, la capacité des stratifies composites de retarder l'amorçage des fissures transverses était observée et liée à l'épaisseur des plis. Néanmoins, l'épaisseur des thin-plies aujourd'hui sur le marché est au moins 10 fois plus

petit que celui des plis des années 1970. Ce fait se traduit par un changement d'échelle du problème, de millimètres à micromètres. Au niveau microscopique, les fissures transverses sont formées à partir de nombreux décollements (ou décohésions) entre fibre et matrice connectés entre eux. Une compréhension détaillée de mécanismes qui empêchent les fissures transverses requiert la connaissance des phénomènes d'amorçage des fissures transverse à l'échelle micromécanique et donc des conditions favorables à l'amorçage et propagation des décollements entre fibre et matrice.

L'étude de l'amorçage et de la propagation d'un décollement entre fibre et matrice rentre dans le domaine des problèmes des fissures à l'interface entre deux matériaux avec propriétés dissimilaires. Cette classe des problèmes fut initialement étudiée par Williams dans les années 1950. En utilisant les outils de l'analyse asymptotique, il dériva le profil des contraintes pour le cas de fissure ouverte, ce-à-dire qu'il n'existe aucun contact entre les lèvres du décollement. Dans l'analyse de Williams, la fissure est placée à la frontière des deux demi-plans (solution bi-dimensionnelle) constitué par deux différents matériaux. A la pointe de fissure il existe un régime oscillatoire à l'approche de la singularité dans les champs élastiques du type

$$r^{-\frac{1}{2}} \sin(\varepsilon \log r) \quad \text{with} \quad \varepsilon = \frac{1}{2\pi} \log\left(\frac{1-\beta}{1+\beta}\right); \tag{0.1}$$

où β représente un des deux paramètres de Dundurs, qui caractérisent les propriétés mécaniques d'un l'interface entre deux matériaux avec propriétés dissimilaires:

$$\beta = \frac{\mu_2(\kappa_1 - 1) - \mu_1(\kappa_2 - 1)}{\mu_2(\kappa_1 + 1) + \mu_1(\kappa_2 + 1)} \tag{0.2}$$

avec $\kappa = 3 - 4\nu$ pour conditions des déformations planes et $\kappa = \frac{3-4\nu}{1+\nu}$ pour conditions des contraintes planes, μ est le module de cisaillement, ν le coefficient de Poisson, les indices $1, 2$ se réfèrent aux deux matériaux. Ensuite, Erdogan détermina la taille de la région du régime oscillatoire de la singularité comme $10^{-6}a$, où a est la longueur de la fissure. England successivement vérifia l'existence d'une zone d'interpénétration entre les lèvres de la fissure, d'un longueur de l'ordre de 10^{-4}. L'existence de cette zone d'interpénétration, qui est une condition physiquement pas acceptable, conduisit à l'introduction par Comninou des contraintes non holonomes sur les déplacements des lèvres pour empêcher leur interpénétration. Ce choix donne lieu à l'émergence d'une région de contact entre lèvres dans le voisinage de la pointe de fissure. Les résultats de Williams et de Erdogan se réfèrent à une fissure droite mais, comme ces résultats sont dus à l'écart entre propriétés mécaniques des deux matériaux, ils s'appliquent à fissures de forme générique.

Dans le domaine de la Mécanique Linéaire Elastique de la Rupture (MLER), l'étude du décollement à l'interface entre fibre et matrice peut être menée en résolvant le problème d'une fissure à l'interface entre un inclusion circulaire et la matrice. Le problème fut résolu initialement avec les outils de l'analyse complexe par England et aussi par Perlman et

Sih, qui donnèrent l'expression des champs des contraintes, déformations et déplacements respectivement avec un seul et plusieurs décollements. A partir de ces travaux, Toya fournit l'expression du taux de restitution d'énergie pour le modèle de décollement ouvert.

L'analyse des configurations plus complexes nécessite l'adoption des outils numériques. Parìs et collaborateurs développèrent un algorithme numérique de solution sur la base de la méthode d'éléments de frontière en utilisant dans le voisinage de la pointe de fissure des éléments singuliers et discontinus. Ils utilisèrent la méthode de l'intégral de fermeture virtuelle de fissure (Virtual Crack Closure Integral en anglais oú VCCI) pour le calcul du taux de restitution d'énergie en Mode I et en Mode II. Dans un premier temps, la méthode fut développée pour le cas de fissure ouverte et validée par rapport aux résultats présentés par Toya. L'effet de la taille du maillage dans le voisinage de la pointe de fissure fut aussi étudié et la précision du calcul des champs des contraintes quantifiée. Ensuite, sur la base du travail de Comninou sur la fissure droite, les conditions non-holonomes de non-interpénétrabilité furent introduits. Ce choix conduisit à la découverte de l'existence d'une région de contact entre les lèvres du décollement si la taille de ce dernier soit plus grande d'un valeur minimal dit *critique*.

Après ces développements initiaux plutôt théoriques, les chercheurs du domaine des composites en fibre focalisèrent leur attention sur les effets de la structure du matériau sur l'amorçage et propagation du décollement au niveau micromécanique. Deux configurations géométriques de l'endommagement surfacique d'une fibre furent étudiées : le cas d'un seul décollement et le cas des deux décollements de la même taille placés symétriquement. Du point de vue du taux de restitution d'énergie, la première configuration est celle qui favorise plus le développement du décollement (ce-à-dire, dans ce cas le taux de restitution d'énergie est majeur). Ensuite, nombreux types and configurations de la charge appliqué furent analysé dans les cas d'un décollement entre une fibre et une matrice polymère de dimensions infinies, ce-à-dire dans un stratifié avec une fraction volumique des fibres tendant à zéro : compression, contraintes thermiques résiduelles, charge biaxiale traction-traction, traction-compression, compression-traction, compression-compression. Successivement, l'effet de la présence des deux fibres vierges, ce-à-dire pas endommagées, placées en différents positions par rapport à la fibre décollée fut analysé pour tous les configurations de charge appliquée précédemment mentionnées. Récemment, l'attention a été placée sur l'effet de l'épaisseur du pli à 90° et des plis à 0° dans stratifiés croisés en étudiant modèles avec une fibre avec décollement située dans un milieu homogénéisé.

Dans le domaine de la Mécanique Linéaire Elastique de la Rupture, il manque un traitement de l'effet des caractéristiques de la microstructure du stratifié à courte et longue distance. En effet, les études précédentes ont considéré des configurations simplifiées : une seule fibre avec décollement dans un milieu (matrice polymère) infinie, une fibre centrale avec décollement et deux autres fibres soit vierge (sans endommagement) ou avec décollement dans un milieu infinie, une seule fibre avec décollement dans un

milieu (pli à 90°) homogénéisé, une fibre centrale avec décollement et deux autres fibres soit vierge (sans endommagement) ou avec décollement dans un milieu (pli à 90°) homogénéisé.

L'objectif principal de cette thèse est d'étudier l'effet de la microstructure sur l'amorçage et propagation de décollements entre fibre et matrice. Dans ce but, des modèles de Volume Elémentaire Représentatif (VER) des composites unidirectionnels et des stratifiés croisés sont développés, caractérisés par différentes configurations des fibres et degré d'endommagement. L'amorçage du décollement est analysé par rapport à la distribution des contraintes à l'interface entre fibre et matrice. En revanche, la propagation du décollement est étudiée avec l'approche de la Mécanique Linéaire Elastique de la Rupture (MLER), et plus spécifiquement avec l'évaluation du taux de restitution d'énergie en Mode I et Mode II. Les champs de déplacement et contrainte sont calculés avec la Méthode des éléments finis (MEF) dans le logiciel Abaqus. La détermination des composants du taux de restitution d'énergie est effectuée avec la technique de fermeture virtuelle de fissure implémentée par l'auteur en langage Python.

La solution élastique du problème de décollement entre fibre et matrice est caractérisée par la présence de deux régimes : celui de fissure ouverte et celui de fissure fermée. Dans le deuxième cas, il existe une zone proche de la pointe de fissure où les lèvres du décollement sont en contact. Dans le premier cas, le décollement est ouvert et il n'existe aucun contact entre les lèvres du décollement. Dans le régime de fissure ouverte, les champs des déplacements et contraintes présentent une singularité oscillatoire. Un 'étude de convergence de la technique de fermeture virtuelle de fissure est donc requis et constitue le premier élément du travail de cette thèse. Il est constaté que le taux de restitution d'énergie total ne dépend pas de la taille des éléments proches de la pointe de fissure, alors que le taux en Mode I et Mode II présent une dépendance significative de la taille des éléments dans le cas de fissure ouverte. Il est montré que le taux de restitution d'énergie en Mode I et Mode II ne converge pas, ce à dire que le comportement asymptotique n'est pas limité. Par conséquence, il n'est pas possible d'utiliser l'erreur entre itérations successives comme mesure de la convergence de la solution et une comparaison est donc nécessaire avec des résultats obtenus avec une autre méthode. Le taux de restitution d'énergie calculé avec la méthode d'éléments de frontière, disponible dans la littérature, est choisi comme référence.

Ensuite, la propagation de décollement entre fibre et matrice est étudiée dans Volume Elémentaire Représentative de : composites unidirectionnels avec épaisseur variable, mesuré par le nombre des rangées des fibres, de ceux extrêmement minces (une rangée des fibres) au plus épais ; stratifié croisé avec un pli central à 90° d'épaisseur variable, mesuré par le nombre des rangées des fibres, de ceux extrêmement minces (une rangée des fibres) au plus épais ; composites unidirectionnels épais, modélisés comme infinis à travers l'épaisseur. Configurations multiples de l'endommagement sont aussi examinées, qui correspondent à différentes étapes du processus d'amorçage des fissures

transverses : décollements isolés ; décollements interagissant distribués dans la direction d'application de la charge mécanique ; décollements localisés sur fibres consécutives à travers l'épaisseur. Entre les résultats plus importants, il est constaté que ni l'épaisseur du pli à 90° ni l'épaisseur du pli à 0° influence le taux de restitution d'énergie du décollement, différemment de ce qu'a été observé pour les fissures transverses. En revanche, il est montré que le taux de restitution d'énergie est affecté de manière significative par l'interaction mutuelle entre décollements dans la direction d'application de la charge et qu'il existe une distance caractéristique (mesuré par le nombre des fibres sans endommagement) déterminant la région d'influence entre décollements.

Enfin, la taille du décollement juste après l'amorçage et la taille ultime du décollement sont estimées à partir de l'analyse de la distribution des contraintes à l'interface entre fibre et matrice (pour l'amorçage) et sur la base du critère de Griffith de la MLER. La taille maximale d'un décollement dans un stratifié croisé est estimé dans l'intervalle 40° - 60°, résultat qui est en très bon accord avec précédentes observations microscopiques disponibles dans la littérature.

List of publications

Appended papers

Paper A
Luca Di Stasio, Zoubir Ayadi (2019). Finite Element solution of the fiber/matrix interface crack problem: convergence properties and mode mixity of the Virtual Crack Closure Technique. *Finite Elements in Analysis and Design*, 167, 103332.

Paper B
Luca Di Stasio, Janis Varna, Zoubir Ayadi (2019). Energy release rate of the fiber/matrix interface crack in UD composites under transverse loading: effect of the fiber volume fraction and of the distance to the free surface and to non-adjacent debonds. *Theoretical and Applied Fracture Mechanics*, 103, 102251.

Paper C
Luca Di Stasio, Janis Varna, Zoubir Ayadi (2019). Effect of the proximity to the 0°/90° interface on Energy Release Rate of fiber/matrix interface crack growth in the 90°-ply of a cross-ply laminate under tensile loading. Submitted to *Journal of Composite Materials*.

Paper D
Luca Di Stasio, Janis Varna, Zoubir Ayadi (2019). Growth of interface cracks on consecutive fibers: on the same or on the opposite sides? Submitted to *Proceedings of the 12^{th} International Conference on Composite Science and Technology (ICCST 12)*, in: *Materials Today: Proceedings*.

Paper E
Luca Di Stasio, Janis Varna, Zoubir Ayadi (2019). Estimating the average size of fiber/matrix interface cracks in UD and cross-ply laminates. *Proceedings of the 7^{th} EC-COMAS Thematic Conference on the Mechanical Response of Composites*.

Other relevant contributions

Peer-reviewed journal publications

Luca Di Stasio, Janis Varna, Zoubir Ayadi (2019). Effect of the mutual interaction between debonds on Energy Release Rate on the potential fracture plane. To be submitted to *Applied Composite Materials*, special issue for the *12th International Conference on Composite Science and Technology (ICCST 12)*.

Conference proceedings

Luca Di Stasio, Janis Varna, Zoubir Ayadi (2018). Effect of boundary conditions on microdamage initiation in thin ply composite laminates *Proceedings of the 18th European Conference on Composite Materials (ECCM18)*.

Conference contributions (oral)

Luca Di Stasio, Janis Varna, Zoubir Ayadi (2019). Estimating the average size of fiber/matrix interface cracks in UD and cross-ply laminates. 7th ECCOMAS Thematic Conference on the Mechanical Response of Composites - September 18-20, 2019 - Girona, Spain.

Luca Di Stasio, Janis Varna, Zoubir Ayadi (2019). Ply-thickness effect on fiber-matrix interface crack growth. 9th International Conference on Composite Testing and Model Identification (COMPTEST2019) - May 27-29, 2019 - Luleå, Sweden.

Luca Di Stasio, Janis Varna, Zoubir Ayadi (2019). Growth of interface cracks on consecutive fibers: on the same or on the opposite sides? 12th International Conference on Composite Science and Technology (ICCST12) - May 8-10, 2019 - Sorrento, Italy.

Luca Di Stasio, Janis Varna, Zoubir Ayadi (2019). Investigation of scaling laws of the fiber/matrix interface crack in polymer composites through finite element-based micromechanical modeling. 10th EEIGM International Conference on Advanced Materials Research - April 25-26, 2019 - Moscow, Russia.

Luca Di Stasio, Janis Varna, Zoubir Ayadi (2018). Effect of boundary conditions on microdamage initiation in thin ply composite laminates. 18th European Conference on Composite Materials (ECCM18) - June 24-28, 2018 - Athens, Greece.

Luca Di Stasio, Janis Varna, Zoubir Ayadi (2017). Micromechanical modeling of thin ply effects on microdamage in Fiber Reinforced Composite laminates. International Materials Research Meeting of the Greater Region (IMRM) - April 6-7, 2017 - Saarbrücken, Germany.

Contents

Part I **1**

Chapter 1 – A journey of scales 3
1.1 Introduction and structure of the thesis . . . 3
1.2 Vision 2030: challenges of the next decade and beyond for the transportation industry . . . 4
1.3 *Thin-ply* laminates and the *spread tow* technology . . . 11
1.4 Onset and propagation of transverse cracking at the microscale: experimental observations and computational modeling . . . 14
1.5 The fiber-matrix interface crack in LEFM . . . 19
1.6 Objectives of the thesis . . . 21

Chapter 2 – Summary of appended papers 23
2.1 Paper A . . . 23
2.2 Paper B . . . 27
2.3 Paper C . . . 33
2.4 Paper D . . . 36
2.5 Paper E . . . 43

References 49

Part II **59**

Paper A 61
1 Introduction . . . 63
2 FEM formulation of the fiber-matrix interface crack problem . . . 66
3 Vectorial formulation of the Virtual Crack Closure Technique (VCCT) . . . 68
4 Rotational invariance of G_{TOT} . . . 73
5 Convergence analysis . . . 75
6 Conclusions & Outlook . . . 80
References . . . 86
A Derivation of the relationship between crack tip forces and displacements for first order quadrilateral elements . . . 89
B Expression of the VCCT weights matrix for quadrilateral elements with or without singularity . . . 97

Paper B 99
A Introduction . . . 101
B RVE models & FE discretization . . . 103
C Results & Discussion . . . 109
D Conclusions & Outlook . . . 120
References . . . 121

Paper C 125
A Introduction . . . 127
B RVE models & FE discretization . . . 129
C Results & Discussion . . . 135
D Conclusions . . . 144
References . . . 146

Paper D 151
A Introduction . . . 153
B Representative Volume Elements (RVEs) . . . 156
C Finite Element solution . . . 159
D Results & discussion . . . 160
E Conclusions . . . 164
References . . . 165

Paper E 169
A Introduction . . . 171
B RVE models and FE discretization . . . 172
C Stress-based analysis of debond initiation ($\Delta\theta = 0^\circ$) . . . 176
D Energy-based analysis of debond propagation . . . 177
E Conclusions . . . 180
References . . . 182

Part I

Chapter 1

A journey of scales

> . . . a "sage", as an anonymous writer has pointed out, "calls up in the average mind the picture of something grey and pedantic if not green and aromatic".
>
> Arthur D. Little [1]

1.1 Introduction and structure of the thesis

Passion and curiosity should always lie at the heart of the scientific practice, and that ought to be enough to define the value of a research effort [2, 3]. Time is the real arbiter of the significance of a piece of research, as many examples in the history of science show [4, 5][1].However, in these years of increasing mistrust towards scientific research and brewing doubts about the value of universities and research institutes [7, 8, 9], it is worthwhile to try to place one's own work into the wider picture of one's own time. It is also a valuable exercise for the researcher, who sensibly progresses in the work by investigating one detail at a time, to spend a moment away from one's own graphs and equations and see their place in the wider perspective of the world outside the laboratory.
It is thus in this spirit that I propose to open the present work with a reflection on the

[1]The Ising-Lenz model is one such example [4, 5, 6]. It was suggested by physicist Wilhelm Lenz to his doctoral student Ernst Ising to study phase transitions in ferromagnetic materials. Ising solved it analytically in 1D as part of his Ph.D. defense in 1925, but the solution for a 1D lattice did not show any phase transition. This apparent failure is thought to be the reason of Ising's decision to take a job outside academia. Almost 20 years later, Onsager solved the 2D version of the model and showed the possibility of phase transitions in the Ising-Lenz model. By the time Ising arrived in the USA in 1947, the Ising-Lenz model was already entering the canon of physics and, to his surprise, he was being asked if he was "the Ising" of the "Ising model".

challenges that the transportation industry faces at the closing of 21^{st} century's second decade. Against this background, in Chapter 1 *thin-ply* laminates are introduced as a very promising material for innovative structural design and their main characteristics are discussed. The focus is then moved to the most renown quality of thin-ply laminates, i.e. their ability to delay and even suppress onset and propagation of transverse cracking, and to discuss the modeling issues that this new material poses. A link is established with the growth of fiber/matrix interface cracks or, as very often called in the rest of the thesis, debonds. The fiber/matrix interface crack is then discussed in detail, and previous analytical, computational and experimental studies available in the literature are reviewed. At the end of this first chapter, the objectives of this thesis are then presented. Finally, Chapter 2 provides a summary of the main results of this work, organized following the order of the publications reported in Part II of the thesis. The first chapter is thus a journey of scales: we start from the challenges of an industrial sector, move to the structural requirements of its products, focus on a promising new material, and concentrate on understanding the mechanisms of damage initiation and propagation.

1.2 Vision 2030: challenges of the next decade and beyond for the transportation industry

The closing of the second decade of the 21^{st} century brings different challenges for the transportation industry, which will likely shape its development in the next decade and beyond. A brief review of the most relevant aspects is proposed here.

Climate action. The issue of climate change is certainly one the "hot" topic of today's public debate. A discussion of the merits of scientific understanding of climate change, public reception, media coverage and socio-political implications is out of the scope of the present work, but it is certainly one of the most relevant topic framing today's public discourse. Given that it is a high-divisive subject, no judgement on the validity of the claims of one side or the other is proposed here, as sufficient space can not be devoted to a thorough analysis of the problem. What is acknowledged here is the emergence of concerted efforts at the institutional level (companies, city administrations, regional governments, sovereign states) to rule into and provide control mechanisms to limit the emission of carbon dioxide, i.e. CO_2. The evidence of this shift in public policy is exemplified in Figure 1.1 and Figure 1.2.

Figure 1.1 reports the evolution over time of the number of signatories of three representative deals on climate action. The selected deals are: the Vienna Convention for the Protection of the Ozone Layer, first signed in 1985 and committing signatories to the reduction of chlorofluorocarbons; the United Nations Framework Convention on Climate Change (UNFCCC), initially agreed in 1992 with the aim of managing the increase in greenhouse emission in order to avoid dangerous interferences with the climate; the Kyoto Protocol, signed in 1997 as an extension of the

UNFCCC and according to which adhering countries pledge to reduce greenhouse emissions to prevent climate change. Figure 1.1 shows how the majority of countries have ratified these deals over time, reaching an almost unanimous agreement on the need of coordinated action towards the issues of climate change.

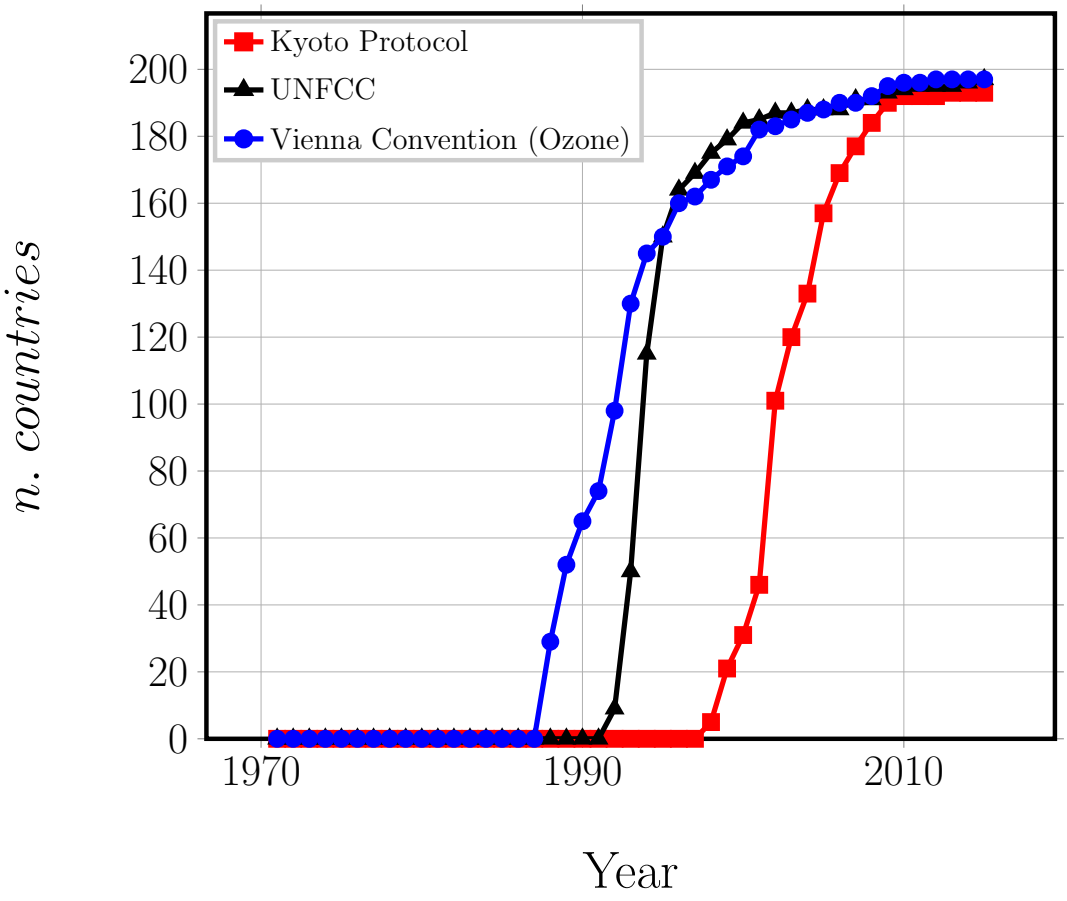

Figure 1.1: Number of signing countries over time for selected deals on climate. Source: UNCTAD Development and Globalization: Facts and Figures (2016). United Nations Conference on Trade and Development. Available at https://stats.unctad.org/Dgff2016/DGFF2016.pdf (last access: September 26, 2019).

Figure 1.2 shows the 10 highest contributions to the Green Climate Fund, which aims to support projects in developing countries focusing on reduction of greenhouse gas emissions and climate adaptation. The commitment to this effort of industrialized countries is evident in Figure 1.2. It is thus apparent from Figure 1.1 and Figure 1.2 that a shift in public attitude and policy towards the issues of climate change has been under way in the last decades. This shift in turn has been materialized in the form of international agreements on climate action, which have led to the introduction of novel regulations aimed at containing the emission of

CO_2 and other pollutants into the atmosphere and biosphere at large.

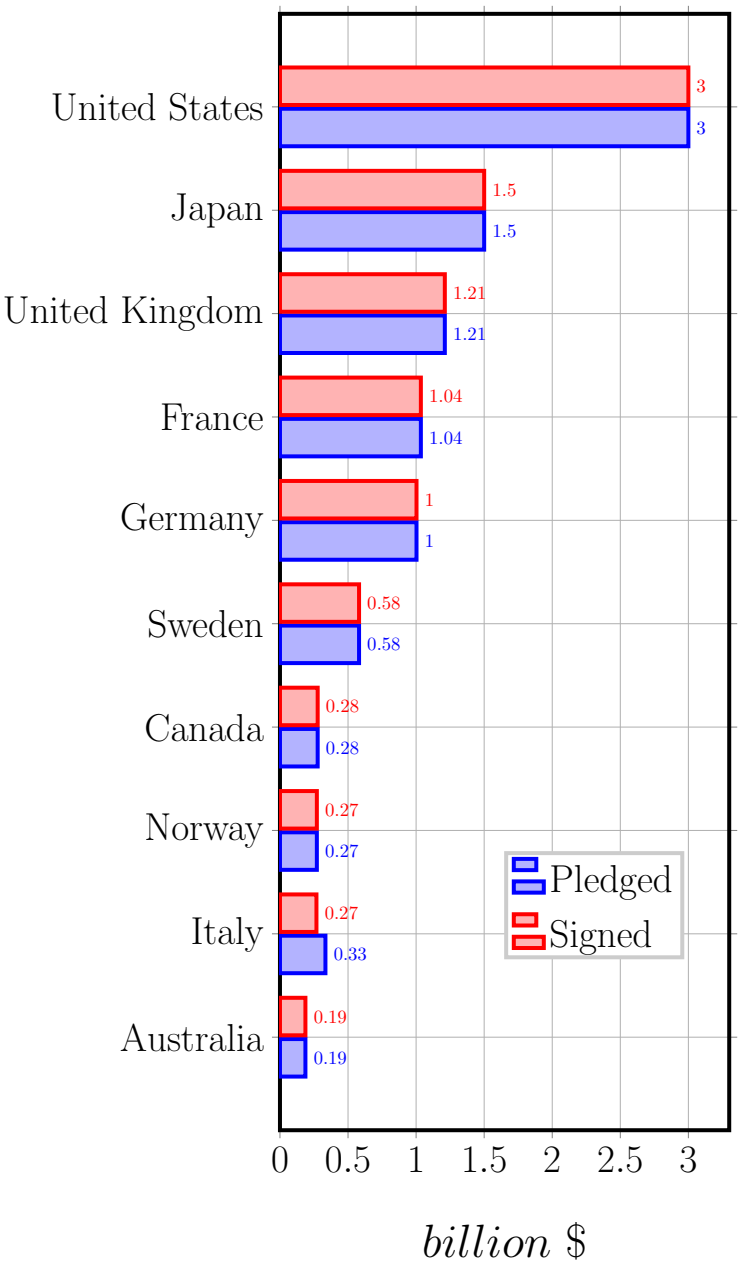

Figure 1.2: Pledged and signed contributions to the Green Climate Fund of the 10 countries with the highest signed contributions. Source: Green Climate Fund, available at https://www.greenclimate.fund/how-we-work/resource-mobilization (last access: September 21, 2019).

It is interesting to understand the impact of this shift on the transport industry by looking at some representative data of its CO_2 emissions. In Figure 1.3 the

share of total CO_2 emissions is reported for some selected countries. The first observation is that the role of the transport industry as a source of CO_2 has been increasing over the years. Today it accounts for around 30% of total emissions in large mature economies such as the United States and the European Union, around 20% of Japan's emissions and 10% of China's.

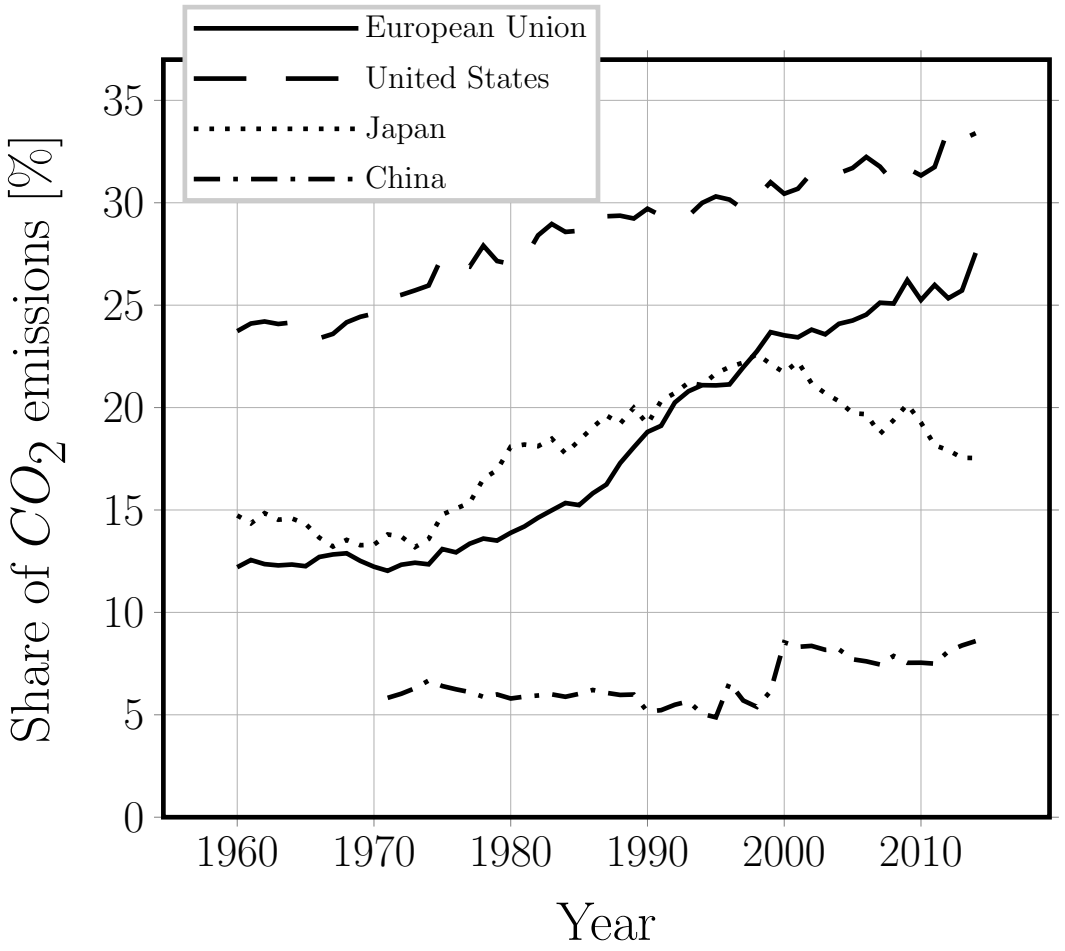

Figure 1.3: Share of total CO_2 emissions due to the transport sector over time for selected countries. Source: International Energy Agency (IEA) via The World Bank, available at http://data.worldbank.org/data-catalog/world-development-indicators (last access: September 21, 2019).

A second perspective on the problem in provided in Figure 1.4, where the evolution of CO_2 total emissions (in absolute terms) for selected world geographical entities is compared with that of international transport. Interestingly, the emissions of the latter has been comparable in the last 50 years to those of the African continent as a whole.

It is thus clear from Figure 1.3 and Figure 1.4 that the transport sector plays a

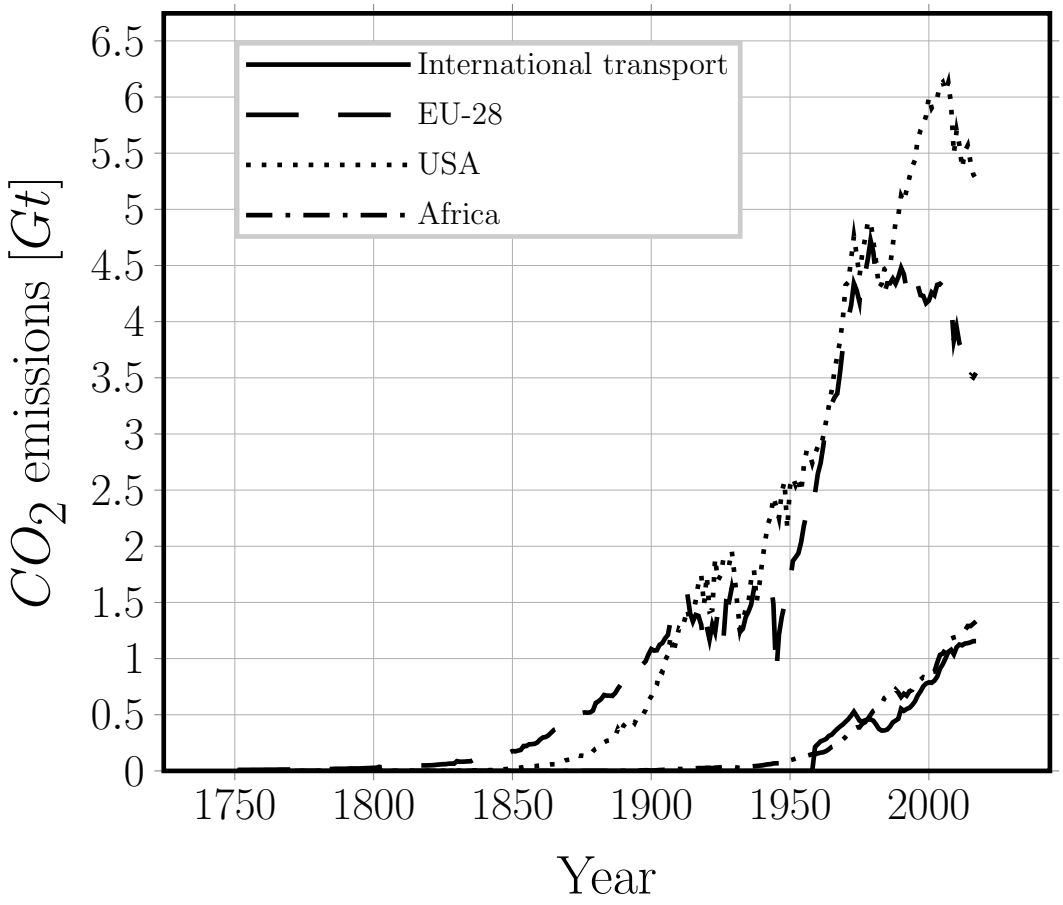

Figure 1.4: Total CO_2 emissions due to transport over time, compared with selected geographical entities. Source: The Global Carbon Project, available at https://www.globalcarbonproject.org/ (last access: September 21, 2019).

prominent role in the emission of CO_2 and other pollutants into the biosphere. It is, and will be, strongly affected by the emphasis on climate change that currently characterizes international public policy. Stricter standards on emissions are planned or expected in several parts of the world and the transport industry, currently one of the biggest emitter, needs to innovate to adapt to this change.

Increased competitiveness. During the last couple of decades, the arrival of new players and the introduction of new business models have increased competitiveness in the transport sector and favored a downward pressure on prices. Several examples exist. In civil aviation, the diffusion of low-cost carriers such as Ryanair^{TM}, easyJet^{TM} and Norwegian^{TM}, which offer very (and sometimes even extreme) low rates by drastically reducing the number of ancillary services comprised in the ticket price, which are then offered as pay-as-you-go additional services. The space sector has seen the arrival of a number of private actors which are developing or are already proposing on the market low-Earth launching technologies signifi-

cantly cheaper than market incumbents. In the car industry, ride-sharing (such as BlaBlaCar^{TM}) and ride-hailing services (like Uber^{TM} and Lyft^{TM}) are leading to a change in the importance of car ownership and, thus, in the role of car manufacturers.

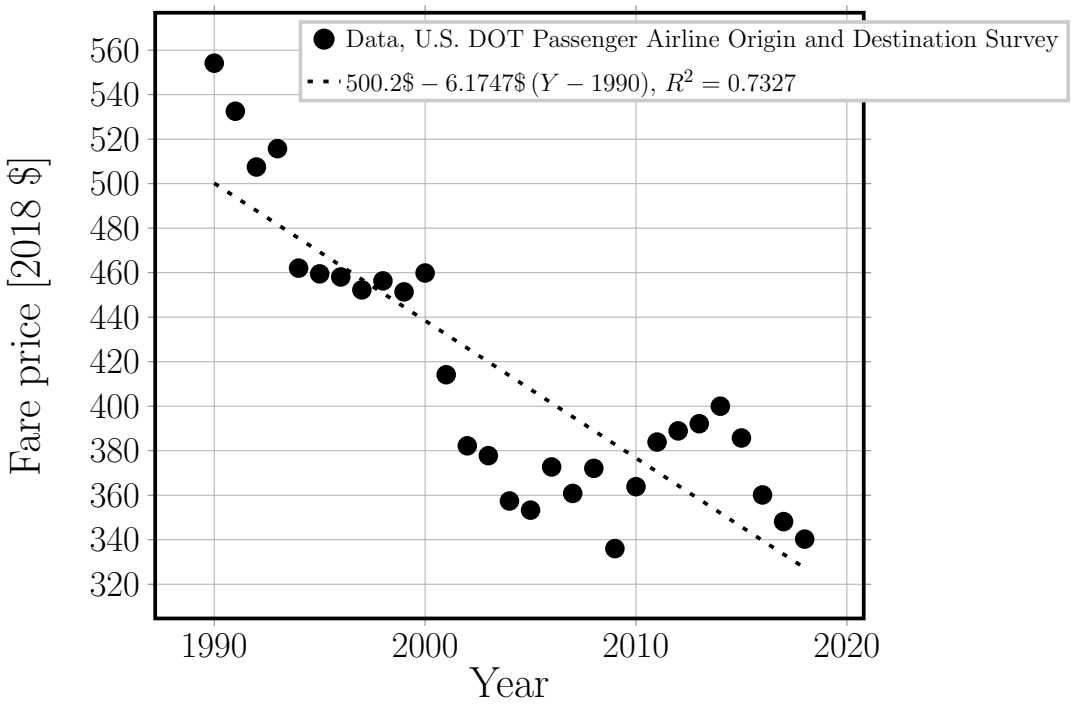

Figure 1.5: Average airline fare in the United States over the years, prices in 2018 $. *Source: U.S. DOT Passenger Airline Origin and Destination Survey, available at https://www.transtats.bts.gov/DatabaseInfo.asp?DB_ID=125 (last access: October 11, 2019).*

Two representative examples of the reduction of prices over time in the transport industry are shown in Figure 1.5 and in Figure 1.6. In Figure 1.5, the evolution of fare prices (expressed in 2018 US $) over the past three decades in the United States is reported. A clear downward trend is observable and a linear regression of the data provides a negative slope with a R^2 coefficient of 0.7327. Figure 1.6 presents the unit cost (expressed in 2018 US $) of payload for several different launch system with respect to time. Three systems are in particular highlighted: the Vanguard, the first one in history; the Space Shuttle, for introducing the concept of launch system reusability; the Falcon Heavy, for bringing to the market a privately managed reusable launcher system. Albeit with some scatter, it is possible to observe a downward trend of prices. A linear regression of the logarithm of price with respect to time provides an estimate of the year-on-year price decrease at around 3%, i.e. a 30% every decade.

Safety and crashworthiness. Strict requirements on vehicles safety and crashworthi-

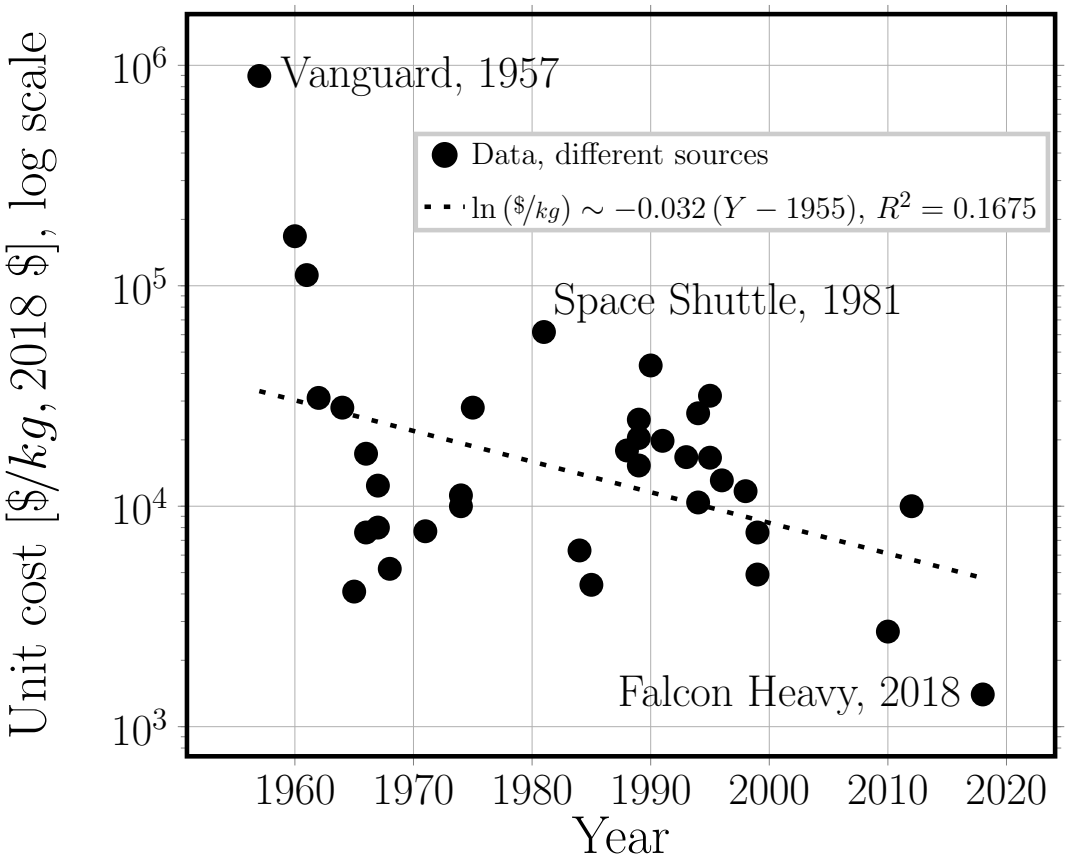

Figure 1.6: Evolution of unit cost of payload for different launching systems over time, prices in 2018 $. *From [10].*

ness are not a novelty of the 2010's, as legislation has been built over the years to create a system of control and verification to ensure that vehicles' structures are reliable under normal operating life as well as exceptional conditions. However, the recent crashes of the two Boeing 737 MAX 8 planes of Lion Air in Indonesia [11] and of Ethiopian Airlines in Ethiopia [12] have put the issue of safety and crashworthiness back into the spotlight, as the cause of the crashes was a technical glitch in the automatic guidance and control system. Thus, although the problem is one of software development and control system engineering, it calls for a revision of current practices of oversight and certification. For the structural designer, requirements of safety and crashworthiness translate into a thorough understanding of structural failure mechanisms, and thus of the evolution of damage in the materials employed.

These issues are framing the evolution of the transport industry over the next decade, particularly in technological terms. Their requirements are often incompatible and current solutions represent often a trade-off between them. Renewed efforts are thus devoted to the development of materials that could satisfy at the same time the needs of sustainability, price reduction and structural safety.

1.3 *Thin-ply* laminates and the *spread tow* technology

A very promising material introduced into the market by the composite industry in recent times is the so-called *thin-ply* laminate, result of a series of advancements in the *spread tow technology*. Conventionally, fibers are produced as bundles or *tows* comprising $12/24k$ filaments; tows are then stacked together and impregnated in order to produce prepreg plies. At the heart of the *spread tow technology* lies the idea of opening or *spreading* such tows to create thinner and wider tapes, to be then used in the production of unidirectional (UD) prepregs or woven fabrics, as schematically depicted in Figure 1.7.

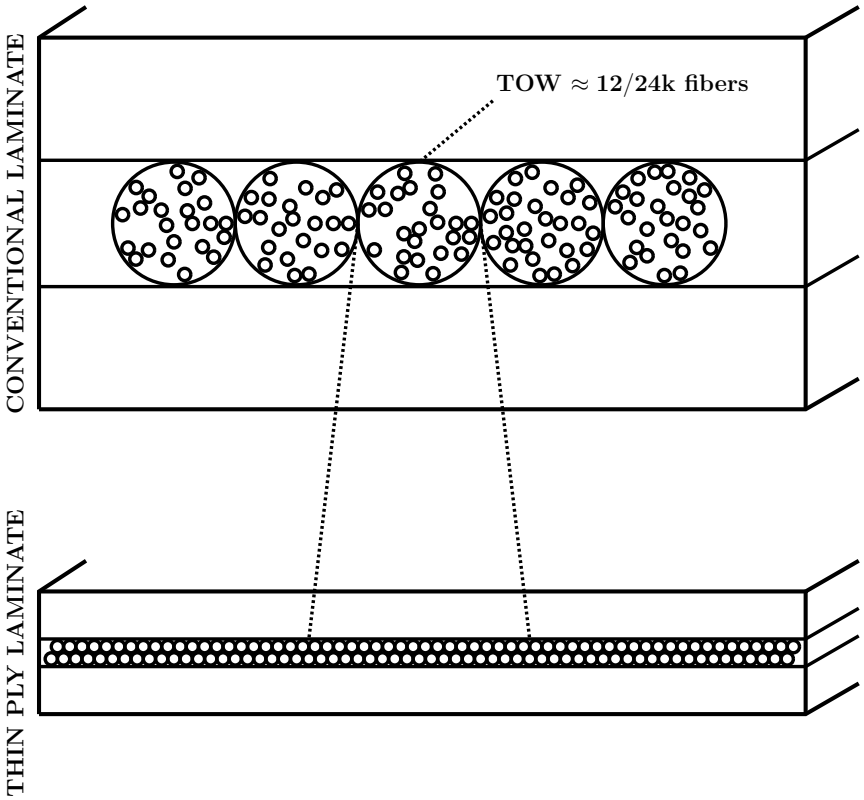

Figure 1.7: Schematic of the difference between laminates with conventional prepreg plies and thin-ply *laminates, issued from the spread tow technology.*

First attempts to turn the idea into practice date back to the 1970's [13], when a Venturi injector opposite to the pulling direction of fibers was employed to split the tow. Other methodologies were then proposed, among others: acoustic vibrations in air generated by a speaker or similar apparatus below the tow [14]; mechanical separation by means of cylindrical rollers [15]; the use of expandable elastic bands (or tubes) mounted on a rotating drum [16]; electrostatic separation employing a corona discharge [17]. Nonethe-

less, they all suffered from a number of drawbacks: among the most critical, widespread breakages of fibers and deterioration of fiber surface properties, in particular wettability. A breakthrough arrived at the end of the 1990's, with the publication in 1997 of a contribution to the 42^{nd} SAMPE USA conference detailing a new spreading technique [18] developed at the Industrial Technology Center in Japan's Fukui Prefecture. The so-called "Fukui" technique (from the name of the Japanese prefecture), further improved in subsequent years [19, 20, 21], is based on the combined use of focused air jets and a vacuum pump perpendicular to the pulling direction of fibers. Thanks to its capacity to avoid fiber breakage and fiber surface property loss, the technology has been applied on industrial scale to produce high-quality extremely thin fiber-reinforced prepreg plies. Only a few manufacturers exist today that produce thin-ply laminates, among them North Thin Ply Technology (NTPT) [22] in Switzerland (founded in 2001), Oxeon [23] in Sweden (founded in 2003), Chomarat [24] in France, Sakai Ovex [25] in Japan. The technology is now reaching a mature stage and proposals have been made to use thin-ply laminates in primary load-carrying structural in safety critical applications such as Low-Earth Orbit (LEO) satellites [26], airplane wings [27], pressure vessels for cryogenic fuels [28], re-usable space launchers [29].

Probably the first assessment of the mechanical performance of thin-ply laminates was published by the developers of the *spread tow* technology themselves in 2004 in the Journal of the Japan Society for Composite Materials [30]. They studied the effect of ply thickness on first-ply failure in quasi-isotropic carbon fiber laminates under static tensile loading and observed an increase of the value of the stress at first ply failure. Soon after, K. Yamaguchi and H. T. Hahn [31] reported that, in cross-ply laminates subjected to static tensile loading, no transverse crack and no delamination was observed in the thin-ply specimen. According to the authors, fatigue behavior was also improved in thin-ply laminates: the rate of growth of micro-cracks density was slowed and no transverse-crack induced delamination appeared even after 10^6 cycles. The same year (2005), two contributions [32, 33] by S. Tsai and collaborators confirmed these observations. They tested cross-ply and quasi-isotropic laminates in simple static tension, static open hole tension and fatigue, and observed the suppression of micro-cracking and transverse-cracking induced delaminations. A number of experimental studies on thin-ply laminates then followed, following the increasing interest from industry and responding to the need of the latter to characterize and standardize the properties of this new type of composite material. A comprehensive mechanical characterization of carbon fiber thin-ply laminates is described in [34]. Here the authors compare the results of different tests between two different types of quasi-isotropic laminates, both made with the same number of ply and with the same *spread-tow* but with different effective thicknesses of the layers: the first type, namely the "thick" laminate, has layers made up by 5 plies for a thickness of 200 μm; the second, namely the "thin" laminate, has layers made up by only 1 ply for a thickness of 40 μm. In the case of unnotched tension, the ultimate strength of the "thin" laminate was found to be 10% higher than that of the "thick" laminate and no transverse crack was observed in the "thin" laminate. Similarly, no micro-damage was detected in the "thin" laminate in the case of unnotched tension-tension cyclic fatigue loading.

The same observation was made in open-hole specimens under static tension and tension-tension fatigue loading, where practically no damage was observed in the "thin" laminate. However, the final static failure of the "thin" laminate occurred at a value roughly 10% lower than that of the "thick" laminate. In-depth ultrasonic scans of plates subjected to impact showed roughly equal delaminated areas between the two types of laminates, but Compression After Impact (CAI) tests seemed to point to a delay in the onset of buckling instability in the "thin" laminate. However the analysis was not conclusive regarding the impact behavior of thin-ply laminates. A subsequent work [35] addressed in more detail this point and focused on the experimental assessment of the compressive and impact behavior of thin-ply laminates. In particular, quasi-isotropic laminates made from standard and thin-ply prepregs made of the same carbon fiber/toughened epoxy system were subjected to static tensile tests, tension-tension cyclic fatigue loading, Non-Hole Compression (NHC), Open Hole Compression (OHC) and CAI tests. The results from static and fatigue tension confirmed the observations of [34]. NHC and OHC tests showed an increase of respectively 16% and 9% of the final failure stress in thin-ply laminates with respect to conventional ones. C-scans after impact and CAI confirmed the results proposed in [34]: delamination areas of similar size but CAI strength 8% higher in thin-ply laminates. The same authors later investigated the response of thin-ply laminates to out-of-plane transverse loads [36], comparing quasi-isotropic laminates made of standard and thin-ply prepreg employing the same carbon fiber/toughened epoxy material system subjected to transverse indentation. They analyzed the evolution of damage through X-ray inspection and reported significantly different damage growth behaviors between thin-ply and standard laminates. Saito and colleagues [37] conducted *in-situ* edge observations of transverse crack onset and propagation in the central 90° layer on thin-ply carbon fiber laminates under tensile loading. The laminates had different thicknesses, controlled by the number of thin-ply prepreg sheets used to manufacture the 90° layer. The 0° layer had always the same thickness and was made of a conventional carbon fiber prepreg. They reported that, by decreasing the thickness of 90° layer, the occurrence of transverse cracks was delayed to higher levels of the applied strain and even, in the thinnest case (only one prepreg ply), suppressed. Recently, extensive experimental assessments of thin-ply laminates were conducted in [38] and [39], with the aim of characterizing the effect of ply thickness, fibre, matrix and interlayer properties. Their results confirmed the previous observations on the delay and suppression of transverse cracking in thinner plies.

Looking at the different experimental investigations on thin-ply laminates, it seems apparent that there exists a point of agreement between all them. And it is that the main advantage of thin-ply laminates is their capability, increasing with decreasing layer thickness, to delay to higher levels of the applied strain, and for very thin layers even suppress, the appearance of transverse cracks and transverse-cracking induced delaminations. In turn it implies that thin-ply laminates undergo a path of damage evolution different from that observed in conventional laminates. Given that subcritical damage, like transverse cracks and transverse-cracking induced delaminations, appears later, or even not at all, in the loading process, the marked degradation of elastic properties observed in con-

ventional laminates is not present in thin-ply ones. In laminates with very thin plies, where subcritical damage is suppressed, the final laminate failure has been recorded to occur practically at fiber failure strain level [39]. This means that, on one side, thin-ply laminates can sustain much higher loads than the conventional counterpart without degradation of their mechanical properties, by using the same fiber and matrix materials and the same layups and by only changing the thickness of the plies. However, on the other hand, final laminate failure occurs more abruptly and in a very brittle manner, which makes the use of thin-ply laminates in structural applications more critical.

1.4 Onset and propagation of transverse cracking at the microscale: experimental observations and computational modeling

The characteristic of thin-ply laminates to delay, and even suppress, the occurrence of transverse cracking is not actually a peculiarity of this material, but the result of a phenomenon, called *ply-thickness effect* or also *in-situ effect*, that has been observed much earlier in conventional laminates. When fiber reinforced polymer composites started to be used in primary structures in aeronautical applications during the 1960's, a comprehensive literature on failure mechanisms and damage accumulation processes in laminates was lacking [40]. Researcher focused on the observation and quantification of failure mechanisms in glass fiber reinforced polymers [40, 41, 42], and later on in carbon fiber reinforced polymers. Working on glass fiber/epoxy cross-ply laminates subjected to tensile loading, Bailey and co-workers first observed the occurrence of transverse cracks [43] (see Figure 1.8 for an example of transverse cracking in a glass fiber/epoxy specimen) at strain levels much lower than the matrix failure strain. They noticed that cracks run parallel to the reinforcement in the ply and were, on average, spaced evenly along the specimen, as exemplified in Figure 1.8. They further observed that [43, 44] the spacing between cracks decreased with decreasing 90° layer thickness. Analysis of the stress-strain response in [44] revealed the occurrence of a decrease in the elastic modulus in the absence of transverse cracks but associated with the appearance of a whitening effect. They provided the first account of the *ply-thickness effect* in a subsequent work [45], where they reported, for glass fiber/epoxy cross-ply specimens, an increase in the value of the applied strain at which the first transverse crack spanning the whole specimen width was recorded. They referred to this value of the strain as ε_{tu} and distinguished it from ε_{ti}, the value of the applied strain at which the first edge crack (not tunneling through the width of the specimen) appeared. They also noticed that, for larger values of the 90° layer thickness, values of ε_{tu} and ε_{ti} were close, as crack propagation through the thickness and through the width occurred almost instantaneously; for thinner 90° layers, ε_{tu} increased faster than ε_{ti} as through-the-width tunneling was much slower than through-the thickness propagation. At very low thicknesses, around $\sim 100\ \mu m$, of the 90° inner layer, transverse cracking was suppressed. The whitening effect first observed in [44] was determined in [46, 47] to be due to the appearance of fiber/matrix interface

cracks (or debonds, shown in a glass fiber/epoxy specimen in Figure 1.10). Fiber/matrix debonding was identified as the microscopic mechanism responsible for onset and propagation of transverse cracks [46].

Onset of debonding at the fiber/matrix interface was addressed by Asp and colleagues, who investigated the behavior epoxy under a tri-axial stress state as the one occurring in the inter-fiber regions [48]. They reported that, under such conditions, epoxy fails at very low strains ($\sim 0.5\% - 0.8\%$) [48] and in a brittle manner [49] through a cavitation-like failure mechanism taking place at, or extremely close to, the fiber/matrix interface. Debond growth was studied in two glass fiber/epoxy systems with in-situ optical microscopy on a single-fiber specimen under tension transverse to the fiber direction in [50]. They observed debond growth along the fiber arc direction until a critical size, after which unstable growth in the fiber longitudinal direction occurred at approximately constant angular size. Recently, Scanning Electron Microscopy (SEM) and synchrotron-based 3D X-ray microtomography were applied to in-situ observations of fiber/matrix debonding in a glass fiber/epoxy single-fiber specimen under tension [51]. The three dimensional quantitative assessment of debonding confirmed the previous observations presented in [50]. The authors, in fact, reported debond initiation to occur at the specimen edge and at the same time at 0° and at 180° with respect to the loading direction. The initial size of debonds was measured and found to be $\sim 18°$. Then, the two debonds propagated symmetrically along the arc direction of the fiber until a critical size of 140° (or $\Delta\theta = 70°$ following the nomenclature used in the rest of thesis) was reached. Finally, unstable propagation along the length of the fiber occurred, reaching conditions of self-similar steady-state growth at constant debond angular size of 48° ($\Delta\theta = 24°$ after a small transition distance from the edge of the specimen.

By taking an holistic view on the observations reported in [43, 44, 45, 46, 47, 50, 51], it is possible to propose a model of initiation and propagation of transverse cracking at the microscale in fiber-reinforced composites organized in several steps:

1. failure at the fiber/matrix interface occurs on a certain number of isolated fibers, i.e. not adjacent to another damage fiber, and an initial debond is formed (Figure 1.11a);

2. stress re-distribution causes other interfaces to fail in the neighborhood, until a contiguous group of partially debonded fibers is present (Figure 1.11b);

3. debond growth occurs along the arc direction until a critical size is reached, then the crack kinks out of the interface (Figure 1.11a);

4. coalescence of debonds occurs and a through-the-thickness crack is formed (Figure 1.11a);

5. the through-the-thickness crack tunnels through the width creating a transverse crack (Figure 1.8).

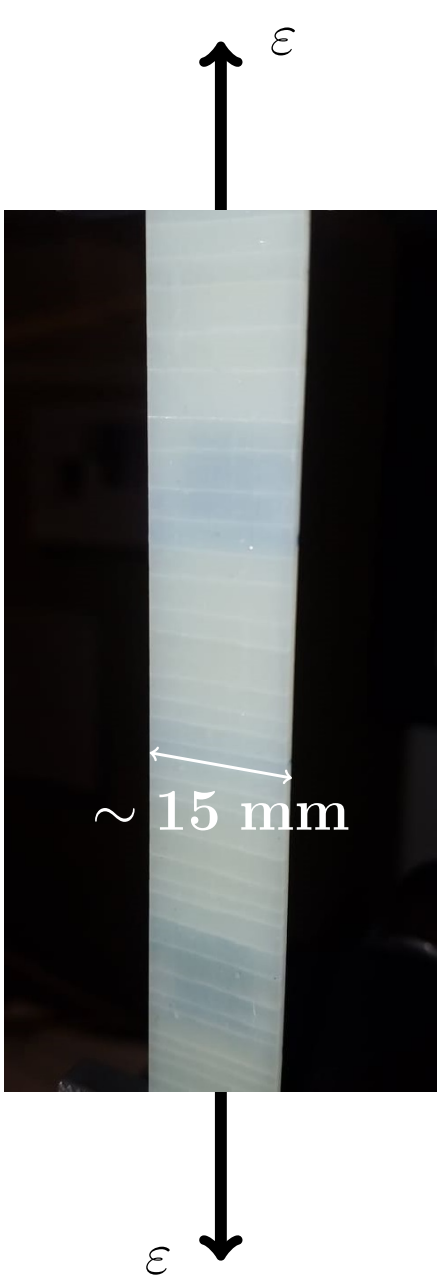

(a) Front view, naked eye, $[0, 90_2]_S$. The horizontal white lines are transverse cracks.

(b) Edge view, optical microscope, $[0, 90]_S$. The horizontal black lines in the central 90° layer are transverse cracks.

Figure 1.8: Transverse cracking in glass fiber/epoxy cross-ply conventional laminates. Pictures taken by the author.

The model is certainly idealized, for example the distinction between step 2 and step 3 might be considered arbitrary. However, it provides a clear mental picture and a working

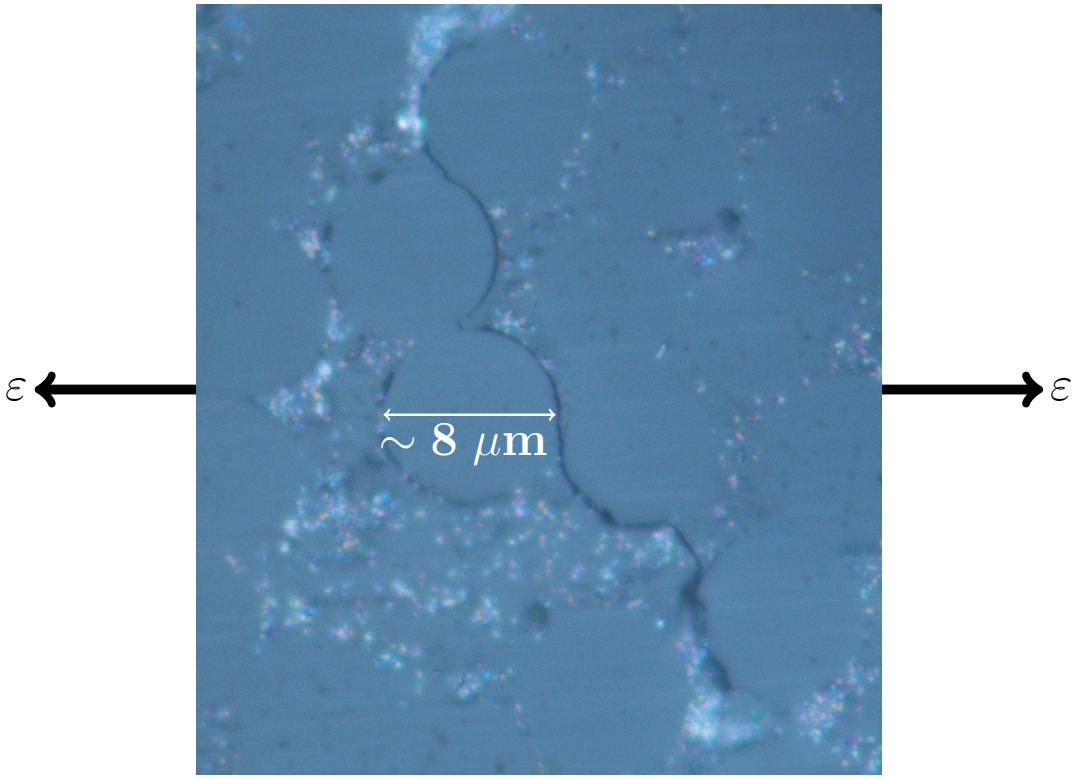

Figure 1.9: Edge view, optical microscope, $[0, 90]_S$.

Figure 1.10: Debonding in glass fiber/epoxy cross-ply conventional laminates. The arc-shaped black lines are debonds at the fiber/matrix interface. Picture taken by the author.

model to categorize the analysis of this complex phenomenon.

The description of the microscopic origin of transverse cracking presented previously leads naturally to the conclusion that a correct understanding of the *ply-thickness effect* and of the mechanisms that delay and suppress transverse cracking in thin-ply laminates requires a thorough comprehension of fiber/matrix debonding.
Different approaches have been adopted to model the fiber/matrix interface crack and provide a theoretical understanding of debonding process. One of the most widely used method is the Cohesive Zone Model (CZM), which has been employed to simulate simultaneously the onset and propagation of debonds along multiple fiber interfaces [52, 53, 54, 55]. Used in conjunction with a failure model for matrix, usually involving an elasto-plastic behavior with hardening [53, 55], such modeling approach aims at computing the location of the transverse crack starting from a virgin, i.e. undamaged. material. It furthermore provides the global force-displacement response of the simulated specimen, which can be directly compared with the results from mechanical tests. Given the interest in reconstructing numerically the growth of a transverse crack, authors working with this approach have usually focused on large Representative Volume Elements (RVEs) with computer-generated pseudo-random fiber distributions [56, 57] or real fiber distributions

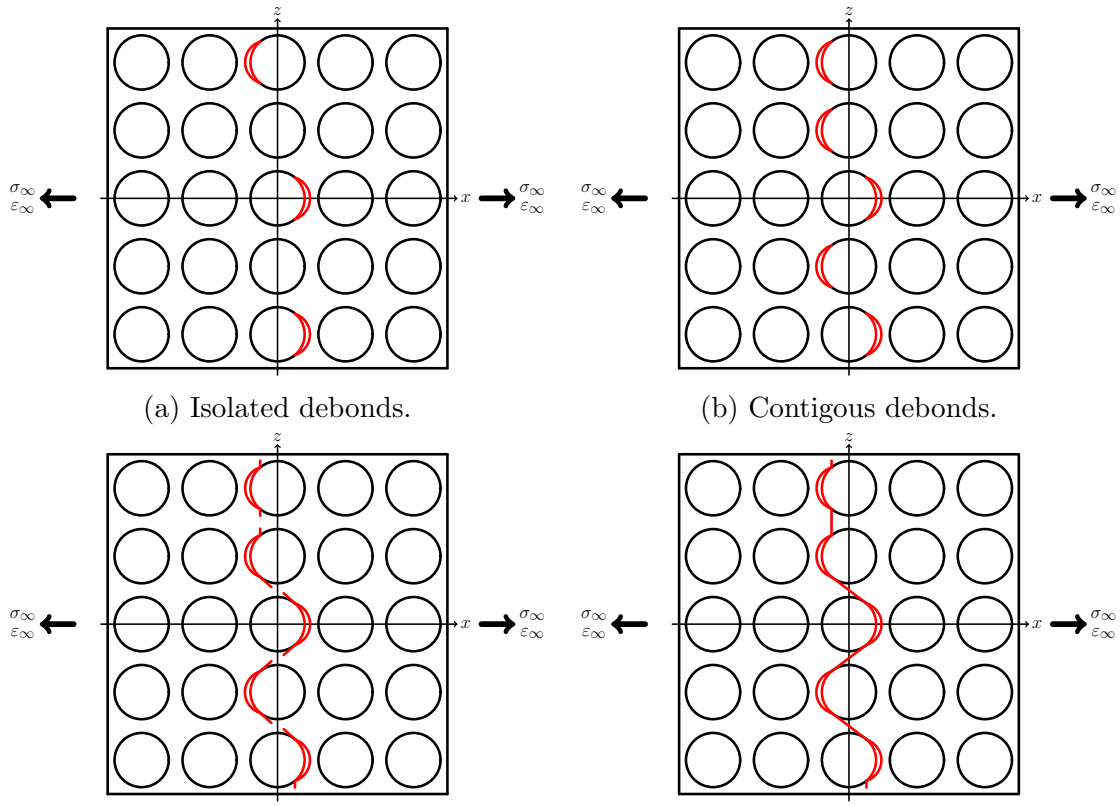

(a) Isolated debonds.

(b) Contigous debonds.

(c) Kinking.

(d) Coalescence.

Figure 1.11: Schematic representation of the formation of a transverse crack across the ply thickness.

reconstructed from microscopy imaging techniques. From the computational point of view, a Cohesive Zone Model coupled with an elasto-plastic matrix has the main advantage of avoiding any singularity in the stress and displacement fields at the crack tip, as it would occur in Linear Elastic Fracture Mechanics (LEFM) or Finite Fracture Mechanics (FFM). The crack tip itself is not directly modelled, on the other hand the fracture process is "smeared" over the finite length of the cohesive element [58]. However, some drawbacks exists. First, a significant number of material properties are required as input of the model, most of which are not experimentally measurable at the microscopic level for fiber/matrix debonding. This leads to the adoption of properties measured at the macroscopic scale or the need to calibrate the numerical procedure with respect to specific macroscopic force-displacement responses [53].The validity and applicability of such approach to then study an arbitrary configuration is an open question. Furthermore, the correct cancellation of the crack tip singularity, which is required to ensure accurate results, depends on Cohesive Elements length and it is thus sensitive to the mesh. For a bi-material interface crack as a debond under mixed-mode conditions, Jin and Sun [59] showed that a single cohesive zone length may not be able to cancel simultaneously both the tensile and shear stress singularity at the crack tip. They further observed that high

values of the Cohesive Element tensile and shear stiffness are required to ensure a negligible energy dissipation at the cohesive zone tip. Finally, the adoption of an elasto-plastic matrix in conjunction with the Cohesive Zone Model might not represent the actual physics of the failure process at the fiber/matrix interface. As mentioned before, the triaxiality of the matrix stress state in the inter-fiber region induces brittle failure of the matrix at or very close to the interface through a cavitation-like mechanism [48, 49, 60]. This process would create a small initial debond at the interface and then debond growth would occur starting from this initial flaw, a situation better modeled by the classic Griffith's criterion of Linear Elastic Fracture Mechanics (LEFM). In a LEFM analysis, Mode I and Mode II Energy Release Rate (ERR) at the crack tip are evaluated by means of the Virtual Crack Closure Technique (VCCT) [61] and/or the J-Integral method [62]. Stress, strain and displacement fields are needed for the computation of the ERR and can be calculated using analytical solutions [63] as well as numerical methods, such as the Boundary Element Method (BEM) [64] or the Finite Element Method (FEM) [65]. Some limitations however exist. LEFM is in fact able to describe only propagation and not initiation of the debond. Furthermore, no agreement still exists among researchers on a propagation criteria that would correctly capture the mode-dependent behavior of the critical ERR at the interface. The interest in this thesis is to investigate debond growth and, by comparing the ERR in different configurations, understand which mechanism favors and which one prevents debond growth. Thus, Linear Elastic Fracture Mechanics is the approach adopted. Furthermore, in Paper E, initiation of debonds is analyzed using a simple approach compatible with the tenets of LEFM.

1.5 The fiber-matrix interface crack in LEFM

The problem of fiber/matrix debonding, called also the fiber/matrix interface crack problem, belongs to the category of bi-material interface cracks, i.e. cracks occurring at the interface between two dissimilar materials. This class of problems was first studied in the context of Linear Elastic Fracture Mechanics by Williams [66] in the 1950's. By using arguments of asymptotic analysis, he derived the stress distribution around an *open* straight crack, i.e. a crack with faces nowhere in contact with each other for any size of the crack itself. He considered the crack as occurring between two infinite half-planes of dissimilar materials (the intended application of his work was in the field of earthquake engineering). He found the existence of a strong oscillatory behavior in the stress singularity at the crack tip of the form

$$r^{-\frac{1}{2}} \sin\left(\varepsilon \log r\right) \quad \text{with} \quad \varepsilon = \frac{1}{2\pi} \log\left(\frac{1-\beta}{1+\beta}\right); \tag{1.1}$$

in which β is one of the two Dundurs [67] parameters used to characterize interfaces between dissimilar materials:

$$\beta = \frac{\mu_2\left(\kappa_1 - 1\right) - \mu_1\left(\kappa_2 - 1\right)}{\mu_2\left(\kappa_1 + 1\right) + \mu_1\left(\kappa_2 + 1\right)} \tag{1.2}$$

where $\kappa = 3-4\nu$ in plane strain and $\kappa = \frac{3-4\nu}{1+\nu}$ in plane stress, μ is the shear modulus, ν Poisson's coefficient, and indexes $1, 2$ refer to the two bulk materials. Later, Erdogan [68] found that oscillatory region size is in the order of $10^{-6}a$, where a is the size of the crack. Notice that the previous results depend on the mismatch in elastic properties at the interface and thus apply equally to the straight as well as to the circular bi-material interface crack (the fiber/matrix interface crack). Due the oscillatory nature of the stress singularity at the crack tip (Eq. 1.1), Stress Intensity Factors (SIFs) are not correctly defined anymore, as the $\lim_{r\to 0}\sqrt{2\pi r}\sigma$ ceases to be finite and returns logarithmically infinite terms [69]. Determination of Mode mixity at the crack tip is thus an ill-posed problem. For the same reason, evaluation of Mode I and Mode II Energy Release Rate at the debond tip is not possible. However, by evaluating the ERR over a finite length instead of an infinitesimal one, it is possible to compute an estimate of Mode I and Mode II ERR with reasonable accuracy. This leads naturally to the use of the Virtual Crack Closure Technique [61], which computes Mode I and Mode II ERR over a finite size.
In the *open crack* case, the existence of an interpenetration zone close to the crack tip was found [70, 71] with a length in the order of 10^{-4} [70]. On the basis of considerations laid out in[71], Comninou [72] introduced the presence of a *contact zone* in the crack tip neighborhood, of a length to be determined from the solution of the elastic problem, showed that it provided a physically consistent solution to the problem of the straight bi-material interface crack.
England [73] and Perlman and Sih [74] employed analytical tools to solve the fiber/matrix interface crack and computed the stress and displacement fields for a circular inclusion with respectively a single debond and an arbitrary number of debonds. Based upon their work, Toya [63] obtained the expression of the Energy Release Rate (ERR) of the *open* debond.
The study of more complex configurations, rather than the single partially debonded fiber in an infinite matrix of [73, 74, 63], requires numerical treatment, thus numerical studies soon followed these first analytical solutions. París and colleagues [64] developed a Boundary Element Method (BEM) employing discontinuous singular elements at the crack tip and the Virtual Crack Closure Integral (VCCI) [75] to compute the Energy Release Rate (ERR) at the debond tip. The method was initially developed for the *open crack* case and was validated with respect to Toya's analytical results [63]. The effect of interface discretization on the accuracy of stress calculations in the debond tip neighborhood was later studied [76]. Based on Comninou's work on the straight crack [72], the possibility of contact zone onset (*closed crack* case) was considered to avoid interpenetration of debond faces [64]. The effect of the presence of a contact zone on debond ERR was analyzed in [77].
Afterwards, several studies aimed to understand the effect of different mechanisms and configurations on debond growth. The two cases of a single debond on a fiber and a two symmetric debonds on the same fiber were compared in [78] under conditions of remote tensions, and it was found that in terms of ERR the case of a single debond is more likely to be observed. Different types and combinations of loads were investigated in models of a single partially debonded fiber embedded in a infinite matrix: compression [79], residual

thermal stresses [80], biaxial loading conditions with different combinations of tension and compression [81, 82]. The presence of two nearby bonded fiber on debond growth was studied under uniaxial transverse tension [83], biaxial tension [84] and uniaxial transverse compression [85]. The effect of inter-fiber distance on debond ERR was considered in the case of a partially debonded fiber placed at the center of a hexagonal cluster inside a homogenized UD composite, with only fully bonded neighboring fibers [65] and with two partially debonded fibers out of the surrounding six [86]. Finally, recent studies have analyzed the effect of ply-thickness on fiber/matrix debonding by embedding a unit cell with one or two fibers inside a homogenized 90° layer in a cross-ply laminate [99, 98].

1.6 Objectives of the thesis

The main objective of the thesis is to investigate the effect of the composite microstructure on debond growth, characterized by its Mode I and Mode II Energy Release Rate. The aim is to understand which mechanisms cause an increase in the ERR, and thus favor the growth of debonds, and which mechanisms lead to a reduction of the ERR at the debond tip, and thus have a mitigating effect on debond growth. Both Uni-Directional (UD) composites (Paper B, Paper D, Paper E) and cross-ply laminates (Paper C and Paper E) are studied, and the aspects of interest are:

- the fiber volume fraction (Paper B);
- the interaction between debonds in the loading direction (Paper B and Paper C);
- the interaction between debonds in the through-the-thickness direction (Paper D);
- the presence of a free surface and its distance from the debond (Paper B);
- the presence of the 0°/90° interface and its distance from the debond (Paper C);
- the thickness of the layer in which debonding occurs (the UD composite in Paper B, the 90° layer in Paper C);
- the thickness of the 0° layer in cross-ply laminates (Paper C).

A second aim is to estimate the initial size of debonds after initiation and the final maximum size of debonds after propagation and how these are affected by the microstructural feature previously highlighted (Paper E). Given the oscillatory behavior of the LEFM crack-tip solution of the fiber/matrix interface crack problem (see previous section), a further objective is to determine the convergence behavior of the Virtual Crack Closure Technique used in conjunction with the Finite Element Method to compute debond Energy Release Rate.

Chapter 2

Summary of appended papers

2.1 Paper A

Finite Element solution of the fiber/matrix interface crack problem: convergence properties and mode mixity of the Virtual Crack Closure Technique

The analysis of bi-material interface cracks, such as the fiber/matrix interface crack or debond, in the context of Linear Elastic Fracture Mechanics hides some peculiar complexities due to the nature of the solution at the crack tip. The solution to the fiber/matrix interface crack problem can be classified into two different regimes [64, 77]: the *open crack* and *closed crack* solution. The distinction between the two lies in the existence of a region of contact between crack faces (contact zone) at the crack tip: if it exists, we talk about a *closed crack* solution, otherwise of an *open crack* solution.
The *open crack* solution to the straight bi-material interface crack problem was first proposed by Williams [66], who found the existence of an oscillatory singularity in the stress field at the crack tip of the form

$$r^{-\frac{1}{2}} \sin\left(\varepsilon \log r\right) \quad \text{with} \quad \varepsilon = \frac{1}{2\pi} \log\left(\frac{1-\beta}{1+\beta}\right), \tag{2.1}$$

in both Mode I and Mode II. In Eq. 2.1, β is one of the two parameters introduced by Dundurs [67] to characterize bi-material interfaces:

$$\beta = \frac{\mu_2\left(\kappa_1 - 1\right) - \mu_1\left(\kappa_2 - 1\right)}{\mu_2\left(\kappa_1 + 1\right) + \mu_1\left(\kappa_2 + 1\right)} \tag{2.2}$$

where $\kappa = 3 - 4\nu$ in plane strain and $\kappa = \frac{3-4\nu}{1+\nu}$ in plane stress, μ is the shear modulus, ν Poisson's coefficient, and indexes $1, 2$ refer to the two bulk materials joined at the

interface. Due to the nature of singular solution at the crack tip in the *open crack* case, the definition of Stress Intensity Factor (SIF) $\lim_{r\to 0}\sqrt{2\pi r}\sigma$ diverges and is not anymore valid [69]. The mismatch in the value of the elastic properties at the bi-material interface makes the configuration a mixed-mode one, but the Mode mixity problem at the crack tip is ill-posed. For the same reason, Mode I and Mode II Energy Release Rate do not converge. A way to circumvent the problem is to evaluate the ERR over a finite instead of an infinitesimal crack increment, which leads naturally to the application of the Virtual Crack Closure Technique (VCCT) [87, 61].
The introduction of a finite crack increment makes the ERR sensitive to the mesh. Several authors have investigated the mesh sensitivity of the VCCT used in conjunction with the Finite Element Method (FEM) in the context of the straight bi-material interface crack [88, 89, 90, 91, 92, 93, 94] and found that: the total Energy Release Rate G_{TOT} does not depend on the mesh size; for a crack under mixed-mode behavior (*open crack* case), Mode I and Mode II depend on the size of the mesh at the crack tip and do not show convergence. The purpose of this first paper is to analyze the mesh dependency of Energy Release Rate in the case of the fiber/matrix interface crack.

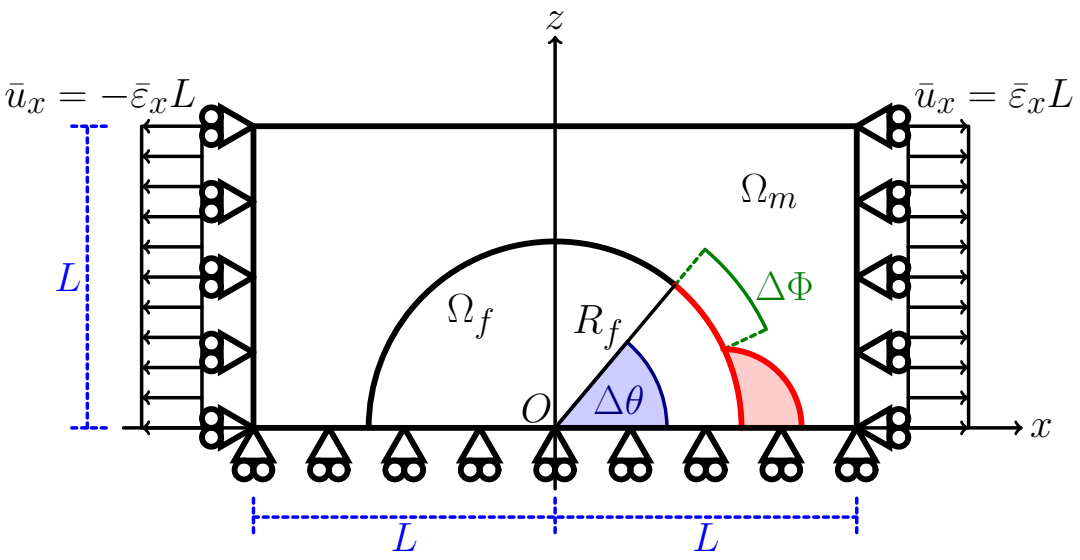

Figure 2.1: Schematic of the model with its main parameters.

The 1-step VCCT in the force-displacement formulation [61] is considered and applied to the evaluation of the ERR of a debond located on a single fiber placed in a square matrix cell, as shown in Figure 2.1. The cell has a size of $2L \times 2L$, where

$$L = \frac{R_f}{2}\sqrt{\frac{\pi}{V_f}}, \tag{2.3}$$

V_f is the fiber volume fraction and R_f is the fiber radius, assumed to be equal to 1 μm. Conditions of plane strain are assumed. The occurrence of a contact zone after a critical

size of the debond is considered and a contact pair interaction is established between crack faces. The interaction is considered frictionless. As the model is symmetric with respect to the x-axis (see Figure 2.1), only half of it is explicitly modeled and symmetry conditions are applied to the lower boundary. A constant x-strain of 1% is applied to the right and left boundary. Glass fiber and epoxy are considered and their properties are reported in Table 2.1.

Table 2.1: Summary of the mechanical properties of fiber and matrix. E stands for Young's modulus, μ for shear modulus and ν for Poisson's ratio.

Material	$E\,[GPa]$	$\mu\,[GPa]$	$\nu\,[-]$
Glass fiber	70.0	29.2	0.2
Epoxy	3.5	1.25	0.4

The main parameter of the mesh sensitivity study is the angular size δ of the elements at the crack tip, as shown in Figure 2.2.

The most important contributions of Paper A are summarized below.

- The total Energy Release Rate is found to invariant to rotations of the crack tip reference frame.

- The total Energy Release Rate does not depend on the size δ of the elements at the debond tip, at least for reasonably small elements, i.e. $\delta \leq 1.0°$. Thus, in *closed crack* case, Mode II ERR does not depend on δ, as $G_{II} = G_{TOT}$ as soon as contact zone onset occurs.

- In *open crack* case, Mode I and Mode II ERR depend on the element size δ at the debond tip. The dependence is described by a logarithmic law of the type $A\,(\Delta\theta) \ln \delta + B\,(\Delta\theta)$, as shown in Figure 2.3 and Figure 2.4. It is found that the sign of the logarithm is always positive for G_I (see Figure 2.3), i.e. it decreases when δ decreases, and negative for G_{II} (see Figure 2.4), i.e. it increases when δ decreases.

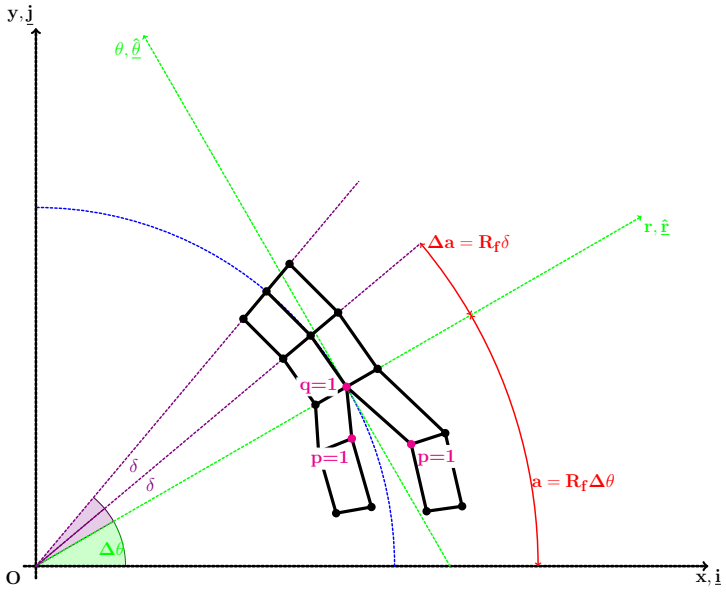

(a) Elements with 1^{st} order shape functions: $m = 1$ and $p, q = 1$.

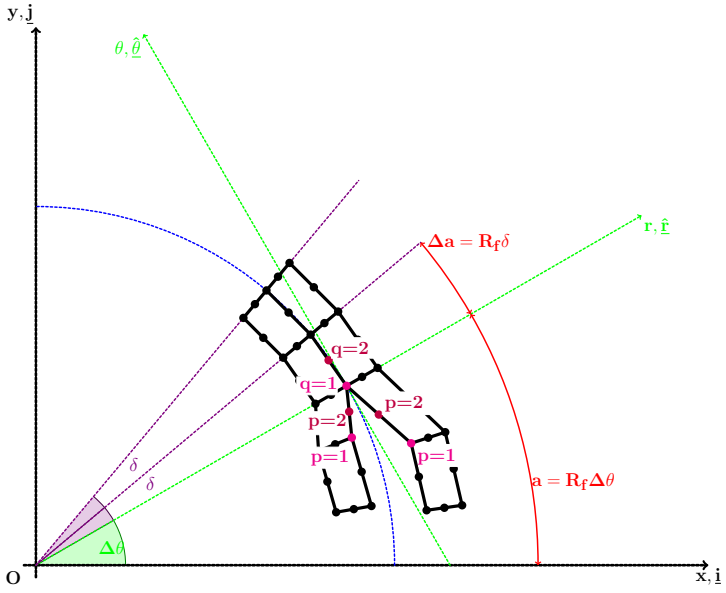

(b) Elements with 2^{nd} order shape functions: $m = 2$ and $p, q = 1, 2$.

Figure 2.2: Schematic of the mesh at the fiber/matrix interface crack tip.

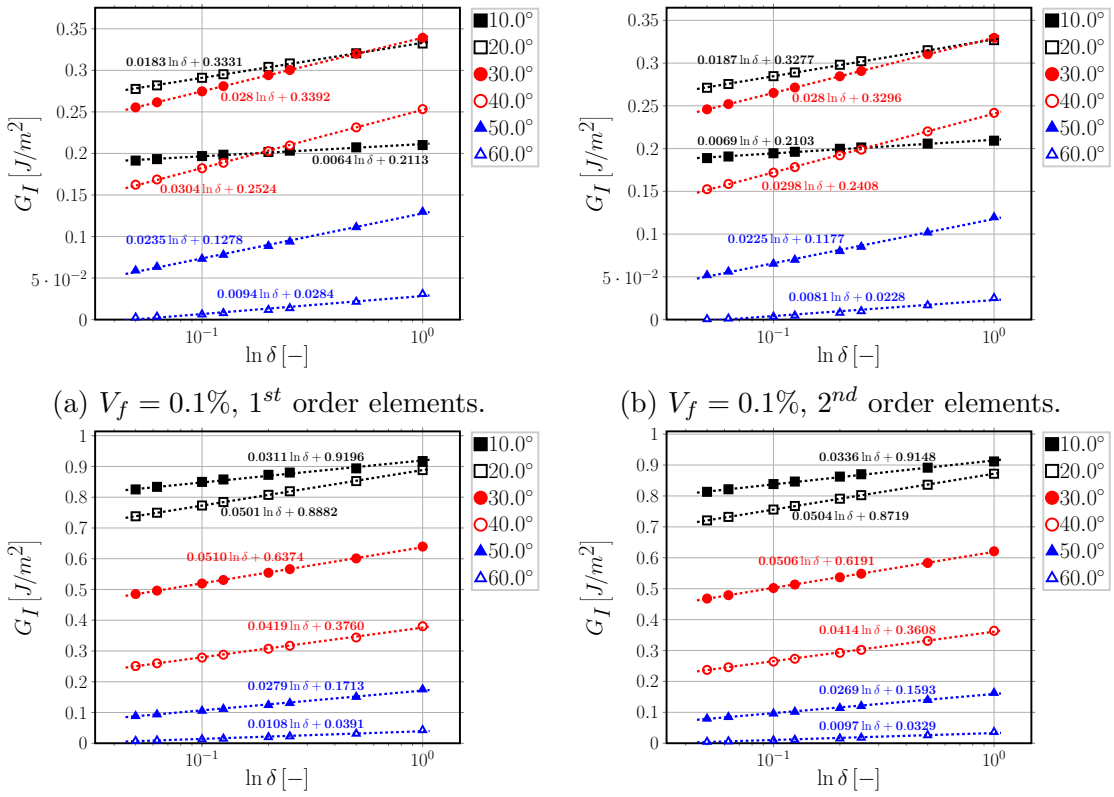

(a) $V_f = 0.1\%$, 1^{st} order elements.

(b) $V_f = 0.1\%$, 2^{nd} order elements.

(c) $V_f = 40\%$, 1^{st} order elements.

(d) $V_f = 40\%$, 2^{nd} order elements.

Figure 2.3: Logarithmic dependence on δ of Mode I ERR: interpolation of numerical results.

2.2 Paper B

Energy release rate of the fiber/matrix interface crack in UD composites under transverse loading: effect of the fiber volume fraction and of the distance to the free surface and to non-adjacent debonds

In Paper B, fiber/matrix interface crack growth is studied in Representative Volume Elements of UD composites subjected to transverse tensile loading. A unit cell constituted by one fiber and the surrounding matrix, shown in Figure 2.5, represents the basic element of the RVE.

The unit cell has a size of $2L \times 2L$, where

$$L = \frac{R_f}{2}\sqrt{\frac{\pi}{V_f}}, \tag{2.4}$$

R_f is the fiber radius, assumed to be equal to 1 μm, and V_f is the fiber volume fraction. Notice that the value of 1 μm for the fiber radius is arbitrary and chosen for

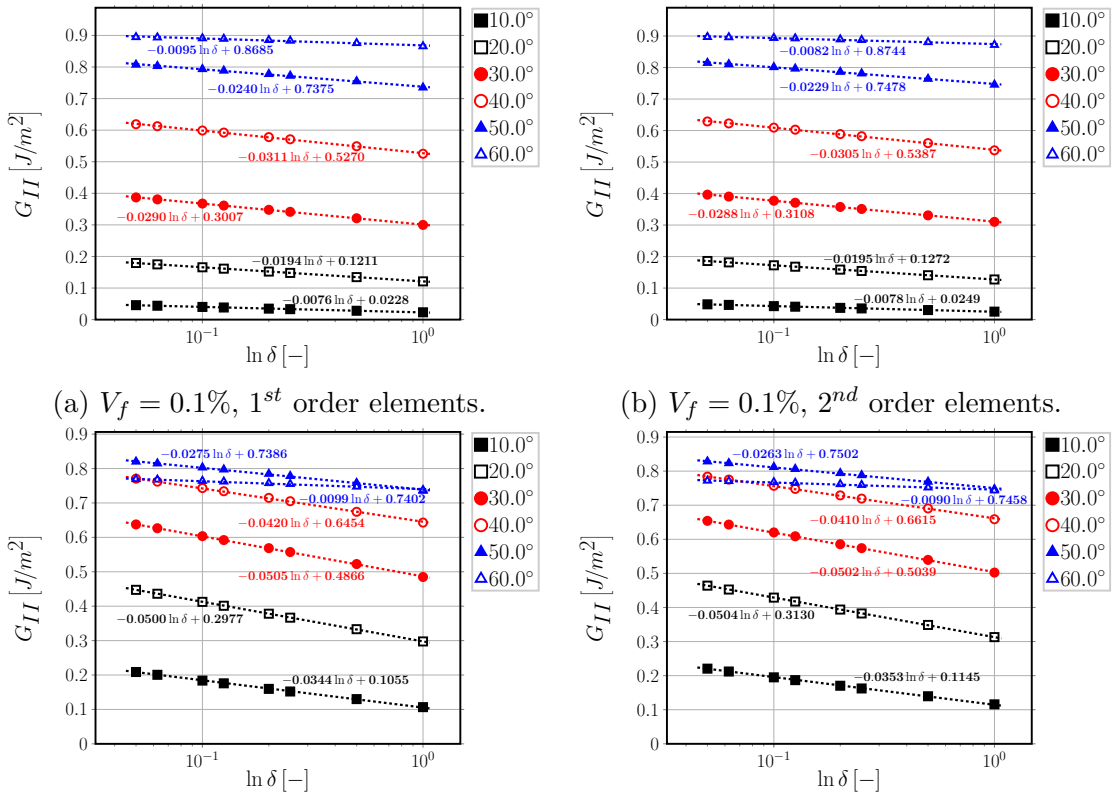

(a) $V_f = 0.1\%$, 1^{st} order elements. (b) $V_f = 0.1\%$, 2^{nd} order elements.

(c) $V_f = 40\%$, 1^{st} order elements. (d) $V_f = 40\%$, 2^{nd} order elements.

Figure 2.4: Logarithmic dependence on δ of Mode II ERR: interpolation of numerical results.

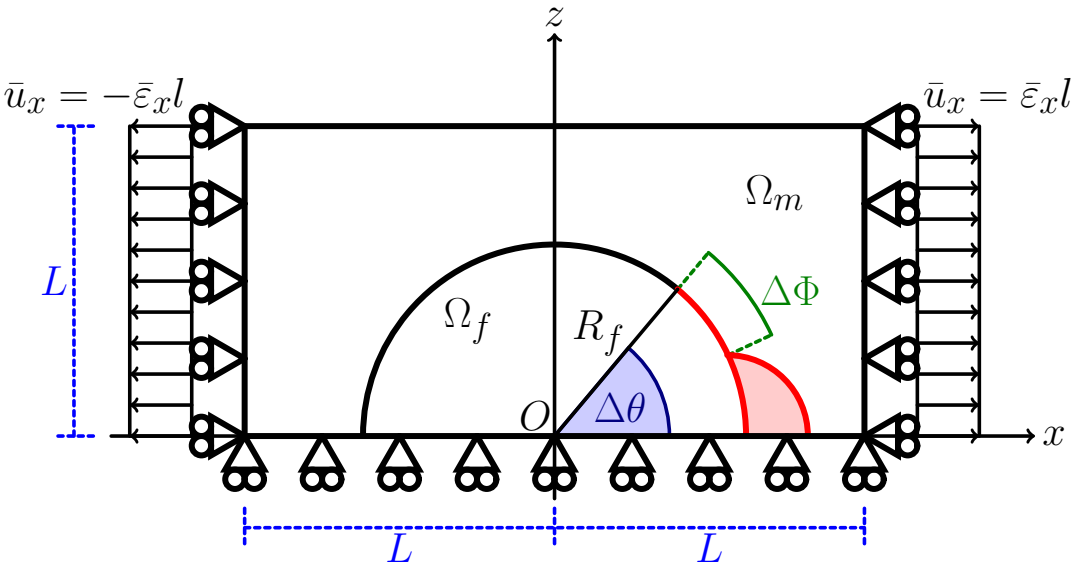

Figure 2.5: Schematic of the reference unit cell with its main parameters.

simplicity: in the context of Linear Elastic Fracture Mechanics (LEFM), the Energy Release Rate (ERR) is directly proportional to the fiber radius, thus evaluation of the ERR for another value requires simply a multiplication.
The RVE is made up by n unit cells as the one of Figure 2.5 in the horizontal (loading) direction and k unit cells in the vertical (through-the-thickness) direction (see Figure 2.6). The fiber of the unit cell placed in the center of the RVE is always partially debonded, and the debond has an angular size $\Delta\theta$ which can vary between 10° and 150°.

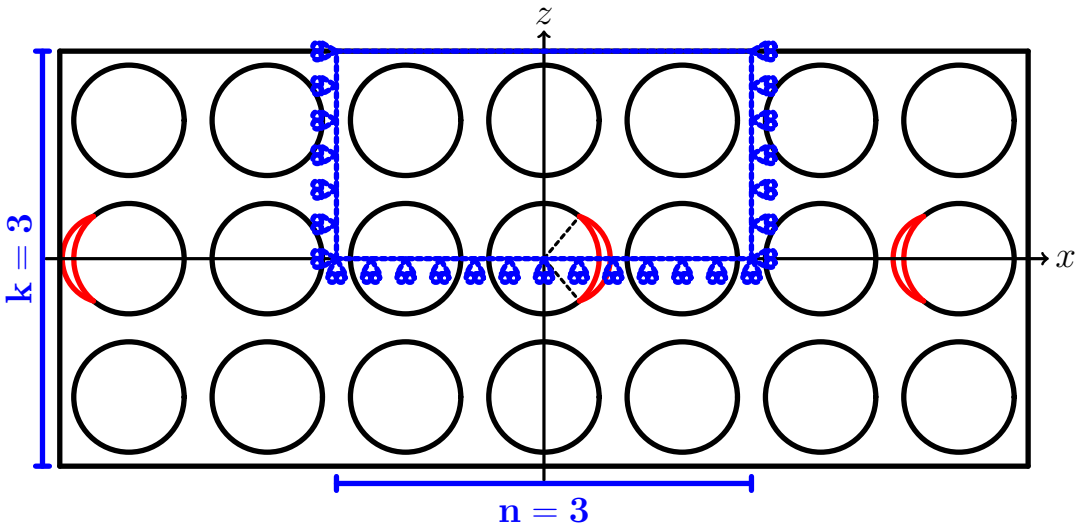

Figure 2.6: Multiple rows of fibers with a debond appearing every n fibers within the central row: model $n \times k - free$ ($n = 3$ and $k = 3$ in the figure).

The RVE is assumed to belong to a central cross-section (i.e. not on the laminate edge) in a slender laminate, i.e. laminate length and width are much greater than the thickness. The debond is assumed to be much more developed in the fiber longitudinal direction than in the arc direction. Thus, conditions of plane strain are adopted.
The RVE is symmetric with respect to the horizontal axis (x-axis), thus only half of it is explicitly modelled and conditions of symmetry are applied on the lower boundary of the RVE. On the left and right boundaries, conditions of coupling of the x-displacement (horizontal displacement) are applied. This implies that the computed solution corresponds to the RVE repeating an infinite number of times to the left and to the right symmetrically with the respect to the side boundary, i.e. if the debond in the central unit cell is placed on the right side of the fiber, then the next one to the right and to the left is on the left side, the successive one is on the right, and so on. As a consequence, the number n of unit cells in the horizontal direction determines the distance between consecutive debonds in the horizontal direction, which corresponds to $n-1$ fully bonded fibers. The upper and lower boundaries (but, given the symmetry with respect to the x-axis, only the upper one is explicitly modeled) are left free. Thus, the family of RVEs studied in this paper is called $n \times k - free$.

A constant x-strain equal to 1% is applied to the left and right boundary. The selected value of 1% is arbitrary, as in LEFM the ERR is proportional to the square of the strain. Thus, the value of the ERR for another level of applied strain can calculated with a multiplication. Contact between debond faces is considered frictionless. The fiber and matrix phases, respectively glass fiber and epoxy, are considered to be homogeneous, isotropic and linear elastic. Their material properties are reported in Table 2.2.

Table 2.2: Summary of the mechanical properties of fiber and matrix. E stands for Young's modulus, μ for shear modulus and ν for Poisson's ratio.

Material	$E\,[GPa]$	$\mu\,[GPa]$	$\nu\,[-]$
Glass fiber	70.0	29.2	0.2
Epoxy	3.5	1.25	0.4

The model is meshed with second order quadrilateral and triangular elements, while at the crack tip only second order quadrilateral elements are used with unitary aspect ratio, determined by the arc size $R_f\delta$ where δ is the angular size. Given the results on convergence of Paper A, the angular size δ of the elements at the crack tip is determined here by comparison with the Boundary Element Method (BEM) results provided in [95, 83] for a single debonded fiber in an infinite matrix. The comparison is conducted using the $1 \times 1 - free$ RVE with $V_f = 0.0079$, which corresponds to $L \sim 100R_f$. A trade-off between accuracy and computational cost (time and memory required for the solution) is found for $\delta = 0.05°$. A comparison between the ERR computed with $\delta = 0.05°$ and the BEM results is shown in Figure 2.7. The error between FEM and BEM solution does not exceed 5% for any value of $\Delta\theta$. This provides a measure of the accuracy of the results proposed here: differences between values of ERR smaller than 5% should not be taken into consideration.

The most important observations and conclusions of the paper are summarized below.

1. The Energy Release Rate, both Mode I and Mode II, decreases with a decreasing number of fully bonded fibers between two consecutive partially debonded fibers in the central row, as shown in Figure 2.8 for Mode I and Figure 2.8 for Mode II in the case of $n \times 1 - free$ RVE. Furthermore, it seems that a characteristic distance between debonds exits that defines the transition between an interactive and a non-interactive solution. However, this distance appears to depend on the thickness of the UD, i.e. on the number k of fiber rows in the vertical direction, and also on the fiber volume fraction. An estimate of such distance provides: around 100 fully bonded fibers for a 1-fiber-row thick UD with $V_f = 30\%$; around 200 fibers for a 1-fiber-row thick UD with $V_f = 60\%$; around 100 fibers for a 5-fibers-row thick UD with $V_f = 60\%$.

2. When the free surface is close to the debond, higher Mode I and Mode II ERRs

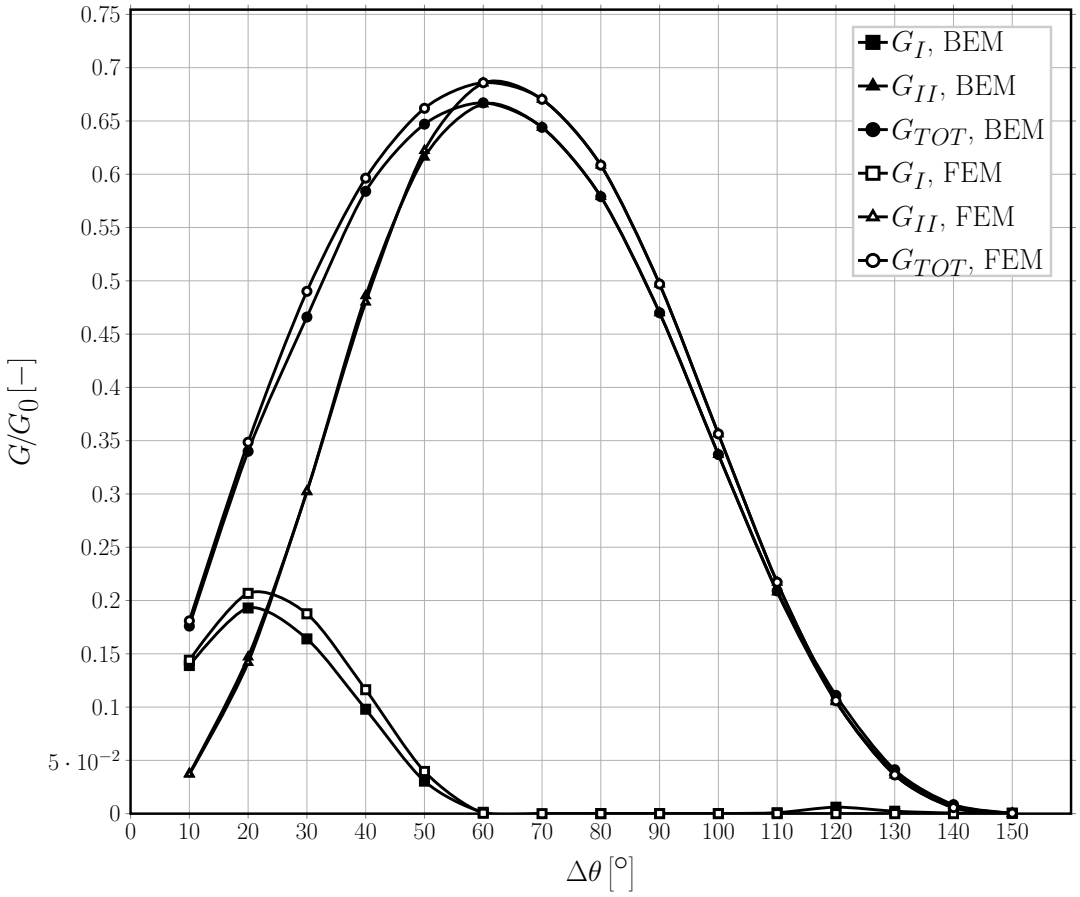

Figure 2.7: Validation of the single fiber model for the infinite matrix case with respect to the BEM solution in [83].

are obtained and the peak G values are shifted to larger debonds (Figure 2.8 and Figure 2.8). However, the effect of the composite free surface on the ERR declines very fast: the presence of at least 2 fully bonded fibers below and above the central row results in stable constant values of ERR.

3. An increase in the fiber volume fraction, which corresponds to a decrease in the inter-fiber distance, leads in general to a magnification of the effects previously described.

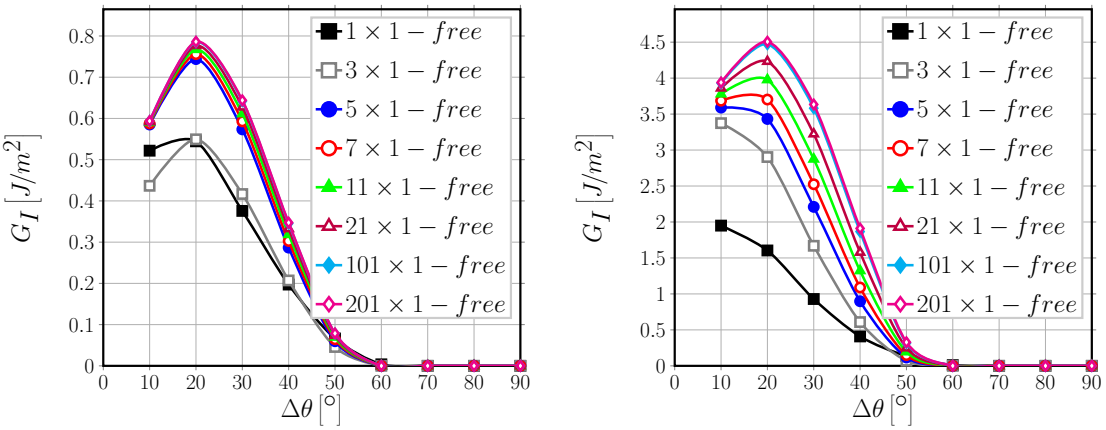

(a) $V_f = 30\%$. (b) $V_f = 60\%$.

Figure 2.8: Effect of the interaction between debonds appearing at regular intervals on Mode I ERR in an UD with a single row of fibers at different levels of fiber volume fraction V_f, subject to an applied transverse strain ε_x of 1%.

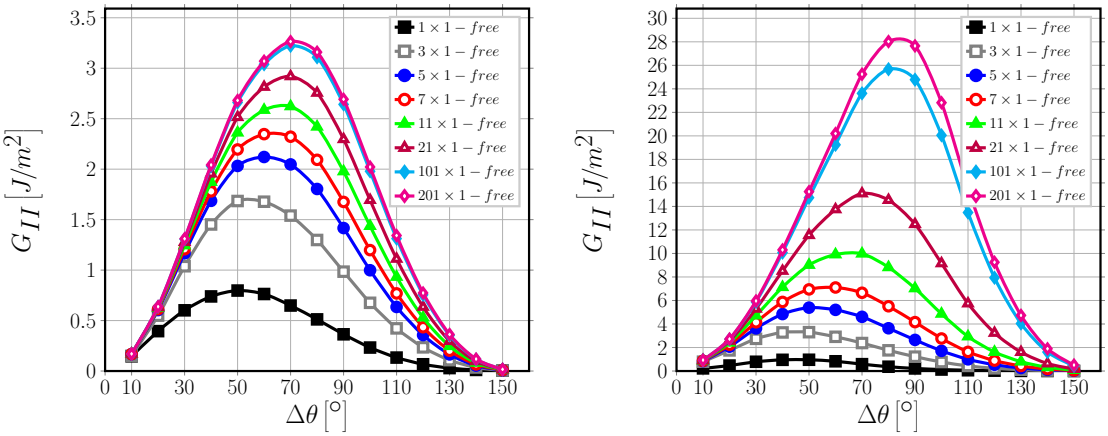

(a) $V_f = 30\%$. (b) $V_f = 60\%$.

Figure 2.9: Effect of the interaction between debonds appearing at regular intervals on Mode II ERR in an UD with a single row of fibers at different levels of fiber volume fraction V_f, subject to an applied transverse strain ε_x of 1%.

2.3 Paper C

Effect of the proximity to the 0°/90° interface on Energy Release Rate of fiber/matrix interface crack growth in the 90°-ply of a cross-ply laminate under tensile loading

In Paper C, fiber/matrix interface crack growth is studied in Representative Volume Elements of cross-ply laminates subjected to tensile loading. Similarly to Paper B, the unit cell constituted by one fiber and the surrounding matrix, shown in Figure 2.5, represents the basic element of the RVE. The unit cell has a size of $2L \times 2L$, where

$$L = \frac{R_f}{2}\sqrt{\frac{\pi}{V_f}}, \tag{2.5}$$

R_f is the fiber radius, assumed again to be equal to 1 μm, and V_f is the fiber volume fraction.
The RVE is constituted by n unit cells in the horizontal (loading) direction and k unit cells in the vertical (through-the-thickness) direction (see Figure 2.10). The fiber of the unit cell placed in the center of the RVE is always partially debonded, and the debond has an angular size $\Delta\theta$ which can vary between 10° and 150°.

On top and below these $n \times k$ fibers, a homogenized 0° ply is explicitly modelled, as shown in Figure 2.10. The thickness of these 0° plies is defined as m times the thickness t_{90° of the central 90° ply, where

$$t_{90^\circ} = k2L. \tag{2.6}$$

Similarly to Paper B, the RVE is assumed to be extracted from a central cross-section (i.e. not on the laminate edge) in a slender laminate, i.e. such that laminate length and width are much greater than the thickness. The debond is further assumed to be much more developed in the fiber longitudinal direction than in the arc direction. Thus, conditions of plane strain are adopted.
The RVE is symmetric with respect to the x-axis (horizontal axis), thus only half of it is explicitly modelled and conditions of symmetry are applied on the lower boundary of the RVE. On the left and right boundaries, conditions of coupling of the x-displacement (horizontal displacement) are applied, which implies that, as for the RVEs of paper A, the computed solution corresponds to the RVE repeating an infinite number of times to the left and to the right in a symmetric way with the respect to the side. Thus, the number n of unit cells in the horizontal direction determines the distance between consecutive debonds in the horizontal direction, equal to $n - 1$ fully bonded fibers. This family of RVEs is called $n \times k - m \cdot t_{90^\circ}$.
In order to understand the mechanisms influencing debond ERR by comparison with known conditions at the boundary, an additional family of RVEs is treated in which the

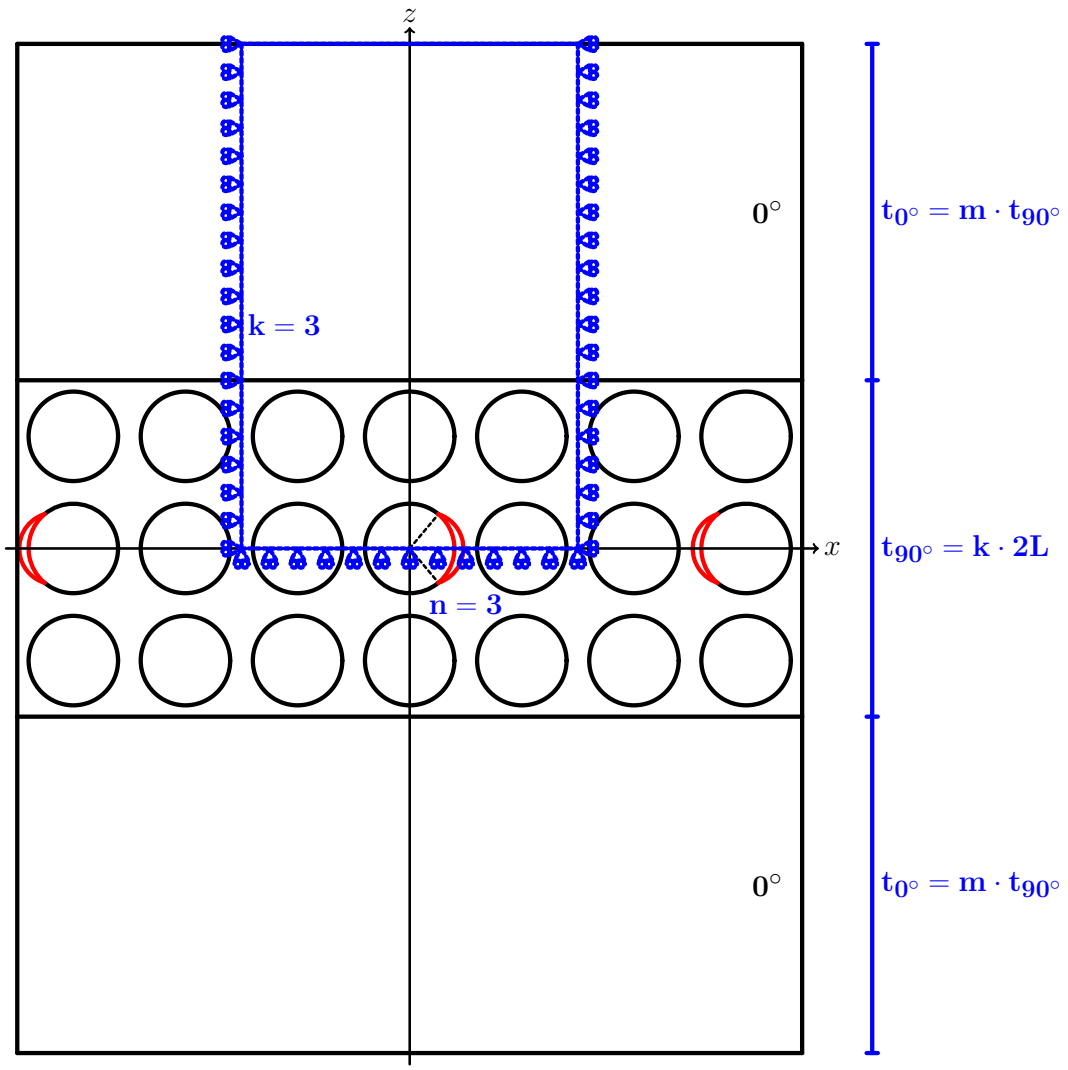

Figure 2.10: Models of $[0°_{m\cdot k\cdot 2L}, 90°_{k\cdot 2L}, 0°_{m\cdot k\cdot 2L}]$ *laminates with a* $90°$ *layer of variable thickness, determined by the number* k *of "rows" of fibers along the vertical direction. Debonds are repeating at different distances along the horizontal direction, measured in terms of the number* $n-1$ *of fully bonded fibers appearing between two consecutive debonds.* $2L$ *is the thickness of one-fiber row.*

$0°$ layer is not present. In its place, different combinations of displacement boundary conditions are applied to the upper boundary. When the upper boundary is free, the $1\times 1-free$ RVE is defined, as in Paper A. The $1\times 1-coupling$ RVE is instead obtained when coupling of the vertical displacements u_z is applied to the upper boundary (coupling condition). In the case a linear distribution of the horizontal displacement u_x is applied to the upper boundary (H-condition), the RVE is refered to as $1\times 1-H$. Finally, when the linear distribution of the horizontal displacement u_x is superimposed to the condition of coupling of the vertical displacements u_z on the upper boundary, the $1\times 1-coupling+H$ RVE is obtained.

A constant x-strain equal to 1% is applied to the left and right boundary. Contact between debond faces is considered frictionless. The fiber and matrix phases, respectively glass fiber and epoxy, are considered to be homogeneous, isotropic and linear elastic. The elastic properties of the 0° ply are computed using Hashin's Concentric Cylinder Assembly model [96] with the self-consistency scheme for the out-of-plane shear modulus of Christensen [97]. The elastic properties of the three phases are reported in Table 2.3.

Table 2.3: Summary of mechanical properties of fiber, matrix and UD layer (GF: glass fiber; EP: epoxy; UD: glass-fiber/epoxy uni-directional properties).

	$V_f\,[\%]$	$E_L\,[GPa]$	$E_T\,[GPa]$	$G_{LT}\,[GPa]$	$\nu_{LT}\,[-]$	$\nu_{TT}\,[-]$
GF	-	70.0	70.0	29.2	0.2	0.2
EP	-	3.5	3.5	1.25	0.4	0.4
UD	60.0	43.442	13.714	4.315	0.273	0.465

The model is meshed with second order quadrilateral and triangular elements, while at the crack tip only second order quadrilateral elements are used with unitary aspect ratio, determined by the arc size $R_f\delta$ where δ is the angular size. The angular size δ of the elements at the crack tip is assumed as equal to 0.05° based on the comparison with the Boundary Element Method (BEM) results provided in [95, 83] conducted in Paper A. Thus, the same level of accuracy of 5% on ERR applies here.

The relevant results of Paper C are summarized in the following.

- Comparison between $n \times k - 1 \cdot t_{90^\circ}$ on one side and $n \times k - free$, $n \times k - H$, $n \times k - coupling$, $n \times k - coupling + H$ on the other (Figure 2.11 and Figure 2.12) shows that the presence of the 0° layer forces the 0°/90° interface to remain approximately straight and controls the uniformity of the horizontal displacement field in the composite, and thus in the 90° ply. The presence of the 0° layer thus causes a more homogeneous strain field, which reduces the Energy Release Rate at the debond tip.

- Increasing the thickness of the 0° layer, such that t_{0°/t_{90°, does not lead to any significant change in debond ERR.

- No effect of the 90° layer thickness, measured in terms of number k of fiber rows, is observed, as shown in Figure 2.13 and Figure 2.14. Only if the thickness is reduced to only one fiber row, the Energy Release Rate decreases in value.

- These results strengthen the claim that the ply-thickness effect does not influence the growth of individual debonds, as observed previously in the literature [37, 55, 98, 99].

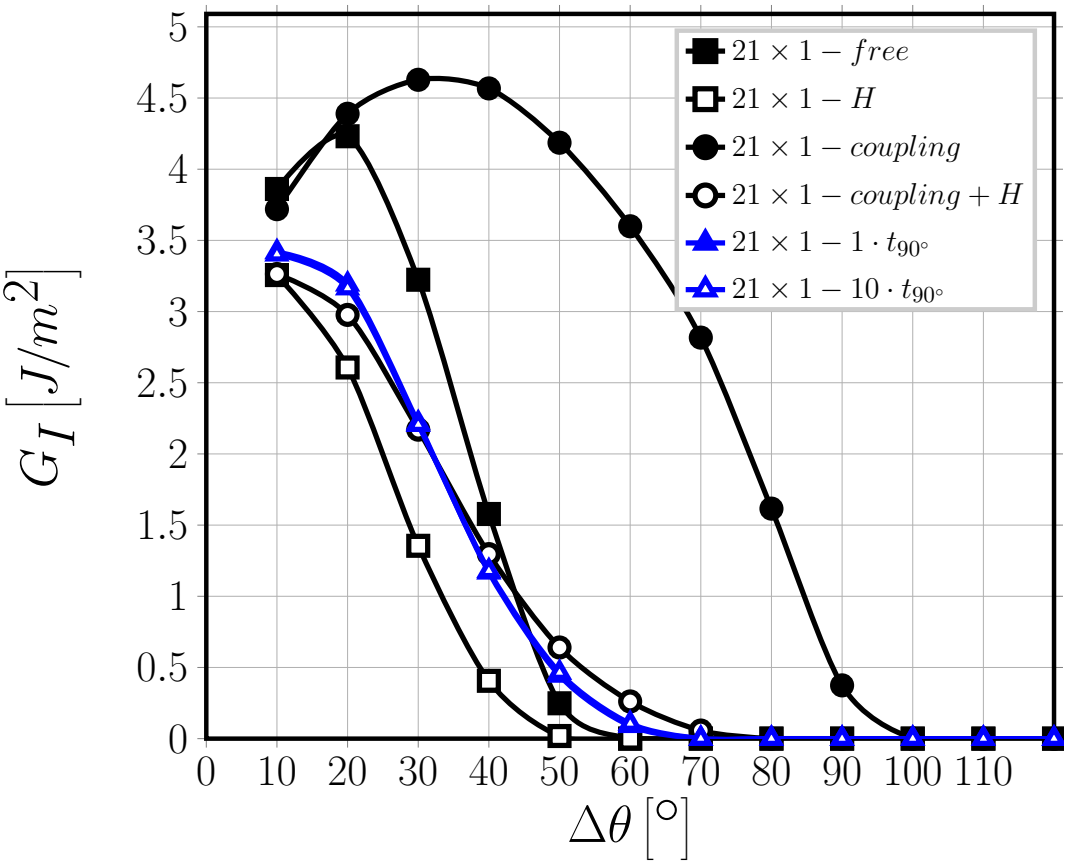

Figure 2.11: Effect of the presence of the 0° *layer on Mode I ERR: models* $21 \times 1 - free$, $21 \times 1 - H$, $21 \times 1 - coupling$, $21 \times 1 - coupling + H$, $21 \times 1 - 1 \cdot t_{90^\circ}$ *and* $21 \times 1 - 10 \cdot t_{90^\circ}$. $V_f = 60\%$, $\bar{\varepsilon}_x = 1\%$.

2.4 Paper D

Growth of interface cracks on consecutive fibers: on the same or on the opposite sides?

In Paper D, fiber/matrix interface crack growth is studied in Representative Volume Elements of thick UD composites subjected to transverse tensile loading. Similarly to PAper A and Paper B, the unit cell of one fiber and its surrounding matrix, shown in Figure 2.5, represents the basic element of the RVE. The unit cell has a size of $2L \times 2L$, where

$$L = \frac{R_f}{2}\sqrt{\frac{\pi}{V_f}}, \tag{2.7}$$

R_f is the fiber radius, assumed again to be equal to 1 μm, and V_f is the fiber volume fraction.

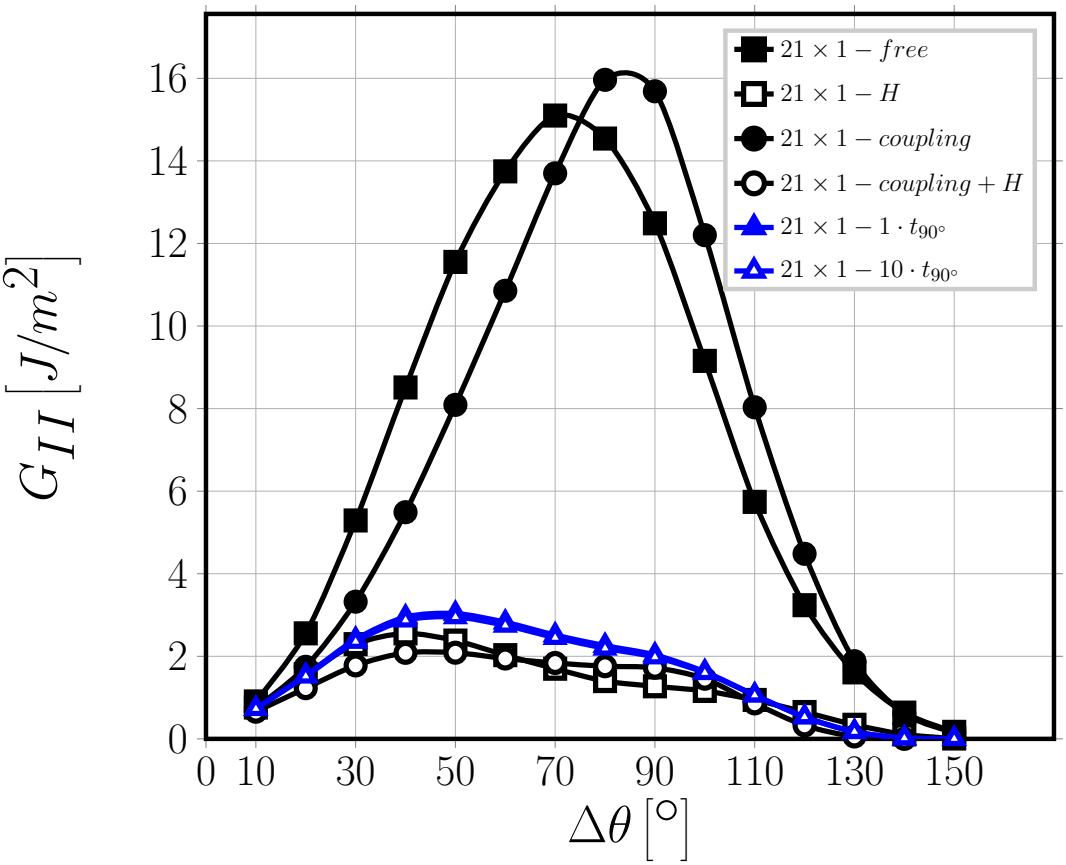

Figure 2.12: Effect of the presence of the 0° *layer on Mode II ERR: models* $21 \times 1 - free$, $21 \times 1 - H$, $21 \times 1 - coupling$, $21 \times 1 - coupling + H$, $21 \times 1 - 1 \cdot t_{90^\circ}$ *and* $21 \times 1 - 10 \cdot t_{90^\circ}$. $V_f = 60\%$, $\bar{\varepsilon}_x = 1\%$.

The RVE is formed by n unit cells in the horizontal (loading) direction and k unit cells in the vertical (through-the-thickness) direction (see Figure 2.15 and Figure 2.16). The fiber of the unit cell placed in the center of the RVE is always partially debonded, and the debond has an angular size $\Delta\theta$ which can vary between 10° and 150°.

The same assumptions made in Paper B and Paper C on laminate and debond geometry hold, and conditions of plane strain are assumed.
The RVE is symmetric with respect to the x-axis (horizontal axis), thus only half of it is explicitly modelled and conditions of symmetry are applied on the lower boundary of the RVE. On the left and right boundaries, conditions of coupling of the x-displacement (horizontal displacement) are applied, which implies that, as for the RVEs of Paper A and Paper B, the computed solution corresponds to the RVE repeating an infinite number of times to the left and to the right in a symmetric way with the respect to the side. Thus, the number n of unit cells in the horizontal direction determines the distance between consecutive debonds in the horizontal direction, equal to $n - 1$ fully bonded fibers. On the top boundary, two different sets of boundary conditions are applied. The first are conditions of coupling of the vertical displacement u_z, expressed as

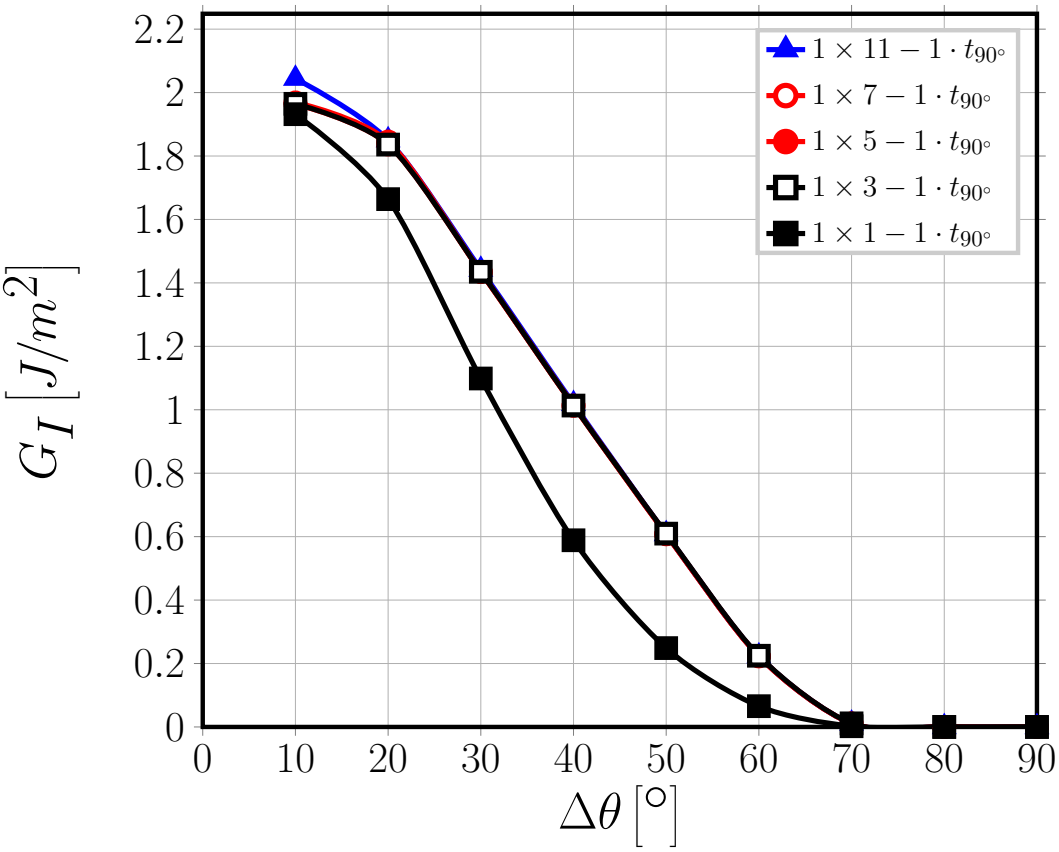

Figure 2.13: Effect of the presence of undamaged fiber rows in the 90° *layer on debond-*0°/90° *interface interaction for Mode I ERR: models* $1\times k-1\cdot t_{90^\circ}$. $V_f = 60\%$, $\bar{\varepsilon}_x = 1\%$.

$$u_z\left(x,h\right) = u_z^{\nu}, \tag{2.8}$$

where $h = kL$ corresponds to the height of the RVE and u_z^{ν} represents the unknown constant vertical displacement of the upper boundary due to Poisson's effect, which is calculated as part of the elastic solution. This set of conditions implies that the computed solution is that of the RVE repeating an infinite number of times in the vertical direction in a symmetric way as shown in Figure 2.15, i.e. if the debond in the central unit cell appears on the right, all the debonds in the vertical direction aligned with it will be placed on the right half of their respective fiber. This family of RVEs is referred to as $n\times k-symm$.

The second set of conditions represents instead anti-symmetric coupling conditions, expressed as

$$u_z\left(x,h\right) - u_z\left(0,h\right) = -\left(u_z\left(-x,h\right) - u_z\left(0,h\right)\right), \tag{2.9}$$

$$u_x\left(x,h\right) = -u_x\left(-x,h\right), \tag{2.10}$$

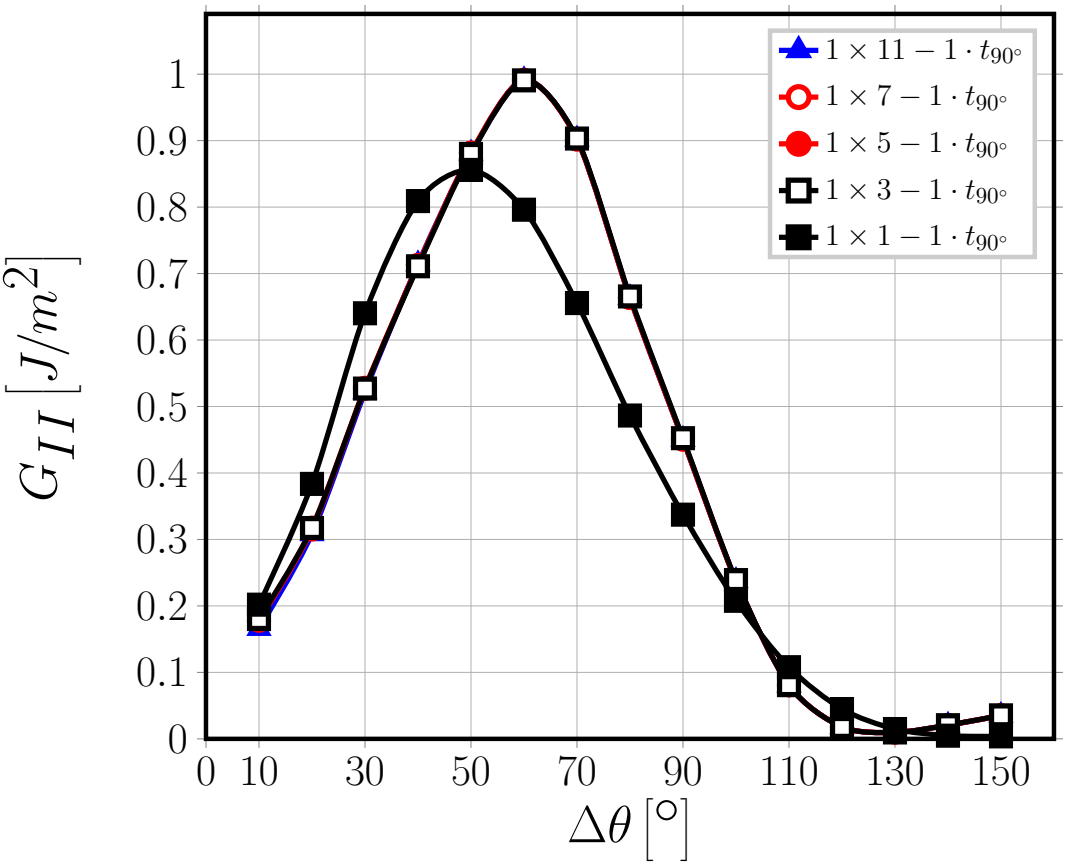

Figure 2.14: Effect of the presence of undamaged fiber rows in the 90° *layer on debond-*0°/90° *interface interaction for Mode II ERR: models* $1 \times k - 1 \cdot t_{90^\circ}$. $V_f = 60\%$, $\bar{\varepsilon}_x = 1\%$.

where h represents the height of the RVE and $u_z\,(0, h)$ stands for the unknown vertical displacement of the upper boundary's mid-point caused by Poisson's effect, which is evaluated as part of the elastic solution. Similarly to $n \times k - symm$, this set of conditions implies that the RVE is repeating infinite times in the vertical direction. However, the unit cell is repeated anti-symmetrically this time: if a debond is placed on the right side of its fiber, the next one aligned in the vertical direction will appear on the left side (Figure 2.16). This second set of RVEs is named $n \times k - asymm$.
A constant horizontal strain (x-strain) equal to 1% is applied to the left and right boundary. Frictionless contact is considered between debond faces. The fiber and matrix phases, respectively glass fiber and epoxy, are considered to be homogeneous, isotropic and linear elastic. The elastic properties of the two phases are reported in Table 2.3.

The model is meshed with second order quadrilateral and triangular elements, while at the crack tip only second order quadrilateral elements are used with unitary aspect ratio, determined by the arc size $R_f\delta$ where δ is the angular size. The angular size δ of the elements at the crack tip is assumed as equal to 0.05° based on the comparison with the Boundary Element Method (BEM) results provided in [95, 83] conducted in Paper A. Thus, the same level of accuracy of 5% on ERR applies here.

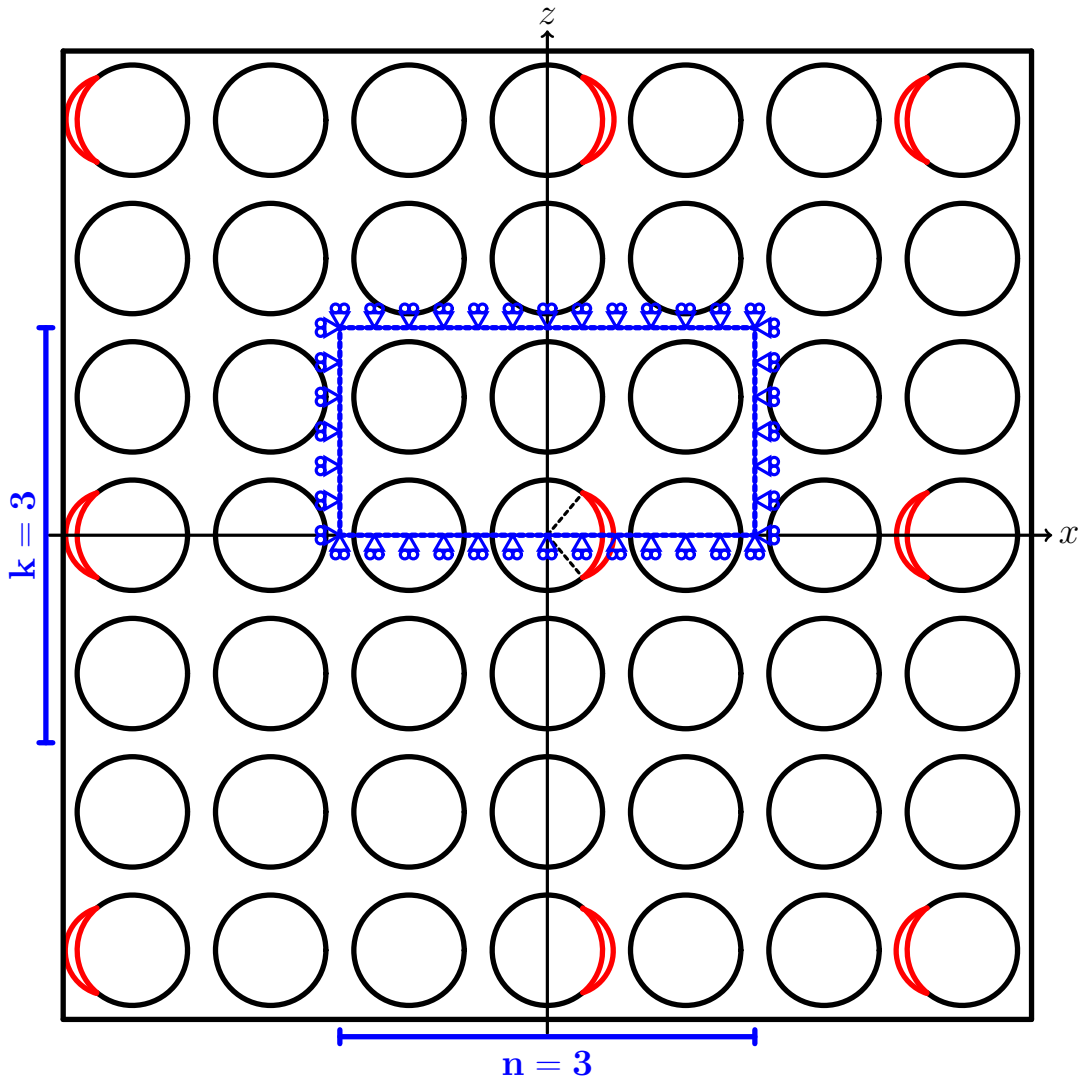

Figure 2.15: Representative Volume Element $n \times k - symm$ of a UD composite with debonds appearing after $n-1$ and after $k-1$ undamaged fibers respectively in the horizontal and vertical direction. In the vertical direction, on fibers belonging to the same Â´Â´column", debonds are located always on the same side.

Table 2.4: Material properties of glass fiber and epoxy adopted in the present study.

Material	$E\,[GPa]$	$\mu\,[GPa]$	$\nu\,[-]$
Glass fiber	70.0	29.2	0.2
Epoxy	3.5	1.25	0.4

The main findings of Paper D are summarized below.

1. The relative position of debonds, i.e. same or opposite sides of their respective

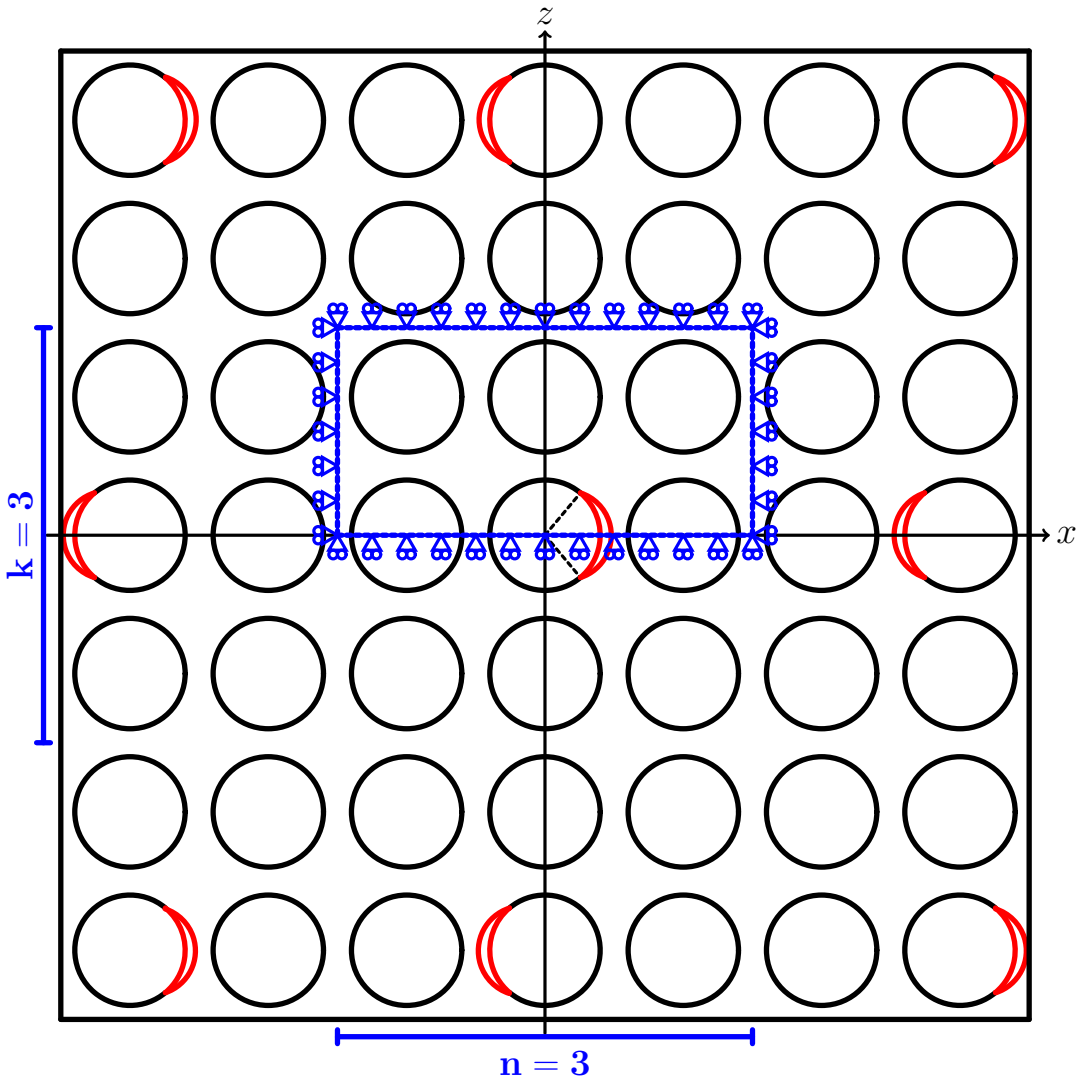

Figure 2.16: Representative Volume Element $n \times k - asymm$ of a UD composite with debonds appearing after $n-1$ and after $k-1$ undamaged fibers respectively in the horizontal and vertical direction. In the vertical direction, on fibers belonging to the same Â´Â´column", debonds are located on the opposite sides of consecutive fibers.

fiber, has an effect on the Energy Release Rate only if debonds are located on consecutive fibers, as shown in Figure 2.17 and Figure 2.18. The sensitivity of the ERR to debonds' relative position disappears with presence of just two fully bonded fiber rows between rows containing debonds (Figure 2.19 and Figure 2.20) and neither configuration (debonds on the same or opposite sides of the debonded fibers) is favored from an energy point of view.

2. In the case of debonds located on consecutive vertically aligned fibers, the values of G_I are higher and contact zone onset is delayed to larger debonds when debonds are on the same side of their respective fibers (Figure 2.17). As debond growth

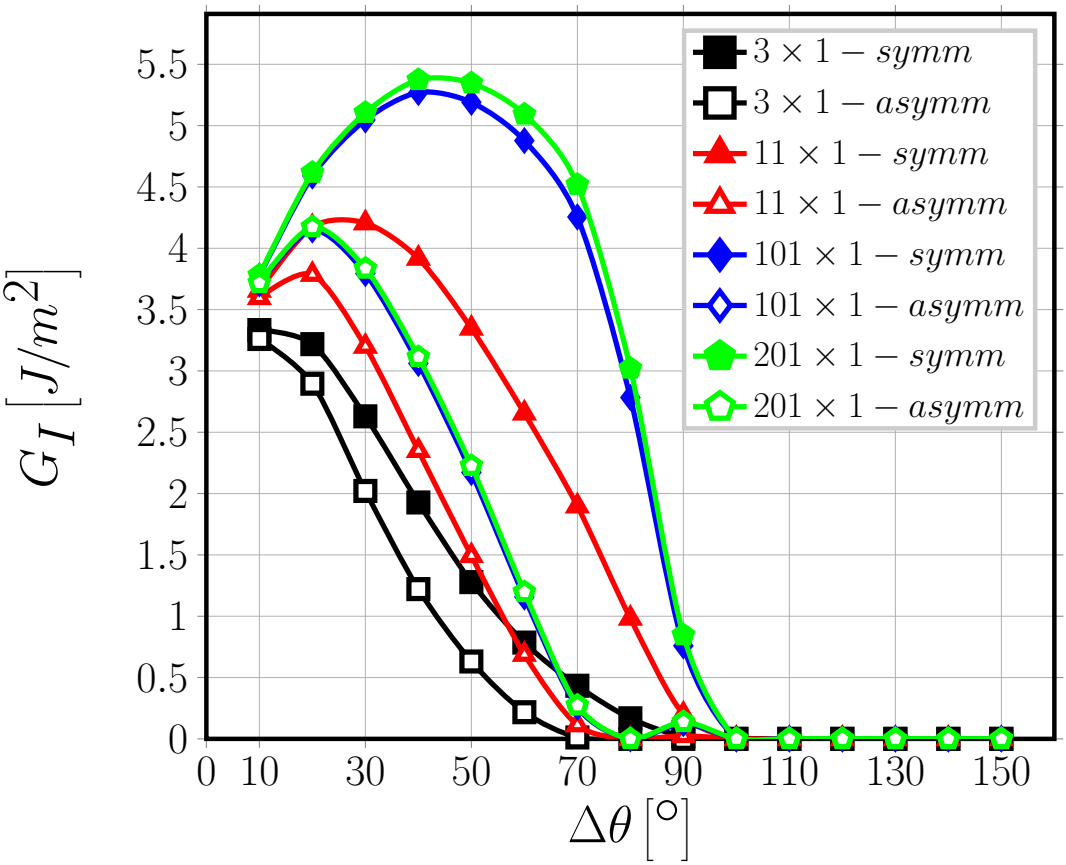

Figure 2.17: Comparison of Mode I ERR between $n \times 1 - symm$ and $n \times 1 - asymm$ RVEs, $V_f = 60\%$, $\varepsilon_x = 1\%$.

is likelier when the Mode Ratio is Mode I dominated, it thus seems reasonable to expect that the growth of consecutive vertically aligned debonds (with no fully bonded fiber in between) is favored when they are located on the same side of their respective fibers.

3. No significant difference in G_{II} between the two RVE families is observed except in the range $\Delta\theta = 80° - 100°$. In this range, the largest values of G_{II} are obtained and G_{II} is higher when debonds are located on opposite sides of consecutive vertically aligned fibers. This means that, assuming the applied strain is high enough to cause debond growth in Mode II with the onset of a contact zone, larger debond sizes will likely be reached when debonds are on opposite sides.

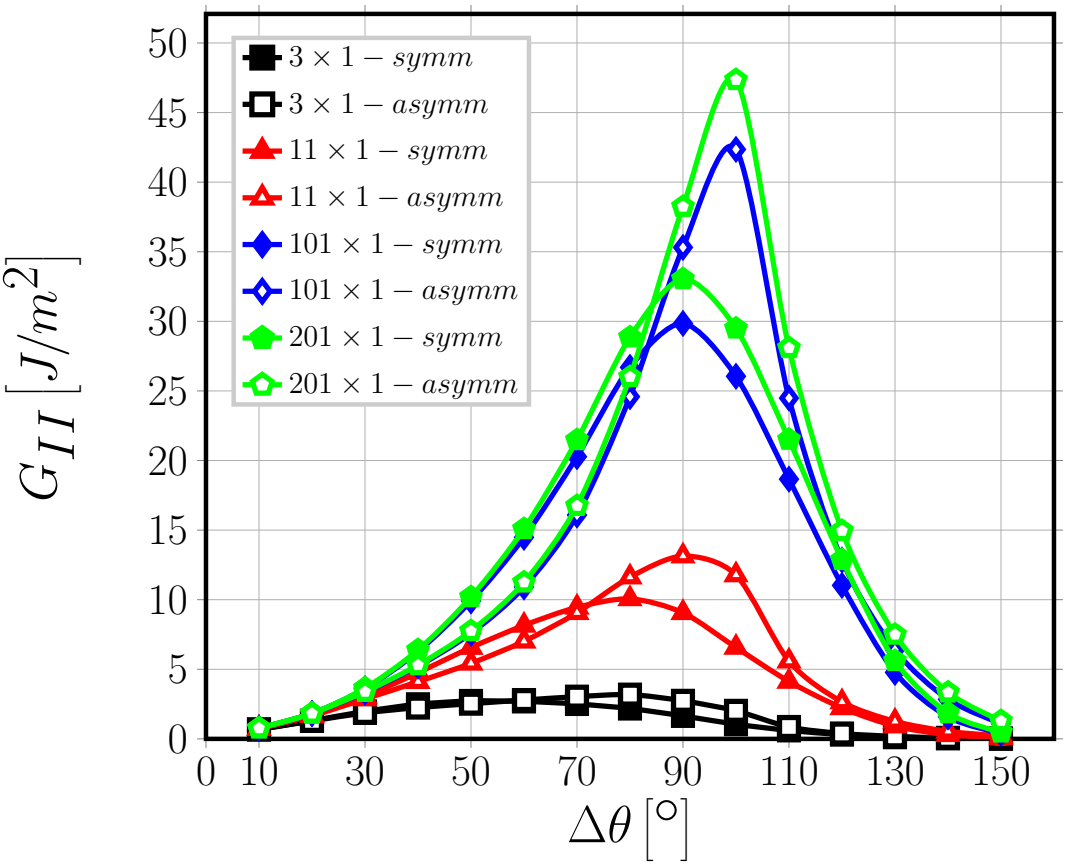

Figure 2.18: Comparison of Mode II ERR between $n\times1-symm$ and $n\times1-asymm$ RVEs, $V_f=60\%$, $\varepsilon_x=1\%$.

2.5 Paper E

Estimating the average size of fiber/matrix interface cracks in UD and cross-ply laminates

In Paper E, initiation and propagation of debonds are studied in Representative Volume Elements of UD composites and cross-ply laminates. The objective in particular is to estimate initial flaw size after debond initiation and the final maximum size after debond propagation. The RVE considered are $n\times k-free$ (see Section 2.2 for details), $n\times k-m\cdot t_{90^\circ}$ (Section 2.3), $n\times k-symm$ and $n\times k-asymm$ (see Section 2.4).
Debond initiation at the undamaged fiber/matrix interface is assumed to be governed by the stress and thus determined by a stess-based criterion. The distribution of stresses at the fiber/matrix interface is thus analyzed in models $1\times k-free$ and $1\times k-1\cdot t_{90^\circ}$ with $k=1,3,11,201$, $\Delta\theta=0^\circ$ (i.e. the undamaged case) and $\bar{\varepsilon}_x=1\%$. Selected stress components are presented, on the basis of their relevance in previous studies on debond initiation and growth available in the literature: the radial σ_{rr} and shear $\tau_{r\psi}$

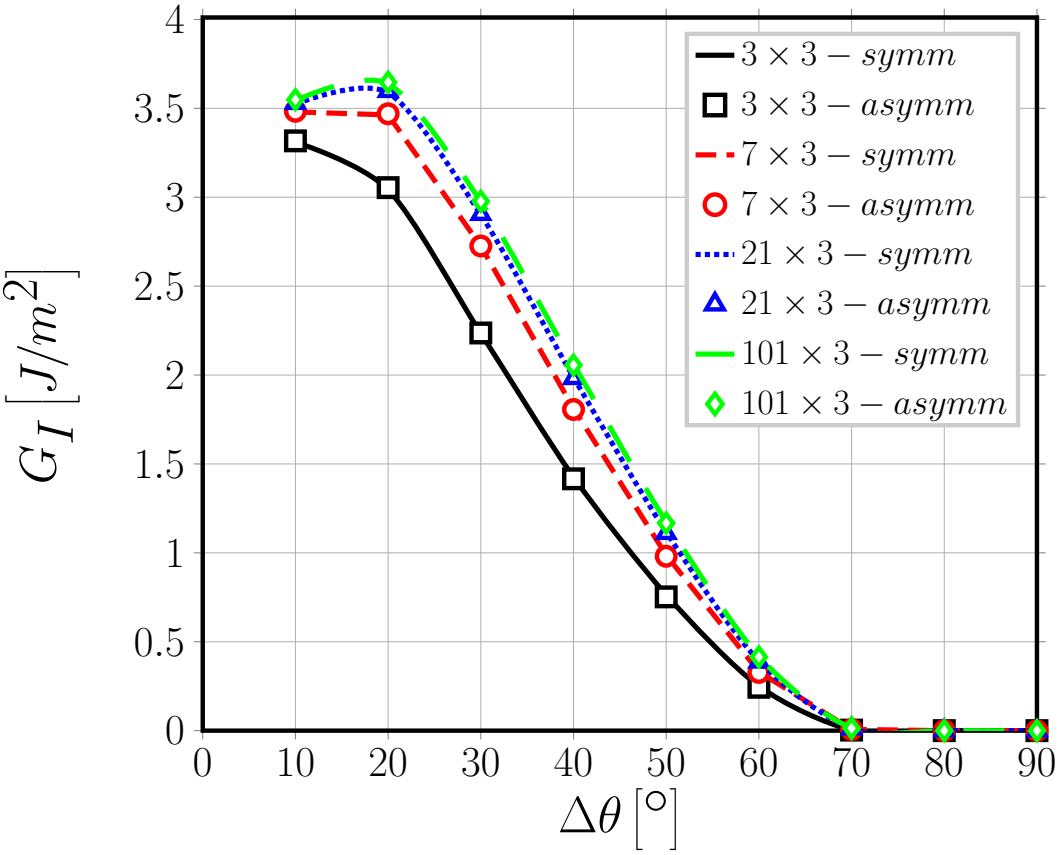

Figure 2.19: Comparison of Mode I ERR between $n\times3-symm$ and $n\times1-asymm$ RVEs, $V_f=60\%$, $\varepsilon_x=1\%$.

stress [100] (Fig. 2.21a and Fig. 2.21b), the Local Hydrostatic Stress (LHS, following [101]) σ_{LHS} [102, 103] (Fig. 2.21c and Fig. 2.21d), the local von Mises stress σ_{vM} [53] (Fig. 2.21e and Fig. 2.21f), the Local Maximum Principal Stress (LMPS, notation of [101]) σ_{LMPS} [104] (Fig. 2.21g and Fig. 2.21h). Conditions of plane strain, considered here in all RVEs, imply the existence of an out-of-plane axial component of the stress (σ_{yy} in the notation of the paper): to study the effect of the out-of-plane component (tri-axial stress state, see [48]), σ_{LHS}, σ_{vM} and σ_{LMPS} are evaluated both neglecting (index $2D$) and considering it (index $3D$).

Observing Figure 2.21, it seems reasonable to conclude that a stress-based criterion would predict, irrespectively of the specific criterion chosen, debond onset to occur at 0° (or 180°, given the symmetry of the geometry considered) with an initial size at least in the range $2^\circ-8^\circ$, corresponding to a 1% margin on the value of the stress to satisfy the criterion, and likely in the range $6^\circ-12^\circ$, corresponding to a 5% margin on the satisfaction of the criterion.
Assuming now that, as in [105], once an initial debond of a size $\Delta\theta_0\sim2^\circ-12^\circ$) is formed, the debond will grow unstably at the same level of global applied strain $\bar{\varepsilon}_x$, according to an energy-based criterion of the form [106, 100]:

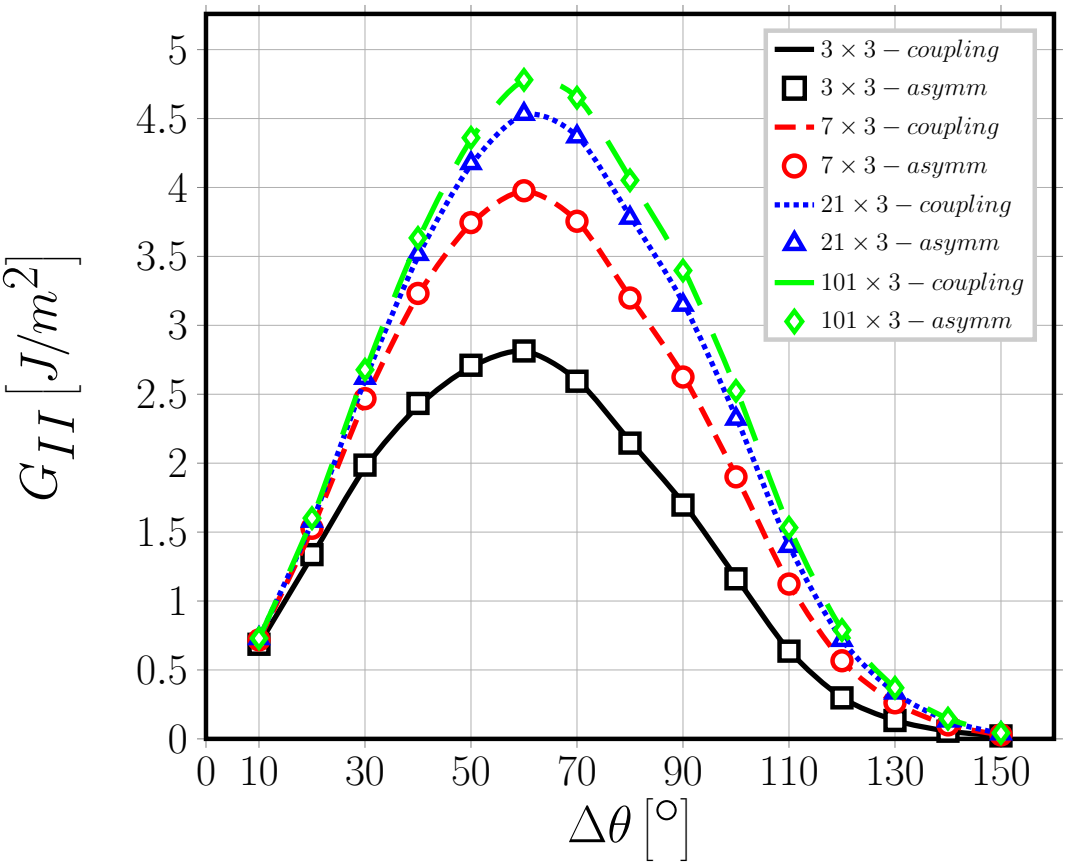

Figure 2.20: Comparison of Mode II ERR between $n\times3-symm$ and $n\times1-asymm$ RVEs, $V_f=60\%$, $\varepsilon_x=1\%$.

$$G_{TOT}\geq G_c=G_{Ic}\left(1+\tan^2\left(\left(1-\lambda\right)\Psi_G\right)\right),\quad \Psi_G=tan^{-1}\left(\sqrt{\frac{G_{II}}{G_I}}\right), \tag{2.11}$$

where Ψ_G represents the energy-based phase angle, G_{TOT} is the total ERR, G_c is the critical ERR, G_{Ic} is the Mode I critical ERR (material property) and λ the mode mixity sensitivity parameter (material property, usually $0.2\leq\lambda\leq0.35$). Given that in the present model debond propagation starts as soon as an initial debond is formed, the propagation criterion in Equation 2.11 is satisfied for the initial debond size $\Delta\theta_0$. Thus, by calculating G_I, G_{II} and G_{TOT} and equating G_c to G_{TOT} in Eq. 2.11, it is possible to evaluate G_{Ic} for different values of the initial debond size $\Delta\theta_0$ and of the parameter λ (Figure 2.22).

It is possible to observe in Figure 2.22 that neither RUC configuration nor λ affects G_{Ic} significantly for $\Delta\theta_0<10^\circ$, which corresponds to the range of initial debond size previously determined. Thus, we can assume a value of G_{Ic} in the range $2-4.5\ \left[\frac{J}{m^2}\right]$, with $0.2\leq\lambda\leq0.35$ and $\bar{\varepsilon}_x=1\%$.

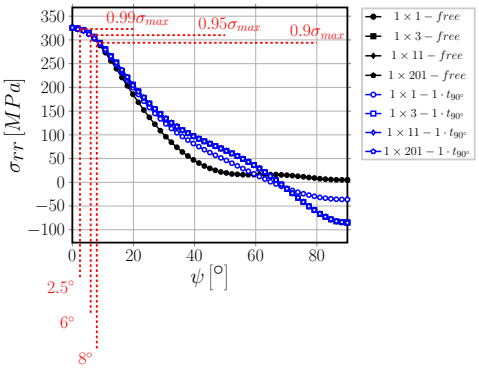

(a) Radial stress σ_{rr}.

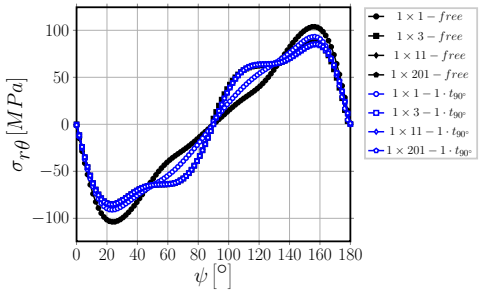

(b) Shear stress $\tau_{r\psi}$.

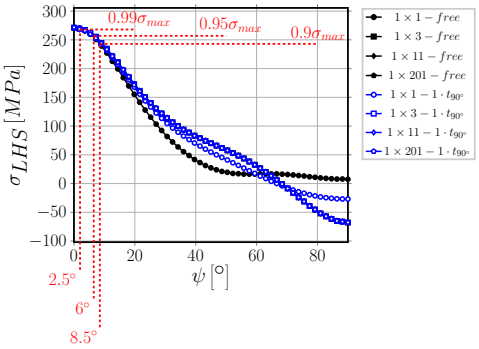

(c) Local Hydrostatic Stress (LHS), neglecting σ_{yy}, $\sigma_{LHS,2D}$.

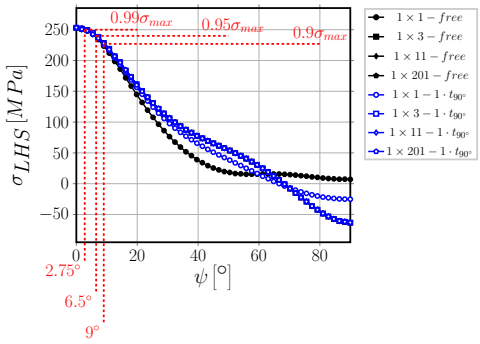

(d) Local Hydrostatic Stress (LHS), considering σ_{yy}, $\sigma_{LHS,3D}$.

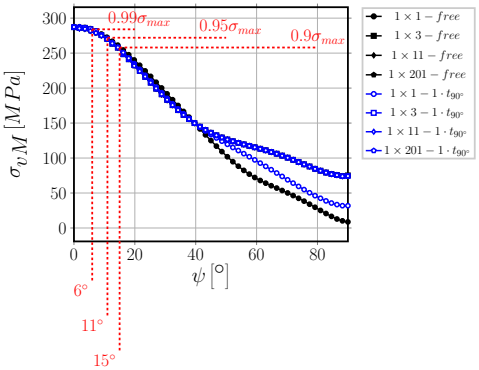

(e) Local von Mises stress, neglecting σ_{yy}, $\sigma_{vM,2D}$.

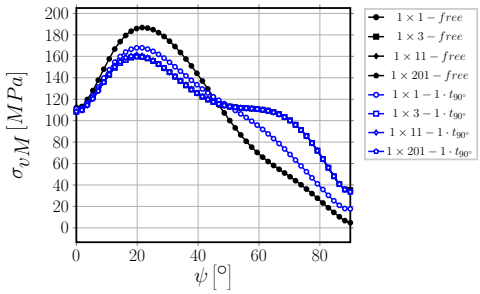

(f) Local von Mises stress, considering σ_{yy}, $\sigma_{vM,3D}$.

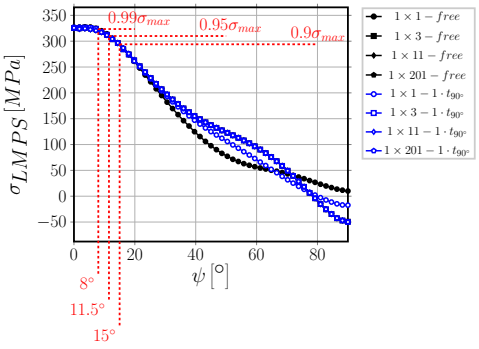

(g) Local Maximum Principal Stress (LMPS), neglecting σ_{yy}, $\sigma_{LMPS,2D}$.

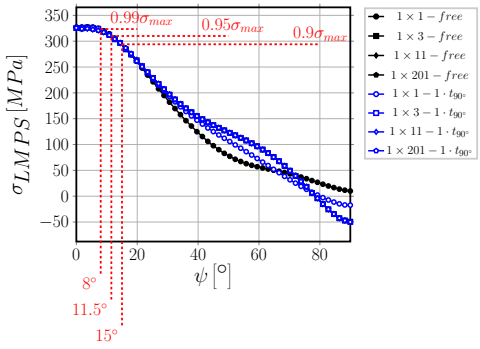

(h) Local Maximum Principal Stress (LMPS), considering σ_{yy}, $\sigma_{LMPS,3D}$.

Figure 2.21: Stress distribution at the fiber/matrix interface in the absence of damage with respect to angular coordinate ψ; applied strain $\bar{\varepsilon}_x = 1\%$.

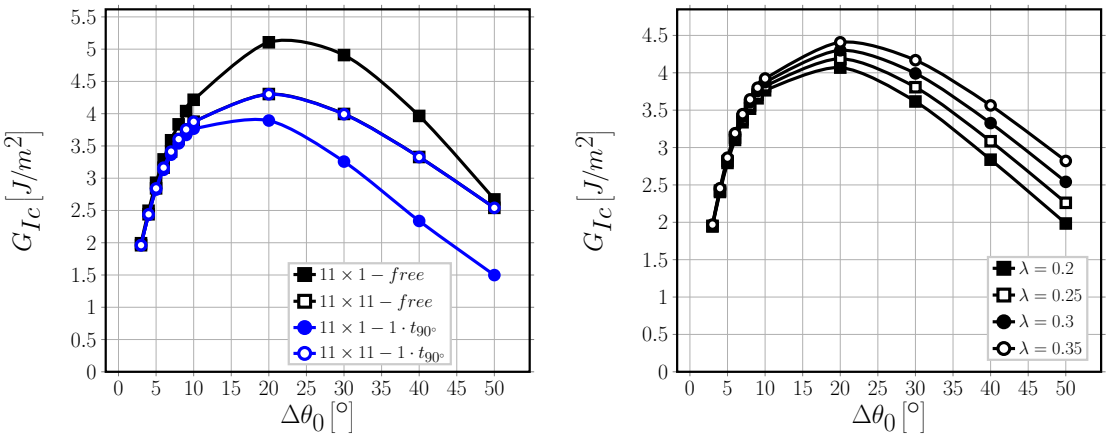

(a) $\lambda = 0.3$. (b) $11 \times 11 - 1 \cdot t_{90^\circ}$.

Figure 2.22: Estimated values of G_{Ic} assuming different values of initial debond size, for different RUCs and varying λ, with global applied strain $\bar{\varepsilon}_x$ equal to 1%.

Finally, by calculating G_c according to Equation 2.11, the expected maximum debond size $\Delta\theta_{max}$ is the value of $\Delta\theta$ such that

$$G_{TOT}\left(\Delta\theta \geq \Delta\theta_{max}\right) \leq G_c\left(\Delta\theta \geq \Delta\theta_{max}\right). \tag{2.12}$$

The following ranges of maximum debond size are obtained (see Figure 2.23): for a 1-fiber row UD composite, $30^\circ - 105^\circ$; for a 1-fiber row 90° ply in a cross-ply laminate, $30^\circ - 45^\circ$; for a multiple fiber-rows UD composite and a multiple fiber-rows 90° ply in a cross-ply laminate , $40^\circ - 60^\circ$; for consecutive debonds along the vertical direction in a UD composite, $80^\circ - 110^\circ$ when debonds are on the same sides and $60^\circ - 115^\circ$ when on opposite sides. The estimate for the RVE of a cross-ply laminate ($n \times k - 1 \cdot t_{90^\circ}$ RVE, $k \geq 3$) is in good agreeement with the debond size distribution estimated in [107] through microscopic observations of $[0_3^\circ, 90_3^\circ]_S$ specimens loaded in tension.

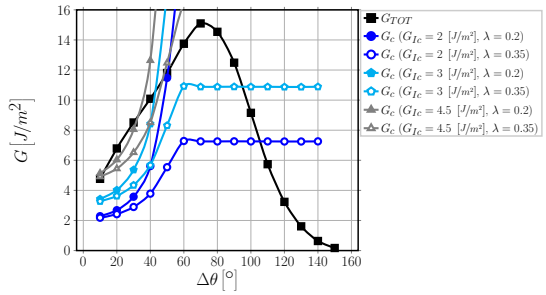

(a) $21 \times 1 - free.$

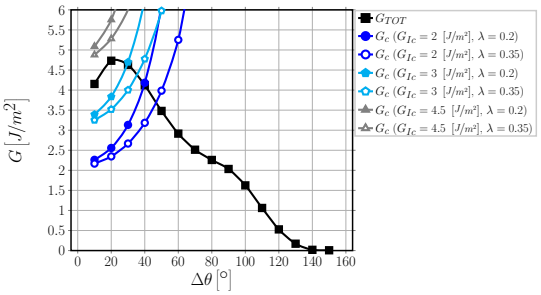

(b) $21 \times 1 - 1 \cdot t_{90°}.$

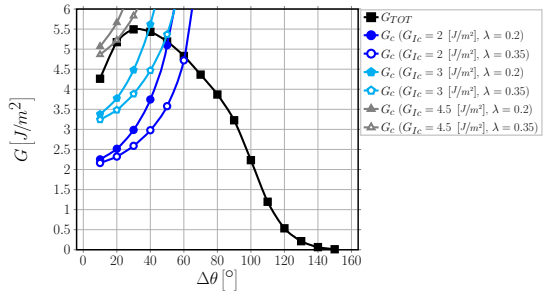

(c) $21 \times 3 - free.$

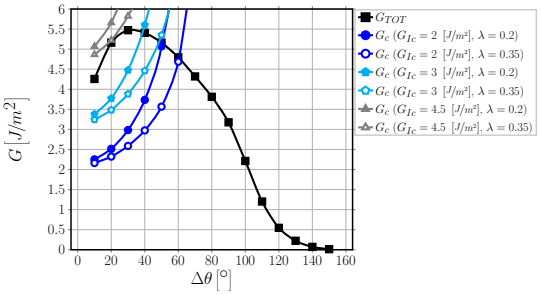

(d) $21 \times 3 - 1 \cdot t_{90°}.$

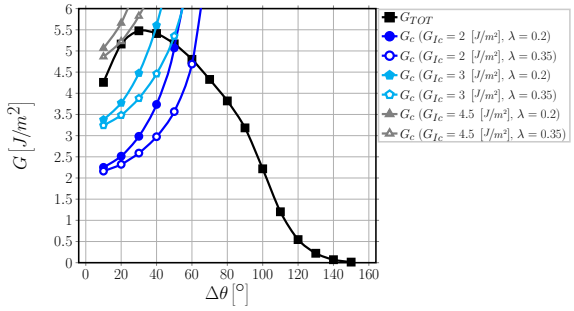

(e) $21 \times 21 - free.$

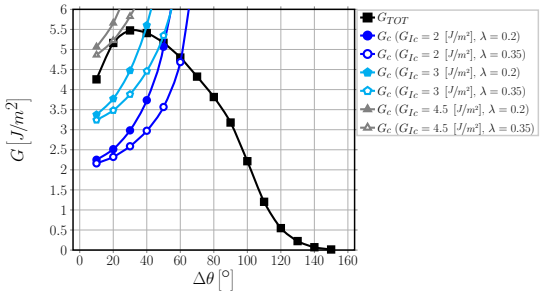

(f) $21 \times 21 - 1 \cdot t_{90°}.$

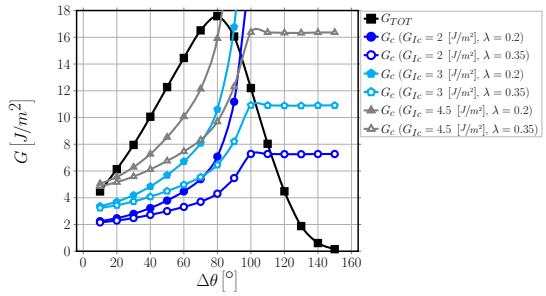

(g) $21 \times 1 - coupling.$

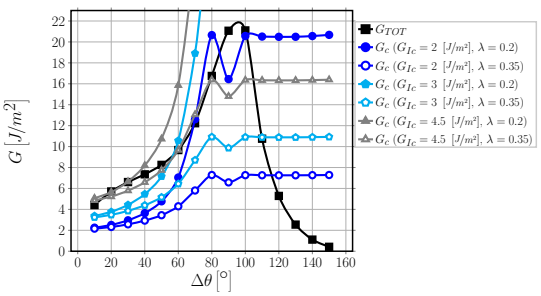

(h) $21 \times 1 - asymm.$

Figure 2.23: G_{TOT} and G_c for several RUCs and different values of G_{Ic} and λ, computed for $\bar{\varepsilon}_x = 1\%$. Each intersection point of G_{TOT} and G_c curves such that $G_{TOT}\,(\Delta\theta \geq \Delta\theta_{intersection}) \leq G_c\,(\Delta\theta \geq \Delta\theta_{intersection})$ determines an estimate of $\Delta\theta_{max}$.

References

[1] A. D. Little. "The Fifth Estate". In: *Science* 60.1553 (Oct. 1924), pp. 299–306. DOI: 10.1126/science.60.1553.299.

[2] Max Weber. "Science as a vocation". In: *The Sociology of Science*. Ed. by B.Barber and W. Hirsch. Vol. 32. New York: Free Press, 1962 [1917], pp. 569–589.

[3] Steven Shapin. "The Virtue of Scientific Thinking". In: *Boston Review* 32 (Jan. 2015). URL: http://bostonreview.net/steven-shapin-scientism-virtue.

[4] Stephen G. Brush. "History of the Lenz-Ising Model". In: *Reviews of Modern Physics* 39.4 (Oct. 1967), pp. 883–893. DOI: 10.1103/revmodphys.39.883.

[5] Martin Niss. "History of the Lenz–Ising Model 1950–1965: from irrelevance to relevance". In: *Archive for History of Exact Sciences* 63.3 (Dec. 2008), pp. 243–287. DOI: 10.1007/s00407-008-0039-5.

[6] Martin Niss. "History of the Lenz–Ising Model 1920–1950: From Ferromagnetic to Cooperative Phenomena". In: *Archive for History of Exact Sciences* 59.3 (Oct. 2004), pp. 267–318. DOI: 10.1007/s00407-004-0088-3.

[7] Gert Biesta. "Bildung and Modernity: The Future of Bildung in a World of Difference". In: *Studies in Philosophy and Education* 21.4/5 (2002), pp. 343–351. DOI: 10.1023/a:1019874106870.

[8] Gert J.J. Biesta. "Education, Accountability, and the Ethical Demand: Can the Democratic Potential of Accountability Be Regained?" In: *Educational Theory* 54.3 (Aug. 2004), pp. 233–250. DOI: 10.1111/j.0013-2004.2004.00017.x.

[9] Boaventura de Sousa Santos. "The European University at a Crossroads". In: *IdeAs* 2 (Feb. 2012). DOI: 10.4000/ideas.276.

[10] Harry W. Jones. "The Recent Large Reduction in Space Launch Cost". In: *Proceedings of the* 48^{th} *International Conference on Environmental Systems (ICES)*. (Albuquerque, New Mexico, USA, July 8–12, 2018). 2018.

[11] Harro Ranter and Fabian I. Lujan. *Aviation Safety Network (ASN), Database 2018*. 2019. URL: https://aviation-safety.net/database/dblist.php?Year=2018 (visited on 10/07/2019).

[12] Harro Ranter and Fabian I. Lujan. *Aviation Safety Network (ASN), Database 2019*. 2019. URL: https://aviation-safety.net/database/dblist.php?Year=2019 (visited on 10/07/2019).

[13] C. Daniels. “Pneumatic spreading of filaments”. USP 3795944. Space Systems/Loral LLC. 1974. USA.

[14] S. Iyer and L. T. Drzal. “Method and system for spreading a tow of fibers”. USP 5042122. Michigan State University. 1991. USA.

[15] N. Nakagawa and Y. Ohsora. “Fiber separator for producing fiber reinforced metallic or resin body”. USP 5101542. Ube Industries Ltd. 1992. Japan.

[16] J. L. Lifke et al. “Method and apparatus for spreading fiber bundles”. USP 6049956. Adherent Tech Inc. 2000. USA.

[17] J. M. Peritt, R. Everett, and A. Edelstein. “Electrostatic fiber spreader including a corona discharge device”. USP 5200620. US Secretary of Navy. 1993. USA.

[18] K. Kawabe, S. Tomoda, and T. Matsuo. “A pneumatic process for spreading reinforcing fiber tow”. In: *Proc. 42nd Int. SAMPE USA (Anaheim, CA, USA)* (1997), pp. 65–76.

[19] K. Kawabe and S. Tomoda. “Method of producing a spread multi-filament bundle and an apparatus used in the same”. JP 2003–193895. Fukui Prefectural Government. 2003. Japan.

[20] K. Kawabe. “New Spreading Technology for Carbon Fiber Tow and Its Application to Composite Materials [in Japanese]”. In: *Sen'i Gakkaishi* 64 (8 2008), pp. 262–267.

[21] H. Sasayama and S. Tomoda. “New Carbon Fiber Tow-Spread Technology and Applications to Advanced Composite Materials”. In: *S.A.M.P.E. journal* 45 (2 2009), pp. 6–17.

[22] *North Thin Ply Technology - Home*. 2016. URL: `https://www.thinplytechnology.com/` (visited on 10/07/2019).

[23] *Oxeon - Technologies*. 2019. URL: `http://oxeon.se/technologies/` (visited on 10/07/2019).

[24] *Innovative and high-performance reinforcements*. 2019. URL: `https://composites.chomarat.com/en/` (visited on 10/07/2019).

[25] *Carbon fiber*. 1997–2019. URL: `http://www.sakaiovex.co.jp/english/carbon/index.html` (visited on 10/07/2019).

[26] Jin-Bum Moon et al. “Improvement of tensile properties of CFRP composites under LEO space environment by applying MWNTs and thin-ply”. In: *Composites Part A: Applied Science and Manufacturing* 42.6 (June 2011), pp. 694–701. DOI: `10.1016/j.compositesa.2011.02.011`.

[27] Yong Han Noel Kim et al. “Effects of Shallow Biangle, Thin-Ply Laminates on Structural Performance of Composite Wings”. In: *AIAA Journal* 55.6 (June 2017), pp. 2086–2092. DOI: `10.2514/1.j055465`.

[28] Douglas A. McCarville et al. "3.5 Design, Manufacture and Test of Cryotank Components". In: *Comprehensive Composite Materials II*. Elsevier, 2018, pp. 153–179. DOI: 10.1016/b978-0-12-803581-8.09958-6.

[29] Alexander Kopp et al. "The Aurora space launcher concept". In: *CEAS Space Journal* 10.2 (Nov. 2017), pp. 167–187. DOI: 10.1007/s12567-017-0184-2.

[30] Hideki Sasayama et al. "Effect of Lamina Thickness on First Ply Failure in Multidirectionally Laminated Composites". In: *Journal of the Japan Society for Composite Materials* 30.4 (2004), pp. 142–148. DOI: 10.6089/jscm.30.142.

[31] K. Yamaguchi and H.T. Hahn. "The improved ply cracking resistance of thin-ply laminates". In: *Proceedings of the* 15^{th} *International Conference on Composite Materials (ICCM-15)*. (Durban, South Africa, June 27–July 2, 2005). 2005.

[32] Stephen W. Tsai. "Thin-ply technology and a strain-based health monitoring system". In: *Proceedings of the* 15^{th} *International Conference on Composite Materials (ICCM-15)*. (Durban, South Africa, June 27–July 2, 2005). 2005.

[33] S.W. Tsai, S. Sihn, and R.Y. Kim. "Thin Ply Composites". In: *Proceedings of* 46^{th} *AIAA/ASME/AHS/ASC Structures, Structural Dynamics & Materials Conference*. (Austin, TX, USA, Apr. 18–21, 2005). 2005.

[34] S. Sihn et al. "Experimental studies of thin-ply laminated composites". In: *Composites Science and Technology* 67.6 (May 2007), pp. 996–1008. DOI: 10.1016/j.compscitech.2006.06.008.

[35] Tomohiro Yokozeki, Yuichiro Aoki, and Toshio Ogasawara. "Experimental characterization of strength and damage resistance properties of thin-ply carbon fiber/toughened epoxy laminates". In: *Composite Structures* 82.3 (Feb. 2008), pp. 382–389. DOI: 10.1016/j.compstruct.2007.01.015.

[36] Tomohiro Yokozeki et al. "Damage characterization in thin-ply composite laminates under out-of-plane transverse loadings". In: *Composite Structures* 93.1 (Dec. 2010), pp. 49–57. DOI: 10.1016/j.compstruct.2010.06.016.

[37] Hiroshi Saito, Hiroki Takeuchi, and Isao Kimpara. "Experimental Evaluation of the Damage Growth Restraining in 90° Layer of Thin-ply CFRP Cross-ply Laminates". In: *Advanced Composite Materials* 21.1 (2012), pp. 57–66. DOI: 10.1163/156855112X629522.

[38] R. Amacher et al. "Thin ply composites: Experimental characterization and modeling of size-effects". In: *Composites Science and Technology* 101 (Sept. 2014), pp. 121–132. DOI: 10.1016/j.compscitech.2014.06.027.

[39] J. Cugnoni et al. "Towards aerospace grade thin-ply composites: Effect of ply thickness, fibre, matrix and interlayer toughening on strength and damage tolerance". In: *Composites Science and Technology* 168 (Nov. 2018), pp. 467–477. DOI: 10.1016/j.compscitech.2018.08.037.

[40] Jr. K. E. Hofer and E. M. Olsen. *An investigation of the fatigue and creep properties of glass reinforced plastics for primary aircraft structures*. Tech. rep. Naval Air Systems Command, Department of the Navy, Apr. 1967.

[41] R. J. Howe. "Cumulative Damage of a Glass Reinforced Plastic". PhD thesis. Journal of Physics D: Applied Physics, 1972.

[42] M. J. Owen and R. J. Howe. "The accumulation of damage in a glass-reinforced plastic under tensile and fatigue loading". In: *Journal of Physics D: Applied Physics* 5.9 (Sept. 1972), pp. 1637–1649. DOI: 10.1088/0022-3727/5/9/319.

[43] K. W. Garrett and J. E. Bailey. "Multiple transverse fracture in 90° cross-ply laminates of a glass fibre-reinforced polyester". In: *Journal of Materials Science* 12.1 (Jan. 1977), pp. 157–168. DOI: 10.1007/bf00738481.

[44] A. Parvizi and J. E. Bailey. "On multiple transverse cracking in glass fibre epoxy cross-ply laminates". In: *Journal of Materials Science* 13.10 (Oct. 1978), pp. 2131–2136. DOI: 10.1007/bf00541666.

[45] A. Parvizi, K. W. Garrett, and J. E. Bailey. "Constrained cracking in glass fibre-reinforced epoxy cross-ply laminates". In: *Journal of Materials Science* 13.1 (Jan. 1978), pp. 195–201. DOI: 10.1007/bf00739291.

[46] J. E. Bailey, P. T. Curtis, and A. Parvizi. "On the Transverse Cracking and Longitudinal Splitting Behaviour of Glass and Carbon Fibre Reinforced Epoxy Cross Ply Laminates and the Effect of Poisson and Thermally Generated Strain". In: *Proceedings of the Royal Society A: Mathematical, Physical and Engineering Sciences* 366.1727 (July 1979), pp. 599–623. DOI: 10.1098/rspa.1979.0071.

[47] J. E. Bailey and A. Parvizi. "On fibre debonding effects and the mechanism of transverse-ply failure in cross-ply laminates of glass fibre/thermoset composites". In: *Journal of Materials Science* 16.3 (Mar. 1981), pp. 649–659. DOI: 10.1007/bf02402782.

[48] Leif E. Asp, Lars A. Berglund, and Peter Gudmundson. "Effects of a composite-like stress state on the fracture of epoxies". In: *Composites Science and Technology* 53.1 (Jan. 1995), pp. 27–37. DOI: 10.1016/0266-3538(94)00075-1.

[49] L.E. Asp, L.A. Berglund, and R. Talreja. "A criterion for crack initiation in glassy polymers subjected to a composite-like stress state". In: *Composites Science and Technology* 56.11 (Jan. 1996), pp. 1291–1301. DOI: 10.1016/s0266-3538(96)00090-5.

[50] H. Zhang et al. "Transverse single-fibre test for interfacial debonding in composites: 1. Experimental observations". In: *Composites Part A: Applied Science and Manufacturing* 28.4 (Jan. 1997), pp. 309–315. DOI: 10.1016/s1359-835x(96)00123-6.

[51] Karolina Martyniuk et al. "3D in situ observations of glass fibre/matrix interfacial debonding". In: *Composites Part A: Applied Science and Manufacturing* 55 (Dec. 2013), pp. 63–73. DOI: 10.1016/j.compositesa.2013.07.012.

[52] V.I. Kushch et al. "Numerical simulation of progressive debonding in fiber reinforced composite under transverse loading". In: *International Journal of Engineering Science* 49.1 (Jan. 2011), pp. 17–29. DOI: 10.1016/j.ijengsci.2010.06.020.

[53] Luis Pablo Canal et al. "Intraply fracture of fiber-reinforced composites: Microscopic mechanisms and modeling". In: *Composites Science and Technology* 72.11 (June 2012), pp. 1223–1232. DOI: 10.1016/j.compscitech.2012.04.008.

[54] Lyazid Bouhala et al. "Modelling of failure in long fibres reinforced composites by X-FEM and cohesive zone model". In: *Composites Part B: Engineering* 55 (Dec. 2013), pp. 352–361. DOI: 10.1016/j.compositesb.2012.12.013.

[55] Miguel Herráez et al. "Transverse cracking of cross-ply laminates: A computational micromechanics perspective". In: *Composites Science and Technology* 110 (Apr. 2015), pp. 196–204. DOI: 10.1016/j.compscitech.2015.02.008.

[56] J. Segurado and J. Llorca. "A numerical approximation to the elastic properties of sphere-reinforced composites". In: *Journal of the Mechanics and Physics of Solids* 50.10 (Oct. 2002), pp. 2107–2121. DOI: 10.1016/s0022-5096(02)00021-2.

[57] Sarah A. Elnekhaily and Ramesh Talreja. "Damage initiation in unidirectional fiber composites with different degrees of nonuniform fiber distribution". In: *Composites Science and Technology* 155 (Feb. 2018), pp. 22–32. DOI: 10.1016/j.compscitech.2017.11.017.

[58] Zdeněk P. Bažant and B. H. Oh. "Crack band theory for fracture of concrete". In: *Matériaux et Constructions* 16.3 (May 1983), pp. 155–177. DOI: 10.1007/bf02486267.

[59] Z.-H. Jin and C.T. Sun. "Cohesive zone modeling of interface fracture in elastic bi-materials". In: *Engineering Fracture Mechanics* 72.12 (Aug. 2005), pp. 1805–1817. DOI: 10.1016/j.engfracmech.2004.09.011.

[60] Andrzej Pawlak, Andrzej Galeski, and Artur Rozanski. "Cavitation during deformation of semicrystalline polymers". In: *Progress in Polymer Science* 39.5 (May 2014), pp. 921–958. DOI: 10.1016/j.progpolymsci.2013.10.007.

[61] Ronald Krueger. "Virtual crack closure technique: History, approach, and applications". In: *Applied Mechanics Reviews* 57.2 (2004), p. 109. DOI: 10.1115/1.1595677.

[62] J. R. Rice. "A Path Independent Integral and the Approximate Analysis of Strain Concentration by Notches and Cracks". In: *Journal of Applied Mechanics* 35.2 (1968), p. 379. DOI: 10.1115/1.3601206.

[63] M. Toya. "A crack along the interface of a circular inclusion embedded in an infinite solid". In: *Journal of the Mechanics and Physics of Solids* 22.5 (Oct. 1974), pp. 325–348. DOI: 10.1016/0022-5096(74)90002-7.

[64] F. París, J. C. Caño, and J. Varna. "The fiber-matrix interface crack — A numerical analysis using Boundary Elements". In: *International Journal of Fracture* 82.1 (May 1996), pp. 11–29. DOI: 10.1007/bf00017861.

[65] Linqi Zhuang et al. "Effects of inter-fiber spacing on fiber-matrix debond crack growth in unidirectional composites under transverse loading". In: *Composites Part A: Applied Science and Manufacturing* 109 (June 2018), pp. 463–471. DOI: 10.1016/j.compositesa.2018.03.031.

[66] M. L. Williams. "The stresses around a fault or crack in dissimilar media". In: *Bulletin of the Seismological Society of America* 49.2 (1959), p. 199.

[67] J. Dundurs. "Discussion: "Edge-Bonded Dissimilar Orthogonal Elastic Wedges Under Normal and Shear Loading" (Bogy, D. B., 1968, ASME J. Appl. Mech., 35, pp. 460–466)". In: *Journal of Applied Mechanics* 36.3 (1969), p. 650. DOI: 10.1115/1.3564739.

[68] Fazil Erdogan. "Stress Distribution in a Nonhomogeneous Elastic Plane With Cracks". In: *Journal of Applied Mechanics* 30.2 (1963), p. 232. DOI: 10.1115/1.3636517.

[69] Maria Comninou. "An overview of interface cracks". In: *Engineering Fracture Mechanics* 37.1 (Jan. 1990), pp. 197–208. DOI: 10.1016/0013-7944(90)90343-f.

[70] A. H. England. "A Crack Between Dissimilar Media". In: *Journal of Applied Mechanics* 32.2 (1965), p. 400. DOI: 10.1115/1.3625813.

[71] B.M. Malyshev and R.L. Salganik. "The strength of adhesive joints using the theory of cracks". In: *International Journal of Fracture Mechanics* 1-1.2 (June 1965). DOI: 10.1007/bf00186749. URL: https://doi.org/10.1007/bf00186749.

[72] Maria Comninou. "The Interface Crack". In: *Journal of Applied Mechanics* 44.4 (1977), p. 631. DOI: 10.1115/1.3424148. URL: https://doi.org/10.1115/1.3424148.

[73] A. H. England. "An Arc Crack Around a Circular Elastic Inclusion". In: *Journal of Applied Mechanics* 33.3 (1966), p. 637. DOI: 10.1115/1.3625132.

[74] A.B. Perlman and G.C. Sih. "Elastostatic problems of curvilinear cracks in bonded dissimilar materials". In: *International Journal of Engineering Science* 5.11 (Nov. 1967), pp. 845–867. DOI: 10.1016/0020-7225(67)90009-2.

[75] George R. Irwin. "Fracture". In: *Elasticity and Plasticity / Elastizität und Plastizität*. Springer Berlin Heidelberg, 1958, pp. 551–590. DOI: 10.1007/978-3-642-45887-3_5.

[76] J. C. Del Caño and F. París. "On stress singularities induced by the discretization in curved receding contact surfaces: a BEM analysis". In: *International Journal for Numerical Methods in Engineering* 40.12 (June 1997), pp. 2301–2320. DOI: 10.1002/(sici)1097-0207(19970630)40:12<2301::aid-nme166>3.0.co;2-8.

[77] J. Varna, Federico París, and J. C.Caño. "The effect of crack-face contact on fiber/matrix debonding in transverse tensile loading". In: *Composites Science and Technology* 57.5 (1997), pp. 523–532. DOI: 10.1016/s0266-3538(96)00175-3.

[78] I.G. García, V. Mantič, and E. Graciani. "Debonding at the fibre–matrix interface under remote transverse tension. One debond or two symmetric debonds?" In: *European Journal of Mechanics - A/Solids* 53 (Sept. 2015), pp. 75–88. DOI: 10.1016/j.euromechsol.2015.02.007.

[79] E. Correa et al. "Effects of the presence of compression in transverse cyclic loading on fibre–matrix debonding in unidirectional composite plies". In: *Composites Part A: Applied Science and Manufacturing* 38.11 (Nov. 2007), pp. 2260–2269. DOI: 10.1016/j.compositesa.2006.11.002.

[80] E. Correa, V. Mantič, and F. París. "Effect of thermal residual stresses on matrix failure under transverse tension at micromechanical level: A numerical and experimental analysis". In: *Composites Science and Technology* 71.5 (Mar. 2011), pp. 622–629. DOI: 10.1016/j.compscitech.2010.12.027.

[81] E. Correa, F. París, and V. Mantič. "Effect of the presence of a secondary transverse load on the inter-fibre failure under tension". In: *Engineering Fracture Mechanics* 103 (May 2013), pp. 174–189. DOI: 10.1016/j.engfracmech.2013.02.026.

[82] E. Correa, F. París, and V. Mantič. "Effect of a secondary transverse load on the inter-fibre failure under compression". In: *Composites Part B: Engineering* 65 (Oct. 2014), pp. 57–68. DOI: 10.1016/j.compositesb.2014.01.005.

[83] C. Sandino, E. Correa, and F. París. "Numerical analysis of the influence of a nearby fibre on the interface crack growth in composites under transverse tensile load". In: *Engineering Fracture Mechanics* 168 (Dec. 2016), pp. 58–75. DOI: 10.1016/j.engfracmech.2016.01.022.

[84] C. Sandino, E. Correa, and F. París. "Composite materials under transverse biaxial loads: Study of the influence of a nearby fibre on the interface crack growth under tension". In: *Proceeding of the* 17^{th} *European Conference on Composite Materials (ECCM-17).* (Munich, Germany, June 26–30, 2016). 2016.

[85] C. Sandino, E. Correa, and F. París. "Interface crack growth under transverse compression: nearby fibre effect". In: *Proceeding of the* 18^{th} *European Conference on Composite Materials (ECCM-18).* (Athens, Greece, June 24–28, 2018). 2018.

[86] Janis Varna et al. "Growth and Interaction of Debonds in Local Clusters of Fibers in Unidirectional Composites during Transverse Loading". In: *Key Engineering Materials* 754 (Sept. 2017), pp. 63–66. DOI: 10.4028/www.scientific.net/kem.754.63.

[87] E.F. Rybicki and M.F. Kanninen. "A finite element calculation of stress intensity factors by a modified crack closure integral". In: *Engineering Fracture Mechanics* 9.4 (Jan. 1977), pp. 931–938. DOI: 10.1016/0013-7944(77)90013-3.

[88] R. Krueger, K. N. Shivakumar, and I. S. Raju. "Fracture Mechanics Analyses for Interface Crack Problems - A Review". In: *54th AIAA, ASME, ASCE, AHS, ASC Structures, Structural Dynamics, and Materials Conference.* American Institute of Aeronautics and Astronautics, Apr. 2013. DOI: 10.2514/6.2013-1476.

[89] C.T Sun and C.J Jih. "On strain energy release rates for interfacial cracks in bimaterial media". In: *Engineering Fracture Mechanics* 28.1 (Jan. 1987), pp. 13–20. DOI: 10.1016/0013-7944(87)90115-9.

[90] C.T. Sun and M.G. Manoharan. "Strain Energy Release Rates of an Interfacial Crack Between Two Orthotropic Solids". In: *Journal of Composite Materials* 23.5 (May 1989), pp. 460–478. DOI: 10.1177/002199838902300503.

[91] M.G. Manoharan and C.T. Sun. "Strain energy release rates of an interfacial crack between two anisotropic solids under uniform axial strain". In: *Composites Science and Technology* 39.2 (Jan. 1990), pp. 99–116. DOI: 10.1016/0266-3538(90)90049-b.

[92] I.S. Raju, J.H. Crews, and M.A. Aminpour. "Convergence of strain energy release rate components for Edge-Delaminated composite laminates". In: *Engineering Fracture Mechanics* 30.3 (Jan. 1988), pp. 383–396. DOI: 10.1016/0013-7944(88)90196-8.

[93] A. Agrawal and A. M. Karlsson. "Obtaining mode mixity for a bimaterial interface crack using the virtual crack closure technique". In: *International Journal of Fracture* 141.1-2 (Sept. 2006), pp. 75–98. DOI: 10.1007/s10704-006-0069-4.

[94] S. Wang, C.M. Harvey, and L. Guan. "Partition of mixed modes in layered isotropic double cantilever beams with non-rigid cohesive interfaces". In: *Engineering Fracture Mechanics* 111 (Oct. 2013), pp. 1–25. DOI: 10.1016/j.engfracmech.2013.09.005.

[95] Federico París, Elena Correa, and Vladislav Mantič. "Kinking of Transversal Interface Cracks Between Fiber and Matrix". In: *Journal of Applied Mechanics* 74.4 (2007), p. 703. DOI: 10.1115/1.2711220.

[96] Z. Hashin. "Analysis of Composite Materials—A Survey". In: *Journal of Applied Mechanics* 50.3 (1983), p. 481. DOI: 10.1115/1.3167081.

[97] R.M. Christensen and K.H. Lo. "Solutions for effective shear properties in three phase sphere and cylinder models". In: *Journal of the Mechanics and Physics of Solids* 27.4 (Aug. 1979), pp. 315–330. DOI: 10.1016/0022-5096(79)90032-2.

[98] M.L. Velasco et al. "BEM multiscale modelling involving micromechanical damage in fibrous composites". In: *Engineering Analysis with Boundary Elements* 93 (Aug. 2018), pp. 1–9. DOI: 10.1016/j.enganabound.2018.03.012.

[99] Federico París, María Luisa Velasco, and Elena Correa. "Micromechanical study on the influence of scale effect in the first stage of damage in composites". In: *Composites Science and Technology* 160 (May 2018), pp. 1–8. DOI: 10.1016/j.compscitech.2018.03.004.

[100] V. Mantič. "Interface crack onset at a circular cylindrical inclusion under a remote transverse tension. Application of a coupled stress and energy criterion". In: *International Journal of Solids and Structures* 46.6 (Mar. 2009), pp. 1287–1304. DOI: 10.1016/j.ijsolstr.2008.10.036.

[101] P.A. Carraro and M. Quaresimin. "Modeling the crack initiation in unidirectional laminates under multiaxial fatigue loading1". In: *Modeling Damage, Fatigue and Failure of Composite Materials*. Elsevier, 2016, pp. 357–375. DOI: 10.1016/b978-1-78242-286-0.00016-9.

[102] L.E. Asp, L.A. Berglund, and R. Talreja. "A criterion for crack initiation in glassy polymers subjected to a composite-like stress state". In: *Composites Science and Technology* 56.11 (Jan. 1996), pp. 1291–1301. DOI: 10.1016/s0266-3538(96)00090-5.

[103] L.E. Asp, L.A. Berglund, and R. Talreja. "Prediction of matrix-initiated transverse failure in polymer composites". In: *Composites Science and Technology* 56.9 (Jan. 1996), pp. 1089–1097. DOI: 10.1016/0266-3538(96)00074-7.

[104] P.A. Carraro and M. Quaresimin. "A damage based model for crack initiation in unidirectional composites under multiaxial cyclic loading". In: *Composites Science and Technology* 99 (July 2014), pp. 154–163. DOI: 10.1016/j.compscitech.2014.05.012.

[105] E. Correa, F. París, and V. Mantič. "Fiber–matrix debonding in composite materials: transverse loading". In: *Modeling Damage, Fatigue and Failure of Composite Materials*. Elsevier, 2016, pp. 97–116. DOI: 10.1016/b978-1-78242-286-0.00006-6.

[106] J.W. Hutchinson and Z. Suo. "Mixed Mode Cracking in Layered Materials". In: *Advances in Applied Mechanics*. Elsevier, 1991, pp. 63–191. DOI: 10.1016/s0065-2156(08)70164-9.

[107] Elena Correa et al. "Microscopical observations of inter-fibre failure under tension". In: *Composites Science and Technology* 155 (Feb. 2018), pp. 213–220. DOI: 10.1016/j.compscitech.2017.12.009.

Part II

Paper A

Finite Element solution of the fiber/matrix interface crack problem: convergence properties and mode mixity of the Virtual Crack Closure Technique

Authors:
Luca Di Stasio and Zoubir Ayadi

Reformatted version of paper originally published in:
Finite Elements in Analysis and Design, Volume 167, December 2019, 103332.

© 2019, The Publisher, Reprinted with permission.

Finite Element solution of the fiber/matrix interface crack problem: convergence properties and mode mixity of the Virtual Crack Closure Technique

Luca Di Stasio[1,2,*] and Zoubir Ayadi[2]

[1]Luleå University of Technology, University Campus, SE-97187 Luleå, Sweden
[2]Université de Lorraine, EEIGM, IJL, 6 Rue Bastien Lepage, F-54010 Nancy, France

[*]Corresponding author: luca.di.stasio@ltu.se

Abstract

The bi-material interface arc crack has been the focus of interest in the composite community, where it is usually referred to as the fiber-matrix interface crack. In this work, we investigate the convergence properties of the Virtual Crack Closure Technique (VCCT) when applied to the evaluation of the Mode I, Mode II and total Energy Release Rate of the fiber-matrix interface crack in the context of the Finite Element Method (FEM). We first propose a synthetic vectorial formulation of the VCCT. Thanks to this formulation, we study the convergence properties of the method, both analytically and numerically. It is found that Mode I and Mode II Energy Release Rate (ERR) possess a logarithmic dependency with respect to the size of the elements in the crack tip neighborhood, while the total ERR is independent of element size.

Keywords: Fiber/matrix interface crack, Bi-material interface arc crack, Linear Elastic Fracture Mechanics (LEFM), Virtual Crack Closure Technique (VCCT), Mode separation, Convergence

1 Introduction

Bi-material interfaces represent the basic load transfer mechanism at the heart of Fiber Reinforced Polymer Composite (FRPC) materials. They are present at the macroscale, in the form of adhesive joints; at the mesoscale, as interfaces between layers with different orientations; at the microscale, as fiber-matrix interfaces. Bi-material interfaces have for long attracted the attention of researchers in Fracture Mechanics [1, 2], due to their hidden complexity.
The problem was first addressed in the 1950's by Williams [3], who derived through a linear elastic asymptotic analysis the stress distribution around an *open* crack (i.e. with crack faces nowhere in contact for any size of the crack) between two infinite half-planes

of dissimilar materials. He found the existence of a strong oscillatory behavior in the stress singularity at the crack tip of the form

$$r^{-\frac{1}{2}} \sin(\varepsilon \log r) \quad \text{with} \quad \varepsilon = \frac{1}{2\pi} \log\left(\frac{1-\beta}{1+\beta}\right), \tag{1}$$

in both Mode I and Mode II. In Eq. 1, β is one of the two parameters introduced by Dundurs [4] to characterize bi-material interfaces:

$$\beta = \frac{\mu_2(\kappa_1 - 1) - \mu_1(\kappa_2 - 1)}{\mu_2(\kappa_1 + 1) + \mu_1(\kappa_2 + 1)} \tag{2}$$

where $\kappa = 3 - 4\nu$ in plane strain and $\kappa = \frac{3-4\nu}{1+\nu}$ in plane stress, μ is the shear modulus, ν Poisson's coefficient, and indexes $1, 2$ refer to the two bulk materials joined at the interface. Defining a as the length of the crack, it was found that the size of the oscillatory region is in the order of $10^{-6}a$ [5]. Given the oscillatory behaviour of the crack tip singularity of Eq. 1, the definition of Stress Intensity Factor (SIF) $\lim_{r\to 0}\sqrt{2\pi r}\sigma$ diverges and ceases to be valid [1]. It implies that the Mode mixity problem at the crack tip is ill-posed.

It was furthermore observed, always in the context of Linear Elastic Fracture Mechanics (LEFM), that an interpenetration zone exists close to the crack tip [6, 7] with a length in the order of $10^{-4}a$ [6]. Following conclusions firstly proposed in [7], the presence of a *contact zone* in the crack tip neighborhood, of a length to be determined from the solution of the elastic problem, was introduced in [8] and shown to provide a physically consistent solution to the straight bi-material interface crack problem.

The curved bi-material interface crack, more often refered to as the fiber-matrix interface crack (or debond) due to its relevance in FRPCs, was first treated by England [9] and by Perlman and Sih [10], who provided the analytical solution of stress and displacement fields for a circular inclusion with respectively a single debond and an arbitrary number of debonds. Building on their work, Toya [11] particularized the solution and provided the expression of the Energy Release Rate (ERR) at the crack tip. The same problems exposed previously for the *open* straight bi-material crack were shown to exist also for the *open* fiber-matrix interface crack: the presence of strong oscillations in the crack tip singularity and onset of crack face interpenetration at a critical flaw size.[1]

In order to treat cases more complex than the single partially debonded fiber in an infinite matrix of [9, 10, 11], numerical studies followed. In the 1990's, París and collaborators [12] developed a Boundary Element Method (BEM) with the use of discontinuous singular elements at the crack tip and the Virtual Crack Closure Integral (VCCI) [13] for the evaluation of the Energy Release Rate (ERR). They validated their results [12] with respect to Toya's analytical solution [11] and analyzed the effect of BEM interface discretization on the stress field in the neighborhood of the crack tip [14]. Following Comninou's work on the straight crack [8], they furthermore recognized the importance

[1] For the fiber-matrix interface crack, flaw size is measured in terms of the angle $\Delta\theta$ subtended by half of the arc-crack, i.e. $a = 2\Delta\theta R_f$ where R_f is the inclusion (fiber) radius and $\Delta\theta$ is expressed in radians .

of contact to retrieve a physical solution avoiding interpenetration [12] and studied the effect of the contact zone on debond ERR [15]. Their algorithm was then applied to investigate the fiber-matrix interface crack under different geometrical configurations and mechanical loadings [16, 17, 18, 19, 20, 21, 22].
Recently the Finite Element Method (FEM) was also applied to the solution of the fiber-matrix interface crack problem [23, 24, 25], in conjunction with the Virtual Crack Closure Technique (VCCT) [26, 27] for the evaluation of the ERR at the crack tip. In [23], the authors validated their model with respect to the BEM results of [12], but no analysis of the effect of the discretization in the crack tip neighborhood comparable to [14] was proposed. Thanks to the interest in evaluating the ERR of interlaminar delamination, different studies exist in the literature on the effect of mesh discretization on Mode I and Mode II ERR of the straight bi-material interface crack when evaluated with the VCCT in the context of the FEM (see for example [28] for a review). An early result on the problem is available in [29]. Here the authors evaluated with the Virtual Crack Closure Technique Mode I and Mode II Energy Release Rate of both a central crack and an edge crack at the interface between two 2D plates of different isotropic materials subjected to tensile loading. They showed analytically that the total ERR G is well defined while Mode I and Mode II ERR, respectively G_I and G_{II}, do not converge. They confirmed their analytical derivations numerically by solving the two problems with the Finite Element Method and evaluating the ERR with the VCCT. Referring to the crack length as a and to the length of an element at the crack tip as Δa, they found that the total ERR was independent of normalized element size $\Delta a/a$ while G_I and G_{II} were dependent on assumed crack extension, i.e. element size at the crack tip. In particular, they showed a decreasing G_I and an increasing G_{II} with decreasing element size for both crack configurations. The same analysis was conducted, and analogous results obtained, in [30] for a central crack under either far-field tensile or shear loading between two orthotropic materials in 2D and in [31] for a central crack subjected to far-field tension between two orthotropic solids in 3D. The convergence of VCCT-based mode decomposition was analyzed in [32] for edge delaminations in laminated composites subjected to tensile loading coplanar and normal to crack propagation direction in a quasi-3D setting. Again, it was observed that the total ERR was independent of mesh size while Mode I and Mode II ERR showed dependency and no convergence could be established. In this configuration however, it was found that G_I increases and G_{II} decreases with decreasing element size. The application of the VCCT to the problem of composite skin-stiffener debonding was considered in [33] in conjunction with 2D plate elements, where the authors studied the effect of different combinations of adherends' layup, thickness and fiber orientation at the interface on Mode decomposition. Only in the case of skin and stiffener with the same layup, same thickness and identical fiber orientation at the interface, Mode I and Mode II were found to be independent of mesh size. In all other cases, G_I and G_{II} were dependent on assumed crack extension and showed a trend similar to the one in [32]. The absence of a converging Mode-decomposed solution with the VCCT has motivated proposals for alternative solution. In [34], the authors analyze several proposals of mode-mixity parameters and suggest a correction to the VCCT-based mode-mixity ratio by

assuming a reference characteristic length. The authors themselves however admit that this characteristic length has no physical interpretation. In [35], the problem of Mode-decomposition is solved through the development of analytical relations based on Euler and Timoshenko beam models. It is however well suited only for those configurations that can be split into beam elements, such as the Double Cantilever Beam (DCB) specimen.
No comparable analysis can be found in the literature on Mode separation and convergence analysis of the VCCT when applied to the fiber-matrix interface crack (circular bi-material interface crack) problem in the context of a linear elastic FEM solution. In the present article, we first present the FEM formulation of the problem, together with the main geometrical characteristics, material properties, boundary conditions and loading. We then propose a vectorial formulation of the VCCT and express Mode I and Mode II ERR in terms of FEM natural variables. Differently from the usual approach found in the literature, we do not express G_I and G_{II} as functions of stress and displacement fields using the results from complex analysis. We instead focus on the mathematical structure of the 1-step VCCT in the context of the Finite Element Method and write the crack tip forces as a linear combination of the crack faces displacements at the crack tip (plus a term representing the influence of the rest of the model). The ERR is consequently a quadratic function of the crack faces displacements. Given that, if the FEM solution is converging, stress and displacement fields are characterized by the oscillating singularity of Equation 1, it is possible to evaluate the behavior of the VCCT-calculated Energy Release Rate in the limit of crack tip element size going to zero. We are thus able to derive analytically a functional form of the dependency of the ERR on crack tip element size. Finally, the functional form thus derived is compared to the numerical results obtained with the Finite Element Method.

2 FEM formulation of the fiber-matrix interface crack problem

In order to investigate the fiber-matrix interface crack problem, a 2-dimensional model of a single fiber inserted in a rectangular matrix element is considered (see Figure 1). Total element length and height are respectively $2L$ and L, where L is determined by the fiber radius R_f and the fiber volume fraction V_f by

$$L = \frac{R_f}{2}\sqrt{\frac{\pi}{V_f}}. \tag{3}$$

The fiber radius R_f is assumed to be equal to 1 μm. This choice is not dictated by physical considerations but for simplicity. It is thus useful to remark that, in a linear elastic solution as the one considered in the present work, the ERR is proportional to the geometrical dimensions of the model and, consequently, recalculation of the ERR for fibers of any size requires a simple multiplication.

As shown in Fig. 1, the debond is placed symmetrically with respect to the x axis

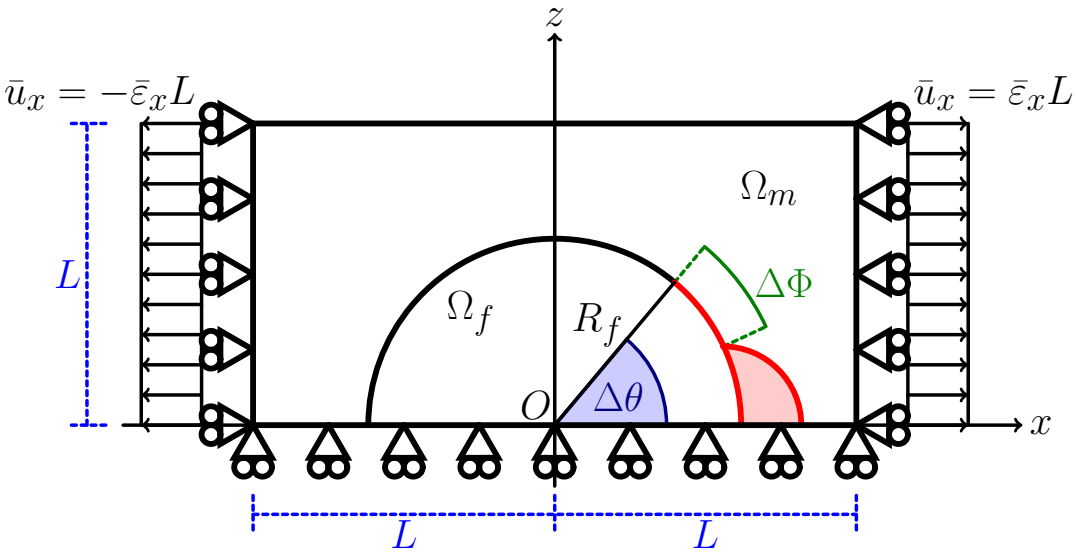

Figure 1: Schematic of the model with its main parameters.

and its size is characterized by the angle $\Delta\theta$ (which makes the full debond size equal to $2\Delta\theta$ and the full crack length equal to $R_f 2\Delta\theta$). A region $\Delta\Phi$ of unknown size appears at the crack tip for large debond sizes (at least $\geq 60° - 80°$), in which the crack faces are in contact with each other and free to slide. Frictionless contact is thus considered between the two crack faces to allow free sliding and avoid interpenetration. Symmetry with respect to the x axis is applied on the lower boundary while the upper surface is left free. Kinematic coupling on the x-displacement is applied along the left and right sides of the model in the form of a constant x-displacement $\pm\bar{\varepsilon}_x L$, which corresponds to transverse strain $\bar{\varepsilon}_x$ equal to 1% in the results here presented.

Table 1: Summary of the mechanical properties of fiber and matrix. E stands for Young's modulus, μ for shear modulus and ν for Poisson's ratio.

Material	$E\,[GPa]$	$\mu\,[GPa]$	$\nu\,[-]$
Glass fiber	70.0	29.2	0.2
Epoxy	3.5	1.25	0.4

The model problem is solved with the Finite Element Method (FEM) within the Abaqus environment, a commercial FEM software [36]. The model is meshed with second order, 2D, plane strain triangular (CPE6) and rectangular (CPE8) elements. A regular mesh of rectangular elements with almost unitary aspect ratio is used at the crack tip. The angular size δ of an element in the crack tip neighborhood represents the main parameter of the numerical analysis. The crack faces are modeled as element-based surfaces and a small-sliding contact pair interaction with no friction is imposed between

them. The Mode I, Mode II and total Energy Release Rates (ERRs) (respectively referred to as G_I, G_{II} and G_{TOT}) are evaluated using the VCCT [27], implemented in a in-house Python routine. A glass fiber-epoxy system is considered in the present work, and it is assumed that their response lies always in the linear elastic domain. The elastic properties of glass fiber and epoxy are reported in Table 1.

3 Vectorial formulation of the Virtual Crack Closure Technique (VCCT)

In order to express the VCCT formulation of the ERR in terms of FEM variables, we need to introduce a few rotation matrices in order to represent the discretized representation (FE mesh) of a crack along a circular interface. The position of the crack tip is characterized by the angular size of the crack (see Sec. 2 and Fig. 1 for reference) and the rotation corresponding to the crack tip reference frame is represented by the matrix $\underline{\underline{R}}_{\Delta\theta}$ defined as

$$\underline{\underline{R}}_{\Delta\theta} = \begin{bmatrix} \cos(\Delta\theta) & \sin(\Delta\theta) \\ -\sin(\Delta\theta) & \cos(\Delta\theta) \end{bmatrix}. \tag{4}$$

Nodes belonging to the elements sharing the crack tip are involved in the VCCT estimation of the ERR and it is assumed that, given a sufficiently fine discretization, they are aligned with the crack propagation direction defined at the crack tip.

However, irrespectively of how small the elements in the crack tip neighborhood are, a misalignment always exists with respect to the assumed crack propagation direction (in the crack tip reference frame). This is measured by the matrices $\underline{\underline{P}}_{\delta}(p)$, defined as

$$\underline{\underline{P}}_{\delta}(p) = \begin{bmatrix} \cos\left(\left(1+\frac{1-p}{m}\right)\delta\right) & \sin\left(\left(1+\frac{1-p}{m}\right)\delta\right) \\ -\sin\left(\left(1+\frac{1-p}{m}\right)\delta\right) & \cos\left(\left(1+\frac{1-p}{m}\right)\delta\right) \end{bmatrix} \tag{5}$$

and $\underline{\underline{Q}}_{\delta}(q)$, equal to

$$\underline{\underline{Q}}_{\delta}(q) = \begin{bmatrix} \cos\left(\frac{q-1}{m}\delta\right) & \sin\left(\frac{q-1}{m}\delta\right) \\ -\sin\left(\frac{q-1}{m}\delta\right) & \cos\left(\frac{q-1}{m}\delta\right) \end{bmatrix}, \tag{6}$$

respectively for the free and bonded nodes involved in the VCCT estimation. In Eqs. 5 and 6, δ is the angular size of an element in the crack tip neighborhood (see Sec. 2 and Fig. 1), m is the order of the element shape functions and $p, q = 1, \ldots, m$ are indices referring to the nodes belonging respectively to free and bonded elements sharing the crack tip. Figure 2 shows the p, q-based numbering of nodes at the crack tip in the case of elements with linear and quadratic (serendipity) shape functions. Introducing the permutation matrix

$$\underline{\underline{P}}_{\pi} = \begin{bmatrix} 0 & 1 \\ -1 & 0 \end{bmatrix}, \tag{7}$$

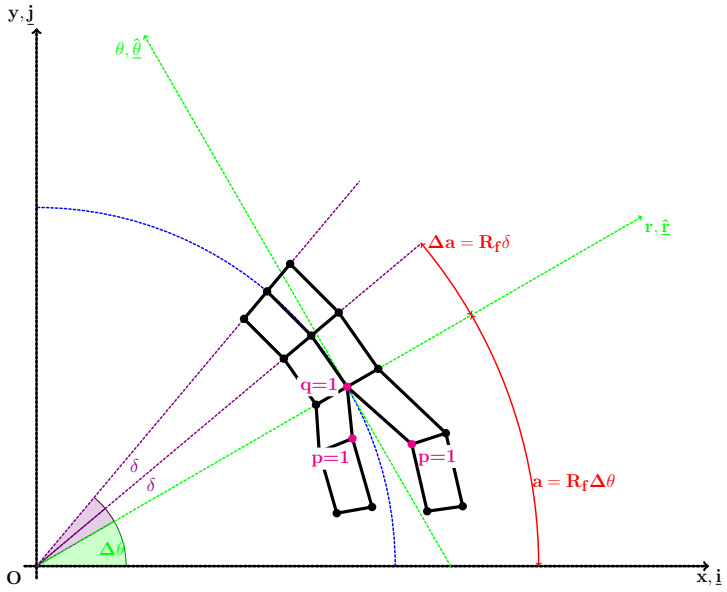

(a) Elements with 1^{st} order shape functions: $m = 1$ and $p, q = 1$.

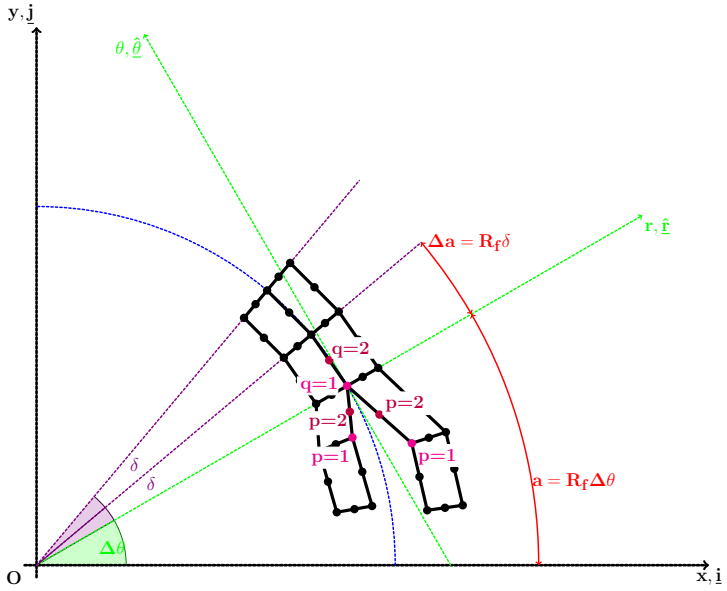

(b) Elements with 2^{nd} order shape functions: $m = 2$ and $p, q = 1, 2$.

Figure 2: Schematic of the mesh at the fiber/matrix interface crack tip.

it is possible to express the derivatives of rotation matrices $\underline{\underline{R}}_{\Delta\theta}$, $\underline{\underline{P}}_{\delta}$ and $\underline{\underline{Q}}_{\delta}$ with respect to their argument:

$$\frac{\partial \underline{\underline{R}}_{\Delta\theta}}{\partial \Delta\theta} = \underline{\underline{P}}_{\pi} \cdot \underline{\underline{R}}_{\Delta\theta}, \quad \frac{\partial \underline{\underline{P}}_{\delta}}{\partial \delta} = \left(1 + \frac{1-p}{m}\right) \underline{\underline{P}}_{\pi} \cdot \underline{\underline{P}}_{\delta}, \quad \frac{\partial \underline{\underline{Q}}_{\delta}}{\partial \delta} = \frac{q-1}{m} \underline{\underline{P}}_{\pi} \cdot \underline{\underline{Q}}_{\delta}. \tag{8}$$

By means of Eqs. 5 and 6, we can express the crack tip forces $\underline{F}_{xy} = \begin{bmatrix} F_x \\ F_y \end{bmatrix}$ and crack displacements $\underline{u}_{xy} = \begin{bmatrix} u_x \\ u_y \end{bmatrix}$ in the crack tip reference frame (where the tangential direction θ correspond to the direction of crack propagation) while taking into account the misalignment to the finite discretization as

$$\underline{F}_{r\theta} = \underline{\underline{Q}}_{\delta} \underline{\underline{R}}_{\Delta\theta} \underline{F}_{xy} \qquad \underline{u}_{r\theta} = \underline{\underline{P}}_{\delta} \underline{\underline{R}}_{\Delta\theta} \underline{u}_{xy} \tag{9}$$

where $\underline{F}_{r\theta} = \begin{bmatrix} F_r \\ F_\theta \end{bmatrix}$ and $\underline{u}_{r\theta} = \begin{bmatrix} u_r \\ u_\theta \end{bmatrix}$.

The crack tip forces can be expressed as a function of the crack opening displacement as

$$\underline{F}_{xy} = \underline{\underline{K}}_{xy} \underline{u}_{xy} + \widetilde{\underline{F}}_{xy}, \tag{10}$$

where $\underline{\underline{K}}_{xy}$ is in general a full matrix of the form $\underline{\underline{K}}_{xy} = \begin{bmatrix} K_{xx} K_{xy} \\ K_{yx} K_{yy} \end{bmatrix}$ and $\widetilde{\underline{F}}_{xy}$ represents the effect of the rest of the FE solution through the remaining nodes of the elements attached to the crack tip. As such, the term $\widetilde{\underline{F}}_{xy}$ can be expressed as a linear combination of the solution vector $\underline{u}_N$ of nodal displacements of the form $\widetilde{\underline{\underline{K}}}_N \underline{u}_N$. Equation 10 thus become

$$\underline{F}_{xy} = \underline{\underline{K}}_{xy} \underline{u}_{xy} + \widetilde{\underline{\underline{K}}}_N \underline{u}_N. \tag{11}$$

An exemplifying derivation of the relationships expressed in Equations 10 and 11 can be found in A. It is worthwhile to observe that another author [37, 38] proposes a similar relationship, but in terms of flexibility $\underline{u} = \underline{\underline{C}} \underline{F}$. In [37, 38], Valvo expresses the forces at the crack tip as a (linear) function of the crack faces displacements at the same point. The technique analyzed in [37, 38] is the 2-steps VCCT [27]: given a structure with a crack of length a, a first simulation is run to compute the forces at the crack tip and, in the case, at the internal nodes of the first bonded element for p-refined meshes; then, a second simulation is conducted with the crack extended by Δa, where in practice Δa is the length of the element at the crack tip, and crack faces displacements are evaluated at the same nodes, now released, where previously forces were extracted. The Energy Release Rate is computed as the product of forces and displacements evaluated at the same nodes. The 2-steps VCCT adheres more strictly to the principle of the crack closure integral [13, 39]: the work needed to open the crack by δa (Energy Release Rate) is equal in magnitude to the work required to close it by the same amount. Forces and displacements should be thus evaluated at the same point respectively in the closed and open crack configuration. In this paper, we consider on the other hand the 1-step VCCT [27]: if the size of the elements at the crack tip is sufficiently small, the error committed by approximating the crack faces displacements at the crack tip with those one element before is negligible. This in turn eliminates the need for a second simulation and thus cut the required computational time by a half. Following the principle of the

crack closure integral [13, 39], Valvo's proposal is based on the observation that the crack face displacements at the crack tip for a virtual crack extension will be equal in magnitude and opposite in sign due the displacements caused by the application of crack tip forces. Thus, namely: $u_{open\ crack} = -u_{closed\ crack} = f\left(F_{closed\ crack}\right)$, and for linear elastic materials $f\left(F_{closed\ crack}\right)$ would be linear, hence the introduction of a flexibility matrix [38]. Given that we instead work with the 1-step VCCT, we start from the observation that, in a Finite Element solution, the forces at a point can be expressed as a linear combination of all the displacements of the model through the global stiffness matrix. We have followed a stiffness approach and we have proceeded to isolate the contribution of crack faces displacements on crack tip forces. This leaves an additional term $\underline{\underline{\widetilde{K}}}_N \underline{u}_N$ in Equation 11, which represents the contribution of the rest of the model and that is not present in Valvo's proposal. Notice that the linearity of Equation 11 does not stem from material linearity, but from the structure of the FEM solution. It can thus, in principle, be applied to non-linear materials, although as part of a secant- or tangent-based linearization. Notice that both the stiffness matrix of Equation 11 and Valvo's flexibility matrix possess out-of-diagonal elements, which represent the contribution of Poisson's effect.

Based upon the work of Raju [40], we introduce the matrix $\underline{\underline{T}}_{pq}$ to represent the weights needed in the VCCT to account for the use of singular elements. As already done previously, indices p and q refer to nodes placed respectively on the free (crack face) and bonded side of the crack tip. Nodes are enumerated so that the crack tip has always index 1, i.e. the higher the index the further the node is from the crack tip. Matrix $\underline{\underline{T}}_{pq}$ has always a size of $d \times d$, where $d = 2$ for a $2D$ problem and $d = 3$ for a $3D$ problem. An element $\underline{\underline{T}}_{pq}(i,j)$ with $i, j = 1, \ldots, d$ represents the weight to be assigned to the product of component i of the displacement extracted at node p with component j of the force extracted at node q. The expression of $\underline{\underline{T}}_{pq}$ for quadrilateral elements with or without singularity is reported in B. Notice that, given m is the order of the element shape functions, the element side has $m+1$ nodes and this represents the upper limit of indices p and q.

By using matrix $\underline{\underline{T}}_{pq}$, it is possible to express the total ERR G evaluated with the VCCT as

$$G_{TOT} = \frac{1}{2R_f\delta} \sum_{p=1}^{m+1} \sum_{q=1}^{m+1} Tr\left(\underline{F}_{r\theta,q} \underline{u}^T_{r\theta,p} \underline{\underline{T}}^T_{pq}\right), \tag{12}$$

where the symbol Tr stands for the *Trace* operator, which sums together the elements on the matrix main diagonal (first matrix invariant). Introducing the vector $\underline{G} = \begin{bmatrix} G_I \\ G_{II} \end{bmatrix}$ of fracture mode ERRs, Mode I and Mode II ERR evaluated with the VCCT can be expressed as

$$\underline{G} = \frac{1}{2R_f\delta} \sum_{p=1}^{m+1} \sum_{q=1}^{m+1} Diag\left(\underline{F}_{r\theta,q} \underline{u}^T_{r\theta,p} \underline{\underline{T}}^T_{pq}\right), \tag{13}$$

where $Diag\,()$ is the function that extracts the main diagonal of the input matrix as a column vector. Substituting Equations 9 and 11 in Equations 12 and 13, we can express the Mode I, Mode II and total Energy Release Rate as a function of the crack displacements and the FE solution (more details in A) as

$$\begin{aligned} G_{TOT} =& \frac{1}{2R_f\delta}\sum_{p=1}^{m+1}\sum_{q=1}^{m+1} Tr\left(\underline{\underline{Q}}_{\delta}\underline{\underline{R}}_{\Delta\theta}\underline{\underline{K}}_{xy,q}\underline{u}_{xy,q}\underline{u}_{xy,p}^{T}\underline{\underline{R}}_{\Delta\theta}^{T}\underline{\underline{P}}_{\delta}^{T}\underline{\underline{T}}_{pq}^{T}\right) + \\ &+ \frac{1}{2R_f\delta}\sum_{p=1}^{m+1}\sum_{q=1}^{m+1} Tr\left(\underline{\underline{Q}}_{\delta}\underline{\underline{R}}_{\Delta\theta}\underline{\underline{\widetilde{F}}}_{xy,q}\underline{u}_{xy,p}^{T}\underline{\underline{R}}_{\Delta\theta}^{T}\underline{\underline{P}}_{\delta}^{T}\underline{\underline{T}}_{pq}^{T}\right) \end{aligned} \tag{14}$$

and

$$\begin{aligned} \underline{G} = \begin{bmatrix} G_I \\ G_{II} \end{bmatrix} =& \frac{1}{2R_f\delta}\sum_{p=1}^{m+1}\sum_{q=1}^{m+1} Diag\left(\underline{\underline{Q}}_{\delta}\underline{\underline{R}}_{\Delta\theta}\underline{\underline{K}}_{xy,q}\underline{u}_{xy,q}\underline{u}_{xy,p}^{T}\underline{\underline{R}}_{\Delta\theta}^{T}\underline{\underline{P}}_{\delta}^{T}\underline{\underline{T}}_{pq}^{T}\right) + \\ &+ \frac{1}{2R_f\delta}\sum_{p=1}^{m+1}\sum_{q=1}^{m+1} Diag\left(\underline{\underline{Q}}_{\delta}\underline{\underline{R}}_{\Delta\theta}\underline{\underline{\widetilde{K}}}_{N,q}\underline{u}_{N}\underline{u}_{xy,p}^{T}\underline{\underline{R}}_{\Delta\theta}^{T}\underline{\underline{P}}_{\delta}^{T}\underline{\underline{T}}_{pq}^{T}\right) \end{aligned} \tag{15}$$

Notice that the matrix appearing in Equation 14 and Equation 15 has the dimension of ERR, i.e. $^{J}/_{m^2}$, and is in general full. Equation 14 states that the total Energy Release Rate is the first invariant of the matrix, i.e. its trace. Equation 15 states on the other hand that the elements on its diagonal are the Mode I and Mode II ERR. The off-diagonal components represent an interaction Energy Release Rate, mention of which can be already found in [41]. However, in [41] the existence of the interaction ERR is assumed based on physical assumptions, here it is derived from the mathematical structure of the VCCT in the context of the Finite Element Method. Valvo [37, 38] derives as well the existence of an interaction ERR from the presence of non-zero off-diagonal elements in his flexibility matrix. He then considers that correct Mode-decomposition is provided when the off-diagonal terms are zero and thus derives a correction to the VCCT. A different perspective is offered here. Dimensional analysis suggests that the Energy Release Rate ($^{J}/_{m^2}$), i.e. the energy required to cause an unit increase in the crack surface size, is dimensionally equivalent to the Crack Driving Force ($^{N}/_{m}$), which is the force required to grow the crack along its path by a unit length. It is then possible to infer a physical interpretation of the elements of the ERR matrix of Equation 14 and Equation 15: the diagonal elements are respectively the Mode I (Mode II) force required to propagate the crack by a unit length in Mode I (Mode II); the off-diagonal elements are respectively the Mode I (Mode II) force required to propagate the crack by a unit length in Mode II (Mode I). The off-diagonal elements capture an interaction due to Poisson's effect and the mismatch of elastic properties between phases that is peculiar of bi-material interface cracks. The assumption by Valvo [37, 38] that correct Mode-decomposition is

recovered by imposing that off-diagonal elements be equal to zero seems thus open to further reflection. A deeper analysis of this issue is however beyond the scope of this paper and it will be left to a future work.

4 Rotational invariance of G_{TOT}

Recalling Equation 14 and observing that matrix $\underline{\underline{T}}_{pq}$ is always equal to the identity matrix pre-multiplied by a suitable real constant (see Eq. B.53 in B), the total Energy Release Rate can be rewritten as

$$\begin{aligned} G_{TOT} &= \frac{1}{2R_f\delta}\sum_{p=1}^{m+1}\sum_{q=1}^{m+1} Tr\left(\underline{\underline{Q}}_{\delta}\underline{\underline{R}}_{\Delta\theta}\left(\underline{\underline{K}}_{xy,q}\underline{u}_{xy,q}+\underline{\widetilde{F}}_{xy,q}\right)\underline{u}_{xy,p}^{T}\underline{\underline{T}}_{pq}^{T}\underline{\underline{R}}_{\Delta\theta}^{T}\underline{\underline{P}}_{\delta}^{T}\right) = \\ &= \frac{1}{2R_f\delta}\sum_{p=1}^{m+1}\sum_{q=1}^{m+1} Tr\left(\underline{\underline{Q}}_{\delta}\underline{\underline{R}}_{\Delta\theta}\underline{F}_{xy,q}\underline{u}_{xy,p}^{T}\underline{\underline{T}}_{pq}^{T}\underline{\underline{R}}_{\Delta\theta}^{T}\underline{\underline{P}}_{\delta}^{T}\right), \end{aligned} \tag{16}$$

where $\underline{F}_{xy}$ and $\underline{u}_{xy}$ are the vectors of respectively the crack tip forces and crack displacements in the global $(x-y)$ reference frame. Given that $\underline{\underline{Q}}_{\delta}$, $\underline{\underline{P}}_{\delta}$ and $\underline{\underline{R}}_{\Delta\theta}$ all represent a linear transformation (a rigid rotation in particular), the invariance of the trace to linear transformations ensures that

$$\begin{aligned} G_{TOT} &= \frac{1}{2R_f\delta}\sum_{p=1}^{m+1}\sum_{q=1}^{m+1} Tr\left(\underline{\underline{Q}}_{\delta}\underline{\underline{R}}_{\Delta\theta}\underline{F}_{xy,q}\underline{u}_{xy,p}^{T}\underline{\underline{T}}_{pq}^{T}\underline{\underline{R}}_{\Delta\theta}^{T}\underline{\underline{P}}_{\delta}^{T}\right) = \\ &= \frac{1}{2R_f\delta}\sum_{p=1}^{m+1}\sum_{q=1}^{m+1} Tr\left(\underline{F}_{xy,q}\underline{u}_{xy,p}^{T}\underline{\underline{T}}_{pq}^{T}\right). \end{aligned} \tag{17}$$

As G_{TOT} was defined according to Equation 12 and given that $Tr\,(AB) = Tr\,(BA)$, it holds that

$$\begin{aligned} G_{TOT} &= \frac{1}{2R_f\delta}\sum_{p=1}^{m+1}\sum_{q=1}^{m+1} \underline{u}_{r\theta,p}^{T}\underline{\underline{T}}_{pq}^{T}\underline{F}_{r\theta,q} = \frac{1}{2R_f\delta}\sum_{p=1}^{m+1}\sum_{q=1}^{m+1} Tr\left(\underline{F}_{r\theta,q}\underline{u}_{r\theta,p}^{T}\underline{\underline{T}}_{pq}^{T}\right) = \\ &= \frac{1}{2R_f\delta}\sum_{p=1}^{m+1}\sum_{q=1}^{m+1} Tr\left(\underline{F}_{xy,q}\underline{u}_{xy,p}^{T}\underline{\underline{T}}_{pq}^{T}\right) = \frac{1}{2R_f\delta}\sum_{p=1}^{m+1}\sum_{q=1}^{m+1} \underline{u}_{xy,p}^{T}\underline{\underline{T}}_{pq}^{T}\underline{F}_{xy,q} \end{aligned} \tag{18}$$

which shows that the total Energy Release Rate is invariant to rigid rotations and can be calculated equivalently with forces and displacements expressed in the local crack tip reference frame or the global reference frame. The analytical result is confirmed by

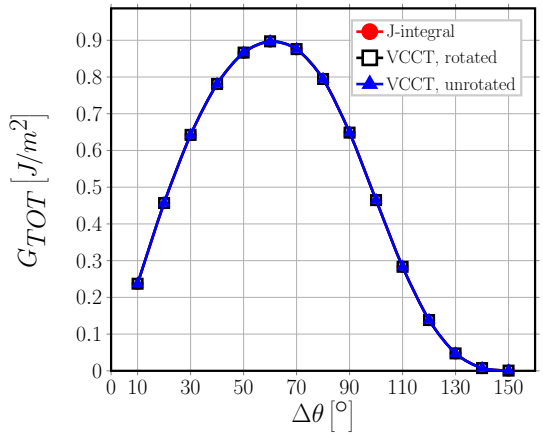

(a) $V_f = 0.1\%$, 1^{st} order elements, $\delta = 0.05°$.

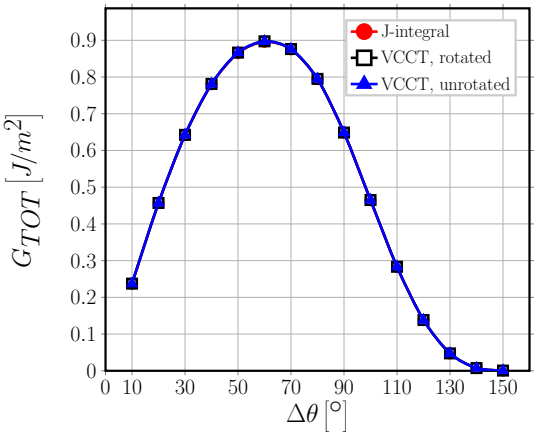

(b) $V_f = 0.1\%$, 2^{nd} order elements, $\delta = 0.05°$.

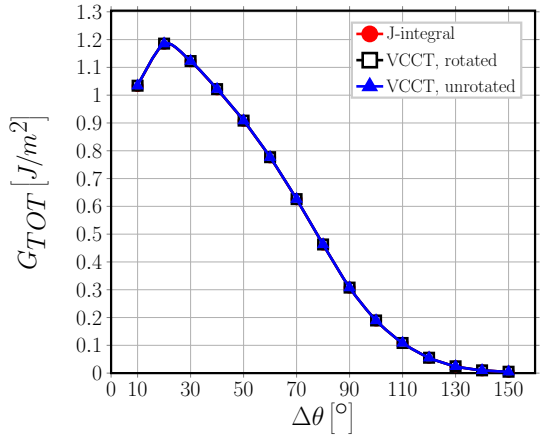

(c) $V_f = 40\%$, 1^{st} order elements, $\delta = 0.05°$.

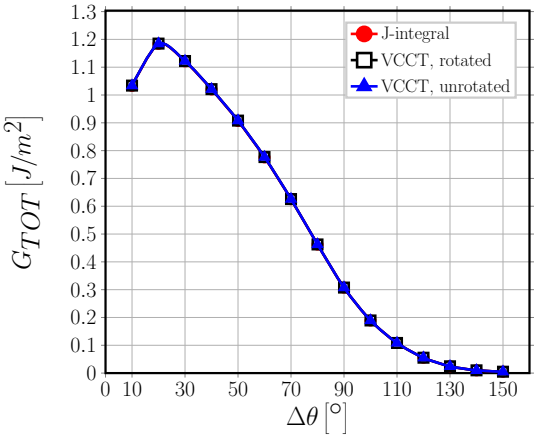

(d) $V_f = 40\%$, 2^{nd} order elements, $\delta = 0.05°$.

Figure 3: Numerical invariance of the total Energy Release Rate: G_{TOT} computed with the VCCT with rotated forces and displacements (label rotated*), with the VCCT with forces and displacements in the global reference frame (label* unrotated*) and with J-integral method (label* J-integral*).*

the numerical solution of the fiber-matrix interface crack with different element orders and model fiber volume fractions, as shown in Figure 3.

The result of Equation 18 has also physical implications:

- given that stress and displacement fields at the crack tip are the same, two cracks with different crack paths are energetically equivalent with respect to the total Energy Release Rate;

- given that laws of the type $G_{TOT} \geq G_c$ govern crack propagation, if G_c do not depend on mode ratio, crack orientation will not affect its growth.

5 Convergence analysis

5.1 Analytical considerations

Substituting Equations 8 in the derivative of Equation 13, we can investigate the dependency of Mode I and Mode II ERR with respect to the size δ of an element in the crack tip neighborhood through

$$\begin{aligned}\frac{\partial \underline{G}}{\partial \delta} =& -\frac{1}{2R_f\delta^2}\sum_{p=1}^{m+1}\sum_{q=1}^{m+1} Diag\left(\underline{\underline{Q}}_{\delta}\underline{\underline{R}}_{\Delta\theta}\underline{\underline{K}}_{xy}\underline{u}_{xy}\underline{u}_{xy}^T\underline{\underline{R}}_{\Delta\theta}^T\underline{\underline{P}}_{\delta}^T\underline{\underline{T}}_{pq}^T\right) - \frac{1}{2R_f\delta^2}\sum_{p=1}^{m+1}\sum_{q=1}^{m+1} Diag\left(\underline{\underline{Q}}_{\delta}\underline{\underline{R}}_{\Delta\theta}\widetilde{\underline{\underline{K}}}_{N}\underline{u}_{N}\underline{u}_{xy}^T\underline{\underline{R}}_{\Delta\theta}^T\underline{\underline{P}}_{\delta}^T\underline{\underline{T}}_{pq}^T\right) + \\ &+\frac{1}{2R_f\delta}\sum_{p=1}^{m+1}\sum_{q=1}^{m+1} Diag\left(\underline{\underline{Q}}_{\delta}\underline{\underline{R}}_{\Delta\theta}\underline{\underline{K}}_{xy}\underline{u}_{xy}\underline{u}_{xy}^T\underline{\underline{R}}_{\Delta\theta}^T\underline{\underline{P}}_{\delta}^T\underline{\underline{D}}^T\underline{\underline{T}}_{pq}^T\right) + \frac{1}{2R_f\delta}\sum_{p=1}^{m+1}\sum_{q=1}^{m+1} Diag\left(\underline{\underline{Q}}_{\delta}\underline{\underline{R}}_{\Delta\theta}\widetilde{\underline{\underline{K}}}_{N}\underline{u}_{N}\underline{u}_{xy}^T\underline{\underline{R}}_{\Delta\theta}^T\underline{\underline{P}}_{\delta}^T\underline{\underline{D}}^T\underline{\underline{T}}_{pq}^T\right) + \\ &+\frac{1}{2R_f\delta}\sum_{p=1}^{m+1}\sum_{q=1}^{m+1} Diag\left(\underline{\underline{DQ}}_{\delta}\underline{\underline{R}}_{\Delta\theta}\underline{\underline{K}}_{xy}\underline{u}_{xy}\underline{u}_{xy}^T\underline{\underline{R}}_{\Delta\theta}^T\underline{\underline{P}}_{\delta}^T\underline{\underline{T}}_{pq}^T\right) + \frac{1}{2R_f\delta}\sum_{p=1}^{m+1}\sum_{q=1}^{m+1} Diag\left(\underline{\underline{DQ}}_{\delta}\underline{\underline{R}}_{\Delta\theta}\widetilde{\underline{\underline{K}}}_{N}\underline{u}_{N}\underline{u}_{xy}^T\underline{\underline{R}}_{\Delta\theta}^T\underline{\underline{P}}_{\delta}^T\underline{\underline{T}}_{pq}^T\right) + \\ &+\frac{1}{2R_f\delta}\sum_{p=1}^{m+1}\sum_{q=1}^{m+1} Diag\left(\underline{\underline{Q}}_{\delta}\underline{\underline{R}}_{\Delta\theta}\underline{\underline{K}}_{xy}\frac{\partial \underline{u}_{xy}}{\partial\delta}\underline{u}_{xy}^T\underline{\underline{R}}_{\Delta\theta}^T\underline{\underline{P}}_{\delta}^T\underline{\underline{T}}_{pq}^T\right) + \frac{1}{2R_f\delta}\sum_{p=1}^{m+1}\sum_{q=1}^{m+1} Diag\left(\underline{\underline{Q}}_{\delta}\underline{\underline{R}}_{\Delta\theta}\widetilde{\underline{\underline{K}}}_{N}\frac{\partial \underline{u}_{N}}{\partial\delta}\underline{u}_{xy}^T\underline{\underline{R}}_{\Delta\theta}^T\underline{\underline{P}}_{\delta}^T\underline{\underline{T}}_{pq}^T\right) + \\ &+\frac{1}{2R_f\delta}\sum_{p=1}^{m+1}\sum_{q=1}^{m+1} Diag\left(\underline{\underline{Q}}_{\delta}\underline{\underline{R}}_{\Delta\theta}\underline{\underline{K}}_{xy}\underline{u}_{xy}\frac{\partial \underline{u}_{xy}^T}{\partial\delta}\underline{\underline{R}}_{\Delta\theta}^T\underline{\underline{P}}_{\delta}^T\underline{\underline{T}}_{pq}^T\right) + \frac{1}{2R_f\delta}\sum_{p=1}^{m+1}\sum_{q=1}^{m+1} Diag\left(\underline{\underline{Q}}_{\delta}\underline{\underline{R}}_{\Delta\theta}\widetilde{\underline{\underline{K}}}_{N}\underline{u}_{N}\frac{\partial \underline{u}_{xy}^T}{\partial\delta}\underline{\underline{R}}_{\Delta\theta}^T\underline{\underline{P}}_{\delta}^T\underline{\underline{T}}_{pq}^T\right);\end{aligned} \tag{19}$$

which, after refactoring, provides

$$\begin{aligned}\frac{\partial \underline{G}}{\partial \delta} =& \frac{1}{\delta}\underline{G} + \frac{1}{2R_f\delta}\sum_{p=1}^{m+1}\sum_{q=1}^{m+1} Diag\left(\underline{\underline{Q}}_{\delta}\underline{\underline{R}}_{\Delta\theta}\left(\underline{\underline{K}}_{xy}\underline{u}_{xy} + \widetilde{\underline{\underline{K}}}_{N}\underline{u}_{N}\right)\underline{u}_{xy}^T\underline{\underline{R}}_{\Delta\theta}^T\underline{\underline{P}}_{\delta}^T\underline{\underline{D}}^T\underline{\underline{T}}_{pq}^T\right) + \\ &+\frac{1}{2R_f\delta}\sum_{p=1}^{m+1}\sum_{q=1}^{m+1} Diag\left(\underline{\underline{DQ}}_{\delta}\underline{\underline{R}}_{\Delta\theta}\left(\underline{\underline{K}}_{xy}\underline{u}_{xy} + \widetilde{\underline{\underline{K}}}_{N}\underline{u}_{N}\right)\underline{u}_{xy}^T\underline{\underline{R}}_{\Delta\theta}^T\underline{\underline{P}}_{\delta}^T\underline{\underline{T}}_{pq}^T\right) + \\ &+\frac{1}{R_f\delta}\sum_{p=1}^{m+1}\sum_{q=1}^{m+1} Diag\left(\underline{\underline{Q}}_{\delta}\underline{\underline{R}}_{\Delta\theta}\underline{\underline{K}}_{xy}\frac{\partial \underline{u}_{xy}}{\partial\delta}\underline{u}_{xy}^T\underline{\underline{R}}_{\Delta\theta}^T\underline{\underline{P}}_{\delta}^T\underline{\underline{T}}_{pq}^T\right) + \frac{1}{2R_f\delta}\sum_{p=1}^{m+1}\sum_{q=1}^{m+1} Diag\left(\underline{\underline{Q}}_{\delta}\underline{\underline{R}}_{\Delta\theta}\widetilde{\underline{\underline{K}}}_{N}\frac{\partial \underline{u}_{N}}{\partial\delta}\underline{u}_{xy}^T\underline{\underline{R}}_{\Delta\theta}^T\underline{\underline{P}}_{\delta}^T\underline{\underline{T}}_{pq}^T\right) + \\ &+\frac{1}{2R_f\delta}\sum_{p=1}^{m+1}\sum_{q=1}^{m+1} Diag\left(\underline{\underline{Q}}_{\delta}\underline{\underline{R}}_{\Delta\theta}\widetilde{\underline{\underline{K}}}_{N}\underline{u}_{N}\frac{\partial \underline{u}_{xy}^T}{\partial\delta}\underline{\underline{R}}_{\Delta\theta}^T\underline{\underline{P}}_{\delta}^T\underline{\underline{T}}_{pq}^T\right).\end{aligned} \tag{20}$$

Following the asymptotic analysis of [3, 1], in the case of an *open crack* the displacement in the crack tip neighborhood will have a functional form of the type

$$u\left(\delta\right) \sim \sqrt{\delta}\left(\sin,\cos\right)\left(\epsilon\log\delta\right) \quad \text{with} \quad \epsilon = \frac{1}{2\pi}\log\left(\frac{1-\beta}{1+\beta}\right) \tag{21}$$

and β is Dundurs' parameter introduced in Section 1. Application of Equation 21 to the terms on the right hand side of Eq. 20 provides:

$$\underline{u}_{xy}, \underline{u}_{N} \sim u\left(\delta\right) \sim \sqrt{\delta}\left(\sin,\cos\right)\left(\epsilon\log\delta\right) \xrightarrow{\delta\to 0} 0; \tag{22}$$

$$\underline{u}_{xy}\underline{u}_{xy}^T, \underline{u}_N\underline{u}_{xy}^T \sim u^2(\delta) \sim \delta\left(\sin^2, \cos^2, \sin\cdot\cos\right)(\epsilon\log\delta) \xrightarrow{\delta\to 0} 0; \tag{23}$$

$$\frac{\partial\underline{u}_{xy}}{\partial\delta}\underline{u}_{xy}^T, \frac{\partial\underline{u}_N}{\partial\delta}\underline{u}_{xy}^T \sim -\frac{1}{2}\left(\sin^2, \cos^2, \sin\cdot\cos\right)(\epsilon\log\delta) + \left(-\sin^2, \cos^2, \pm\sin\cdot\cos\right)(\epsilon\log\delta) \xrightarrow{\delta\to 0} finite; \tag{24}$$

$$\underline{G} \sim \frac{1}{\delta}\underline{u}_{xy}\underline{u}_{xy}^T \sim \frac{1}{\delta}u^2(\delta) \sim \left(\sin^2, \cos^2, \sin\cdot\cos\right)(\epsilon\log\delta) \xrightarrow{\delta\to 0} finite. \tag{25}$$

In Equations 22-25, the multiplication by a trigonometric function of the type $\left(\sin, \cos, \sin^2, \cos^2, \sin\cdot\cos\right.$ prevents the divergence of the asymptote. Recalling Eqs. 5 and 6, in the limit of $\delta \to 0$ the rotation matrices become equal to the identity matrix:

$$\underline{\underline{P}}_\delta, \underline{\underline{Q}}_\delta \xrightarrow{\delta\to 0} \begin{bmatrix} 1 & 0 \\ 0 & 1 \end{bmatrix}. \tag{26}$$

Applying the results of Equations 22-26 to Eq. 20, it can be shown that the derivative of $\underline{G}$ can be split in a factor that goes to 0 in the limit of $\delta \to 0$ and in a factor independent of δ:

$$\lim_{\delta\to 0}\frac{\partial\underline{G}}{\partial\delta} \sim \frac{1}{\delta}\left(\cancelto{0}{\underline{F}(\delta)} + \underline{C}\right). \tag{27}$$

Thus, asymptotically, the Mode I and Mode II Energy Release Rate behave like the logarithm of the angular size δ of the elements in the crack tip neighborhood:

$$\lim_{\delta\to 0}\frac{\partial\underline{G}}{\partial\delta} \sim \frac{1}{\delta} \quad \xrightarrow{\int d\delta} \quad \lim_{\delta\to 0}\underline{G} \sim \underline{A}\log(\delta) + \underline{B}. \tag{28}$$

5.2 Numerical results

Evaluations of the Mode I, Mode II and total Energy Release Rate using the VCCT applied to the FE solution of the fiber-matrix interface crack in the single fiber model of Sec. 2 are reported respectively in Fig. 4, Fig. 5 and Fig. 6.

Results for Mode I ERR in Fig. 4 show clearly the transition from the *open* crack regime, where Mode I ERR is different from zero, to the *closed* crack regime of the debond, where $G_I = 0$. Looking at Fig. 4, the crack is *open* for $\Delta\theta \leq 60°$ and it is *closed*, i.e. a contact zone is present, for $\Delta\theta \geq 70°$. As expected from the analysis of the previous section, and given that Mode I ERR is different from zero only in the *open* crack regime, a significant dependence on the element size δ can be observed in Fig. 4 when using both 1^{st} and 2^{nd} order elements and with both an effectively infinite ($V_f = 0.1\%$) and finite size ($V_f = 40\%$) matrix. At first sight, it is immediate to see from Fig. 4 that a decrease in δ leads to a decrease in G_I. However, two further effects can be observed due to the refinement of the mesh at the crack tip, i.e. the decrease of the element size δ. First, the occurrence of the peak G_I is shifted to lower angles for very low volume

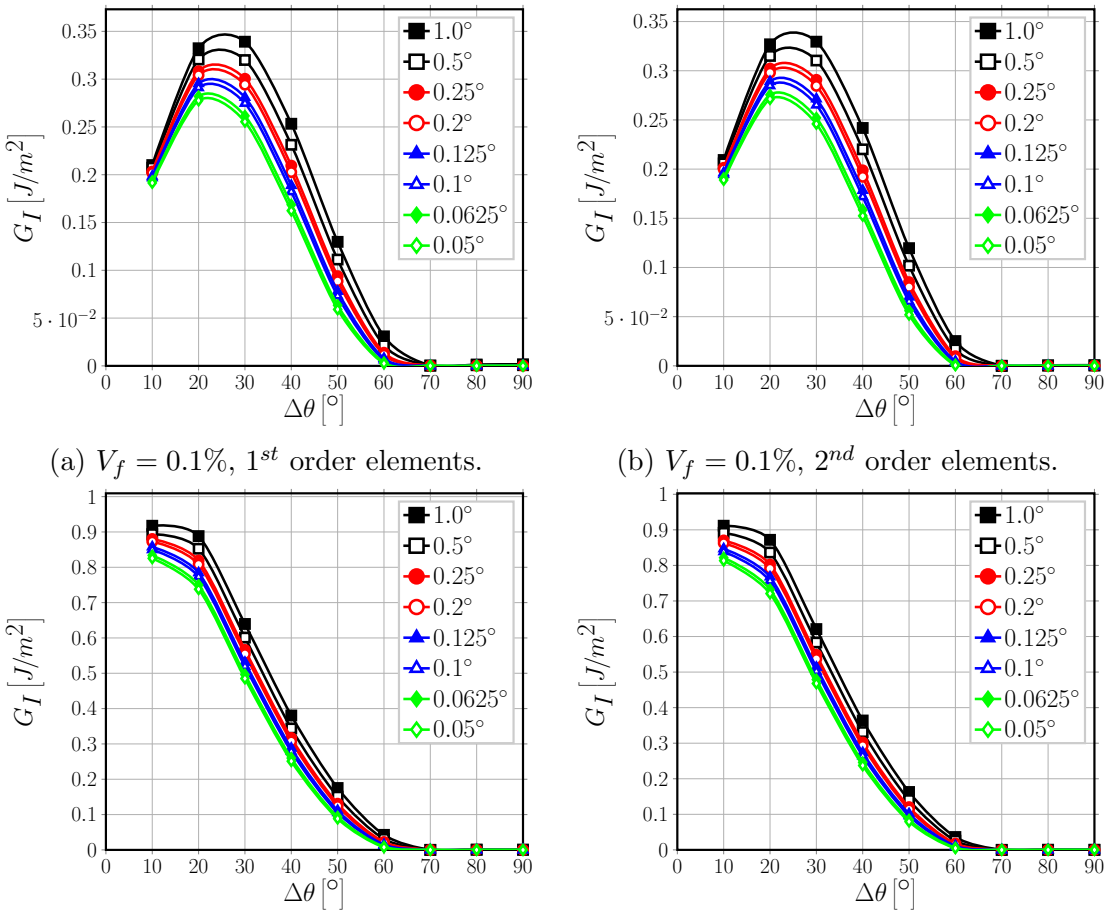

(a) $V_f = 0.1\%$, 1^{st} order elements.

(b) $V_f = 0.1\%$, 2^{nd} order elements.

(c) $V_f = 40\%$, 1^{st} order elements.

(d) $V_f = 40\%$, 2^{nd} order elements.

Figure 4: Effect of the size δ of an element at the crack tip on Mode I ERR.

fractions: it occurs at $\Delta\theta = 30°$ with $\delta = 1.0°, 0.5°$ and at $\Delta\theta = 20°$ with $\delta \leq 0.25°$ for both 1^{st} and 2^{nd} order elements and $V_f = 0.1\%$. Second, the apperance of the contact zone, i.e. the switch to the *closed* crack regime, is anticipated to smaller debonds: it occurs at $\Delta\theta = 70°$ with $\delta \geq 0.2°$ and at $\Delta\theta = 60°$ with $\delta < 0.2°$ for both 1^{st} and 2^{nd} order elements and both $V_f = 0.1\%$ and $V_f = 40\%$.

Observing Figure 5, it possible to notice the existence of two distinct regimes in the behavior of G_{II} with respect to the element size δ. For $\Delta\theta \leq 60°$ G_{II} depends on the value of δ, while $\Delta\theta \geq 70°$ it is effectively independent of the element size at the crack tip for both 1^{st} and 2^{nd} order elements and both an effectively infinite ($V_f = 0.1\%$) and finite size ($V_f = 40\%$) matrix. Comparing the value of $\Delta\theta$ at which the change from the δ-dependency regime to the δ-independency regime occurs for G_{II} with Mode I ERR in Fig. 4, it is possible to observe that the δ-dependency regime change of Mode II ERR coincides with the onset of the contact zone, i.e. the transition from *open* crack regime to the *closed* crack regime. The result confirms the analytical considerations of the previous section: for an *open* crack both Mode I and Mode II ERR depend on the element size δ

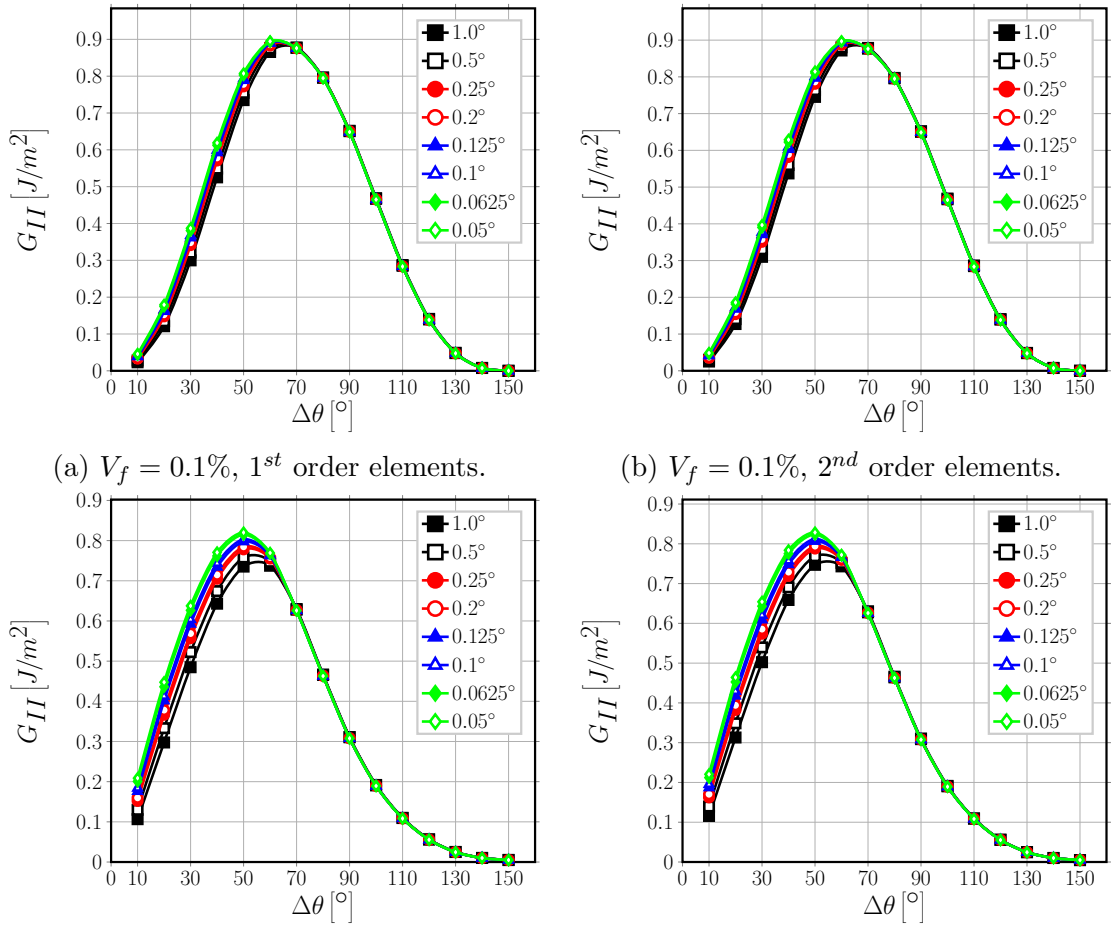

(a) $V_f = 0.1\%$, 1^{st} order elements.

(b) $V_f = 0.1\%$, 2^{nd} order elements.

(c) $V_f = 40\%$, 1^{st} order elements.

(d) $V_f = 40\%$, 2^{nd} order elements.

Figure 5: Effect of the size δ of an element at the crack tip on Mode II ERR.

at the crack tip.

Further observation of Figure 5 reveals that, in the *open* crack regime, decreasing the element size δ causes an increase of Mode II ERR. Similarly to Mode I ERR, a shift of the peak G_{II} can also observed for $V_f = 0.1\%$: the maximum value of G_{II} occurs at $\Delta\theta = 70^\circ$ for $\delta > 0.25^\circ$ for 1^{st} order elements and for $\delta > 0.5^\circ$ for 2^{nd} order elements, while it is shifted to $\Delta\theta = 60^\circ$ for $\delta \leq 0.25^\circ$ for 1^{st} order elements and for $\delta \leq 0.5^\circ$ for 2^{nd} order elements.

Analysis of the total ERR in Figure 6 leads to an observation that was not predicted by the considerations of the previous section: G_{TOT} is effectively independent of the element size δ in both the *open* and the *closed* crack regimes, at least for reasonably small elements ($\delta \leq 1.0^\circ$). Given that $G_{II} = G_{TOT}$ for the *closed* crack, it explains the independency of G_{II} from δ after the onset of the contact zone.

Analysis of Fig. 4, Fig. 5 and Fig. 6 has shown the dependency of Mode I and Mode II ERR on the element size δ. Following the derivations of the previous section, we model the dependency of G_I and G_{II} with respect to δ as

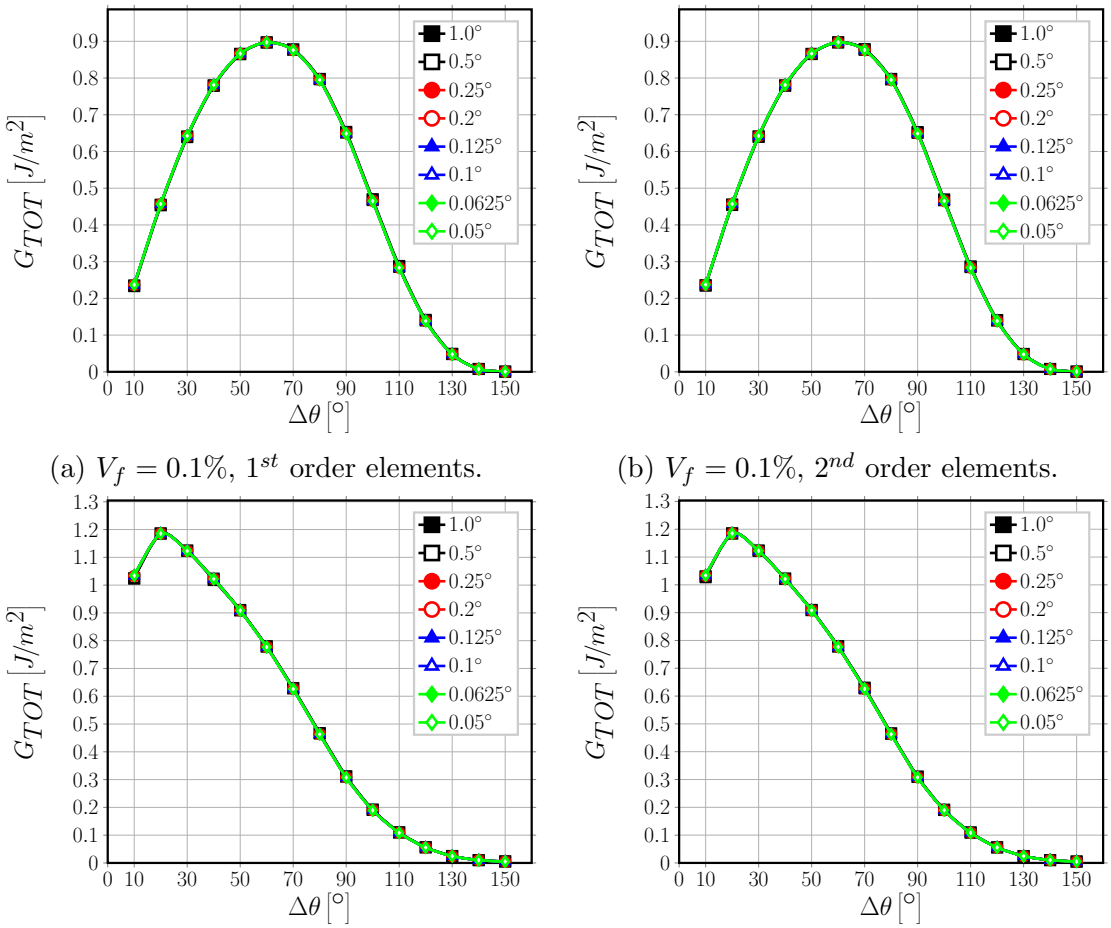

(a) $V_f = 0.1\%$, 1^{st} order elements.

(b) $V_f = 0.1\%$, 2^{nd} order elements.

(c) $V_f = 40\%$, 1^{st} order elements.

(d) $V_f = 40\%$, 2^{nd} order elements.

Figure 6: Effect of the size δ of an element at the crack tip on total ERR.

$$G_{(\cdot)} = A\left(\Delta\theta\right)\ln\delta + B\left(\Delta\theta\right), \tag{29}$$

where $A\left(\Delta\theta\right)$ and $B\left(\Delta\theta\right)$ are parameters dependent on $\Delta\theta$ estimated through linear regression (with $x = \ln\delta$) of the numerical results.

As shown in Fig. 7, Fig. 8, Fig. 9 and Fig. 10 both in linear and logarithmic scales of δ, the result is remarkable: both the correlation coefficient r and the r^2 ratio (of explained to total variance) are always greater than 0.95 and the p-values of the coefficients A and B are at least $< 1E-6$ and often $< 1E-11$ (see Table 2 for G_I and Table 3 for G_{II}). The results of the linear regression confirm the analytical derivations of the previous section, which showed the logarithmic behavior of Mode I and Mode II ERR. Similar conclusions were reached in [29, 31] for a straight bi-material crack with respect to the parameter $\Delta a/a$; however, no functional expression of $G_{(\cdot)}$ was proposed.

Table 2: Summary of linear regression results and main statistical tests for Mode I ERR

$\mathbf{V_f}$ [%]	Order	$\boldsymbol{\Delta\theta}$ [°]	$\mathbf{A}\left[\frac{\mathbf{J}}{\mathbf{m^2}}\right]$	$\mathbf{B}\left[\frac{\mathbf{J}}{\mathbf{m^2}}\right]$	$\mathbf{r}$ [−]	$\mathbf{r^2}$ [−]	$\mathbf{p(A)}$ [−]	$\mathbf{p(B)}$ [−]
0.1	1	10.0	0.0064	0.2113	0.9933	0.9866	7.48E-07	3.49E-14
		20.0	0.0183	0.3331	0.9996	0.9992	1.44E-10	2.40E-16
		30.0	0.0280	0.3392	1.0000	1.0000	2.25E-16	4.26E-21
		40.0	0.0304	0.2524	0.9997	0.9995	4.38E-11	7.94E-15
		50.0	0.0235	0.1278	0.9985	0.9970	8.61E-09	2.01E-11
		60.0	0.0094	0.0284	0.9854	0.9709	7.75E-06	6.14E-07
0.1	2	10.0	0.0069	0.2103	0.9962	0.9924	1.36E-07	1.03E-14
		20.0	0.0187	0.3277	0.9997	0.9994	7.85E-11	1.62E-16
		30.0	0.0280	0.3296	1.0000	1.0000	3.28E-16	7.29E-21
		40.0	0.0298	0.2408	0.9997	0.9995	4.82E-11	1.04E-14
		50.0	0.0225	0.1177	0.9984	0.9967	1.10E-08	3.27E-11
		60.0	0.0081	0.0228	0.9811	0.9626	1.66E-05	2.17E-06
40	1	10.0	0.0311	0.9196	0.9963	0.9927	1.03E-07	9.33E-15
		20.0	0.0501	0.8882	1.0000	0.9999	1.21E-13	2.33E-19
		30.0	0.0510	0.6374	0.9998	0.9996	1.66E-11	2.58E-16
		40.0	0.0419	0.3760	0.9988	0.9976	4.56E-09	5.25E-13
		50.0	0.0279	0.1713	0.9980	0.9961	2.22E-08	2.52E-11
		60.0	0.0108	0.0391	0.9901	0.9804	3.44E-06	9.46E-08
40	2	10.0	0.0336	0.9148	0.9988	0.9977	3.45E-09	5.09E-16
		20.0	0.0504	0.8719	1.0000	1.0000	3.70E-14	8.26E-20
		30.0	0.0506	0.6191	0.9999	0.9997	7.63E-12	1.35E-16
		40.0	0.0414	0.3608	0.9994	0.9989	4.95E-10	6.80E-14
		50.0	0.0269	0.1593	0.9982	0.9964	1.66E-08	2.31E-11
		60.0	0.0097	0.0329	0.9890	0.9781	4.96E-06	1.99E-07

6 Conclusions & Outlook

The application of the Virtual Crack Closure Technique to the calculation of Mode I, Mode II and total Energy Release Rate was analyzed in the context of the Finite Element solution of the bi-material circular arc crack, or fiber-matrix interface crack. A synthetic vectorial formulation of the VCCT has been proposed and its usefulness exemplified in the analysis of the mesh dependency. By both analytical considerations and numerical simulations, it has been shown that:

- the total ERR is invariant to rotations of the reference frame (and more in general to linear transformations), which implies that rotation of crack tip forces and displacement is actually not required in the use of the VCCT for the calculation of G_{TOT};

Table 3: Summary of linear regression results and main statistical tests for Mode II ERR

$\mathbf{V_f}$ [%]	Order	$\mathbf{\Delta\theta}$ [°]	$\mathbf{A}\left[\frac{\mathbf{J}}{\mathbf{m^2}}\right]$	$\mathbf{B}\left[\frac{\mathbf{J}}{\mathbf{m^2}}\right]$	$\mathbf{r}$ [−]	$\mathbf{r^2}$ [−]	$\mathbf{p(A)}$ [−]	$\mathbf{p(B)}$ [−]
0.1	1.0	10.0	-0.0076	0.0228	-0.9996	0.9991	2.09E-10	1.64E-11
		20.0	-0.0194	0.1211	-1.0000	1.0000	1.99E-15	2.02E-18
		30.0	-0.0290	0.3007	-0.9999	0.9998	4.12E-12	1.97E-16
		40.0	-0.0311	0.5270	-0.9995	0.9989	4.13E-10	1.05E-15
		50.0	-0.0240	0.7375	-0.9979	0.9958	2.32E-08	1.66E-15
		60.0	-0.0095	0.8685	-0.9835	0.9672	1.12E-05	1.22E-15
0.1	2.0	10.0	-0.0078	0.0249	-0.9996	0.9992	1.91E-10	1.06E-11
		20.0	-0.0196	0.1272	-1.0000	1.0000	3.48E-15	2.78E-18
		30.0	-0.0288	0.3108	-0.9999	0.9998	1.45E-12	5.47E-17
		40.0	-0.0305	0.5387	-0.9995	0.9990	3.32E-10	6.55E-16
		50.0	-0.0229	0.7478	-0.9979	0.9959	2.17E-08	1.09E-15
		60.0	-0.0082	0.8744	-0.9806	0.9615	1.81E-05	8.26E-16
40.0	1.0	10.0	-0.0344	0.1055	-0.9997	0.9995	3.82E-11	2.73E-12
		20.0	-0.0500	0.2977	-1.0000	0.9999	4.22E-14	5.66E-17
		30.0	-0.0505	0.4866	-0.9999	0.9997	6.44E-12	4.82E-16
		40.0	-0.0420	0.6454	-0.9996	0.9991	2.12E-10	9.66E-16
		50.0	-0.0275	0.7386	-0.9985	0.9971	9.01E-09	1.44E-15
		60.0	-0.0099	0.7402	-0.9926	0.9853	1.41E-06	5.13E-16
40.0	2.0	10.0	-0.0353	0.1145	-0.9998	0.9995	2.92E-11	1.50E-12
		20.0	-0.0504	0.3130	-1.0000	0.9999	4.00E-14	4.17E-17
		30.0	-0.0502	0.5039	-0.9999	0.9998	2.87E-12	1.69E-16
		40.0	-0.0410	0.6615	-0.9996	0.9992	2.02E-10	6.89E-16
		50.0	-0.0263	0.7502	-0.9987	0.9973	6.87E-09	7.76E-16
		60.0	-0.0090	0.7458	-0.9921	0.9842	1.79E-06	3.37E-16

- the total ERR does not depend on the size δ of the elements at the crack tip, at least for reasonably small elements ($\delta \leq 1.0°$) ;
- as a consequence, Mode II ERR for the *closed* interface crack does not depend on δ, as $G_{II} = G_{TOT}$ after the onset of the contact zone;
- for the *open* interface crack, Mode I and Mode II ERR depend on the element size δ through a logarithmic law of the type $A\left(\Delta\theta\right)\ln\delta + B\left(\Delta\theta\right)$;
- the sign of the logarithm is always positive for G_I, i.e. it decreases when δ decreases, and negative for G_{II}, i.e. it increases when δ decreases.

The conclusion is significant: as the behavior of Mode I and Mode II is logarithmic with respect to mesh size, there exists no asymptotic limit and thus no convergence of

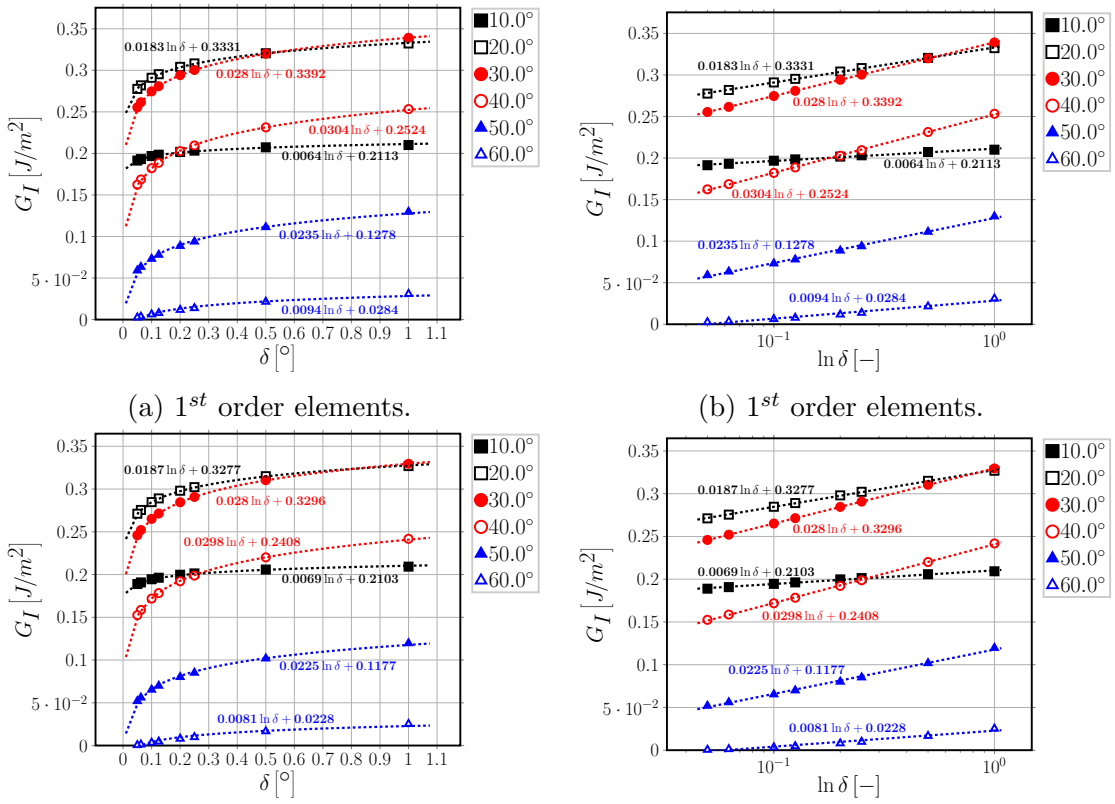

(a) 1^{st} order elements.

(b) 1^{st} order elements.

(c) 2^{nd} order elements.

(d) 2^{nd} order elements.

Figure 7: Logarithmic dependence on δ of Mode I ERR: interpolation of numerical results for $V_f = 0.1\%$.

the values. A convergence analysis based on the reduction of the error between successive iterations would not provide a reliable assessment of the accuracy of the FE solution of Mode I and Mode II Energy Release Rate of the fiber-matrix interface crack. A validation is thus required with respect to data obtained through a different method, be it analytical, numerical or experimental. Moreover, it has been shown that: first, the same behavior appears when using 1^{st} as well as 2^{nd} order elements; second, no improvement is expected with the use of singular elements, as the logarithmic dependency of G_I and G_{II} is governed by the definition of ERR itself together with the asymptotic behavior of the displacement field at the crack tip. These two conclusions put into discussion recommendations often provided by manuals of commercial FEM packages such as Abaqus [36]. The latter for example, in the context of VCCT-based crack propagation (Section 11.4.2 of the *Abaqus Analysis User's Guide*), suggests that *in most cases mesh refinement will help with obtaining a realistic result*, that *results with nonlinear materials are more sensitive to meshing than results with small-strain linear elasticity* and that *first-order elements generally work best for crack propagation analysis.* . The previous considerations might apply for cracks in isotropic mediums; however, the VCCT-based crack propagation technique is proposed in Abaqus as a suitable technique for surface-based simulation of

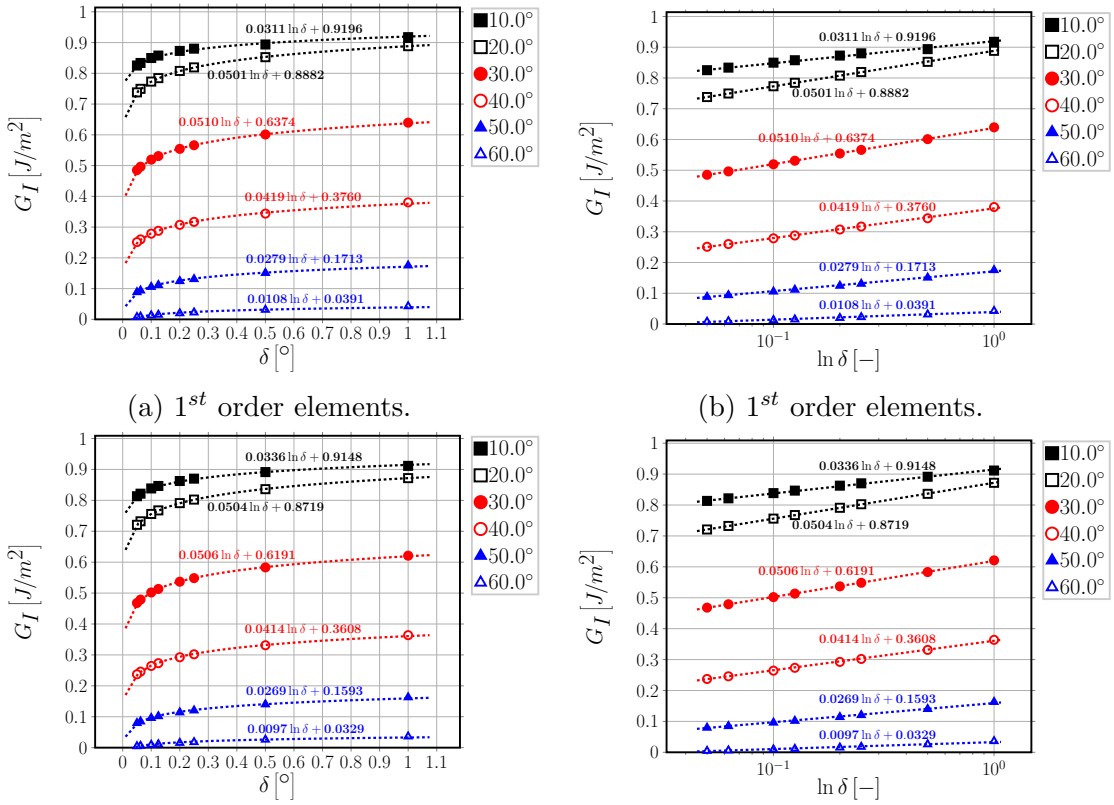

(a) 1^{st} order elements.

(b) 1^{st} order elements.

(c) 2^{nd} order elements.

(d) 2^{nd} order elements.

Figure 8: Logarithmic dependence on δ of Mode I ERR: interpolation of numerical results for $V_f = 40\%$.

bi-material interface debonding. We have shown that, for a circular interface crack: mesh-refinement (h-refinement) does not guarantee convergence of Mode I and Mode II ERR, as their dependency on element size is logarithmic; sensitivity to meshing is actually very significant in small-strain linear elasticity and depends on the nature of the linear elastic solution at the crack tip; no difference in convergence trends is observable between first and second order elements (p-refinement). This closing considerations are not meant to be a critique *per se* to commercial software, but rather as a source of reflection on the best use of software tools. Apart from the scientific merit of the results proposed, the conclusions presented here stand as an invitation to the practitioner to avoid black-box thinking and blind application of built-in software solutions. .

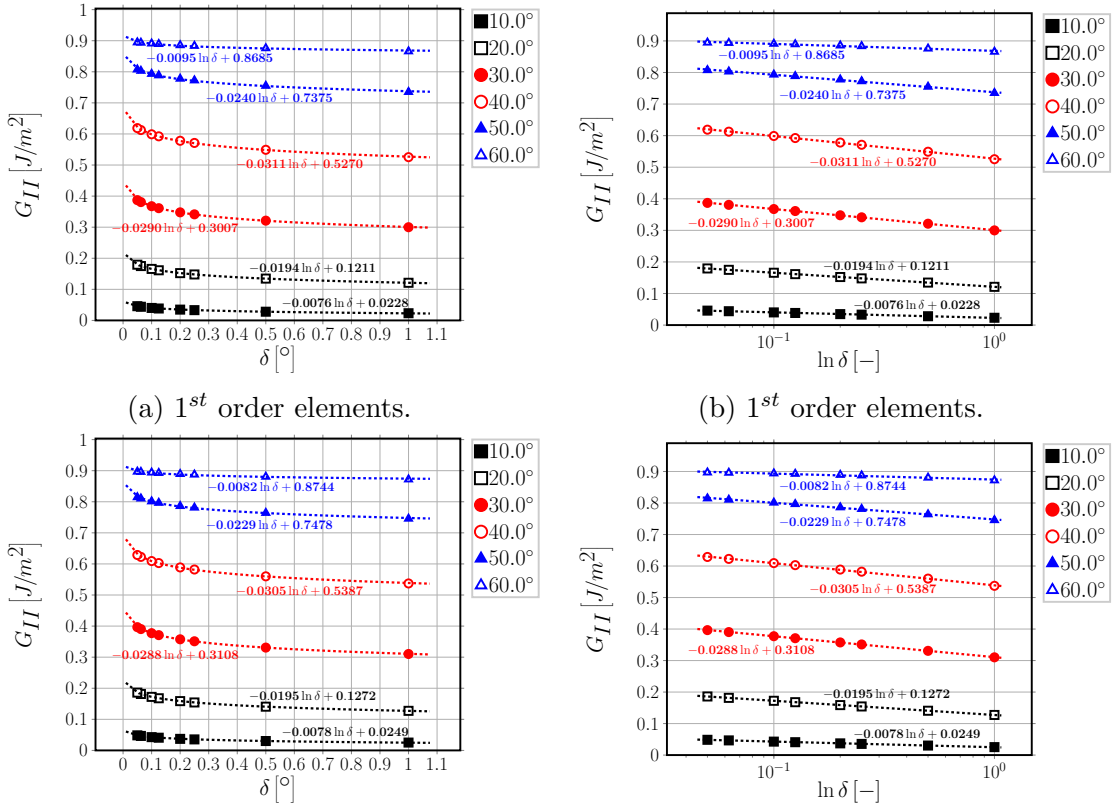

(a) 1^{st} order elements.

(b) 1^{st} order elements.

(c) 2^{nd} order elements.

(d) 2^{nd} order elements.

Figure 9: Logarithmic dependence on δ of Mode II ERR: interpolation of numerical results for $V_f = 0.1\%$.

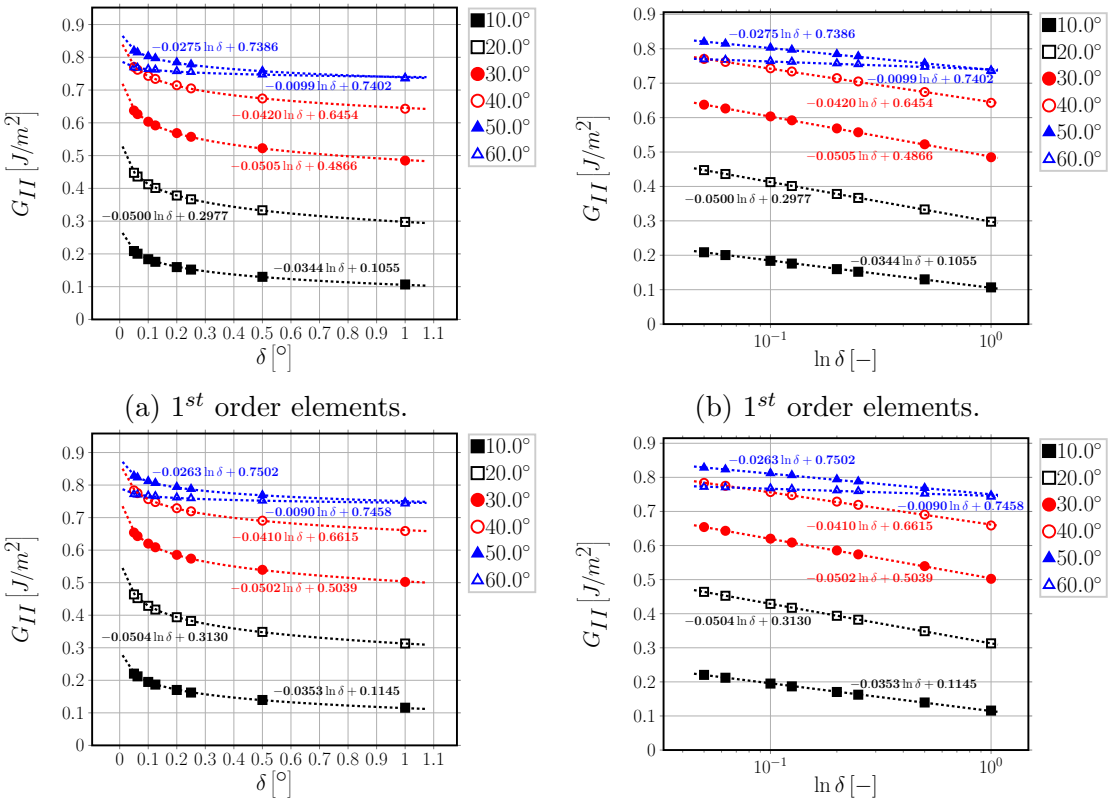

(a) 1^{st} order elements.

(b) 1^{st} order elements.

(c) 2^{nd} order elements.

(d) 2^{nd} order elements.

Figure 10: Logarithmic dependence on δ of Mode II ERR: interpolation of numerical results for $V_f = 40\%$.

Acknowledgements

Luca Di Stasio thanks Prof. Janis Varna for the useful discussions and suggestions. Luca Di Stasio gratefully acknowledges the support of the European School of Materials (EUSMAT) through the DocMASE Doctoral Programme and the European Commission through the Erasmus Mundus Programme.

References

[1] Maria Comninou. "An overview of interface cracks". In: *Engineering Fracture Mechanics* 37.1 (Jan. 1990), pp. 197–208. DOI: 10.1016/0013-7944(90)90343-f.

[2] D.A. Hills and J.R. Barber. "Interface cracks". In: *International Journal of Mechanical Sciences* 35.1 (Jan. 1993), pp. 27–37. DOI: 10.1016/0020-7403(93)90062-y.

[3] M. L. Williams. "The stresses around a fault or crack in dissimilar media". In: *Bulletin of the Seismological Society of America* 49.2 (1959), p. 199.

[4] J. Dundurs. "Discussion: "Edge-Bonded Dissimilar Orthogonal Elastic Wedges Under Normal and Shear Loading" (Bogy, D. B., 1968, ASME J. Appl. Mech., 35, pp. 460–466)". In: *Journal of Applied Mechanics* 36.3 (1969), p. 650. DOI: 10.1115/1.3564739.

[5] Fazil Erdogan. "Stress Distribution in a Nonhomogeneous Elastic Plane With Cracks". In: *Journal of Applied Mechanics* 30.2 (1963), p. 232. DOI: 10.1115/1.3636517.

[6] A. H. England. "A Crack Between Dissimilar Media". In: *Journal of Applied Mechanics* 32.2 (1965), p. 400. DOI: 10.1115/1.3625813.

[7] B.M. Malyshev and R.L. Salganik. "The strength of adhesive joints using the theory of cracks". In: *International Journal of Fracture Mechanics* 1-1.2 (June 1965). DOI: 10.1007/bf00186749. URL: https://doi.org/10.1007/bf00186749.

[8] Maria Comninou. "The Interface Crack". In: *Journal of Applied Mechanics* 44.4 (1977), p. 631. DOI: 10.1115/1.3424148. URL: https://doi.org/10.1115/1.3424148.

[9] A. H. England. "An Arc Crack Around a Circular Elastic Inclusion". In: *Journal of Applied Mechanics* 33.3 (1966), p. 637. DOI: 10.1115/1.3625132.

[10] A.B. Perlman and G.C. Sih. "Elastostatic problems of curvilinear cracks in bonded dissimilar materials". In: *International Journal of Engineering Science* 5.11 (Nov. 1967), pp. 845–867. DOI: 10.1016/0020-7225(67)90009-2.

[11] M. Toya. "A crack along the interface of a circular inclusion embedded in an infinite solid". In: *Journal of the Mechanics and Physics of Solids* 22.5 (Oct. 1974), pp. 325–348. DOI: 10.1016/0022-5096(74)90002-7.

[12] F. París, J. C. Caño, and J. Varna. "The fiber-matrix interface crack — A numerical analysis using Boundary Elements". In: *International Journal of Fracture* 82.1 (May 1996), pp. 11–29. DOI: 10.1007/bf00017861.

[13] George R. Irwin. "Fracture". In: *Elasticity and Plasticity / Elastizität und Plastizität*. Springer Berlin Heidelberg, 1958, pp. 551–590. DOI: 10.1007/978-3-642-45887-3_5.

[14] J. C. Del Caño and F. París. "On stress singularities induced by the discretization in curved receding contact surfaces: a BEM analysis". In: *International Journal for Numerical Methods in Engineering* 40.12 (June 1997), pp. 2301–2320. DOI: 10.1002/(sici)1097-0207(19970630)40:12<2301::aid-nme166>3.0.co;2-8.

[15] J. Varna, Federico París, and J. C.Caño. "The effect of crack-face contact on fiber/matrix debonding in transverse tensile loading". In: *Composites Science and Technology* 57.5 (1997), pp. 523–532. DOI: 10.1016/s0266-3538(96)00175-3.

[16] Federico París, Elena Correa, and Vladislav Mantič. "Kinking of Transversal Interface Cracks Between Fiber and Matrix". In: *Journal of Applied Mechanics* 74.4 (2007), p. 703. DOI: 10.1115/1.2711220.

[17] E. Correa et al. "Effects of the presence of compression in transverse cyclic loading on fibre–matrix debonding in unidirectional composite plies". In: *Composites Part A: Applied Science and Manufacturing* 38.11 (Nov. 2007), pp. 2260–2269. DOI: 10.1016/j.compositesa.2006.11.002.

[18] E. Correa, V. Mantič, and F. París. "Effect of thermal residual stresses on matrix failure under transverse tension at micromechanical level: A numerical and experimental analysis". In: *Composites Science and Technology* 71.5 (Mar. 2011), pp. 622–629. DOI: 10.1016/j.compscitech.2010.12.027.

[19] E. Correa, F. París, and V. Mantič. "Effect of the presence of a secondary transverse load on the inter-fibre failure under tension". In: *Engineering Fracture Mechanics* 103 (May 2013), pp. 174–189. DOI: 10.1016/j.engfracmech.2013.02.026.

[20] E. Correa, F. París, and V. Mantič. "Effect of a secondary transverse load on the inter-fibre failure under compression". In: *Composites Part B: Engineering* 65 (Oct. 2014), pp. 57–68. DOI: 10.1016/j.compositesb.2014.01.005.

[21] C. Sandino, E. Correa, and F. París. "Numerical analysis of the influence of a nearby fibre on the interface crack growth in composites under transverse tensile load". In: *Engineering Fracture Mechanics* 168 (Dec. 2016), pp. 58–75. DOI: 10.1016/j.engfracmech.2016.01.022.

[22] C. Sandino, E. Correa, and F. París. "Interface crack growth under transverse compression: nearby fibre effect". In: *Proceeding of the* 18^{th} *European Conference on Composite Materials (ECCM-18)*. (Athens, Greece, June 24–28, 2018). 2018.

[23] Linqi Zhuang et al. "Effects of inter-fiber spacing on fiber-matrix debond crack growth in unidirectional composites under transverse loading". In: *Composites Part A: Applied Science and Manufacturing* 109 (June 2018), pp. 463–471. DOI: 10.1016/j.compositesa.2018.03.031.

[24] Janis Varna et al. "Growth and Interaction of Debonds in Local Clusters of Fibers in Unidirectional Composites during Transverse Loading". In: *Key Engineering Materials* 754 (Sept. 2017), pp. 63–66. DOI: 10.4028/www.scientific.net/kem.754.63.

[25] Linqi Zhuang, Ramesh Talreja, and Janis Varna. "Transverse crack formation in unidirectional composites by linking of fibre/matrix debond cracks". In: *Composites Part A: Applied Science and Manufacturing* 107 (Apr. 2018), pp. 294–303. DOI: 10.1016/j.compositesa.2018.01.013.

[26] E.F. Rybicki and M.F. Kanninen. "A finite element calculation of stress intensity factors by a modified crack closure integral". In: *Engineering Fracture Mechanics* 9.4 (Jan. 1977), pp. 931–938. DOI: 10.1016/0013-7944(77)90013-3.

[27] Ronald Krueger. "Virtual crack closure technique: History, approach, and applications". In: *Applied Mechanics Reviews* 57.2 (2004), p. 109. DOI: 10.1115/1.1595677.

[28] R. Krueger, K. N. Shivakumar, and I. S. Raju. "Fracture Mechanics Analyses for Interface Crack Problems - A Review". In: *54th AIAA, ASME, ASCE, AHS, ASC Structures, Structural Dynamics, and Materials Conference*. American Institute of Aeronautics and Astronautics, Apr. 2013. DOI: 10.2514/6.2013-1476.

[29] C.T Sun and C.J Jih. "On strain energy release rates for interfacial cracks in bimaterial media". In: *Engineering Fracture Mechanics* 28.1 (Jan. 1987), pp. 13–20. DOI: 10.1016/0013-7944(87)90115-9.

[30] C.T. Sun and M.G. Manoharan. "Strain Energy Release Rates of an Interfacial Crack Between Two Orthotropic Solids". In: *Journal of Composite Materials* 23.5 (May 1989), pp. 460–478. DOI: 10.1177/002199838902300503.

[31] M.G. Manoharan and C.T. Sun. "Strain energy release rates of an interfacial crack between two anisotropic solids under uniform axial strain". In: *Composites Science and Technology* 39.2 (Jan. 1990), pp. 99–116. DOI: 10.1016/0266-3538(90)90049-b.

[32] I.S. Raju, J.H. Crews, and M.A. Aminpour. "Convergence of strain energy release rate components for Edge-Delaminated composite laminates". In: *Engineering Fracture Mechanics* 30.3 (Jan. 1988), pp. 383–396. DOI: 10.1016/0013-7944(88)90196-8.

[33] E. Glaessgen, W. Riddell, and I. Raju. "Effect of shear deformation and continuity on delamination modeling with plate elements". In: *39th AIAA/ASME/ASCE/AHS/ASC Structures, Structural Dynamics, and Materials Conference and Exhibit*. American Institute of Aeronautics and Astronautics, Apr. 1998. DOI: 10.2514/6.1998-2023.

[34] A. Agrawal and A. M. Karlsson. "Obtaining mode mixity for a bimaterial interface crack using the virtual crack closure technique". In: *International Journal of Fracture* 141.1-2 (Sept. 2006), pp. 75–98. DOI: 10.1007/s10704-006-0069-4.

[35] S. Wang, C.M. Harvey, and L. Guan. "Partition of mixed modes in layered isotropic double cantilever beams with non-rigid cohesive interfaces". In: *Engineering Fracture Mechanics* 111 (Oct. 2013), pp. 1–25. DOI: 10.1016/j.engfracmech.2013.09.005.

[36] *ABAQUS/Standard User's Manual, Version 6.12*. Simulia. Providence, RI, USA, 2012.

[37] Paolo S. Valvo. "A revised virtual crack closure technique for physically consistent fracture mode partitioning". In: *International Journal of Fracture* 173.1 (Dec. 2011), pp. 1–20. DOI: 10.1007/s10704-011-9658-y.

[38] Paolo S. Valvo. "A further step towards a physically consistent virtual crack closure technique". In: *International Journal of Fracture* 192.2 (Mar. 2015), pp. 235–244. DOI: 10.1007/s10704-015-0007-4.

[39] G. R. Irwin. "Analysis of Stresses and Strains near the End of a Crack Traversing a Plate". In: *Journal of Applied Mechanics - Transactions of the ASME* E24 (1957), pp. 351–369.

[40] I.S. Raju. "Calculation of strain-energy release rates with higher order and singular finite elements". In: *Engineering Fracture Mechanics* 28.3 (Jan. 1987), pp. 251–274. DOI: 10.1016/0013-7944(87)90220-7.

[41] W. T. Chow and S. N. Atluri. "Finite element calculation of stress intensity factors for interfacial crack using virtual crack closure integral". In: *Computational Mechanics* 16.6 (Nov. 1995), pp. 417–425. DOI: 10.1007/bf00370563.

A Derivation of the relationship between crack tip forces and displacements for first order quadrilateral elements

A.1 Foundational relations

We review and present in this Section the foundational relations of the isoparametric formulation of the Finite Element Method. The objective here is to provide a theoretical foundation to the expressions in Equation 10 and Equation 11 and a reference for the explicit calculation of the nodal stiffness matrices proposed in Eq. 10 and Eq. 11. We propose a general treatment, valid for 2- and 3-dimensional problems, so that the interested reader could evaluate the nodal stiffness matrices for both a 2- and a 3-dimensional crack. However, in order to clarify the structure of some specific objects, we explicitly write their 2-dimensional form, which is of interest for the problem of this paper.

Denoting by d the number of geometrical dimensions of the problem ($d = 2$ in the present work), the element Jacobian J and its inverse J^{-1} can be expressed in general as

$$J_{ij} = \left(e_{\xi_j}\right)_i = \frac{\partial x_i}{\partial \xi_j} \quad J^{-1}_{ij} = \left(e^{x_j}\right)_i = \frac{\partial \xi_i}{\partial x_j} \quad i,j = 1,\ldots,d \tag{A.30}$$

where $\left(e_{\xi_j}\right)$ and $\left(e^{x_j}\right)$ are respectively the covariant and contravariant basis vectors of the mapping between global $\{x_i\}$ and local element $\{\xi_i\}$ coordinates.
In 2D, assuming the global coordinates are $\{x, y\}$ and the local element coordinates are $\{\xi, \eta\}$, the covariant and contravariant basis vectors assume the form

$$\underline{e}_\xi = \begin{bmatrix} \frac{\partial x}{\partial \xi} \\ \frac{\partial y}{\partial \xi} \end{bmatrix} \quad \underline{e}_\eta = \begin{bmatrix} \frac{\partial x}{\partial \eta} \\ \frac{\partial y}{\partial \eta} \end{bmatrix}, \tag{A.31}$$

$$\underline{e}_x = \begin{bmatrix} \frac{\partial \xi}{\partial x} \\ \frac{\partial \eta}{\partial x} \end{bmatrix} \quad \underline{e}_y = \begin{bmatrix} \frac{\partial \xi}{\partial y} \\ \frac{\partial \eta}{\partial y} \end{bmatrix}. \tag{A.32}$$

and the element Jacobian J and its inverse J^{-1} can be computed for a 2D problem as

$$\underline{\underline{J}} = \left[\underline{e}_\xi | \underline{e}_\eta\right] = \begin{bmatrix} \frac{\partial x}{\partial \xi} & \frac{\partial x}{\partial \eta} \\ \frac{\partial y}{\partial \xi} & \frac{\partial y}{\partial \eta} \end{bmatrix} \qquad \underline{\underline{J}}^{-1} = \left[\underline{e}^x | \underline{e}^y\right] = \begin{bmatrix} \frac{\partial \xi}{\partial x} & \frac{\partial \xi}{\partial y} \\ \frac{\partial \eta}{\partial x} & \frac{\partial \eta}{\partial y} \end{bmatrix}. \tag{A.33}$$

Denoting by $\underline{p}$ the $d \times 1$ position vector in global coordinates, we can formally introduce the $3\,(d-1) \times d$ matrix operator of partial differentiation $\underline{\underline{\widetilde{B}}}$ such that

$$\underline{\varepsilon}\left(\underline{p}\right) = \underline{\underline{\widetilde{B}}} \cdot \underline{u}\left(\underline{p}\right), \tag{A.34}$$

where $\underline{u}$ and $\underline{\varepsilon}$ are respectively the $d \times 1$ displacement vector and the $3\,(d-1) \times 1$ strain vector in Voigt notation. Denoting by n the number of nodes of a generic element, it holds that $n = s \times m$ where s represents the number of sides of the element (3 for a triangle, 4 for a rectangle, ...) and m the order of the shape functions (1 for linear shape functions, 2 for quadratic shape functions, ...). We can now introduce the $d \times d \cdot n$ matrix $\underline{\underline{N}}$ of shape functions such that

$$\underline{u} = \underline{\underline{N}} \cdot \underline{u}_N, \tag{A.35}$$

where $\underline{u}_N$ is the $d \cdot n \times 1$ vector of element nodal variables. Having introduced $\underline{\underline{\widetilde{B}}}$ and $\underline{\underline{N}}$ in Equations A.34 and A.35 respectively, it is possible to define the $3\,(d-1) \times d \cdot n$ matrix $\underline{\underline{B}}$ of derivatives (with respect to global coordinates) of shape functions as

$$\underline{\underline{B}} = \underline{\underline{\widetilde{B}}} \cdot \underline{\underline{N}}. \tag{A.36}$$

We introduce the linear elastic material behavior in the form of the $3\,(d-1) \times 3\,(d-1)$ rigidity matrix $\underline{\underline{D}}$ such that

$$\underline{\sigma} = \underline{\underline{D}} \cdot \underline{\varepsilon}, \tag{A.37}$$

where $\underline{\sigma}$ the $3\left(d-1\right)\times 1$ stress vector in Voigt notation. It is finally possible to define the $n \times n$ element stiffness matrix $\underline{\underline{k_e}}$ as

$$\underline{\underline{k_e}} = \int_{V_e(x_i)} \left(\underline{\underline{B}}^T \underline{\underline{D}} \cdot \underline{\underline{B}}\right) dV_e\left(x_i\right) = \int_{V_e(\xi_i)} \left(\underline{\underline{B}}^T \underline{\underline{D}} \cdot \underline{\underline{B}}\right) \sqrt{g} dV_e\left(\xi_i\right), \tag{A.38}$$

where $g = det\left(\underline{\underline{J}}^T \underline{\underline{J}}\right)$ and V_e is the element volume. Given that isoparametric elements are always defined between -1 and 1 in each dimension, Equation A.38 can simplified to

$$\underline{\underline{k_e}} = \int_{-1}^{1} \cdots \int_{-1}^{1} \left(\underline{\underline{B}}^T \underline{\underline{D}} \cdot \underline{\underline{B}}\right) \sqrt{g} d\xi_i, \tag{A.39}$$

which is amenable to numerical integration by means of a Gaussian quadrature of the form

$$\underline{\underline{k_e}} \approx \underbrace{\sum_{k=1}^{N} \cdots \sum_{h=1}^{N}}_{d \ times} w_k \ldots w_h \left(\underline{\underline{B}}^T \left(\xi_i\left(k, \ldots, h\right)\right) \cdot \underline{\underline{D}} \cdot \underline{\underline{B}}\left(\xi_i\left(k, \ldots, h\right)\right) \sqrt{g}\right), \tag{A.40}$$

where $\xi_i\left(k, \ldots, h\right)$ are the coordinates of the N Gaussian quadrature points. The element stiffness matrix as evaluated in Eq. A.40 is in general a full symmetric matrix in the case of linear elasticity. For 2D rectangular elements with quadratic shape functions (8-nodes serendipity elements), the element stiffness matrix has the form

$$k_e = \begin{bmatrix} k_{e|11} & k_{e|12} & k_{e|13} & k_{e|14} & k_{e|15} & k_{e|16} & k_{e|17} & k_{e|18} \\ k_{e|12} & k_{e|22} & k_{e|23} & k_{e|24} & k_{e|25} & k_{e|26} & k_{e|27} & k_{e|28} \\ k_{e|13} & k_{e|23} & k_{e|33} & k_{e|34} & k_{e|35} & k_{e|36} & k_{e|37} & k_{e|38} \\ k_{e|14} & k_{e|24} & k_{e|34} & k_{e|44} & k_{e|45} & k_{e|46} & k_{e|47} & k_{e|48} \\ k_{e|15} & k_{e|25} & k_{e|35} & k_{e|45} & k_{e|55} & k_{e|56} & k_{e|57} & k_{e|58} \\ k_{e|16} & k_{e|26} & k_{e|36} & k_{e|46} & k_{e|56} & k_{e|66} & k_{e|67} & k_{e|68} \\ k_{e|17} & k_{e|27} & k_{e|37} & k_{e|47} & k_{e|57} & k_{e|67} & k_{e|77} & k_{e|78} \\ k_{e|18} & k_{e|28} & k_{e|38} & k_{e|48} & k_{e|58} & k_{e|68} & k_{e|78} & k_{e|88} \end{bmatrix}. \tag{A.41}$$

A.2 Calculation of displacements and reaction forces

With reference to Fig. 11, we define:

$u_{x,M}$, $u_{x,F}$ the x-displacement of the nodes belonging to the free side of the first element belonging to the crack, respectively on the matrix (bulk) and fiber (inclusion) side;

$u_{y,M}$, $u_{y,F}$ the y-displacement of the nodes belonging to the free side of the first element belonging to the crack, respectively on the matrix (bulk) and fiber (inclusion) side;

$u_{r,M}$, $u_{r,F}$ the r-displacement of the nodes belonging to the free side of the first element belonging to the crack, respectively on the matrix (bulk) and fiber (inclusion) side;

$u_{\theta,M}$, $u_{\theta,F}$ the θ-displacement of the nodes belonging to the free side of the first element belonging to the crack, respectively on the matrix (bulk) and fiber (inclusion) side;

$F_{x,CT}$, $F_{y,CT}$ respectively the x- and y-component of the reaction force at the crack tip;

$F_{r,CT}$, $F_{\theta,CT}$ respectively the r- and θ-component of the reaction force at the crack tip.

The $x-y$ reference frame is the global reference frame, while the $r-\theta$ reference frame is such that the θ direction coincides with the crack propagation direction at the crack tip and r the in-plane normal to the propagation direction. For an arc-crack as the present one, the r-direction coincides with the radial direction of the inclusion.

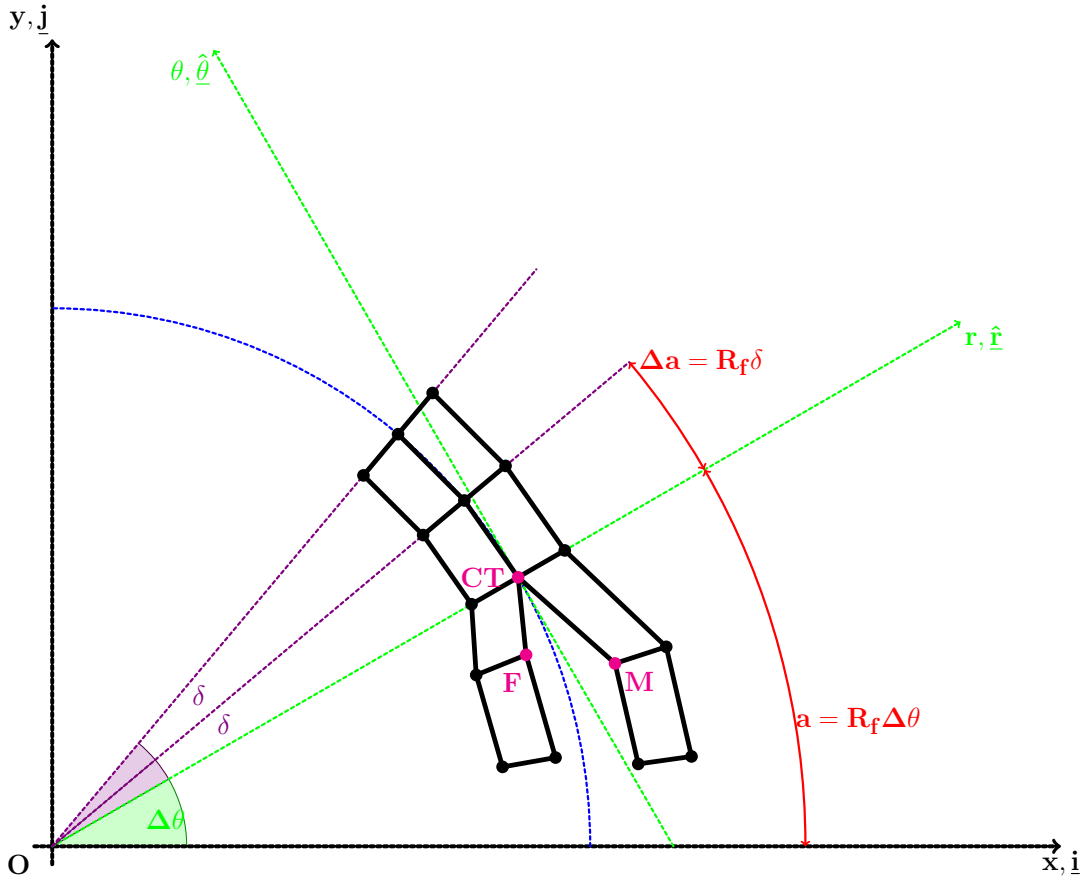

Figure 11: Schematic representation of the discretized crack tip geometry for 1^{st} order quadrilateral elements.

The crack opening displacement u_r and the crack shear displacement u_θ at the crack tip can thus be written as

$$u_r = \cos(\Delta\theta)\, u_x + \sin(\Delta\theta)\, u_y \qquad u_\theta = -\sin(\Delta\theta)\, u_x + \cos(\Delta\theta)\, u_y, \tag{A.42}$$

where u_x and u_y are defined as

$$u_x = u_{x,M} - u_{x,F} \qquad u_y = u_{y,M} - u_{y,F} \tag{A.43}$$

and $2\Delta\theta$ is total angular size of the debond. The corresponding forces at the crack tip are

$$F_r = \cos(\Delta\theta)\, F_{x,CT} + \sin(\Delta\theta)\, F_{y,CT} \qquad F_\theta = -\sin(\Delta\theta)\, F_{x,CT} + \cos(\Delta\theta)\, F_{y,CT}. \tag{A.44}$$

At the crack tip, the FE mesh possesses two coincident points, labeled FCT and MCT. Continuity of the displacements at the crack tip must be ensured. Furthermore, in order to measure the force at the crack tip, a fully-constraint dummy node needs to be created and formally linked to the two nodes at the crack tip by the conditions

$$\begin{cases} u_{x,FCT} - u_{x,MCT} - u_{x,DUMMY} = 0 \\ u_{y,FCT} - u_{y,MCT} - u_{y,DUMMY} = 0 \\ \\ u_{x,DUMMY} = 0 \\ u_{y,DUMMY} = 0 \end{cases}, \tag{A.45}$$

which can be simplified to

$$\begin{cases} u_{x,FCT} = u_{x,MCT} \\ u_{y,FCT} = u_{y,MCT} \\ \\ R_{x,DUMMY} = R_{x,FCT} = -R_{x,MCT} = F_{x,CT} \\ R_{y,DUMMY} = R_{y,FCT} = -R_{y,MCT} = F_{y,CT} \end{cases}. \tag{A.46}$$

Making use of Eq. A.41, four equations can be written in the four displacement $u_{x,FCT}$, $u_{x,MCT}$, $u_{y,FCT}$ and $u_{y,MCT}$:

$$
\begin{cases}
\left(k_{e,M|11}+k_{e,M|33}\right)u_{x,MCT}+\left(k_{e,M|12}+k_{e,M|34}\right)u_{y,MCT}+ \\
+k_{e,M|13}u_{x,M}+k_{e,M|14}u_{y,M}+\left(k_{M|17}+k_{M|35}\right)u_{N,MC|7}+\left(k_{M|18}+k_{M|36}\right)u_{N,MC|8}+ \\
+\sum_{i=5}^{6}k_{M|1i}u_{N,MC|i}+\sum_{i=7}^{8}k_{M|3i}u_{N,MB|i}+k_{M|31}u_{x,NCOI}+k_{M|32}u_{y,NCOI}=0 \\
\\
\left(k_{e,M|21}+k_{e,M|43}\right)u_{x,MCT}+\left(k_{e,M|22}+k_{e,M|44}\right)u_{y,MCT}+ \\
+k_{e,M|23}u_{x,M}+k_{e,M|24}u_{y,M}+\left(k_{M|27}+k_{M|45}\right)u_{N,MC|7}+\left(k_{M|28}+k_{M|46}\right)u_{N,MC|8}+ \\
+\sum_{i=5}^{6}k_{M|2i}u_{N,MC|i}+\sum_{i=7}^{8}k_{M|4i}u_{N,MB|i}+k_{M|41}u_{x,NCOI}+k_{M|42}u_{y,NCOI}=0 \\
\\
\left(k_{e,F|77}+k_{e,F|55}\right)u_{x,FCT}+\left(k_{e,F|78}+k_{e,F|56}\right)u_{y,FCT}+ \\
+k_{e,F|75}u_{x,F}+k_{e,F|76}u_{y,F}+\left(k_{F|71}+k_{F|53}\right)u_{N,FC|1}+\left(k_{F|72}+k_{F|54}\right)u_{N,FC|2}+ \\
+\sum_{i=2}^{3}k_{F|7i}u_{N,FC|i}+\sum_{i=1}^{2}k_{F|5i}u_{N,FB|i}+k_{F|57}u_{x,NCOI}+k_{F|58}u_{y,NCOI}=0 \\
\\
\left(k_{e,F|87}+k_{e,F|65}\right)u_{x,FCT}+\left(k_{e,F|88}+k_{e,F|66}\right)u_{y,FCT}+ \\
+k_{e,F|85}u_{x,F}+k_{e,F|86}u_{y,F}+\left(k_{F|81}+k_{F|63}\right)u_{N,FC|1}+\left(k_{F|82}+k_{F|64}\right)u_{N,FC|2}+ \\
+\sum_{i=2}^{3}k_{F|8i}u_{N,FC|i}+\sum_{i=1}^{2}k_{F|6i}u_{N,FB|i}+k_{F|67}u_{x,NCOI}+k_{F|68}u_{y,NCOI}=0
\end{cases}
\tag{A.47}
$$

Solving for $u_{y,FCT}$ and $u_{y,MCT}$ the third and fourth relations in Eq. A.47 and substituting in the first two expressions of Eq. A.47, we get

$$
\begin{cases}
\left(k_{e,M|11}+k_{e,M|33}+k_{e,F|77}+k_{e,F|55}\right)u_{x,MCT}+\left(k_{e,M|12}+k_{e,M|34}+k_{e,F|78}+k_{e,F|56}\right)u_{y,MCT}+ \\
+k_{e,M|13}u_{x,M}+k_{e,M|14}u_{y,M}+k_{e,F|75}u_{x,F}+k_{e,F|76}u_{y,F}+ \\
+\left(k_{M|31}+k_{F|57}\right)u_{x,NCOI}+\left(k_{M|32}+k_{F|58}\right)u_{y,NCOI}+ \\
+\left(k_{M|17}+k_{M|35}\right)u_{N,MC|7}+\left(k_{M|18}+k_{M|36}\right)u_{N,MC|8}+\left(k_{F|71}+k_{F|53}\right)u_{N,FC|1}+\left(k_{F|72}+k_{F|54}\right)u_{N,FC|2}+ \\
+\sum_{i=5}^{6}k_{M|1i}u_{N,MC|i}+\sum_{i=7}^{8}k_{M|3i}u_{N,MB|i}+\sum_{i=2}^{3}k_{F|7i}u_{N,FC|i}+\sum_{i=1}^{2}k_{F|5i}u_{N,FB|i}=0 \\
\\
\left(k_{e,M|21}+k_{e,M|43}+k_{e,F|87}+k_{e,F|65}\right)u_{x,MCT}+\left(k_{e,M|22}+k_{e,M|44}+k_{e,F|88}+k_{e,F|66}\right)u_{y,MCT}+ \\
+k_{e,M|23}u_{x,M}+k_{e,M|24}u_{y,M}+k_{e,F|85}u_{x,F}+k_{e,F|86}u_{y,F}+ \\
+\left(k_{M|41}+k_{F|67}\right)u_{x,NCOI}+\left(k_{M|42}+k_{F|68}\right)u_{y,NCOI}+ \\
+\left(k_{M|27}+k_{M|45}\right)u_{N,MC|7}+\left(k_{M|28}+k_{M|46}\right)u_{N,MC|8}+\left(k_{F|81}+k_{F|63}\right)u_{N,FC|1}+\left(k_{F|82}+k_{F|64}\right)u_{N,FC|2}+ \\
+\sum_{i=2}^{3}k_{F|8i}u_{N,FC|i}+\sum_{i=1}^{2}k_{F|6i}u_{N,FB|i}+\sum_{i=5}^{6}k_{M|2i}u_{N,MC|i}+\sum_{i=7}^{8}k_{M|4i}u_{N,MB|i}=0
\end{cases}
\tag{A.48}
$$

Solving the system of two equations and observing that $u_{x,F}, u_{y,F} \sim 0$ for a stiffer inclusion as a fiber in a polymeric composite, we can express $u_{x,MCT}$ as a function of u_x and u_y (see Eq. A.43) as

$$
\begin{aligned}
&\left[\left(k_{e,M|21}+k_{e,M|43}+k_{e,F|87}+k_{e,F|65}\right)+\frac{k_{e,M|11}+k_{e,M|33}+k_{e,F|77}+k_{e,F|55}}{k_{e,M|12}+k_{e,M|34}+k_{e,F|78}+k_{e,F|56}}\left(k_{e,M|22}+k_{e,M|44}+k_{e,F|88}+k_{e,F|66}\right)\right]u_{x,MCT}+\\
&+\left(k_{e,M|23}-\frac{k_{e,M|22}+k_{e,M|44}+k_{e,F|88}+k_{e,F|66}}{k_{e,M|12}+k_{e,M|34}+k_{e,F|78}+k_{e,F|56}}k_{e,M|13}\right)u_x+\\
&+\left(k_{e,M|24}-\frac{k_{e,M|22}+k_{e,M|44}+k_{e,F|88}+k_{e,F|66}}{k_{e,M|12}+k_{e,M|34}+k_{e,F|78}+k_{e,F|56}}k_{e,M|14}\right)u_y+\\
&+\left(k_{e,M|23}+k_{e,F|85}-\frac{k_{e,M|22}+k_{e,M|44}+k_{e,F|88}+k_{e,F|66}}{k_{e,M|12}+k_{e,M|34}+k_{e,F|78}+k_{e,F|56}}\left(k_{e,M|13}+k_{e,M|75}\right)\right)\cancelto{\approx 0}{u_{x,F}}+\\
&+\left(k_{e,M|24}+k_{e,F|86}-\frac{k_{e,M|22}+k_{e,M|44}+k_{e,F|88}+k_{e,F|66}}{k_{e,M|12}+k_{e,M|34}+k_{e,F|78}+k_{e,F|56}}\left(k_{e,M|14}+k_{e,M|76}\right)\right)\cancelto{\approx 0}{u_{y,F}}+\\
&+\left[\left(k_{M|41}+k_{F|67}\right)-\frac{k_{e,M|22}+k_{e,M|44}+k_{e,F|88}+k_{e,F|66}}{k_{e,M|12}+k_{e,M|34}+k_{e,F|78}+k_{e,F|56}}\left(k_{M|31}+k_{F|57}\right)\right]u_{x,NCOI}+\\
&+\left[\left(k_{M|42}+k_{F|68}\right)-\frac{k_{e,M|22}+k_{e,M|44}+k_{e,F|88}+k_{e,F|66}}{k_{e,M|12}+k_{e,M|34}+k_{e,F|78}+k_{e,F|56}}\left(k_{M|32}+k_{F|58}\right)\right]u_{y,NCOI}+\\
&+\left(k_{M|27}+k_{M|45}\right)u_{N,MC|7}+\left(k_{M|28}+k_{M|46}\right)u_{N,MC|8}+\left(k_{F|81}+k_{F|63}\right)u_{N,FC|1}+\left(k_{F|82}+k_{F|64}\right)u_{N,FC|2}+\\
&-\frac{k_{e,M|22}+k_{e,M|44}+k_{e,F|88}+k_{e,F|66}}{k_{e,M|12}+k_{e,M|34}+k_{e,F|78}+k_{e,F|56}}\left[\left(k_{M|17}+k_{M|35}\right)u_{N,MC|7}+\left(k_{M|18}+k_{M|36}\right)u_{N,MC|8}\right]+\\
&-\frac{k_{e,M|22}+k_{e,M|44}+k_{e,F|88}+k_{e,F|66}}{k_{e,M|12}+k_{e,M|34}+k_{e,F|78}+k_{e,F|56}}\left[\left(k_{F|71}+k_{F|53}\right)u_{N,FC|1}+\left(k_{F|72}+k_{F|54}\right)u_{N,FC|2}\right]\\
&+\sum_{i=2}^{3}k_{F|8i}u_{N,FC|i}+\sum_{i=1}^{2}k_{F|6i}u_{N,FB|i}+\sum_{i=5}^{6}k_{M|2i}u_{N,MC|i}+\sum_{i=7}^{8}k_{M|4i}u_{N,MB|i}+\\
&-\frac{\sum_{i=5}^{6}k_{M|1i}u_{N,MC|i}+\sum_{i=7}^{8}k_{M|3i}u_{N,MB|i}+\sum_{i=2}^{3}k_{F|7i}u_{N,FC|i}+\sum_{i=1}^{2}k_{F|5i}u_{N,FB|i}}{k_{e,M|12}+k_{e,M|34}+k_{e,F|78}+k_{e,F|56}}=0,
\end{aligned}
\tag{A.49}
$$

while the reaction forces at the crack tip can be expressed as

$$
\begin{cases}
F_{x,CT} & = R_{x,FCT} = \\
& = \left(k_{e,F|77}+k_{e,F|55}\right)u_{x,FCT}+\left(k_{e,F|78}+k_{e,F|56}\right)u_{y,FCT}+\\
& +k_{e,F|75}\cancelto{\approx 0}{u_{x,F}}+k_{e,F|76}\cancelto{\approx 0}{u_{y,F}}+\\
& +\sum_{i=1}^{4}k_{e,F|7i}u_{N,FC|i}+\sum_{i=1,i\neq(5,6)}^{8}k_{e,F|5i}u_{N,FB|i}\\
F_{y,CT} & = R_{y,FCT} = \\
& = \left(k_{e,F|87}+k_{e,F|65}\right)u_{x,FCT}+\left(k_{e,F|88}+k_{e,F|66}\right)u_{y,FCT}+\\
& +k_{e,F|85}\cancelto{\approx 0}{u_{x,F}}+k_{e,F|86}\cancelto{\approx 0}{u_{y,F}}+\\
& +\sum_{i=1}^{4}k_{e,F|8i}u_{N,FC|i}+\sum_{i=1,i\neq(5,6)}^{8}k_{e,F|6i}u_{N,FB|i}
\end{cases}
.
\tag{A.50}
$$

Substituting Eq. A.47 in Eq. A.48, Eq. A.49 and Eq. A.50 and solving, we obtain an expression of the form

$$\begin{cases} F_{x,CT} & = K_{xx}u_x + K_{xy}u_y + \\ & + \sum_{i=1}^{4} K_{FC,x|i}u_{N,FC|i} + \sum_{i=1,i\neq(3,4,5,6)}^{8} K_{FB,x|i}u_{N,FB|i} + \\ & + \sum_{i=5}^{8} K_{FC,x|i}u_{N,MC|i} + \sum_{i=7}^{8} K_{MB,x|i}u_{N,FB|i} \\ F_{y,CT} & = K_{yx}u_x + K_{yy}u_y + \\ & + \sum_{i=1}^{4} K_{FC,y|i}u_{N,FC|i} + \sum_{i=1,i\neq(3,4,5,6)}^{8} K_{FB,y|i}u_{N,FB|i} + \\ & + \sum_{i=5}^{8} K_{FC,y|i}u_{N,MC|i} + \sum_{i=7}^{8} K_{MB,y|i}u_{N,FB|i} \end{cases}, \tag{A.51}$$

which can be reformulated synthetically as

$$\begin{cases} F_{x,CT} & = K_{xx}u_x + K_{xy}u_y + \widetilde{F}_x \\ F_{y,CT} & = K_{yx}u_x + K_{yy}u_y + \widetilde{F}_y \end{cases}, \tag{A.52}$$

where $\widetilde{F}_x$ and $\widetilde{F}_y$ represent the influence of the FE solution through the nodes of the elements sharing the crack tip that do not belong to any of the phase interfaces, i.e. the nodes of the elements sharing the crack tip that belong to the bulk of each phase.

B Expression of the VCCT weights matrix for quadrilateral elements with or without singularity

The expression of $\underline{\underline{T}}_{pq}$ for quadrilateral elements with or without singularity is

$$
\begin{aligned}
\underline{\underline{T}}_{pq} &= \begin{cases} \underline{\underline{I}} \; for \; p = q < 2 \\ \underline{\underline{0}} \; otherwise \end{cases} && \text{for } 1^{st} \text{ order quadrilateral elements} \\
&= \begin{cases} \underline{\underline{I}} \; for \; p = q < 3 \\ \underline{\underline{0}} \; otherwise \end{cases} && \text{for } 2^{nd} \text{ order quadrilateral elements} \\
&= \begin{cases} \underline{\underline{I}} \; for \; p = q < 4 \\ \underline{\underline{0}} \; otherwise \end{cases} && \text{for } 3^{rd} \text{ order quadrilateral elements} \\
&= \begin{cases} \left(14 - \frac{33\pi}{8}\right) \underline{\underline{I}} \; for \; p = 1, q = 1 \\ \left(-52 + \frac{33\pi}{2}\right) \underline{\underline{I}} \; for \; p = 1, q = 2 \\ \left(17 - \frac{21\pi}{4}\right) \underline{\underline{I}} \; for \; p = 2, q = 1 \\ \left(-\frac{7}{2} + \frac{21\pi}{16}\right) \underline{\underline{I}} \; for \; p = 2, q = 2 \\ \left(8 - \frac{21\pi}{8}\right) \underline{\underline{I}} \; for \; p = 1, q = 3 \\ \left(-32 + \frac{21\pi}{2}\right) \underline{\underline{I}} \; for \; p = 2, q = 3 \\ \underline{\underline{0}} \; otherwise \end{cases} && \text{for } 2^{nd} \text{ order quarter-point quadrilateral elements} \\
&= \begin{cases} \left(-11187 + \frac{7155\pi}{2}\right) \underline{\underline{I}} \; for \; p = 1, q = 1 \\ \left(38556 - \frac{24543\pi}{2}\right) \underline{\underline{I}} \; for \; p = 1, q = 2 \\ \left(-53055 + \frac{33777\pi}{2}\right) \underline{\underline{I}} \; for \; p = 1, q = 3 \\ \left(\frac{11396}{3} - \frac{9575\pi}{8}\right) \underline{\underline{I}} \; for \; p = 2, q = 1 \\ \left(-12936 + \frac{33003\pi}{8}\right) \underline{\underline{I}} \; for \; p = 2, q = 2 \\ \left(17988 - \frac{45837\pi}{8}\right) \underline{\underline{I}} \; for \; p = 2, q = 3 \\ \left(-\frac{8453}{3} + \frac{3595\pi}{4}\right) \underline{\underline{I}} \; for \; p = 3, q = 1 \\ \left(9804 - \frac{12411\pi}{4}\right) \underline{\underline{I}} \; for \; p = 3, q = 2 \\ \left(-13587 + \frac{17289\pi}{4}\right) \underline{\underline{I}} \; for \; p = 3, q = 3 \\ \left(6948 - \frac{17685\pi}{8}\right) \underline{\underline{I}} \; for \; p = 1, q = 4 \\ \left(-23976 + \frac{60993\pi}{8}\right) \underline{\underline{I}} \; for \; p = 2, q = 4 \\ \left(33372 - \frac{84807\pi}{8}\right) \underline{\underline{I}} \; for \; p = 3, q = 4 \\ \underline{\underline{0}} \; otherwise \end{cases} && \text{for } 3^{rd} \text{ order quarter-point quadrilateral elements}
\end{aligned}
\tag{B.53}
$$

where $\underline{\underline{I}}$ is the identity matrix.

Paper B

Energy release rate of the fiber/matrix interface crack in UD composites under transverse loading: effect of the fiber volume fraction and of the distance to the free surface and to non-adjacent debonds

Authors:
Luca Di Stasio, Janis Varna and Zoubir Ayadi

Reformatted version of paper originally published in:
Theoretical and Applied Fracture Mechanics, Volume 103, October 2019, 102251.

© 2019, The Publisher, Reprinted with permission.

Energy release rate of the fiber/matrix interface crack in UD composites under transverse loading: effect of the fiber volume fraction and of the distance to the free surface and to non-adjacent debonds

Luca Di Stasio[1,2], Janis Varna[2] and Zoubir Ayadi[1]

[1]Université de Lorraine, EEIGM, IJL, 6 Rue Bastien Lepage, F-54010 Nancy, France
[2]Luleå University of Technology, University Campus, SE-97187 Luleå, Sweden

*Corresponding author: luca.di.stasio@ltu.se

Abstract

The effects of crack shielding, finite thickness of the composite and fiber content on fiber/matrix debond growth in thin unidirectional composites are investigated analyzing Representative Volume Elements (RVEs) of different ordered microstructures. Debond growth is characterized by estimation of the Energy Release Rates (ERRs) in Mode I and Mode II using the Virtual Crack Closure Technique (VCCT) and the J-integral. It is found that increasing fiber content, a larger distance between debonds in the loading direction and the presence of a free surface close to the debond have all a strong enhancing effect on the ERR. The presence of fully bonded fibers in the composite thickness direction has instead a constraining effect, and it is shown to be very localized. An explanation of these observations is proposed based on mechanical considerations.

Keywords: Polymer-matrix Composites (PMCs), Thin-ply, Energy Release Rate, Debonding, Finite Element Analysis (FEA)

A Introduction

Stimulated by the ever more stringent requirements in terms of weight and mechanical performances of the aerospace industry, in recent years the composite community has returned its attention to the mechanisms of intralaminar crack initiation with a focus on thin-ply laminates. Alternative design approaches are now considered based on this non-conventional laminate in applications ranging from cryogenic pressure vessels [1], to airplanes' wings [2], and even reusable space launchers [3].
Thin-ply laminates are the result of a technological innovation, the *spread tow technology*, which consists in opening or spreading the tows, in which fibers (carbon, glass, aramid,

basalt among others) are usually shipped in, into very thin tapes used for laminate production. Ply thicknesses of less than 50 μm can nowadays be mass-produced, and record thicknesses of around $20-25$ μm, or $\sim 4-5$ times the average fiber's diameter, have been achieved. In its current form the technique, sometimes referred to as "FUKUI method", was firstly proposed towards the end of the 1990s [4] and perfected in the subsequent decade [5, 6].

Several experimental investigations on *thin ply* laminates have highlighted their main properties [7, 8, 9, 10, 11, 12, 13]: increased fiber content; more uniform packing of fibers; delay and even suppression of intralaminar cracking (called also transverse-, matrix- or micro-cracking) and delamination. A very insightful work documenting how these phenomena are affected by the morphology of *thin-ply* laminates is the microscopic study of Saito & al. [14], which focuses on the effect of ply thickness on the onset and propagation of intralaminar cracking. In their investigation, tensile tests were performed on carbon fiber/epoxy $[0_2, 90_n, 0_2]$ *thin-ply* laminates for $n = 1, 2, 4$ and the crack density was measured with a digital microscope at several levels of applied tensile strain in the range between 0% and 1.5%. Furthermore, they performed microscopic observations on the specimen's edge at each level of strain. They observed the onset of fiber/matrix interface cracks (referred to as debonds in the following) at lower levels of strain in thinner plies, while at the same time coalescence of debonds and through-the-thickness propagation of transverse cracks in thin plies were delayed and even suppressed as ply thickness decreased. In particular, they reported the first onset of debonds at 0.4% for $n = 1, 2$ and 0.7% for $n = 4$. For $n = 1$, however, at $\varepsilon = 1.5\%$ coalescence of debonds had started to take place but the crack had not completely propagated through the thickness, while for $n = 2$ and $n = 4$ the latter alreay happened at a value of strain respectively of 1.3% and 1%. Our inability to explain these observations with the currently accumulated knowledge demonstrates the necessity of further investigation of interactions between debonds and studies of the constraining (or accelerating) effect of presence of bonded fibers, free and constrained boundaries in the vicinity of a partially debonded fiber.

Early studies on the effect of ply thickness on the onset and propagation of transverse cracks were conducted on glass fiber/epoxy cross-ply laminates by Bailey, Parvizi and collaborators [15, 16, 17], who firstly observed the beneficial effect of thickness reduction on the delay of transverse cracking. They furthermore pointed the attention to the appearance of debonds at the fiber/matrix interface and their subsequent coalescence as the mechanism at the origin of transverse cracks [18]. Moreover, they identified the main mechanical driver of the damage process in the mismatch of elastic properties, and particularly of Poisson's ratios, between fibers and matrix [19]. A full understanding of damage onset and propagation in *thin-ply* laminates thus requires comprehension of the mechanisms governing its very first stage, i.e. the fiber/matrix interface crack. First results were obtained through analytical models in the case of a single fiber with an arc crack (debond) in an infinite matrix under transverse tension by England [20] and Perlman & Sih [21], who obtained the stresses at the interface and calculated the stress intensity factors at the crack tip, and by Toya [22], who evaluated the Energy Release Rate (ERR). Drawing upon the results for the straight bi-material interface crack by

Comninou [23], the effect of crack face contact in fiber-matrix debonding was investigated in [24, 25]. In [26], it was showed in terms of ERR why the case of a single asymmetric debond is more likely to be observed under remote transverse tension than two symmetric debonds on the same fiber. The effect of different types and combinations of loads on debonding have been studied for the single fiber model: compression [27], residual thermal stresses [28], and biaxial configurations with different combinations of tension and compression [29, 30]. The effect of the presence of nearby bonded fibers on the debonding of a fiber embedded in an infinite matrix has been studied under uniaxial transverse tension [31], biaxial tension [32] and uniaxial transverse compression [33]. The effect of inter-fiber distance on debond growth has been studied for a partially debonded fiber at the center of a hexagonal cluster inside a homogenized UD composite in the case of fully bonded neighbouring fibers [34] and of two partially debonded fibers out of the surrounding six [35]. An understanding of crack shielding and finite ply thickness effects on debond growth in non-homogenized microstructural models of UDs seems thus to be lacking: this is the problem that we want to address in the present work. Mode I and Mode II energy release rates will be analyzed using stress fields calculated with the FEM for a variety of Repeating Unit Cell (RUC) of the composite with square packing of fibers under transverse tensile loading. The choice of a square packing configuration for the fibers is motivated by its simplicity, as it allows to easily separate the effect of fibers (fully bonded and/or partially debonded) placed along the loading direction from that of fibers placed in the through-the-ply-thickness direction. These RUCs represent composites with different distances between partially debonded fibers and a varying number of bonded fibers between them, which allows to study the effect of crack shielding on the ERR. In the ply thickness direction, the varying number of perfectly bonded fiber rows exposes the effect of the proximity of the free boundary of the composite on debond growth. Finally, using coupling of thickness direction displacements on horizontal boundaries of the RUC, the accelerating effect of the interaction between debonds of fibers located on the same vertical line is studied.

B RVE models & FE discretization

B.1 Introduction & Nomenclature

In this paper, we analyze debond development in unidirectional (UD) composites subjected to in-plane transverse tensile loading. The interaction between debonds in UD composites is studied developing models of different Repeating Unit Cells (RUC) of laminates (see Fig. 1 to Fig. 3) where only the central fiber in the cell has a damage in the form of a fiber/matrix interface crack (debond). The composite RUC may be repeating in the in-plane transverse direction only (representing an ultra-thin composite) or repeating also in the composite thickness direction, representing an infinite composite in a limiting case. Thus, the conditions at the UD composite's upper and lower boundaries are one of the parameters for the investigation. The used RUCs allow for considering the composite with debonds as a sequence of stacked damaged and undamaged fiber rows, each

row with only one fiber in the thickness direction. Since all of these RUCs feature regular microstructures with fibers placed according to a square-packing configuration, they are Representative Volume Elements (RVE) of composites with a certain distribution of debonds. Introducing in-plane coordinates x and y, where x is in the transverse direction of the UD composite under consideration, the strain in the y-direction due to a load in the x-direction is small, caused in turn by the very small minor Poisson's ratio of the UD composite. Additionally, debonds are considered to be significantly longer in the fiber direction than in the arc direction. Therefore, we use 2D models under the assumption of plane strain, defined in the $x - z$ section of the composite. Thus, the analysis presented applies to long debonds, with a focus on understanding the mechanisms of growth along their arc direction. The composites are subjected to transverse tensile strain, applied as a constant displacement in the x-direction along the vertical boundary of the RUC as shown in Figures 1 to 4. As the models are differentiated by the number of rows of fibers and by the spacing between debonds along the vertical and horizontal directions, the corresponding RUCs can be distinguished from each other based on the number n of fibers in the horizontal direction and k in the vertical direction. Furthermore, the horizontal surfaces can be either free or vertical displacement coupling can be applied. We thus introduce a common notation $n \times k - free$ and $n \times k - coupling$ to denote a RUC with $n \times k$ fibers and, respectively, a free upper surface or with kinematic coupling applied to it. The specific combinations of particular choices of n, k, and boundary conditions are detailed in Section B.2, together with the description of the corresponding models of damaged composite they are representing.

B.2 Models of Representative Volume Element (RVE)

The first two models feature, as shown in Fig. 1, an ultra-thin UD laminate with only one row of fibers across its thickness, $k = 1$. This is quite an extreme model from the microstructural point of view; however, it allows to focus the analysis on the interaction between debonded fibers placed along the x-direction. Furthermore, as the horizontal surfaces are considered free, the interaction is stronger in this case than in any other, making the trends very clear and the predictions of this model rather conservative. In retrospective, if only 20 years ago such a model would have been considered too abstracted from the physical reality, the recent advancements in the spread tow technology make this approach appealing also as a limiting case for practical considerations.

In the sub-model of Fig. 1a, every n^{th} fiber in the composite is partially debonded on alternating sides of the fiber. The symmetries of the model allow the use of the upper part of the RUC, as highlighted in Fig. 1 to 3. Following the notation introduced in Section B.1, we will refer to this model as $n \times 1 - free$. In the sub-model $n = 1$, Fig. 1b, a debond appears on each fiber on alternating sides and the corresponding RUC contains only one fiber. We will refer to this model as $1 \times 1 - free$.

The second set of models in Fig. 2 and Fig. 3 considers laminates with multiple rows of fibers across the thickness: a finite number of rows in the first two sub-models in Fig. 2; an infinite number in the model of Fig. 3. In Fig. 2a, the RUC contains $n = 1$ fiber

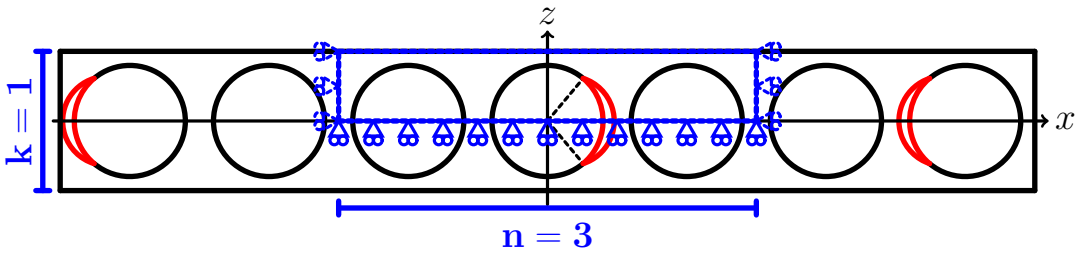

(a) Single row of fibers with a debond appearing every n fibers: model $n \times 1 - free$ ($n = 3$ in the figure).

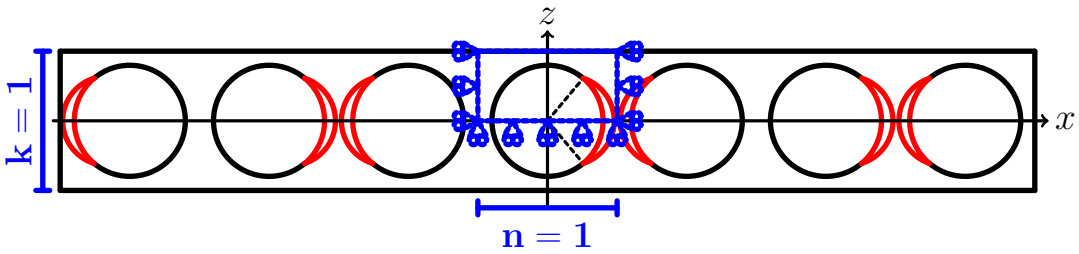

(b) Single row of fibers with debonds appearing on each fiber: model $1 \times 1 - free$.

Figure 1: Models of ultra-thin UD composites with a single "row" of fibers and debonds repeating at different distances.

in the x-direction, k fibers across the thickness and the central fiber is debonded. This model will be referred to in the following as $1 \times k - free$. Thinking in terms of rows, in this model we have a central row where each fiber is debonded. This row is surrounded from each side by $^{(k-1)}/_{2}$ rows with perfectly bonded fibers. In the sub-model in Fig. 2b, each n^{th} fiber in the central row is debonded and this row is surrounded by $^{(k-1)}/_{2}$ rows of undamaged fibers from each side. We will refer to this model as $n \times k - free$ (because the horizontal boundary of the RUC is free of any constraint).

Finally, the model in Fig. 3 represents an UD composite with an infinite number of rows; all of them with partially debonded fibers. As all fibers have debonds, the corresponding RUC is made of a single partially debonded fiber with kinematic coupling conditions applied to the upper boundary to assure periodicity. This model is referred to as $1 \times 1 - coupling$.

B.3 Finite Element (FE) discretization

Each RUC is discretized using the Finite Element Method (FEM) within the Abaqus environment, a commercial FEM package [36]. The length l and height h of the model are determined by the number of fibers n in the horizontal direction and k across the thickness (see B.2) according to Eq. B.1:

$$l = 2nL \qquad h = kL; \tag{B.1}$$

where $2L$ is the length of a one-fiber unit, see Fig. 4, defined as a function of the fiber

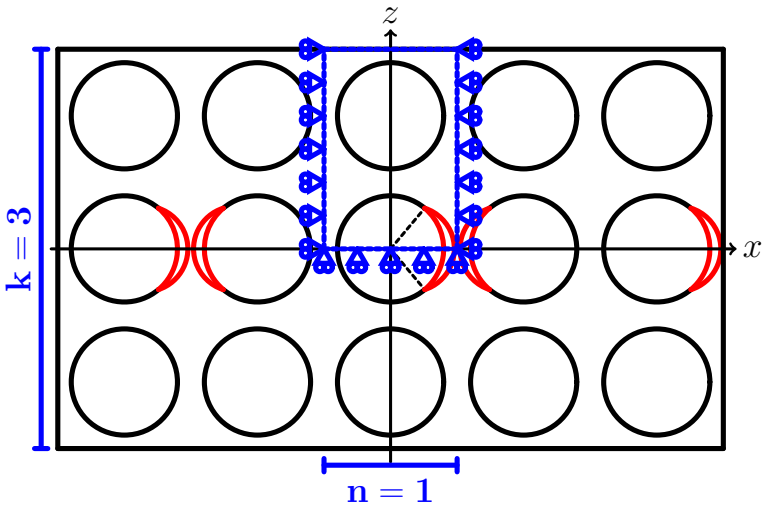

(a) Multiple rows of fibers with debonds appearing on each fiber beloging to the central row: model $1 \times k - free$ ($k = 3$ in the figure).

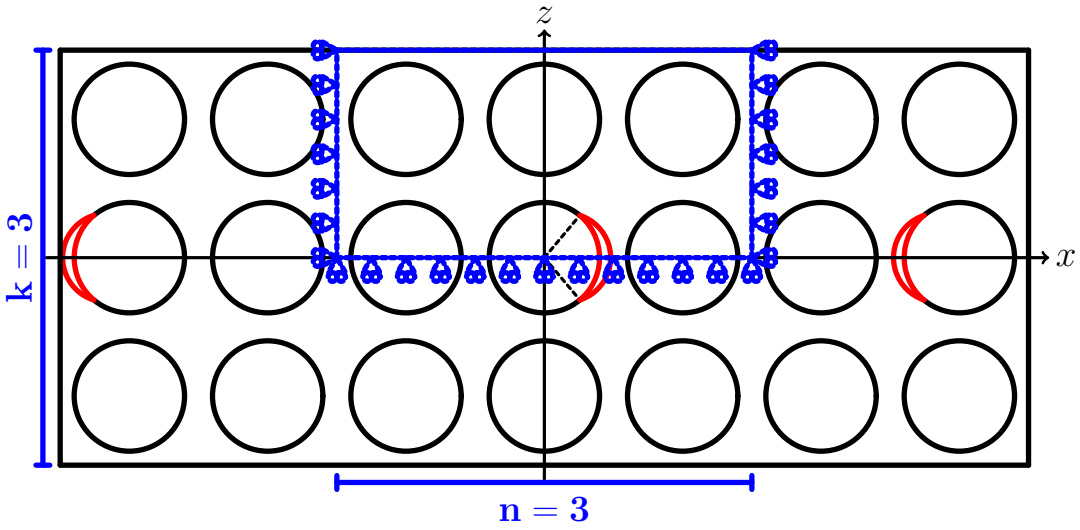

(b) Mutiple rows of fibers with a debond appearing every n fibers within the central row: model $n \times k - free$ ($n = 3$ and $k = 3$ in the figure).

Figure 2: Models of UD composites with different "rows" of fibers and debonds repeating at different distances.

volume fraction V_f and the fiber radius according to

$$L = \frac{R_f}{2}\sqrt{\frac{\pi}{V_f}}. \tag{B.2}$$

The fiber radius R_f is assumed to be the same for each fiber in the model and equal to 1 μm. The latter value is not physical and it has been chosen for simplicity. It is worth to note at this point that, in a linear elastic solution as the one presented here, the ERR is proportional to the geometrical dimensions and recalculation of the ERR for

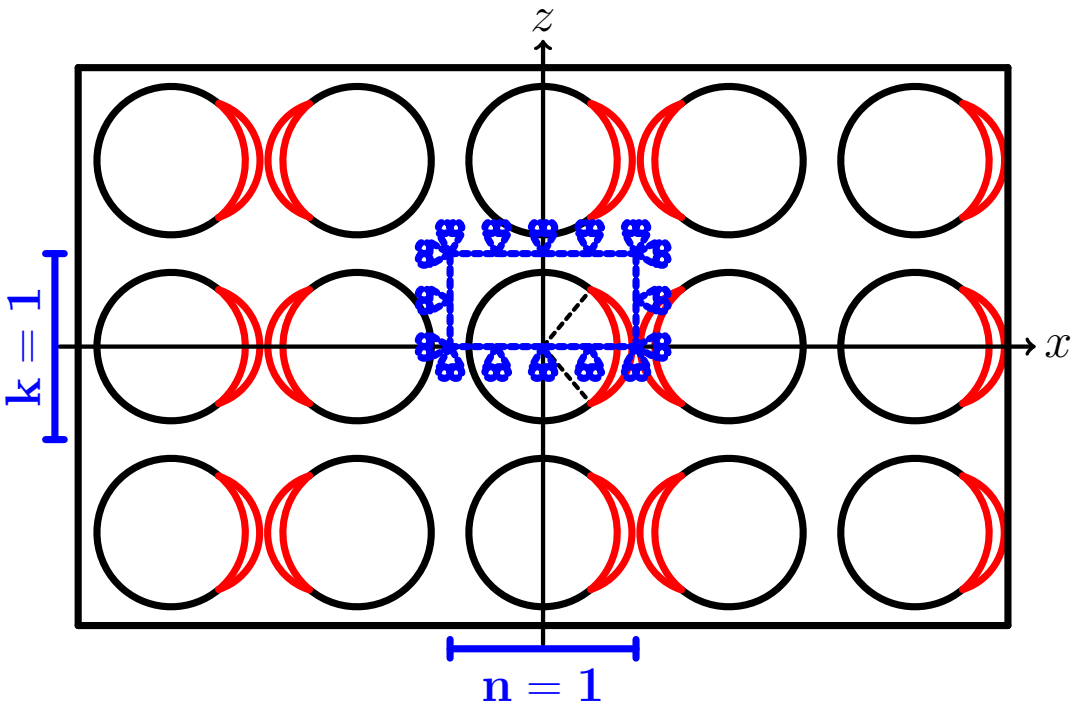

Figure 3: Model of UD composites with an infinite number of "rows" of fibers and debonds appearing on each fiber: model $1 \times 1 -$ *coupling .*

fibers of any size, thus, requires a simple multiplication. Furthermore, notice that the relationships in Eqs. B.1 and B.2 ensure that the local and global V_f are everywhere equal.

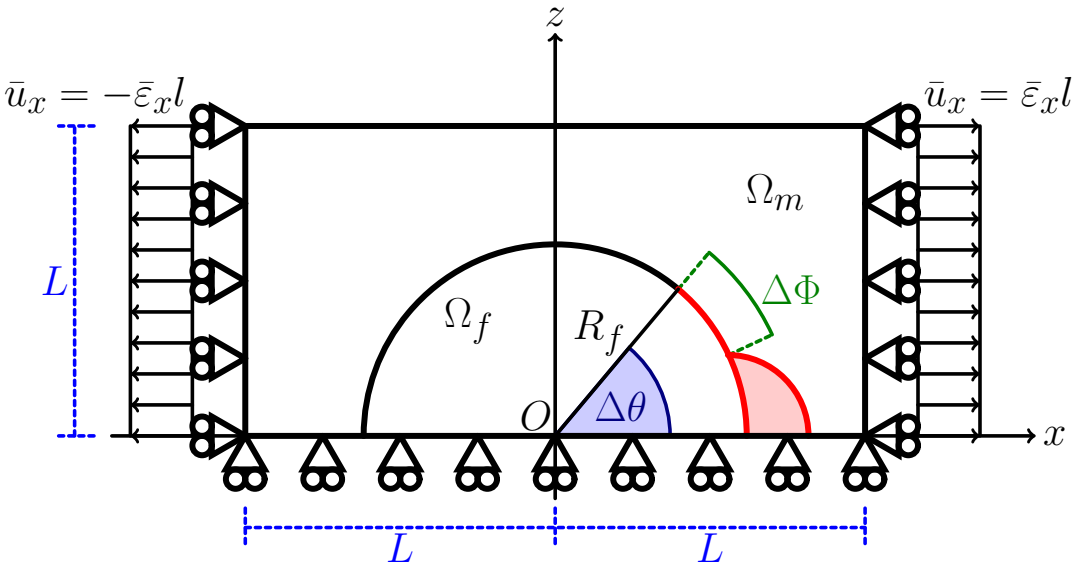

Figure 4: Schematic of the model with its main parameters.

The debond is placed symmetrically with respect to the x axis (see Fig. 4) and we characterize it with an angular size of $\Delta\theta$ (the full debond size is thus $2\Delta\theta$). For large debond sizes ($\geq 60° - 80°$), a region of variable size $\Delta\Phi$ appears at the crack tip in which the crack faces are in contact and slide on each other. Due to its appearance, frictionless contact is considered between the two crack faces to allow free sliding and avoid interpenetration. The presence of friction at the interface is considered in [37], where the authors model the contact interaction between crack faces using Coulomb's friction with a coefficient $\mu = 0.25$ and show that, for a debond with $\Delta\theta = 80°$, the crack sliding displacement is always different from zero in every point of the crack and only slightly lower than that of the frictionless case. This in turn means that the estimation of G_{II} in the case of frictionless contact provide an upper bound and thus the results presented here represent a conservative estimation (a higher ERR corresponds to higher likelihood of crack propagation). Symmetry with respect to the x axis is applied on the lower boundary. The upper boundary is in general free, except for the model $1 \times 1 - coupling$ (Fig. 3) which requires kinematic coupling of vertical displacements also on the upper side. Kinematic coupling on the x-displacement is applied along the left and right sides of the model in the form of a constant x-displacement $\pm\bar{\varepsilon}_x l$, corresponding to transverse strain $\bar{\varepsilon}_x$ equal to 1%.

Table 1: Summary of the mechanical properties of fiber and matrix. E stands for Young's modulus, μ for shear modulus and ν for Poisson's ratio.

Material	$E\,[GPa]$	$\mu\,[GPa]$	$\nu\,[-]$
Glass fiber	70.0	29.2	0.2
Epoxy	3.5	1.25	0.4

The model is meshed using second order, 2D, plane strain triangular (CPE6) and rectangular (CPE8) elements, which have respectively 6 and 8 nodes per element. Each node has 2 degrees of freedom, i.e. the horizontal displacement u_x and the vertical displacement u_z. A regular mesh of quadrilateral elements with an almost unitary aspect ratio is required at the crack tip. The angular size δ of an element in the crack tip region is always equal to 0.05°. The overall number of elements needed to discretize the model depends on the debond size $\Delta\theta$ (larger debonds have larger contact zones which require more elements for their correct resolution), the fiber volume fraction (which determines the size of the RVE) and the number of fully bonded fibers present in the model. As an example, the discretization of the $1 \times 1 - free$ model at $V_f = 60\%$ requires a total of 132507 elements for $\Delta\theta = 10°$ and of 296606 elements for $\Delta\theta = 140°$, which corresponds to a minimum required RAM respectively of 445 MB and 1014 MB and to a minimum RAM needed to minimize I/O operations respectively of 1.63 GB and 3.87 GB. To put it into perspective, the wallclock time required for their solution is respectively 1.3 $[min]$ and 14.95 $[min]$ on a laptop with a 2.5 GHz Intel Core i5 processor and 6 GB of installed

RAM. The crack faces are modeled as element-based surfaces and a small-sliding contact pair interaction with no friction is established between them. The Mode I, Mode II and total Energy Release Rates (ERRs) (respectively referred to as G_I, G_{II} and G_{TOT}) represent the main output of the FEM analysis; they are evaluated using the VCCT [38] implemented in a custom Python routine and, for the total ERR, the J-integral [39] is obtained by application of the Abaqus built-in functionality. A glass fiber-epoxy system is considered throughout this paper, and it is assumed that their response lies always in the linear elastic domain. The latter assumption lies on the work of Asp and co-workers, who show that epoxy subjected to a tri-axial stress state as the one observable in the inter-fibers region fails at very low strains ($\sim 0.5\% - 0.8\%$) [40] and in a brittle manner [41], and that the magnitude of deviatoric stresses (evaluated in terms of equivalent Von Mises stress) in the fiber/matrix interface neighborhood does not justify the occurrence of plastic deformations in the case of debond propagation [41]. The properties used are listed in Table 1.

B.4 Validation of the model

The model is validated in Fig. 5 against the results reported in [42, 31], obtained with the Boundary Element Method (BEM) for a single fiber with a symmetric debond placed in an infinite matrix. This situation is modeled using the $1 \times 1 - free$ RVE with $V_f = 0.0079\%$, which corresponds to a RUC's length and height of respectively $\sim 200R_f$ and $\sim 100R_f$.

To allow for a comparison, the results are normalized following [31] with respect to a reference Energy Release Rate G_0 defined as

$$G_0 = \frac{1 + k_m}{8\mu_m}\sigma_0^2 \pi R_f \tag{B.3}$$

where μ is the shear modulus, k is the Kolosov's constant defined as $3 - 4\nu$ for plane strain conditions, R_f is the fiber radius and the index m refers to the properties of the matrix. σ_0 is the stress at the boundary, computed as the average of the stress extracted at each boundary node along the right side (arithmetic average as nodes are equispaced by design along both the left and right sides). The agreement is good: the difference between the BEM solution, which is considered more accurate, and the FEM solution does not exceed 5%. The ERRs' maxima are in the same positions and the size of the contact zone is the same. Nevertheless, an analysis of phenomena leading to less than 5% differences in ERR would not be reliable and, therefore, it is not recommended.

C Results & Discussion

C.1 Effect of Fiber Volume Fraction

As shown in Figs. 6 and 7, respectively for Mode I and Mode II, the fiber content has a drastic effect on the Energy Release Rate at the tip of the fiber/matrix interface crack. The effect of four levels of fiber volume fraction are compared, 30%, 50%, 60% and 65%,

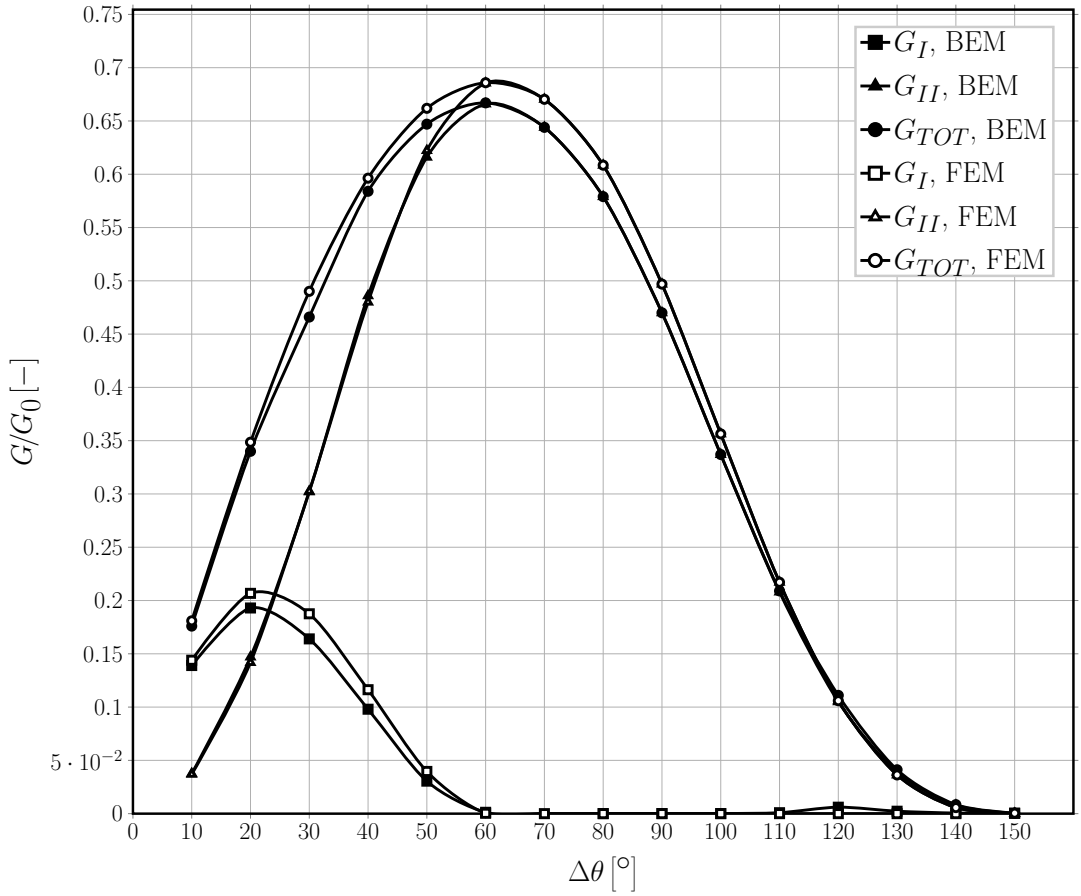

Figure 5: Validation of the single fiber model for the infinite matrix case with respect to the BEM solution in [31].

on two microstructural models: a $11 \times 11 - free$ (every 11^{th} fiber in the central fiber row is partially debonded and, on the top of this row, we have 5 undamaged fiber rows), Figs. 6a and 7a, and a $21 \times 21 - free$ (every 21^{th} fiber in the central fiber row is partially debonded and, on the top of this row, we have 10 undamaged fiber rows), Figs. 6b and 7b.

Comparing Fig. 6a with 6b, and Fig. 7a with 7b, we can observe that the ERRs' values are very similar for RUCs with 11×11 and 21×21 fibers, though they are slightly higher for the larger RUC where the next debonded fiber and the free surface are further away from the debonded fiber. From these results we conclude that both RUCs are large enough to represent a single debonded fiber in an infinite array of bonded fibers. Obviously, there exists a specific effect of the fiber content. For Mode I, Fig. 6, the maximum value of the ERR increases by ~ 5.2 times when V_f changes from 30% to 65%. The debond's angular size for which the peak value occurs remains unchanged at 20°, but for $V_f = 60\%$ and 65% the values of Mode I ERR are rather similar when measured at 10° and at 20°, approximately creating a plateau. Furthermore, increasing the fiber volume fraction delays the onset of the contact zone, which corresponds in Fig. 6 to the first value of $\Delta\theta$ for which G_I is equal to zero. For $V_f = 30\%$, the contact zone first

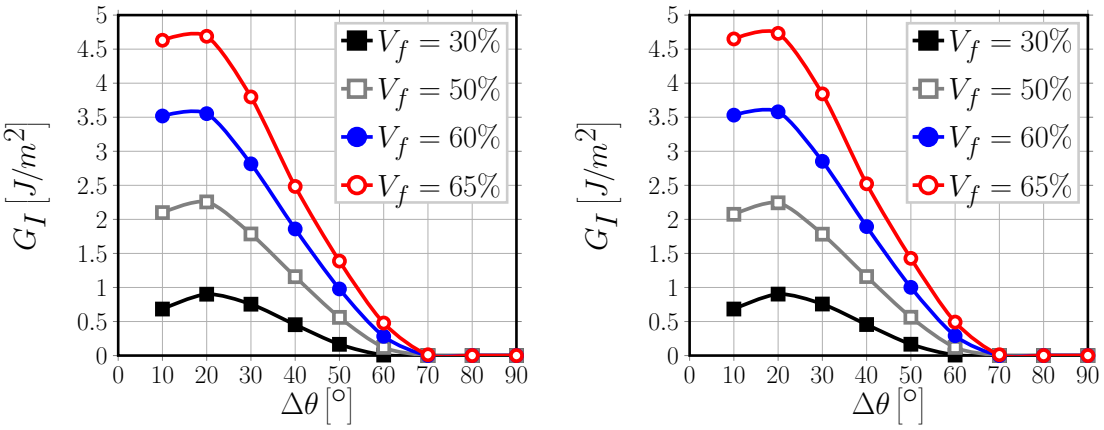

(a) Model $11 \times 11 - free$. (b) Model $21 \times 21 - free$.

Figure 6: A view of the effect of fiber volume fraction on Mode I ERR in two exemplificative models, subject to an applied transverse strain ε_x of 1%.

appears for a debond of 60°, similarly to what happens in the single fiber in infinite matrix model (Fig. 5). For higher fiber contents, the contact zone's onset is delayed to a debond's size approximately equal to 70°.

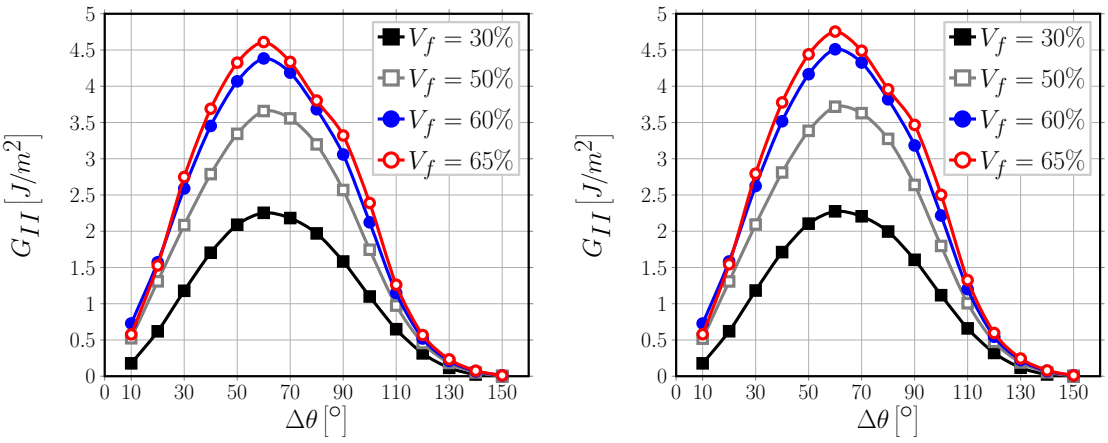

(a) Model $11 \times 11 - free$. (b) Model $21 \times 21 - free$.

Figure 7: A view of the effect of fiber volume fraction on Mode II ERR in two exemplificative models, subject to an applied transverse strain ε_x of 1%.

For Mode II, Fig. 7, there is a distinct maximum in the curve and its shape does not depend on the fiber content. The maximum value of the ERR increases by ~ 2.1 times when V_f changes from 30% to 65%. The effect is thus similar to Mode I, but with a significantly lower magnitude. Similar to Mode I, the debond size for which the peak value of Mode II occurs remains unchanged, at 60°. It is worthwhile to notice that the

ratio of Mode II to Mode I peak values is $\frac{max(G_{II})}{max(G_I)} \sim \frac{2.2}{0.9} \sim 2.4$ for $V_f = 30\%$, while it is $\sim \frac{4.7}{4.7} \sim 1$ for $V_f = 65\%$.

The general increasing trends observed in Figs. 6 and 7 are related to the fact that, given that the global and local V_f are everywhere identical in the models presented, an increase in fiber content corresponds to a decrease in the average distance between fibers. Thus, the distances for the decay of the local stress and strain fields in the matrix domain become shorter, leading to higher stresses in general and causing higher values at the crack tip. The difference in relative magnitude between Mode I and Mode II and the delay in the contact zone's onset are instead due to the interplay between two different mechanisms, both caused by the ordered microstructural arrangement of the model. In the models considered, a fully bonded fiber is always placed along the horizontal direction, aligned with the partially debonded fiber and exactly in front of the debond. By increasing V_f, the former moves closer to the latter and for small debonds this causes a magnification of the x-strain at the crack tip. For small debonds ($\leq 20° - 30°$) in fact, the crack tip is approximately normal to the x-direction and thus an increase in ε_x causes an increase in G_I. On the other hand, for large debonds ($\geq 70° - 80°$) the crack growth direction is almost aligned with the x-axis, thus a magnification in the x-strain translates into an increase of Mode II ERR. However, this increasing effect on G_{II} is partially counteracted by the presence of a fully bonded fiber on top of the debonded fiber and aligned with it. As fibers are more rigid than the surrounding matrix, the presence of the former will restrain horizontal displacements, thus hampering strong increases in G_{II} for large debonds. Furthermore, due to the mismatch in the Poisson's ratios, the fully bonded fiber placed above generates an upward-directed component of the vertical displacement field in the matrix, which tends to open the debond and causes the delay in the contact zone's onset. The interplay between these mechanisms is governed by the average inter-fiber distance and, in turn, by the fiber volume fraction.

These observations are in agreement with the results reported in [31], where the effect on the ERR of a partially debonded fiber of two fully bonded nearby fibers, placed symmetrically with respect to the loading direction, is studied for different angular positions (denoted as θ_2) and radial distances in a model with an effectively infinite matrix ($V_f \sim 0.09\%$). The effect of the former is studied for a constant value of the radial distance between the debonded and bonded fibers, which corresponds to a local V_f^{local} of $\sim 62\%$ assuming hexagonal packing. They report an increase in both Mode I and Mode II ERR with respect to the single fiber case when the two fibers are placed at an angle of respectively $\pm 25°, \pm 30°, \pm 140°, \pm 150°, \pm 155°$, i.e. closest to the loading direction. Notice that for $\pm 25°$ and $\pm 155°$ the two fully bonded fibers are almost in contact, with an inter-fiber distance of ~ 0.04 times their radius. This result confirms the considerations made in the previous paragraph about the x-strain magnification caused by the presence of fully bonded fibers along the loading direction. The effect is further analyzed and discussed in Sec. C.2 and Sec. C.4. In the range $\pm 40° - \pm 130°$ instead, the presence of the other fibers causes a reduction of the ERR and, particularly in the range $80° - 120°$, results are very close and almost insensitive to variations in θ_2, which supports the previous conclusion about the effect of a fully bonded fiber on top the partially debonded

one. This effect is treated in more detail in Sec. C.3.
Comparing the results from [31] with those presented in this paper, an hypothesis can be furthermore formulated about the robustness of the results of the present article with respect to deviations in fiber position: it seems reasonable to assume a tolerance to deviations of max. $\pm 30°$ with respect to the loading direction and of max. $\pm 20°$ with respect to the through-the-thickness direction.
The effect of the local fiber content is also investigated in [31], by changing the radial distance between the partially debonded fiber and the fully bonded ones. They observe that the further the fully bonded fibers are placed from the central one, i.e. the lower the local V_f, the lower is their effect on the ERR. The magnitude of the effect is however small: the maximum increase of the total ERR is of ~ 1.15 times for $\theta_2 = 30°$ and $150°$ when increasing V_f^{local} from 28% to 62%; the total ERR decreases by a factor of ~ 0.62 for $\theta_2 = 60°$, ~ 0.74 for $\theta_2 = 90°$ and ~ 0.5 for $\theta_2 = 120°$ when increasing V_f^{local} from 28% to 62%. Analogous results can be found in [34], where the authors consider a centrally-placed partially debonded fiber sorrounded by an hexagonal cluster inside an homogenized UD composite. They observe a reduction in the ERR when the local fiber volume fraction is increased, i.e. when the spacing between fibers is reduced. The strongest change is reported for Mode II, which decreases by a factor of ~ 0.73 when the local fiber volume fraction is decreased from 66% to 78%. Thus, the trends presented in [31, 34] are in agreement with our results on the effect of V_f and support the considerations made so far. The stark difference in magnitude however highlights the contrast between the effect of the local fiber volume fraction of a cluster of fibers inside an infinite medium and of the global V_f of long-range microstructural arrangements, such the ones considered in this article. The similarity in trends with the concurrent difference in magnitudes can be explained in relation to the characteristics of the elastic solution computed. In the first case the local fiber volume fraction controls the distance, with respect to the central partially debonded fiber, at which a localized perturbation zone appears in the far-field elastic solution; in the second case the global V_f determines the characteristic lengths of a global periodic solution.

C.2 Interaction between debonds in UD composites with a single row of fibers

The interaction of debonds appearing at regular intervals in an ultra-thin UD composite with a single row of fibers is studied for Mode I (Fig. 8) and Mode II (Fig. 9) and fiber content equal to 30% (Figs. 8a and 9a) and 60% (Figs. 8b and 9b). The models treated are $3\times1-free$, $5\times1-free$, $7\times1-free$, $11\times1-free$, $21\times1-free$, $101\times1-free$ and $201\times1-free$, corresponding respectively to a debond every 3^{rd}, 5^{th}, 7^{th}, 11^{th}, 21^{st}, 101^{st} and 201^{st} fiber (Fig. 1a). Given that the upper surface of the UD row is left free, the interaction with the debonded fiber in the next RUC is stronger than in any other case and the results of this section are thus the most conservative in terms of debond's growth: the ERRs should be the largest. The effect is enhanced in composites with high V_f and especially for G_{II}: at $V_f = 60\%$ the highest G_{II} value for the $201 \times 1 - free$ composite

in Fig. 9b is more than 3 times higher than the G_{II} value value for the $21 \times 21 - free$ composite in Fig. 7b. Even the maximum is shifted to larger angles. The G_I value is for some cases only 30% higher.
From both Fig. 8 and Fig. 9, it can be seen that the presence of a debond close to the analyzed debond decreases the strain magnification effect discussed in Sec. C.1 and thus reduces the value of the ERR. This phenomenon is called "crack shielding" [26].

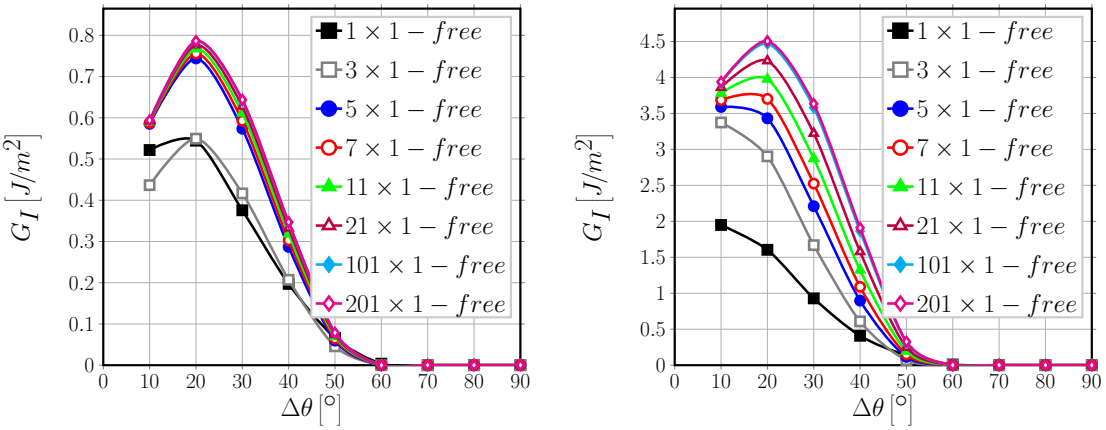

(a) $V_f = 30\%$. (b) $V_f = 60\%$.

Figure 8: Effect of the interaction between debonds appearing at regular intervals on Mode I ERR in an UD with a single row of fibers at different levels of fiber volume fraction V_f, subject to an applied transverse strain ε_x of 1%.

For Mode I, the presence of a free surface, and inversely the absence of a fully bonded fiber along the vertical direction, implies the absence of the counteracting upward-oriented vertical component of the displacement field due to the mismatch in Poisson's ratios. This in turn translates into the constancy of the value of $\Delta\theta$ corresponding to contact zone's onset, always equal to 60°. For $V_f = 30\%$, Mode I is reduced when the spacing between debonds (in terms of number of fully bonded fibers between them in our models) decreases, but the magnitude of change is significant only in the range when the spacing is reduced from a debond every 5^{th} fiber to one every 3^{rd}. For comparison, the difference of peak G_I values for $V_f = 30\%$ between $5 \times 1 - free$ and $3 \times 1 - free$ is $\sim 0.2\ \frac{J}{m^2}$ (around 30% of the lower value), while between $201 \times 1 - free$ and $5 \times 1 - free$ is $\sim 0.05\ \frac{J}{m^2}$ (around 7% of the lower value). A similar observation can be made for $V_f = 60\%$, but for larger spacings: no difference can be seen between the case of a debond placed every 101^{st} and every 201^{st} fiber. These observations suggest the existence of characteristic distance dependent on the fiber volume fraction which governs the interaction between debonds: in low V_f composites ($V_f = 30\%$) the convergence to a non-interactive solution is faster (less interaction between debonded fibers in neighboring RUCs).

Without costraint on the upper surface, the strain magnification effect creates a larger displacement gap in the x-direction, which increases Mode II for larger debonds. When

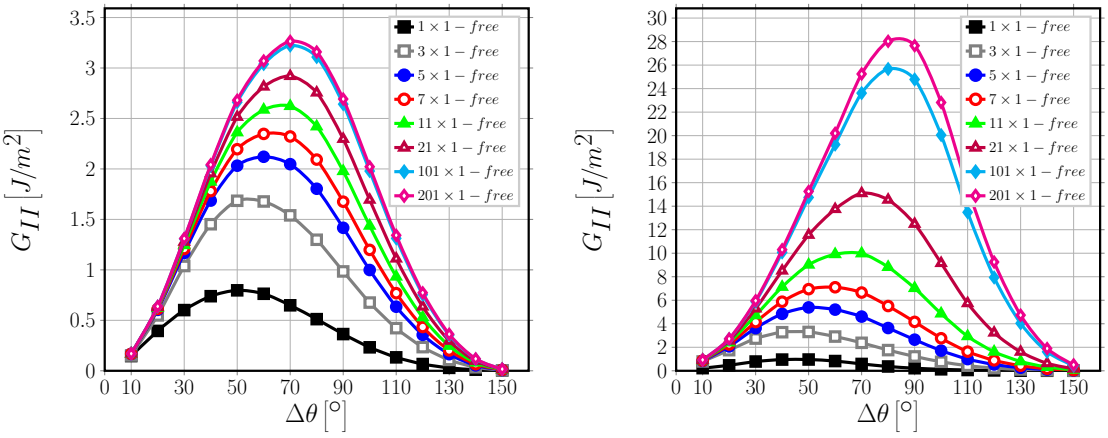

(a) $V_f = 30\%$. (b) $V_f = 60\%$.

Figure 9: Effect of the interaction between debonds appearing at regular intervals on Mode II ERR in an UD with a single row of fibers at different levels of fiber volume fraction V_f, subject to an applied transverse strain ε_x of 1%.

debonds are far apart, the series of rigid elements in the ultra-thin composite row (constituted by fully bonded fibers and their surrounding matrix) creates higher x-strains than in average in the element with the debonded fiber, which in turn generates higher tangential displacements at the crack tip for larger debonds. Conversely, when debonds are closer (smaller number of rigid elements between them), the strain concentration in the debonded element is more similar to the applied strain (the magnification is reduced) and the tangential displacement component at the crack tip decreases for large $\Delta\theta$. This is the mechanism behind the change in the value of $\Delta\theta$ for which the peak of G_{II} occurs: from 70° to 50° at 30%, and from 80° to 40° at 60% going from the higher to the smaller spacing of debonds. Differently from Mode I, the presence of a characteristic distance is harder to establish. For $V_f = 30\%$ (Fig. 9a), it seems reasonable to establish it at around 100 fully bonded fibers between each debond. For $V_f = 60\%$ (Fig. 9b), the difference between models $101 \times 1 - free$ and $201 \times 1 - free$ is still sizable, thus preventing the establishment of such characteristic distance. It is possible to observe, however, that the change between $101 \times 1 - free$ and $201 \times 1 - free$ is significantly smaller than between $21 \times 1 - free$ and $101 \times 1 - free$ ($2\left[\frac{J}{m^2}\right]$ vs $11\left[\frac{J}{m^2}\right]$), thus suggesting the existence of the characteristic distance outside the range studied. Nevertheless, one should question whether the single row composite with free surface is an appropriate RUC for defining the upper bound for G_{II}: G_{II} may be more affected by the free surface than by the effect of the interaction between debonds in the row.

C.3 Influence of rows of fully bonded fibers on debond's ERR in the middle row

The effect of the presence of rows of fully bonded fibers on debond's growth in the central row with all fibers partially debonded is studied for Mode I (Fig. 10) and Mode II (Fig. 11)

and fiber content equal to 30% (Figs. 10a and 11a) and 60% (Figs. 10b and 11b). The models treated are $1 \times 3 - free$, $1 \times 5 - free$, $1 \times 7 - free$, $1 \times 11 - free$, $1 \times 21 - free$, $1 \times 101 - free$ and $1 \times 201 - free$, corresponding to a UD composite with respectively 3, 5, 7, 11, 21, 101 and 201 rows of fibers (Fig. 2a).

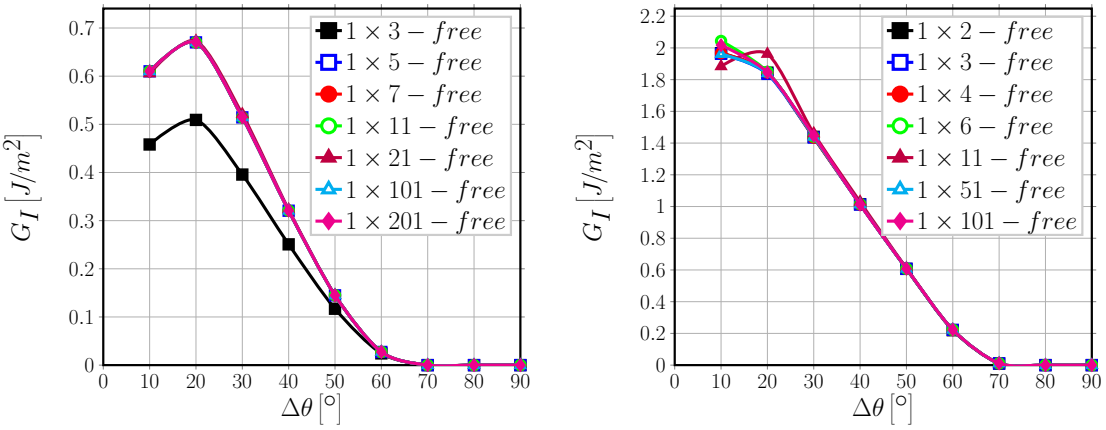

(a) $V_f = 30\%$. (b) $V_f = 60\%$.

Figure 10: Influence of rows of fully bonded fibers on debond's growth in Mode I ERR in a centrally located row of debonded fibers at different levels of fiber volume fraction V_f, subject to an applied transverse strain ε_x of 1%.

The results shown strengthen the arguments made in Sec. C.1 and Sec. C.2. It can, in fact, be seen in Fig. 10 that an increasing number of bonded fiber rows across the thickness delays the onset of the contact zone to a debond of 70° in size, due to the introduction of an additional positive component of the vertical displacement which translates into an opening displacement at the debond's tip.
Comparing Fig. 9b with Fig. 11b, we observe that the presence of bonded fiber rows significantly reduce the G_{II} and its maximum is shifted back to 60°, thus confirming the hypothesis in Section C.2 that the absence of G_{II} convergence with the increasing distance in a single-row composite is caused more by the free surface than by the interaction between debonds.

The results of both Mode I and Mode II show that the introduction of an increasing number of fully bonded fiber rows doesn't change the ERR calculated at the crack tip after adding more than one row (the convergence is very fast). A small effect, mostly on Mode I, of the number of bonded fiber rows can be observed at low fiber content (Figs. 10a and 11a), while for high fiber content the smaller model with only one fiber row above the partially debonded one is already representative.

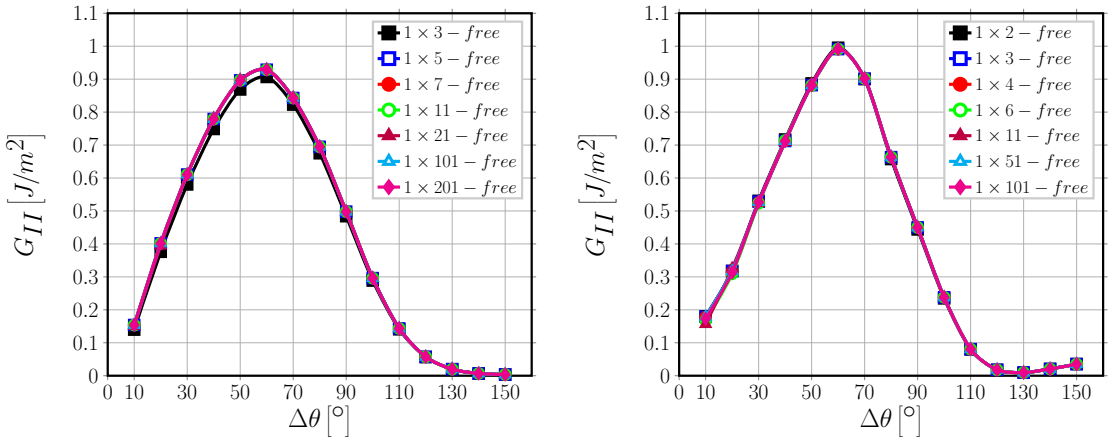

(a) $V_f = 30\%$. (b) $V_f = 60\%$.

Figure 11: Influence of rows of fully bonded fibers on debond's growth in Mode II ERR in a centrally located row of debonded fibers at different levels of fiber volume fraction V_f, subject to an applied transverse strain ε_x of 1%.

C.4 Effect of multiple rows of bonded fibers on debonding in the central row of a UD composite with different distances between debonded fibers

The ERR of debonds appearing at regular intervals in the central row of fibers in UD composites is affected by the number of rows with bonded fibers. The effect is investigated using different combinations of horizontal debond spacing, controlled by the number of bonded fibers in the central row of the RUC, and the number of rows of bonded fibers on top of it. The following models have been studied: $3\times3-free$, $5\times3-free$, $5\times5-free$, $7\times3-free$, $7\times5-free$, $7\times7-free$, $11\times3-free$, $11\times5-free$, $11\times7-free$, $11\times11-free$, $21\times3-free$, $21\times5-free$, $21\times7-free$, $21\times11-free$, $21\times21-free$, $101\times3-free$, $101\times5-free$, $101\times7-free$, $101\times11-free$, $201\times3-free$, $201\times5-free$, $201\times7-free$, $201\times11-free$ (Fig. 2b).

The results shown in Fig. 12 confirm the observations discussed in Sec. C.2 and Sec. C.3: the presence of fully bonded fiber rows on top of the central row with debonded fibers reduces the interaction with the free surface and thus has a restraining effect on the ERR, that counteracts the magnification due to an increasing number of fully bonded fibers in the horizontal direction. The interplay is further modulated by the fiber content. Observing Fig. 12, it is possibe to note how the free surface interaction decays fast: the presence of 5 fiber rows across the thickness is already sufficient to prevent any significant effect of additional fiber rows on the ERR of a debond in the central row.

The results in Fig. 13 show instead the effect of increasing the distance between two consecutive debonds in the central row of a UD composite of given thickness. In agreement with the observations of Section C.2, increasing the distance between debonds (measured in terms of fully bonded fibers between them) causes an increase in the ERR in both Mode I and Mode II. For both Mode I and Mode II, it is possible to observe the

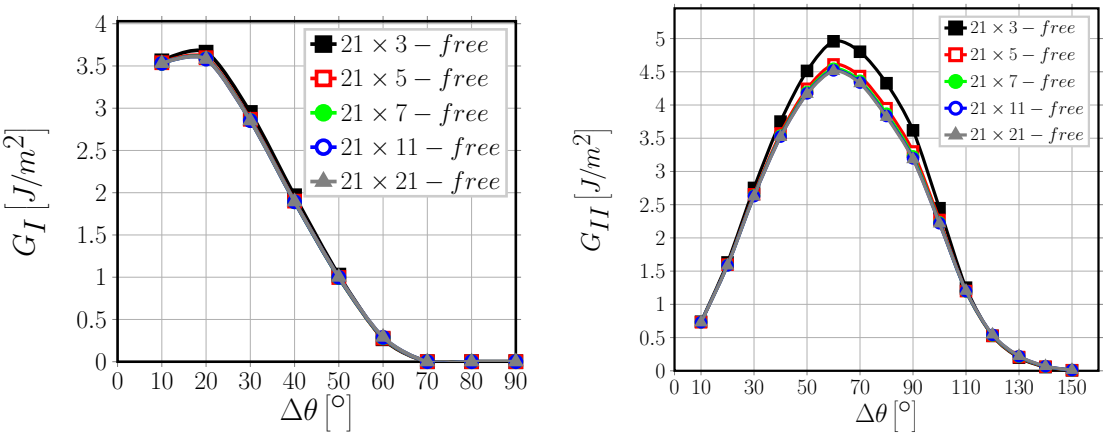

(a) G_I. (b) G_{II}.

Figure 12: Effect on Mode I and Mode II ERR of the presence of an increasing number of rows of fully bonded fibers in UD composites with debonds appearing every 10^{th} fiber (model $21 \times k - free$). $V_f = 60\%$ and $\varepsilon_x = 1\%$.

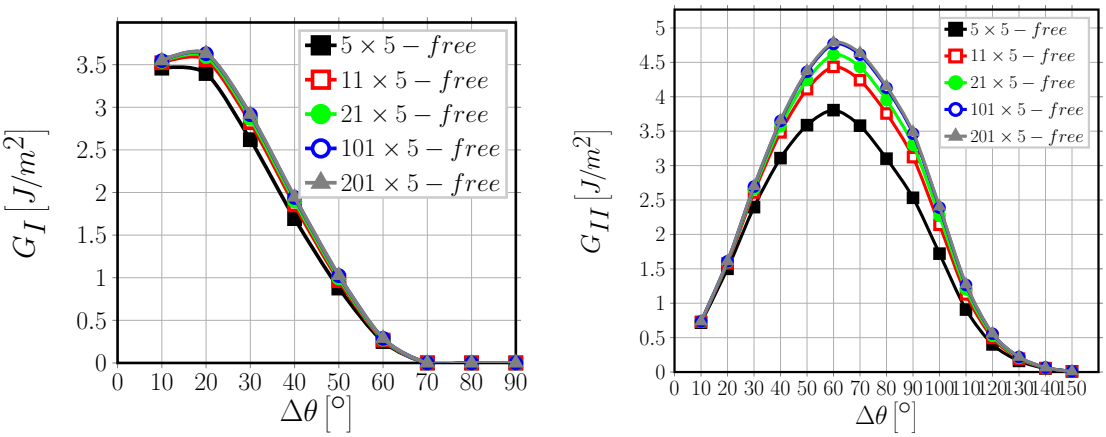

(a) G_I. (b) G_{II}.

Figure 13: Effect on Mode I and Mode II ERR of increasing the spacing between debonds appearing in the central row of fibers in a UD composite with a fixed number of rows across the thickness. $V_f = 60\%$, $k = 5$ and $\varepsilon_x = 1\%$.

existence of a characteristic distance which defines the limit between the interactive and the non-interactive solution. Furthermore, comparing Figure 13a and 13b, it is possible to notice that Mode I is less sensitive than Mode II to the horizontal spacing of debonds.

C.5 Comparison with the single fiber model with equivalent boundary conditions

The single fiber RUC ($1\times1-free$ or $1\times1-coupling$) corresponds to the most damaged state of the composite, i.e. the state in which all fibers have debonds. The $1\times1-free$ model represents an ultra-thin UD composite with a single row of partially debonded fibers. The $1\times1-coupling$ model, where the displacement coupling is used to enforce periodic boundary conditions, represents an infinite composite.
The comparison of the $1\times1-free$ model with one row multi-fiber models $n\times1-free$ in Figure 8 and Figure 9 show that the former provides in general the lowest value of the ERR (the highest crack shielding case).

The $1\times1-coupling$ model is compared with $1\times3-free$ and $1\times201-free$ models in Fig. 14. In all three models the distance between debonds in the x-direction is the same and the difference is in the vertical direction. The $1\times1-coupling$ model describes the interaction between debonds in different rows of debonded fibers whereas the $1\times k-free$ models describe the effect of the proximity of the composite's free surface. The Mode I ERR in the $1\times3-free$ and $1\times201-free$ model is very similar to the $1\times1-coupling$ model, which leads to a rather surprising conclusion. In both models we have, on the top of the central one, a large amount of fibers (bonded in two cases and debonded in the third case). It appears that the effect of bonded and debonded fibers on the central debond is the same. This implies that, for Mode I ERR, the interaction between debonds in elements placed on top of each other is small.

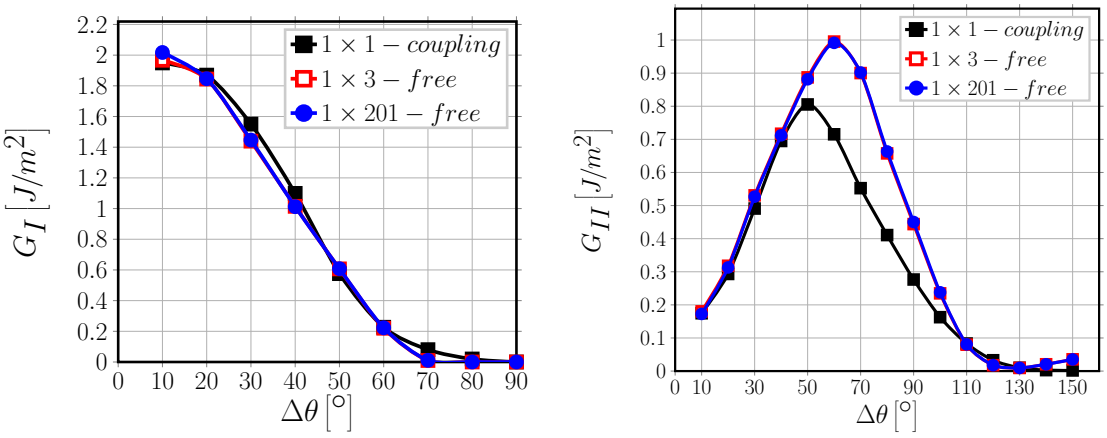

(a) G_I. (b) G_{II}.

Figure 14: Comparison of the ERR between the single fiber model with coupling conditions along the upper boundary and the $1\times k-free$ model. $V_f=60\%$ and $\varepsilon_x=1\%$.

The same comparison for Mode II shows a sizeable difference in the range $50^\circ-90^\circ$, while the results almost coincide for smaller values of $\Delta\theta$. The lower values of G_{II} of the $1\times1-coupling$ model in the range $50^\circ-90^\circ$ are due to the shielding effect of a

debond of the same size in the fiber just above the central one (modeled by the coupling boundary condition), which leaves the strip of matrix between the two fibers free to deform away from both of them due to the Poisson's effect and thus favors Mode I and reduces Mode II. This translates into the delay in the appearance of the contact zone, particularly evident in Fig. 14a.

D Conclusions & Outlook

Several models of Repeating Unit Cell, representative of different microstructural arrangements of a unidirectional (UD) composite, have been studied in order to investigate the effect on fiber/matrix interface crack growth of the presence of partially debonded and/or fully bonded fibers. Regular microstructures based on square-packing arrangements of fibers have been loaded in transverse tension, with debonds appearing in the central row of fibers at regular intervals measured in terms of number of fully bonded fibers between them. This central row is embedded in-between a varying number of rows with perfectly bonded fibers. The surface of the composite is either traction-free or with imposed vertical displacement constraint imitating a periodic structure in the composite thickness direction.
In each RUC, the fiber volume fraction is spatially homogeneous (no fiber clustering is considered) and the fiber distribution is uniform by design, which establishes a direct relationship between fiber content and inter-fiber distance. The main conclusions of this work are summarized here.

1. With a decreasing number of fully bonded fibers between two partially debonded fibers in the central row, the ERR decreases. It seems to exist a characteristic distance between debonds which defines the transition to a non-interactive solution. However, this distance depends on the number of perfectly bonded fiber rows surrounding the central row and on the fiber volume fraction. This distance can be estimated to be around 100 fully bonded fibers for a 1-fiber-row thick UD with $V_f = 30\%$ and 200 for a 1-fiber-row thick UD with $V_f = 60\%$, while it is expected to be around 100 fibers for a 5-fibers-row thick UD with $V_f = 60\%$.

2. The presence of a free surface close to the debond leads to higher Mode I and Mode II ERRs and a shift of the peak G values to larger debonds.

3. The presence of fibers (fully or partially bonded) in the composite thickness direction, along the same vertical line as the analyzed central fiber, appears to have a restraining effect on both G_I and G_{II}. The free composite surface effect on the ERR decays very fast: adding more than 2 fully bonded fibers below and above the central row leads to stable constant values of ERR.

4. The presence of a debond in the fiber above the central partially debonded one only delays the appearance of the contact zone, while no significant effect on the ERR has been observed.

5. Increasing the fiber content (decreasing the inter-fiber distance), magnifies in general the effects described in the previous points.

6. The results and conclusions presented agree well with previous observations reported in the literature [31, 34]. A mechanical explanation of the observed trends has been presented based on the mismatch in elastic properties, particularly Poisson's ratios, and the positions of fibers and debonds with respect to the loading direction.

Acknowledgements

Luca Di Stasio gratefully acknowledges the support of the European School of Materials (EUSMAT) through the DocMASE Doctoral Programme and the European Commission through the Erasmus Mundus Programme.

References

[1] Douglas A. McCarville et al. "3.5 Design, Manufacture and Test of Cryotank Components". In: *Comprehensive Composite Materials II*. Elsevier, 2018, pp. 153–179. DOI: 10.1016/b978-0-12-803581-8.09958-6.

[2] Yong Han Noel Kim et al. "Effects of Shallow Biangle, Thin-Ply Laminates on Structural Performance of Composite Wings". In: *AIAA Journal* 55.6 (June 2017), pp. 2086–2092. DOI: 10.2514/1.j055465.

[3] Alexander Kopp et al. "The Aurora space launcher concept". In: *CEAS Space Journal* 10.2 (Nov. 2017), pp. 167–187. DOI: 10.1007/s12567-017-0184-2.

[4] K. Kawabe, S. Tomoda, and T. Matsuo. "A Pneumatic Process for Spreading Reinforcing Fiber Tow". In: *Proceedings of the* 42^{nd} *International SAMPE Symposium and Exhibition*. (Anaheim, CA, USA). SAMPE, 1997, pp. 65–76.

[5] Kazumasa Kawabe. "New Spreading Technology for Carbon Fiber Tow and Its Application to Composite Materials". Japanese. In: *Sen'i Gakkaishi* 64.8 (2008), pp. 262–267. DOI: 10.2115/fiber.64.p_262.

[6] K. Kawabe, H. Sasayama, and S. Tomoda. "New Carbon Fiber Tow-Spread Technology and Applications to Advanced Composite Materials". In: *SAMPE Journal* 45.2 (2008), pp. 6–17.

[7] H. Sasayama et al. "Effect of lamina thickness on first ply failure in multidirectionally laminated composites". In: *Proceedings of the* 8^{th} *Japan SAMPE Symposium*. (Tokyo, Japan). SAMPE, 2003.

[8] S. Sihn et al. "Experimental studies of thin-ply laminated composites". In: *Composites Science and Technology* 67.6 (May 2007), pp. 996–1008. DOI: 10.1016/j.compscitech.2006.06.008.

[9] Tomohiro Yokozeki, Yuichiro Aoki, and Toshio Ogasawara. "Experimental characterization of strength and damage resistance properties of thin-ply carbon fiber/toughened epoxy laminates". In: *Composite Structures* 82.3 (Feb. 2008), pp. 382–389. DOI: 10.1016/j.compstruct.2007.01.015.

[10] Tomohiro Yokozeki et al. "Damage characterization in thin-ply composite laminates under out-of-plane transverse loadings". In: *Composite Structures* 93.1 (Dec. 2010), pp. 49–57. DOI: 10.1016/j.compstruct.2010.06.016.

[11] A. Arteiro et al. "Large damage capability of non-crimp fabric thin-ply laminates". In: *Composites Part A: Applied Science and Manufacturing* 63 (Aug. 2014), pp. 110–122. DOI: 10.1016/j.compositesa.2014.04.002.

[12] R. Amacher et al. "Thin ply composites: Experimental characterization and modeling of size-effects". In: *Composites Science and Technology* 101 (Sept. 2014), pp. 121–132. DOI: 10.1016/j.compscitech.2014.06.027.

[13] J. Cugnoni et al. "Towards aerospace grade thin-ply composites: Effect of ply thickness, fibre, matrix and interlayer toughening on strength and damage tolerance". In: *Composites Science and Technology* 168 (Nov. 2018), pp. 467–477. DOI: 10.1016/j.compscitech.2018.08.037.

[14] Hiroshi Saito, Hiroki Takeuchi, and Isao Kimpara. "Experimental Evaluation of the Damage Growth Restraining in 90° Layer of Thin-ply CFRP Cross-ply Laminates". In: *Advanced Composite Materials* 21.1 (2012), pp. 57–66. DOI: 10.1163/156855112X629522.

[15] K. W. Garrett and J. E. Bailey. "Multiple transverse fracture in 90° cross-ply laminates of a glass fibre-reinforced polyester". In: *Journal of Materials Science* 12.1 (Jan. 1977), pp. 157–168. DOI: 10.1007/bf00738481.

[16] A. Parvizi and J. E. Bailey. "On multiple transverse cracking in glass fibre epoxy cross-ply laminates". In: *Journal of Materials Science* 13.10 (Oct. 1978), pp. 2131–2136. DOI: 10.1007/bf00541666.

[17] A. Parvizi, K. W. Garrett, and J. E. Bailey. "Constrained cracking in glass fibre-reinforced epoxy cross-ply laminates". In: *Journal of Materials Science* 13.1 (Jan. 1978), pp. 195–201. DOI: 10.1007/bf00739291.

[18] J. E. Bailey and A. Parvizi. "On fibre debonding effects and the mechanism of transverse-ply failure in cross-ply laminates of glass fibre/thermoset composites". In: *Journal of Materials Science* 16.3 (Mar. 1981), pp. 649–659. DOI: 10.1007/bf02402782.

[19] J. E. Bailey, P. T. Curtis, and A. Parvizi. "On the Transverse Cracking and Longitudinal Splitting Behaviour of Glass and Carbon Fibre Reinforced Epoxy Cross Ply Laminates and the Effect of Poisson and Thermally Generated Strain". In: *Proceedings of the Royal Society A: Mathematical, Physical and Engineering Sciences* 366.1727 (July 1979), pp. 599–623. DOI: 10.1098/rspa.1979.0071.

[20] A. H. England. "An Arc Crack Around a Circular Elastic Inclusion". In: *Journal of Applied Mechanics* 33.3 (1966), p. 637. DOI: 10.1115/1.3625132.

[21] A.B. Perlman and G.C. Sih. "Elastostatic problems of curvilinear cracks in bonded dissimilar materials". In: *International Journal of Engineering Science* 5.11 (Nov. 1967), pp. 845–867. DOI: 10.1016/0020-7225(67)90009-2.

[22] M. Toya. "A crack along the interface of a circular inclusion embedded in an infinite solid". In: *Journal of the Mechanics and Physics of Solids* 22.5 (Oct. 1974), pp. 325–348. DOI: 10.1016/0022-5096(74)90002-7.

[23] Maria Comninou. "The Interface Crack". In: *Journal of Applied Mechanics* 44.4 (1977), p. 631. DOI: 10.1115/1.3424148. URL: https://doi.org/10.1115/1.3424148.

[24] F. París, J. C. Caño, and J. Varna. "The fiber-matrix interface crack — A numerical analysis using Boundary Elements". In: *International Journal of Fracture* 82.1 (May 1996), pp. 11–29. DOI: 10.1007/bf00017861.

[25] J. Varna, Federico París, and J. C.Caño. "The effect of crack-face contact on fiber/matrix debonding in transverse tensile loading". In: *Composites Science and Technology* 57.5 (1997), pp. 523–532. DOI: 10.1016/s0266-3538(96)00175-3.

[26] I.G. García, V. Mantič, and E. Graciani. "Debonding at the fibre–matrix interface under remote transverse tension. One debond or two symmetric debonds?" In: *European Journal of Mechanics - A/Solids* 53 (Sept. 2015), pp. 75–88. DOI: 10.1016/j.euromechsol.2015.02.007.

[27] E. Correa et al. "Effects of the presence of compression in transverse cyclic loading on fibre–matrix debonding in unidirectional composite plies". In: *Composites Part A: Applied Science and Manufacturing* 38.11 (Nov. 2007), pp. 2260–2269. DOI: 10.1016/j.compositesa.2006.11.002.

[28] E. Correa, V. Mantič, and F. París. "Effect of thermal residual stresses on matrix failure under transverse tension at micromechanical level: A numerical and experimental analysis". In: *Composites Science and Technology* 71.5 (Mar. 2011), pp. 622–629. DOI: 10.1016/j.compscitech.2010.12.027.

[29] E. Correa, F. París, and V. Mantič. "Effect of the presence of a secondary transverse load on the inter-fibre failure under tension". In: *Engineering Fracture Mechanics* 103 (May 2013), pp. 174–189. DOI: 10.1016/j.engfracmech.2013.02.026.

[30] E. Correa, F. París, and V. Mantič. "Effect of a secondary transverse load on the inter-fibre failure under compression". In: *Composites Part B: Engineering* 65 (Oct. 2014), pp. 57–68. DOI: 10.1016/j.compositesb.2014.01.005.

[31] C. Sandino, E. Correa, and F. París. "Numerical analysis of the influence of a nearby fibre on the interface crack growth in composites under transverse tensile load". In: *Engineering Fracture Mechanics* 168 (Dec. 2016), pp. 58–75. DOI: 10.1016/j.engfracmech.2016.01.022.

[32] C. Sandino, E. Correa, and F. París. "Composite materials under transverse biaxial loads: Study of the influence of a nearby fibre on the interface crack growth under tension". In: *Proceeding of the* 17^{th} *European Conference on Composite Materials (ECCM-17)*. (Munich, Germany, June 26–30, 2016). 2016.

[33] C. Sandino, E. Correa, and F. París. "Interface crack growth under transverse compression: nearby fibre effect". In: *Proceeding of the* 18^{th} *European Conference on Composite Materials (ECCM-18)*. (Athens, Greece, June 24–28, 2018). 2018.

[34] Linqi Zhuang et al. "Effects of inter-fiber spacing on fiber-matrix debond crack growth in unidirectional composites under transverse loading". In: *Composites Part A: Applied Science and Manufacturing* 109 (June 2018), pp. 463–471. DOI: 10.1016/j.compositesa.2018.03.031.

[35] Janis Varna et al. "Growth and Interaction of Debonds in Local Clusters of Fibers in Unidirectional Composites during Transverse Loading". In: *Key Engineering Materials* 754 (Sept. 2017), pp. 63–66. DOI: 10.4028/www.scientific.net/kem.754.63.

[36] *ABAQUS/Standard User's Manual, Version 6.12*. Simulia. Providence, RI, USA, 2012.

[37] Janis Varna, Federico Paris, and Juan Carlos del Cano. "The effect of crack-face contact on fiber/matrix debonding in transverse tensile loading". In: *Composites Science and Technology* 57.5 (1997), pp. 523–532. DOI: 10.1016/s0266-3538(96)00175-3.

[38] Ronald Krueger. "Virtual crack closure technique: History, approach, and applications". In: *Applied Mechanics Reviews* 57.2 (2004), p. 109. DOI: 10.1115/1.1595677.

[39] J. R. Rice. "A Path Independent Integral and the Approximate Analysis of Strain Concentration by Notches and Cracks". In: *Journal of Applied Mechanics* 35.2 (1968), p. 379. DOI: 10.1115/1.3601206.

[40] Leif E. Asp, Lars A. Berglund, and Peter Gudmundson. "Effects of a composite-like stress state on the fracture of epoxies". In: *Composites Science and Technology* 53.1 (Jan. 1995), pp. 27–37. DOI: 10.1016/0266-3538(94)00075-1.

[41] L.E. Asp, L.A. Berglund, and R. Talreja. "A criterion for crack initiation in glassy polymers subjected to a composite-like stress state". In: *Composites Science and Technology* 56.11 (Jan. 1996), pp. 1291–1301. DOI: 10.1016/s0266-3538(96)00090-5.

[42] Federico París, Elena Correa, and Vladislav Mantič. "Kinking of Transversal Interface Cracks Between Fiber and Matrix". In: *Journal of Applied Mechanics* 74.4 (2007), p. 703. DOI: 10.1115/1.2711220.

Paper C

Effect of the proximity to the 0°/90° interface on Energy Release Rate of fiber/matrix interface crack growth in the 90°-ply of a cross-ply laminate under tensile loading

Authors:
Luca Di Stasio, Janis Varna and Zoubir Ayadi

Reformatted version of paper submitted to:
Journal of Composite Materials, 2019.

© 2019, The Authors.

Effect of the proximity to the 0°/90° interface on Energy Release Rate of fiber/matrix interface crack growth in the 90°-ply of a cross-ply laminate under tensile loading

Luca Di Stasio[1,2], Janis Varna[1] and Zoubir Ayadi[2]

[1]Luleå University of Technology, University Campus, SE-97187 Luleå, Sweden
[2]Université de Lorraine, EEIGM, IJL, 6 Rue Bastien Lepage, F-54010 Nancy, France

*Corresponding author: luca.di.stasio@ltu.se

Abstract

Models of Representative Volume Elements (RVEs) of cross-ply laminates with different geometric configurations and damage states are studied. Debond growth is characterized by the estimation of the Mode I and Mode II Energy Release Rate (ERR) using the Virtual Crack Closure Technique (VCCT). It is found that the presence of the 0°/90° interface and the thickness of the 0° layer have no effect, apart from laminates with *ultra-thin* 90° plies where it is however modest. The present analysis support the claim that debond growth is not affected by the ply-thickness effect.

Keywords: Polymer-matrix Composites (PMCs), Fibre/matrix bond, Debonding, Finite Element Analysis (FEA)

A Introduction

Since the development of the *spread tow* technology or "FUKUI method" [1], significant efforts have been directed toward the characterization of *thin-ply* laminates [2, 3, 4, 5, 6, 7, 8, 9, 10, 11] and their application to mission-critical structures in the aerospace sector [12].
At the lamina level, the use of *thin-plies* leads to more regular and homogeneous microstructures [6, 9]. Measurements of ply level properties (tensile and compressive modulus, Poisson's ratio, ultimate tensile strength,tensile onset of damage, interlaminar shear strength) on Uni-Directional (UD) specimens ($[0^\circ_m]$ and $[90^\circ_m]$) revealed no remarkable difference with average properties available in the literature for the same type of fiber, nor showed any particular dependence on the ply thickness [9]. Only an increase of the ultimate compressive strength in the fiber direction was observed with very thin plies (~ 4 fiber diameters), although with very scattered values. The authors claim the increase

to be due to the fiber arrangement's increased regularity which prevents the onset of fiber microbuckling [9]. A number of researchers [2, 3, 4] has reported improvements in fatigue life with the use of *thin-plies*, which are explained as a consequence of delayed propagation of free edge delaminations and intralaminar cracks. Several researchers have analyzed the effect of *thin-plies* on damage development under static [3, 4, 5, 6, 7, 8, 9], fatigue [2, 3, 4, 5, 9] and impact loadings [3, 4, 5, 9]. It seems apparent that *thin-ply* laminates possess an increased ability to delay, and in some cases even suppress, the onset and propagation of intralaminar cracks (called often transverse or matrix or micro-cracks).

The first stage in the appearance of transverse cracks is known to be the occurrence of fiber/matrix interface cracks (also referred to as debonds), which grow along the fiber arc direction, then kink out of the interface and coalesce forming a transverse crack [13]. Different approaches have been applied to model the initiation and growth of debonds [14]. The Cohesive Zone Model (CZM) has been used to mimic the propagation of debonds along fiber interfaces; coupled with a failure criterion for the matrix, it has provided simulations of the growth of transverse cracks starting from a virgin material [15, 16, 17, 18]. The strength of the CZM, and its main requirement for a correct implemetation, lies in the elimination of the stress and displacement singularity that exists at the crack tip in the Linear Elastic Fracture Mechanics (LEFM) solution, as the crack tip is not explicitly modeled and the failure process is "smeared" over the finite length of the cohesive element. The main advantages of this approach are the possibility to observe the development of a simulated crack path and to record a load-displacement curve to be compared with experimental measurements. The fracture toughness (or critical Energy Release Rate) dependence on mode-mixity in the case of the interface crack [19] was successfully incorporated in a cohesive zone model by Freed and Banks-Sills [20]. However, different problems were reported [21] on the use of cohesive elements to simulate a bimaterial interface crack. It was observed that, for mixed-mode fracture in general, a single cohesive zone length might not simultaneously cancel both the tensile and shear stress singularity at the crack tip and thus fail to satisfy the fundamental requirement of the CZM approach. Also, it was concluded that energy dissipation at the cohesive zone tip could be neglected only with high enough values of the initial tensile and shear stiffnesses. A further issue which arises in the use of cohesive elements is the selection of appropriate values for the material parameters required by the model (critical stress and Energy Release Rate). Two options are available: adopting values measured from macroscopic tests (e.g. Double Cantilever Beam) or calibrating the parameters through inverse estimation by approximation of the macroscopic stress-strain response of the specific specimen the RVE modeled is representing. Finally, the failure mechanisms proposed by the Cohesive Zone Model might not represent the actual physics of the fiber/matrix interface failure process. It was shown [22] that the triaxiality of the matrix stress state in the inter-fiber region may be the driver of brittle matrix failure at or very close to the interface through a cavitation-like mechanism [23]. It thus seems likely that brittle failure at the interface may create an initial flaw from which debonding occurs in a fast and unstable manner, that could be modeled by the classic Griffith's criterion of LEFM. Linear Elastic Fracture

Mechanics obviates many of the drawbacks highlighted for Cohesive Zone Modeling. The analysis focuses on the evaluation of Mode I and Mode II Energy Release Rate (ERR) at the crack tip by means of the Virtual Crack Closure Technique (VCCT) [24] or the J-Integral method [25]. The stress and strain fields, required for the ERR computation, can be solved by application of different methodologies such as analytical solutions [26], the Boundary Element Method (BEM) [27] or the Finite Element Method (FEM) [28]. This approach presents nonetheless some limitations: it describes propagation of the debond and not its initiation; the role of friction in the contact zone is still an open issue; consensus is still lacking on a proper criterion for crack propagation in mixed mode. Finite fracture mechanics [29] is one way to address the initiation problem. Different studies have followed the LEFM approach and analyzed models of one or two fibers in an effectively infinite matrix [30, 31, 32, 33, 34] and of an hexagonal cluster of fibers in an effectively infinite homogenized UD composite [35, 28]. The problem of debond growth along the fiber-matrix interface in a cross-ply laminate has been only treated very recently in [36, 37], where authors embed a single partially debonded fiber in an effectively infinite homogenized 90° ply bounded by homogenized 0° layers. Thus, the effect of debond-debond interaction and of the relative proximity of a 0°/90° interface on debond ERR in cross-ply laminates is yet to be addressed. The present work is devoted to this problem. Our interest however is not to investigate the sequence of failure events, which would require knowledge of appropriate failure criteria and properties, but rather to understand which parameters may make debond growth energetically favorable and which may prevent it. Models of Repeating Unit Cells (RUCs) are developed to represent laminates with different degrees of damage in the 90° ply (here only in the form of debonds). The number of fully bonded fibers across the thickness of the 90° ply is varied in order to investigate the effect of the proximity of the 0°/90° interface. The thickness of the bounding 0° layers is also used as a parameter of the study. The stress and strain fields are solved with the Finite Element Method in Abaqus [38] and the debond (crack) is characterized by its Mode I and Mode II ERR calculated with the VCCT.

B RVE models & FE discretization

B.1 Introduction & nomenclature

In the present work, we investigate debond development under in-plane longitudinal tension in $[0^\circ_{m\cdot k\cdot 2L}, 90^\circ_{k\cdot 2L}, 0^\circ_{m\cdot k\cdot 2L}]$ laminates. The interaction between debonds in the presence of an interface with a stiff layer is studied with the use of different Repeating Unit Cells (RUCs) (see Figures 1 and 2), in which only the central fiber is partially debonded. Repetition of the composite RUC occurs along the in-plane laminate 0°-direction (corresponding to specimen axial direction and RUC horizontal direction in Figures 1 and 2), thus representing a cross-ply laminate with a thin or even ultra-thin 90° ply in the middle.

All the RUCs present regular microstructures with fibers placed according to a square-packing configuration characterized by the repetition of the same one-fiber unit cell of

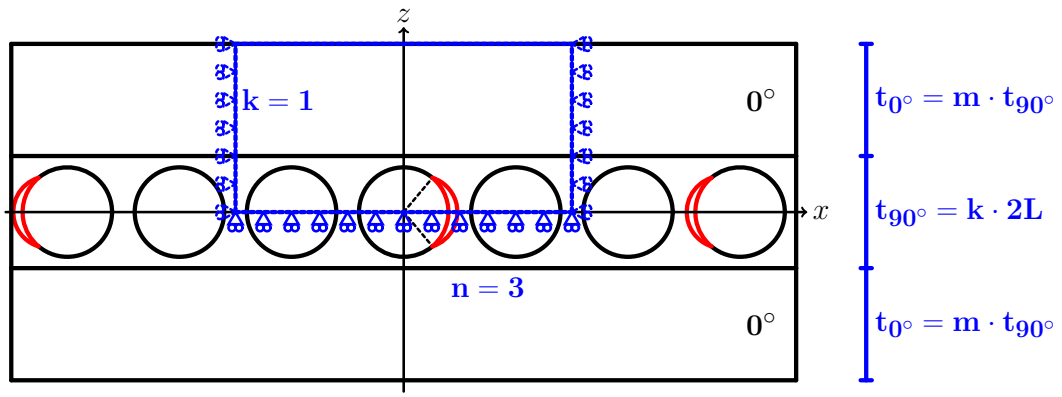

Figure 1: Models of $[0^\circ_{m\cdot 1\cdot 2L}, 90^\circ_{1\cdot 2L}, 0^\circ_{m\cdot 1\cdot 2L}]$ *laminates with an ultra-thin* 90° *layer, where the* 90° *ply is made up by a single "row" of fibers. Debonds are repeating at different distances, measured in terms of the number* $n-1$ *of fully bonded fibers appearing between two consecutive debonds.* $2L$ *is the thickness of one-fiber row.*

size $2L \times 2L$, where L is a function of the fiber volume fraction V_f and the fiber radius according to

$$L = \frac{R_f}{2}\sqrt{\frac{\pi}{V_f}}. \tag{B.1}$$

The choice of a square-packing configuration with a controlled number of fibers is motivated by the fact that our objective is to determine the effect of different geometrical and mechanical factors on debond Energy Release Rate, such as fiber volume fraction, the presence of undamaged and partially debonded fibers, the presence of the 0°/90° interface. The use of a regular microstructure allows us to isolate and identify the different contributions, which would be otherwise "smeared out" with the use of randomized distribution with a large number of fibers. Each fiber in the model has the same radius R_f, equal to 1 μm. This specific value has no physical meaning per se and it has been selected for simplicity. It is useful to observe that, in a linear elastic solution subject to non-holonomic constraints as the one described in the present article, the ERR is proportional to the geometrical dimensions of the model and thus re-evaluation of the ERR for fibers of any size requires just a multiplication. Furthermore, it is worth to point out that V_f is the same in the one-fiber unit and in the overall RUC, i.e. no clustering of fibers is considered.

The thickness of the 90° ply depends on the number k of fiber rows present across the thickness (the vertical or z direction in Figures 1 and 2) according to

$$t_{90^\circ} = k \cdot 2L. \tag{B.2}$$

On the other hand, the thickness of 0° layers can be assigned freely as a multiple of the 90° ply thickness as

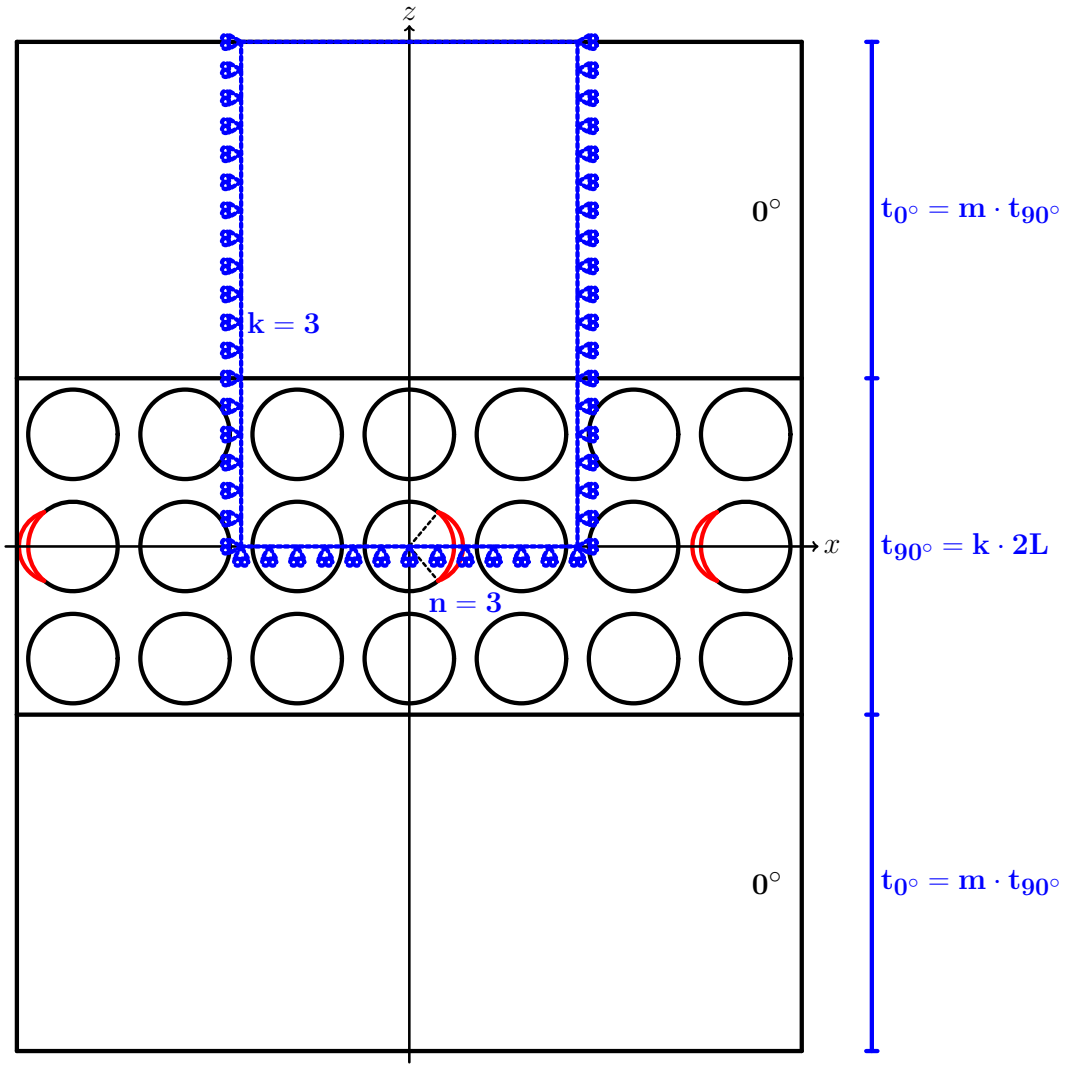

Figure 2: Models of $[0°_{m\cdot k\cdot 2L}, 90°_{k\cdot 2L}, 0°_{m\cdot k\cdot 2L}]$ *laminates with a* 90° *layer of variable thickness, determined by the number* k *of "rows" of fibers along the vertical direction. Debonds are repeating at different distances along the horizontal direction, measured in terms of the number* $n-1$ *of fully bonded fibers appearing between two consecutive debonds.* $2L$ *is the thickness of one-fiber row.*

$$t_{0°} = m \cdot t_{90°} \tag{B.3}$$

where m is an arbitrary integer. Thus, the thickness ratio m represents one additional parameter for the investigation.

In the following, let us consider in-plane coordinates x and y, and assume that the laminate 0°-direction is aligned with the x-axis. In the presence of a load in the x-direction, the strain in the y-direction is small, due to the very small Poisson's ratio of the laminate. Debonds are present only in the 90° layer and are considered to be significantly longer in the fiber direction than in the arc direction [39]. Therefore we use 2D models under

the assumption of plane strain, defined in the $x-z$ section of the composite. The study presented in this paper thus applies to long debonds and its focus is on understanding the mechanisms of growth along their arc direction. The laminates are assumed to be subject to tensile strain, which is applied in the form of a constant displacement in the x-direction along both vertical boundaries of the RUC as shown in Figure 3.
We assume damage to be present only in the central "row" of fibers of the 90° layer in the form of multiple debonds appearing at different regular intervals along the loading (horizontal) direction. The number of fibers n present in the horizontal direction of the RUC (Figures 1 and 2) controls the distance, in terms of fully bonded fibers, between consecutive debonds: if the RUC has n fibers in the horizontal direction, two consecutive debonds are separated by $n-1$ undamaged fibers. The RUCs considered are thus Representative Volume Elements (RVEs) of cross-ply laminates with a certain distribution of debonds in the middle 90° layer.
In summary, the models are differentiated by: first, the spacing between debonds along the horizontal direction in the 90° layer, which corresponds to the number n of fibers in the RUC's horizontal direction; second, the thickness of the middle 90° ply measured in terms of the number k of fiber rows in the vertical direction; third, the factor m which provides the thickness of 0° layers as a multiple of the 90° ply thickness. It thus seems natural to introduce a common notation for the RUCs as $n \times k - m \cdot t_{90^\circ}$.
An additional family of RUCs is considered, in which: only one partially debonded fiber is present; the 0° layer is absent; different combinations of displacement boundary conditions are applied to the upper surface. The application of coupling of horizontal displacements u_x along the right and left sides allows for repetition along the horizontal direction. When the upper boundary of the RUC is left free, we define the $1 \times 1 - free$ model. If coupling of the vertical displacements u_z is applied to the upper boundary (coupling condition), we define instead the $1 \times 1 - coupling$ model. In the case a linear distribution of the horizontal displacement u_x is applied to the upper boundary (H-condition), the model is refered to as $1 \times 1 - H$. Finally, when the linear distribution of the horizontal displacement u_x is superimposed to the condition of coupling of the vertical displacements u_z on the upper boundary, we have the $1 \times 1 - coupling + H$. Further details about this family of RUCs and the corresponding laminate RVE can be found in [40].

B.2 Description of modelled Representative Volume Elements (RVEs)

The first family of Representative Volume Elements (RVEs) is represented in Figure 1. It represents a set of $[0^\circ_{m\cdot 1\cdot 2L}, 90^\circ_{1\cdot 2L}, 0^\circ_{m\cdot 1\cdot 2L}]$ laminates with an ultra-thin 90° layer, constituted by a single row of fibers across the thickness. Debonds appear at regular intervals measured in terms of number $n-1$ of fully bonded fibers present between them, which in turn correspond to the number of fibers along the horizontal direction of the RVE as highlighted in Fig. 1. They are thus the $n \times 1 - m \cdot t_{90^\circ}$ models, where $m = 1, 10$ and n is an integer ≥ 1 ($n = 1$ corresponds to the case of a debond appearing on all the fibers in the central 90° layer). These models are geometrically extreme, but allow to focus on the

interaction between debonds and the inter-ply 0°/90° interface. Furthermore, the *spread tow* technology is today capable of producing cross-ply laminates with the central 90° layer thickness only $4-5$ times the fiber diameter, as shown for example in [6], which may in future give practical relevance even to such extreme case.
The second set of models considers instead cross-ply laminates with a central 90° ply of variable thickness, measured in terms of number k of fiber rows "stacked" in the vertical direction in Figure 2. Once again, debonds appear in the central row only at regular intervals measured in terms of number $n-1$ of fully bonded fibers present between them, as highlighted in Fig. 2. These models are thus the $n \times k - m \cdot t_{90^\circ}$ models, where $m = 1, 10$, $k > 1$ and n is an integer ≥ 1 ($n = 1$ corresponds to the case of a debond appearing on all fibers of the central fiber row in the 90° layer). By increasing the number n of fibers in the horizontal direction in the RUC, decreasing levels of damage (debonds spaced further apart and the interaction between debonds becomes less important) are considered to be present in the laminate. By increasing the number k of fiber rows, the thickness of the 90° layer is increased and the effect of the relative proximity of the inter-ply 0°/90° interface can thus be studied. Finally, by increasing the factor m, the thickness of the 0° layers is increased for a given thickness of the 90°, which allows the investigation of the 0° ply-block effect [41].

B.3 Finite Element (FE) discretization

The RUCs are discretized and solved with the Finite Element Method (FEM) using the commercial FEM package Abaqus [38]. The total length and height of a RUC are determined by the number of fibers n in the horizontal direction, the number of fiber rows k across the thickness and the thickness ratio m (see Sec. B.1 and Sec. B.2). The debond appears symmetrically with respect to the x axis (see Fig. 3) and we characterize it with the angular size $\Delta\theta$ (the full debond size is thus $2\Delta\theta$). In the case of large debond sizes ($\geq 60^\circ - 80^\circ$), a region of size $\Delta\Phi$ to be determined by the solution itself appears at the crack tip. In this region, called the *contact zone*, the crack faces are in contact and slide on each other. Due to existence of the contact zone, frictionless contact is considered between the two crack faces to avoid interpenetration and allow free sliding. Symmetry with respect to the x axis is applied on the lower boundary. Kinematic coupling on the x-displacement is applied along the left and right boundaries of the model in the form of a constant x-displacement $\pm\bar{\varepsilon}_x nL$, corresponding to laminate x-strain $\bar{\varepsilon}_x$ equal to 1%. The bimaterial interface crack problem belongs to the class of *receding contact* [27, 42], i.e. such that the contact zone in the final configuration is smaller than in the initial one. It was shown that this class of problems has some peculiar properties [43, 44], which are valid both with and without friction at the interface [27, 42]: size and shape of the contact zone remain the same upon a change in the magnitude of the applied load; only a change in the disposition of the applied load causes a change in the size and shape of the contact zone; displacements, stresses and strains (and consequently, Energy Release Rate) are directly proportional to the value of the applied load. Thus, although our interest is to compare the relative magnitude of Mode I and Mode II ERR among differ-

ent configurations, the results presented could be used to compute the ERR at different levels of the applied strain through a simple multiplication.

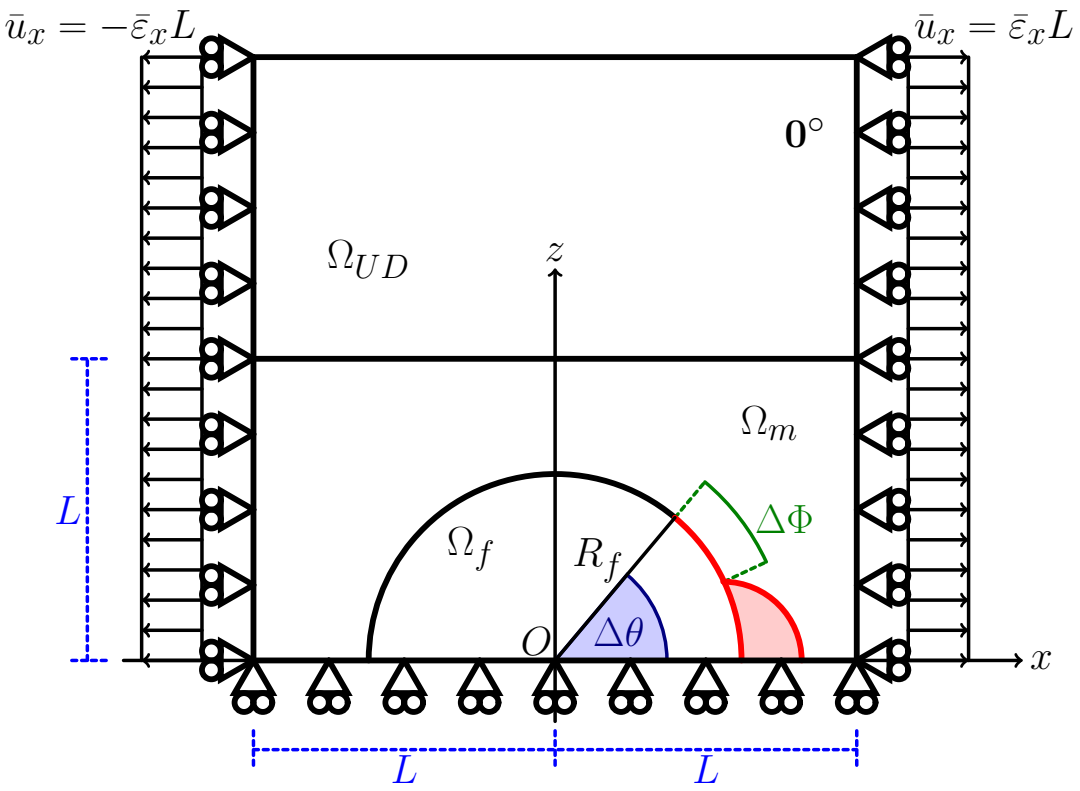

Figure 3: Schematic of the model with its main parameters.

The FEM model is discretized using second order, 2D, plane strain triangular (CPE6) and rectangular (CPE8) elements. In the crack tip neighborhood, a refined regular mesh of quadrilateral elements with almost unitary aspect ratio is needed to ensure a correct evaluation of the ERR. The angular size δ of an element in this refined region close to the crack tip is by design equal to 0.05°. The crack faces are modeled as element-based surfaces with a frictionless small-sliding contact pair interaction. The Mode I, Mode II and total Energy Release Rates (ERRs) (respectively G_I, G_{II} and G_{TOT}) represent the main result of the numerical analysis. They are computed using the VCCT [24] implemented in a custom Python routine. Glass fiber and epoxy are considered throughout this article, and it is assumed that their response always lies in the linear elastic domain. The effective UD properties are computed using Hashin's Concentric Cylinder Assembly model [45] with the self-consistency scheme for the out-of-plane shear modulus of Christensen [46]. The properties used are listed in Table 1. The model was validated with respect to BEM results of [47, 33]; considerations about the order of accuracy can be found in [40].

Table 1: Summary of mechanical properties of fiber, matrix and UD layer (GF: glass fiber; EP: epoxy; UD: glass-fiber/epoxy uni-directional properties).

	$V_f\,[\%]$	$E_L\,[GPa]$	$E_T\,[GPa]$	$G_{LT}\,[GPa]$	$\nu_{LT}\,[-]$	$\nu_{TT}\,[-]$
GF	-	70.0	70.0	29.2	0.2	0.2
EP	-	3.5	3.5	1.25	0.4	0.4
UD	60.0	43.442	13.714	4.315	0.273	0.465

C Results & Discussion

C.1 Effect of the proximity of the $0°/90°$ interface and of the thickness of the $0°$ layer on debond ERR for highly interactive debonds

We first focus our attention on the model $1 \times 1 - m \cdot t_{90°}$, which represents a particular case of the family $n \times 1 - m \cdot t_{90°}$. It corresponds to a cross-ply laminate in which the central 90° ply is constituted by only one fiber row, in which each fiber possesses a debond appearing on alternating sides. The model thus represents an extreme idealization, in the sense that: first, the central 90° layer is the thinniest that can be conceived, which allows us to investigate the direct effect of the proximity of the $0°/90°$ interface on debond ERR; second, a very particular damage state is present for which every fiber is partially debonded from the sorrounding matrix, corresponding to the most severe damage state that can occur in the 90° ply when considering debonds as the only mechanism of damage. We are thus focusing on the presence of the $0°/90°$ interface and on the thickness of the 0° layer, by considering the ratio $m = \frac{t_{0°}}{t_{90°}}$ of ply thicknessess as a free parameter.

In Figures 4 and 5 it is possible to observe respectively the Mode I and Mode II ERR for models $1 \times 1 - m \cdot t_{90°}$ with $m = 1, 10, 100$. Mode I ERR is practically unaffected by the 0° layer thickness, only a marginal increase $\leq 1\%$ can be seen when m is increased from 1 to 10. No further observable change is present when m is increased to 100. Moreover, the contact zone onset, which corresponds to the first value of $\Delta\theta$ such that $G_I = 0$, is always equal to 70° irrespective of the value of m. A more remarkable, albeit small, effect of the 0° layer thickness can be observed for Mode II when m is increased from 1 to values ≥ 10. For open cracks, i.e. when no contact zone is present and thus $\Delta\theta$ is smaller than 70°, increasing the 0° layer thickness causes a reduction of Mode II ERR; while for closed cracks, when a contact zone is present and $\Delta\theta > 70°$, the increase in thickness leads to an increase in ERR.

In order to understand the interaction mechanism between the $0°/90°$ interface and the debond, Mode I and Mode II ERR are reported respectively in Figures 4 and 5 for models $1 \times 1 - free$, $1 \times 1 - H$, $1 \times 1 - coupling$ and $1 \times 1 - coupling + H$. These RUCs all present equivalent boundary conditions and it is here useful to recall their characteristics:

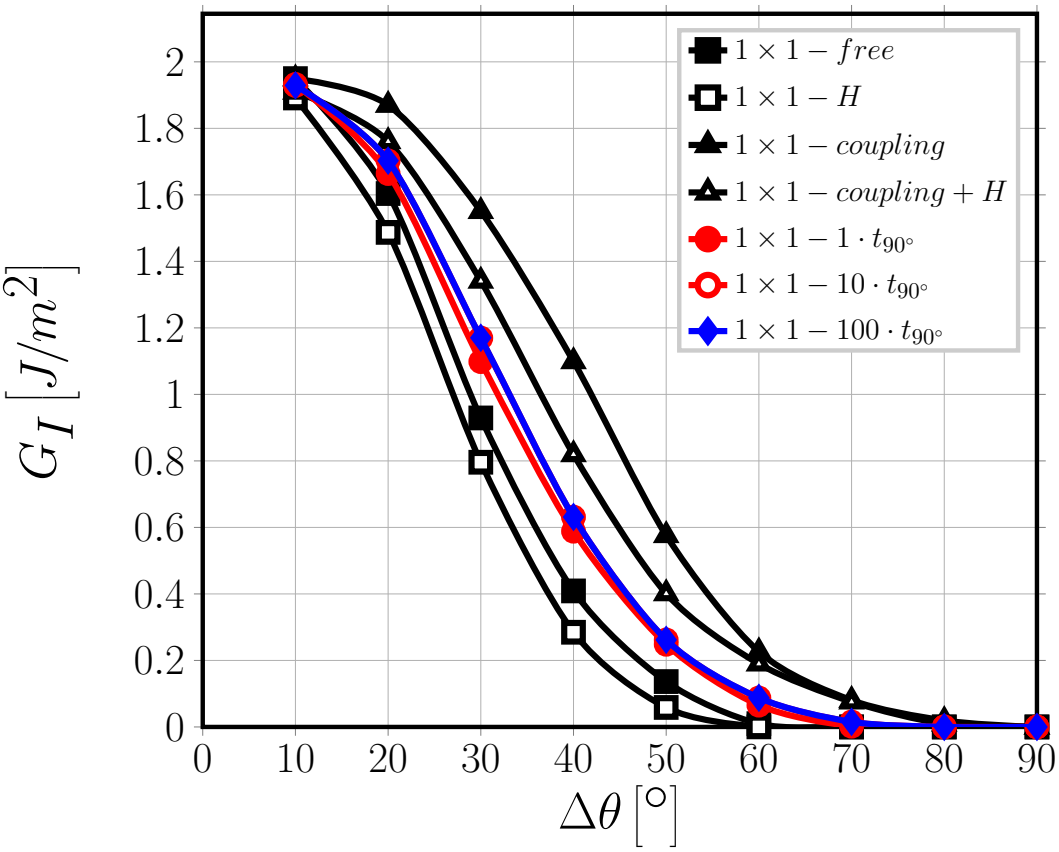

Figure 4: Effect of the proximity of the $0°/90°$ *interface and of the thickness of the* $0°$ *layer on Mode I ERR: models* $1 \times 1 - free$, $1 \times 1 - H$, $1 \times 1 - coupling$, $1 \times 1 - coupling + H$ *and* $1 \times 1 - m \cdot t_{90^\circ}$. $V_f = 60\%$, $\bar{\varepsilon}_x = 1\%$.

in model $1 \times 1 - free$ the upper bounday is left free; coupling conditions on the vertical displacements u_z are applied to the upper boundary in model $1 \times 1 - coupling$ (coupling condition); in model $1 \times 1 - H$ a linearly distributed horizontal displacement u_x is applied to the upper boundary (H-condition); in model $1 \times 1 - coupling + H$ coupling conditions on the vertical displacements u_z and a linearly distributed horizontal displacement u_x are imposed together on the upper boundary. Given that the presence of a $0°$ layer provides two constraints: first, it tends to keep the $90°$ layer boundary straight; second, it forces a more homogeneous horizontal displacement at the $90°$ layer boundary; the equivalent boundary conditions of $1 \times 1 - coupling$, $1 \times 1 - H$ and $1 \times 1 - coupling + H$ represent an extreme case respectively of the first constraint ($1 \times 1 - coupling$), the second constraint ($1 \times 1 - H$) and the two together ($1 \times 1 - coupling + H$). The case $1 \times 1 - free$ constitutes instead the base case (absence of $0°$ layer), on which comparisons are built.
Observing Figure 4, it is possible to notice that the values of G_I for the $1 \times 1 - free$ and the $1 \times 1 - coupling$ models represent respectively a lower and an upper bound for the $1 \times 1 - m \cdot t_{90^\circ}$ RVEs: this is true with respect to the value of G_I as well as of contact zone onset ($60°$ for $1 \times 1 - free$, $70°$ for $1 \times 1 - m \cdot t_{90^\circ}$, $80°$ for $1 \times 1 - coupling$). When the

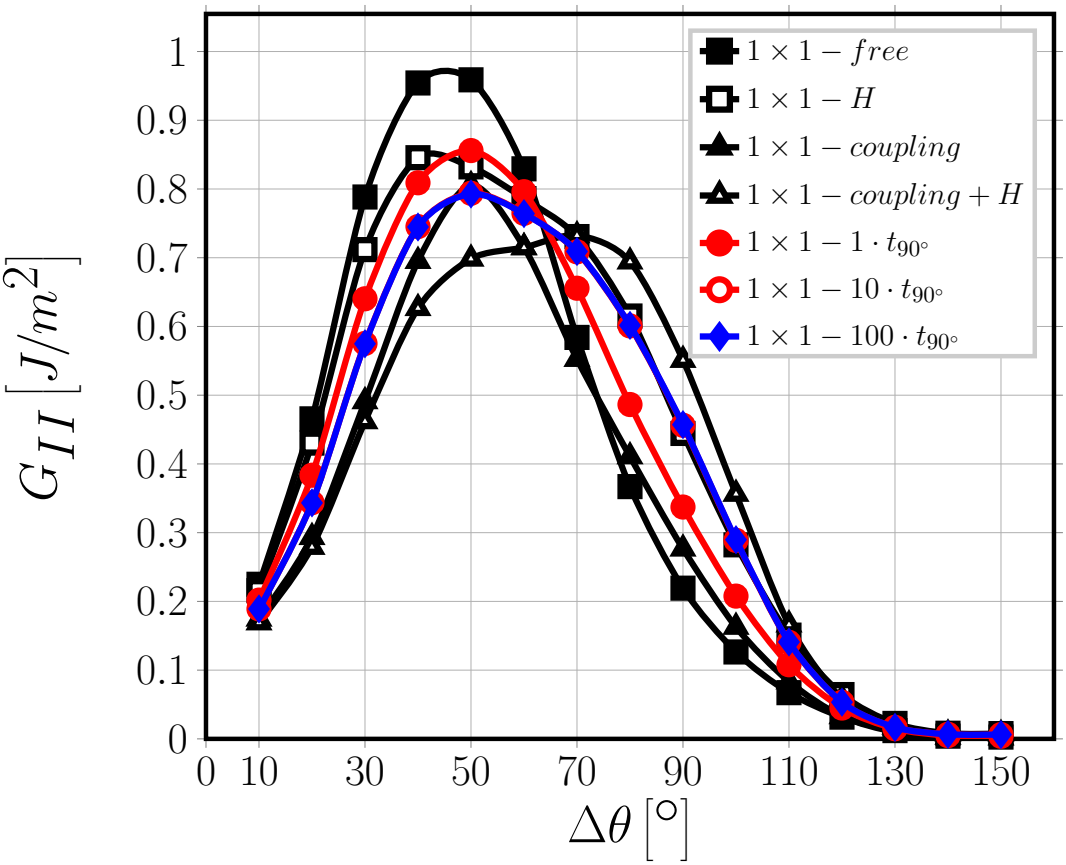

Figure 5: Effect of the proximity of the $0°/90°$ *interface and of the thickness of the* $0°$ *layer on Mode II ERR: models* $1\times1-free$, $1\times1-H$, $1\times1-coupling$, $1\times1-coupling+H$ *and* $1\times1-m\cdot t_{90^\circ}$. $V_f = 60\%$, $\bar{\varepsilon}_x = 1\%$.

H-condition is added to the $1\times1-free$ and the $1\times1-coupling$ models, thus obtaining the $1\times1-H$ and $1\times1-coupling+H$ models, G_I decreases while the value of $\Delta\theta$ at contact zone onset remains unchanged ($60°$ for $1\times1-free$ and $1\times1-H$, $80°$ for $1\times1-coupling$ and $1\times1-coupling+H$). Moreover, it is possible to observe that the values of G_I of $1\times1-coupling+H$ are much closer to but always greater than those of $1\times1-m\cdot t_{90^\circ}$ RVEs, thus constituting a more representative upper bound for the latter. Analogous considerations are drawn with regard to Mode II (see Fig. 5). For small debonds, $\Delta\theta \leq 30°$, no significant difference in G_{II} can be seen between $1\times1-free$ and $1\times1-H$ and between $1\times1-coupling$ and $1\times1-coupling+H$ in this region. With respect to $1\times1-m\cdot t_{90^\circ}$ RVEs, the first pair ($1\times1-free$ and $1\times1-H$) represents the lower bound while the second pair ($1\times1-coupling$ and $1\times1-coupling+H$) the upper bound. For $30° < \Delta\theta \leq 60°$, $1\times1-H$ and $1\times1-coupling+H$ provide significantly lower values of G_{II} than respectively $1\times1-free$ and $1\times1-coupling$. G_{II} values of $1\times1-H$ are very close to $1\times1-1\cdot t_{90^\circ}$, even coincident for $\Delta\theta = 60°$. On the other hand, G_{II} values of $1\times1-coupling$ are very close to $1\times1-m\cdot t_{90^\circ}$ with $m \geq 10$ and even coincident for $\Delta\theta = 50°$. For $60° < \Delta\theta \leq 110°$, the situation changes. $1\times1-free$ and

$1 \times 1 - coupling$ provides values of G_{II} close to each other, even coincident for $\Delta\theta = 70°$. Values of G_{II} of $1 \times 1 - H$ and $1 \times 1 - coupling + H$ are significantly larger than both $1 \times 1 - free$ and $1 \times 1 - coupling$. Furthermore, G_{II} values of $1 \times 1 - H$ coincide with those of $1 \times 1 - m \cdot t_{90°}$ with $m \geq 10$. Mode II ERR of $1 \times 1 - 1 \cdot t_{90°}$ is instead close, but not coincident, to that of $1 \times 1 - coupling$. For $\Delta\theta > 110°$, G_{II} is the same for all models and reaches 0 at a debond size of around 130°.

These results help to understand the effect of the 0°/90° interface on debond ERR. Two constraining mechanisms are present in the case of 0°/90° interface that are absent in the free surface case: first, the boundary of the 90° layer remains straighter (effect modelled by the coupling condition in $1 \times 1 - coupling$); second, the x-strain on the 90° layer boundary is more uniform (effect modelled by the H-condition in $1 \times 1 - H$).

For small debonds ($\Delta\theta < 60° - 70°$), the presence of the 0°/90° interface causes an increase of G_I and a decrease of G_{II} with respect to the free surface case. For Mode I, the fact that the 90° layer boundary remains straight (coupling condition) forces the debond to open more than in the free case, thus increasing G_I. However, the uniformity of the x-strain on the 90° layer boundary reduces the local (in the debond neighborhood) x-strain magnification and contains the increase in G_I. This corresponds in Figure 4 to the fact that Mode I ERR for $1 \times 1 - m \cdot t_{90°}$ is always higher than $1 \times 1 - free$ but lower than $1 \times 1 - coupling$, and it is best approximated by $1 \times 1 - coupling + H$. For Mode II in the case of small debonds, the presence of the 0° layer keeps the 0°/90° interface straighter and reduces the vertical contraction of the matrix, which contributes for the most part to Mode II in this range, thus leading to a decrease of G_{II}. The small effect of 0° layer thickness on Mode II (Fig. 5) can be explained in terms of local bending stiffness: a thinner 0° layer ($\frac{t_{0°}}{t_{90°}} = 1$) does not keep the 90° layer boundary as straight as thicker 0° layers ($\frac{t_{0°}}{t_{90°}} \geq 10$). In the case $\frac{t_{0°}}{t_{90°}} = 1$, the 90° layer boundary deforms in a way that is similar to the free surface case, but smaller in magnitude. This corresponds to the fact that for $\Delta\theta < 60° - 70°$, in Figure 5: $1 \times 1 - 1 \cdot t_{90°}$ is best approximated by $1 \times 1 - H$ (curved 90° layer boundary but uniform x-strain at the 90° layer boundary that disfavors G_{II}), $1 \times 1 - m \cdot t_{90°}, m \geq 10$ is best approximated by $1 \times 1 - coupling$ (straight 90° layer boundary).

For debonds larger than 70°, the presence of the 0°/90° interface causes an increase of G_{II} with respect to the free surface case. The uniform x-strain distribution on the 90° layer boundary determined by the presence of the 0° layer causes, with respect to the free case, the matrix x-strain to be higher in the $x \sim 0$ neighborhood and lower around $x \sim \pm L$, in order to keep the average ε_x at 1%. Given that for large debonds Mode II ERR is determined mostly by the magnitude of the x-strain gap (between the matrix x-strain and the fiber x-strain), an increase of G_{II} is thus observed in the presence of the 0°/90° interface. Again, the observed effect of the 0° layer thickness on Mode II for $\Delta\theta > 60° - 70°$ (Fig. 5) can be discussed in terms of local 0° layer bending stiffness. In the free case, it is the curvature of the material around the fiber that causes the x-strain reduction and thus a lower G_{II}. Thicker 0° layers ($\frac{t_{0°}}{t_{90°}} \geq 10$) prevent this 90° boundary deformation to a greater extent than the thinner $t_{0°} = t_{90°}$ case: the x-strain (and thus G_{II}) increase is greater for $\frac{t_{0°}}{t_{90°}} \geq 10$ than $\frac{t_{0°}}{t_{90°}} = 1$.

C.2 Effect of the proximity of the $0°/90°$ interface and of the thickness of the $0°$ layer on non-interactive debonds in a one-fiber row $90°$ ply

We turn now our attention to models $n \times 1 - m \cdot t_{90°}$, which correspond to a cross-ply laminate in which the central 90° ply is constituted by only one fiber row where multiple partially debonded fibers are present with $n-1$ fully bonded fibers between them and debonds appear on alternating sides of consecutive damaged fibers (see Figure 1). As observed in a previous work [40], the presence of fully bonded fibers between partially debonded ones in the loading direction has a strong effect on debond ERR and controls the interaction between debonds. When n is increased, both Mode I and Mode II increase: the addition of stiffer elements, in the form of fully bonded fibers, increase the strain applied to the damaged unit and thus causes higher values of ERR. Looked from this perspective, i.e. moving from the most to the least severe state of damage, this effect is referred to as "strain magnification" [40]. There seems to exist a characteristic distance, measured in terms of fully bonded fibers, above which a change in the number of undamaged fibers affects only marginally, or even not at all, debond ERR. This distance, generally $n \sim 20$, marks the transition between a non-interactive solution ($n > 20$) and an interactive one ($n < 20$). The "strain magnification" effect thus represents the transition from the interactive to the non-interactive solution. If in Sec. C.1 we studied the effect of the proximity of the $0°/90°$ interface and of the thickness of the $0°$ layer on interactive debonds ($1 \times 1 - \dots$), we analyze in the present section the effect of the $0°/90°$ interface and of the $0°$ layer thickness on non-interactive ones ($n \times 1 - \dots$ with $n > 20$).

Comparing Fig. 6 with Fig. 4 and Fig. 7 with Fig. 5, it is possible to observe how, as previously described, increasing the number of fully bonded fibers between consecutive debonds in the loading direction leads to an increase in Mode I and Mode II ERR. The peak G_I increases from 1.93 $\left[\frac{J}{m^2}\right]$ in $1 \times 1 - 1 \cdot t_{90°}$ to 3.42 $\left[\frac{J}{m^2}\right]$ in $21 \times 1 - 1 \cdot t_{90°}$, while the peak G_{II} from 0.86 $\left[\frac{J}{m^2}\right]$ to 3.04 $\left[\frac{J}{m^2}\right]$. The value of $\Delta\theta$ at contact zone onset remains however the same (70°).
The effect of the $0°$ layer thickness is instead non-existent: values of both G_I and G_{II} are coincident for $21 \times 1 - 1 \cdot t_{90°}$ and $21 \times 1 - 10 \cdot t_{90°}$.

In agreement with the introductory considerations of this section and the results in [40], it is possible to observe in Figures 6 and 7 that $21 \times 1 - free$ and $21 \times 1 - coupling$ (in which the horizontal displacement u_x is left uncostrained on the upper boundary) show both the highest values of Mode I and Mode II ERR as well as the maximum increase with respect to the interactive case ($1 \times 1 - free$ and $1 \times 1 - coupling$). When the H-condition is applied to the upper boundary, thus constraining the magnitude of the strain magnification effect, both the magnitude of Mode I and Mode II ERR as well as their relative increase with respect to the interactive case are significantly reduced. $21 \times 1 - coupling + H$ represents, when considering both Mode I and Mode II ERR, the best approximation to the results of $21 \times 1 - m \cdot t_{90°}$. The mechanisms at play are the

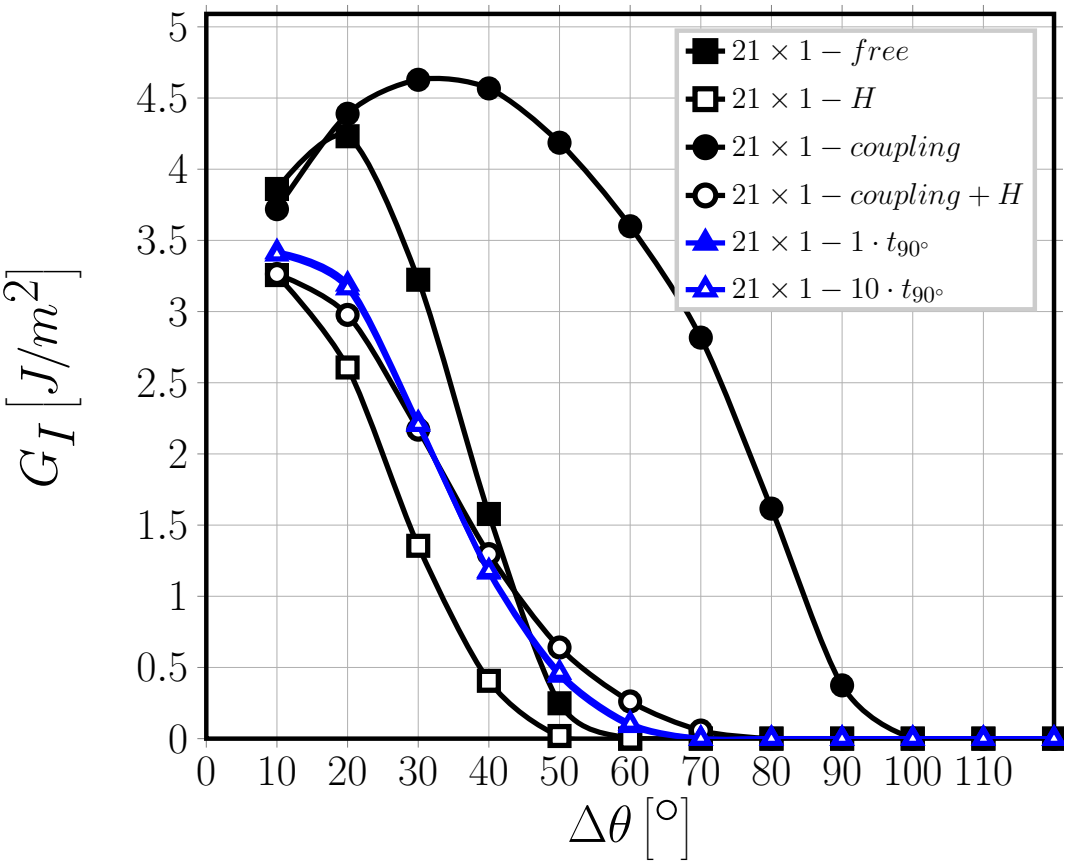

Figure 6: Effect of the presence of the 0° *layer on Mode I ERR of non-interactive debonds: models* $21\times1-free$, $21\times1-H$, $21\times1-coupling$, $21\times1-coupling+H$, $21\times1-1\cdot t_{90^\circ}$ *and* $21\times1-10\cdot t_{90^\circ}$. $V_f=60\%$, $\bar{\varepsilon}_x=1\%$.

same as in Sec. C.1: by keeping the $0^\circ/90^\circ$ interface straight (coupling condition), the 0° layer favors an increase in G_I and decrease in G_{II} for small debonds and an increase in G_{II} for large debonds; by applying a uniform x-strain on the 90° layer boundary (H-condition), the 0° layer promotes a more uniform x-strain in the 90° layer and acts against the strain magnification effect, reducing debond ERR. Results in Fig. 6 and Fig. 7 show that the latter effect (H-condition) is dominant. It seems reasonable to conclude that debond growth is favored (i.e. debond ERR is higher) in the presence of strain or stress concentrations (as for example in the presence of a free surface or only coupling conditions on the vertical displacement), while more uniform strain and stress fields as those created by the proximity of the $0^\circ/90^\circ$ interface reduce both Mode I and Mode II ERR and thus tend to prevent debond growth.

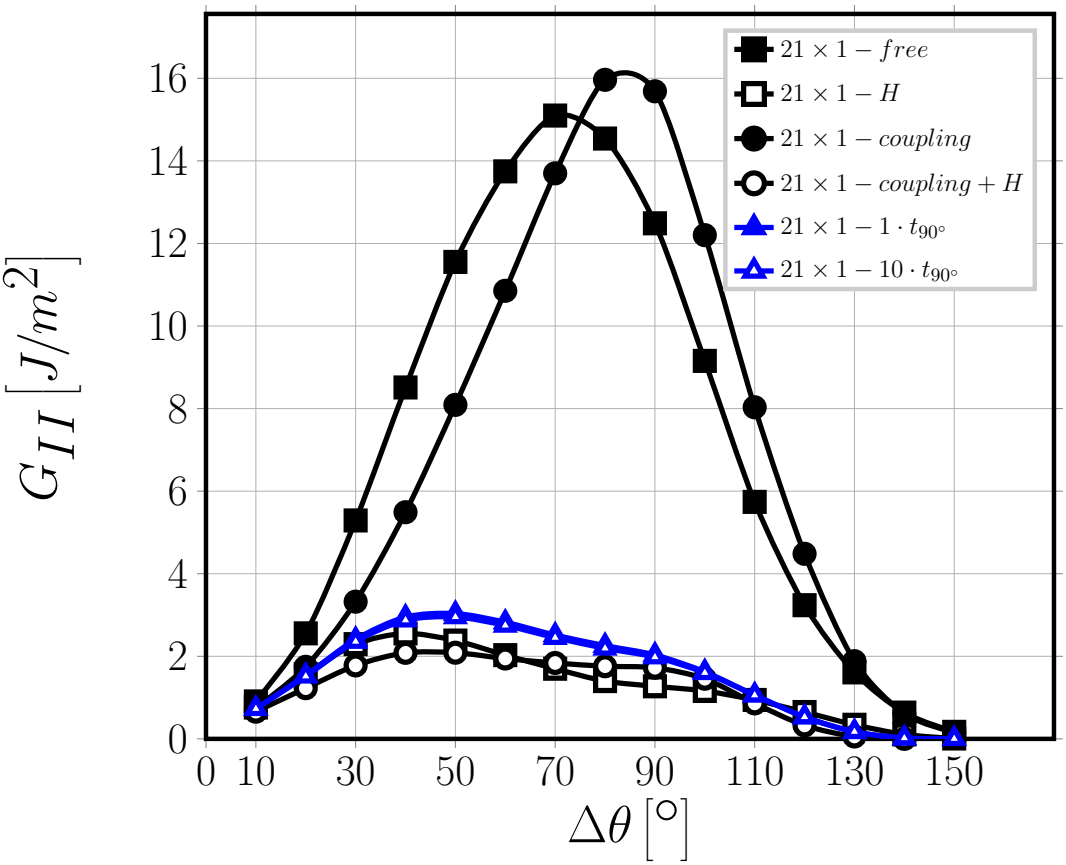

Figure 7: Effect of the presence of the 0° *layer on Mode II ERR of non-interactive debonds: models* $21 \times 1 - free$, $21 \times 1 - H$, $21 \times 1 - coupling$, $21 \times 1 - coupling + H$, $21 \times 1 - 1 \cdot t_{90^\circ}$ *and* $21 \times 1 - 10 \cdot t_{90^\circ}$. $V_f = 60\%$, $\bar{\varepsilon}_x = 1\%$.

C.3 Effect of the presence of fiber rows with no damage on the debond-$0^\circ/90^\circ$ interface interaction

After having investigated the effect of the proximity of the $0^\circ/90^\circ$ interface and of the thickness of the 0° layer on debond ERR for different cases of debond-debond interaction in the same fiber row, we address in this section the effect of the presence of fiber rows with only fully bonded fibers between debonds and the $0^\circ/90^\circ$ interface. In other words, we are separating the debond from the $0^\circ/90^\circ$ interface by inserting rows of fully bonded fibers in between. We consider only the case $m = 1$, i.e. $t_{0^\circ} = t_{90^\circ}$, given that increasing the 0° layer thickness does not result in any remarkable effect on ERR as shown in Sec. C.1 and Sec. C.2. Following the same philosophy of Sec. C.1 and Sec. C.2, we analyze the effect of the presence of fiber rows with no damage on debond ERR: first, when the central fiber row possesses only partially debonded fibers, which represents the most severe damage state for these RUCs and the solution for interactive debonds (models $1 \times k - 1 \cdot t_{90^\circ}$ in Figures 8 and 9); second, the case of debonds separated by $n - 1$ fully bonded fibers in the central fiber row, which corresponds to the least severe

state of damage and to the solution for non-interactive debonds (models $21 \times k - 1 \cdot t_{90^\circ}$ in Figures 10 and 11).

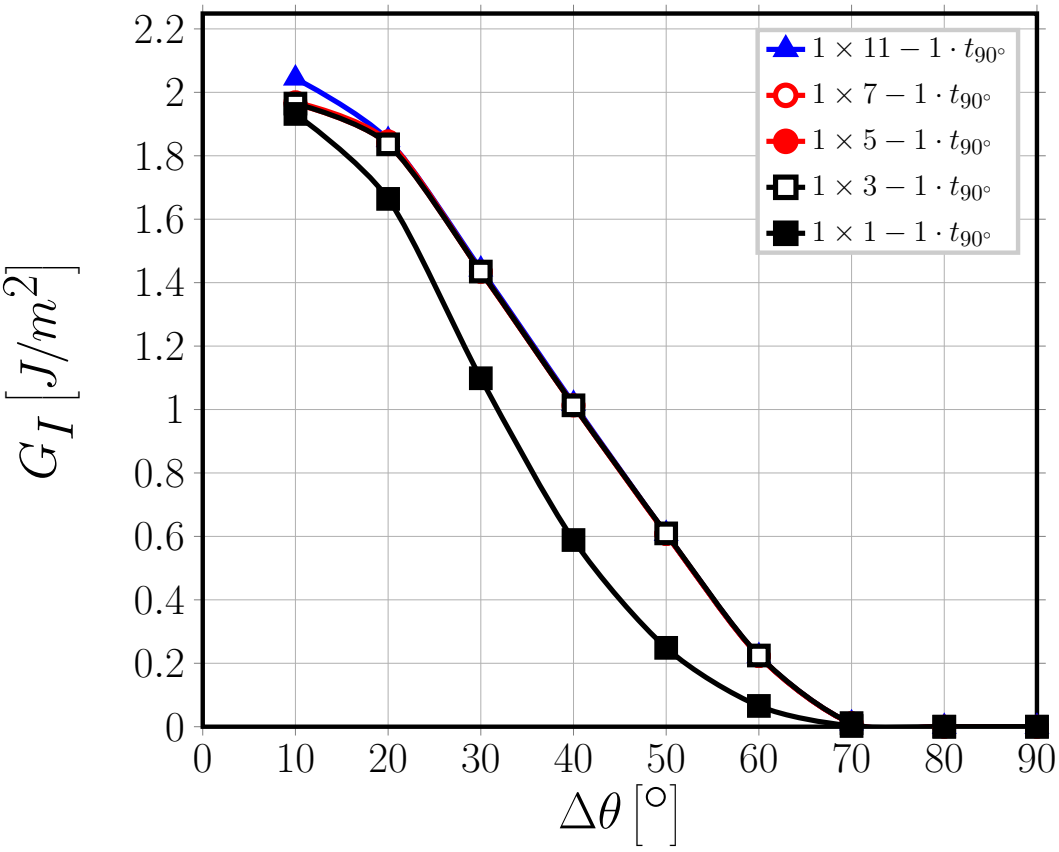

Figure 8: Effect of the presence of undamaged fiber rows in the 90° *layer on debond-*0°/90° *interface interaction for Mode I ERR: models* $1 \times k - 1 \cdot t_{90^\circ}$. $V_f = 60\%$, $\bar{\varepsilon}_x = 1\%$.

Observation of Fig. 8, Fig. 9, Fig. 10 and Fig. 11 reveals that no difference can be seen in Mode I and Mode II ERR by increasing the number k of rows with undamaged fibers when $k \geq 3$, which means that debond ERR does not change once at least 1 row of undamaged fibers is present between the debond and the 0°/90° interface. A significant change is visible only when $k = 1$, which means that no row of undamaged fibers is present between the debond and the 0°/90° interface. This change, from $k \geq 3$ to $k = 1$, corresponds in particular to a reduction of both G_I and G_{II}.

The results of Figures 8, 9, 10 and 11 imply that the mechanisms of debond-0°/90° interface interaction described in Sec. C.1 and Sec. C.2 are actually very localized and that debond ERR is affected by the presence of the 0°/90° interface only when no fully bonded fiber is placed in between. Given that the number k of fibers in the RUC vertical direction corresponds to the thickness of the 90° ply measured in terms of number

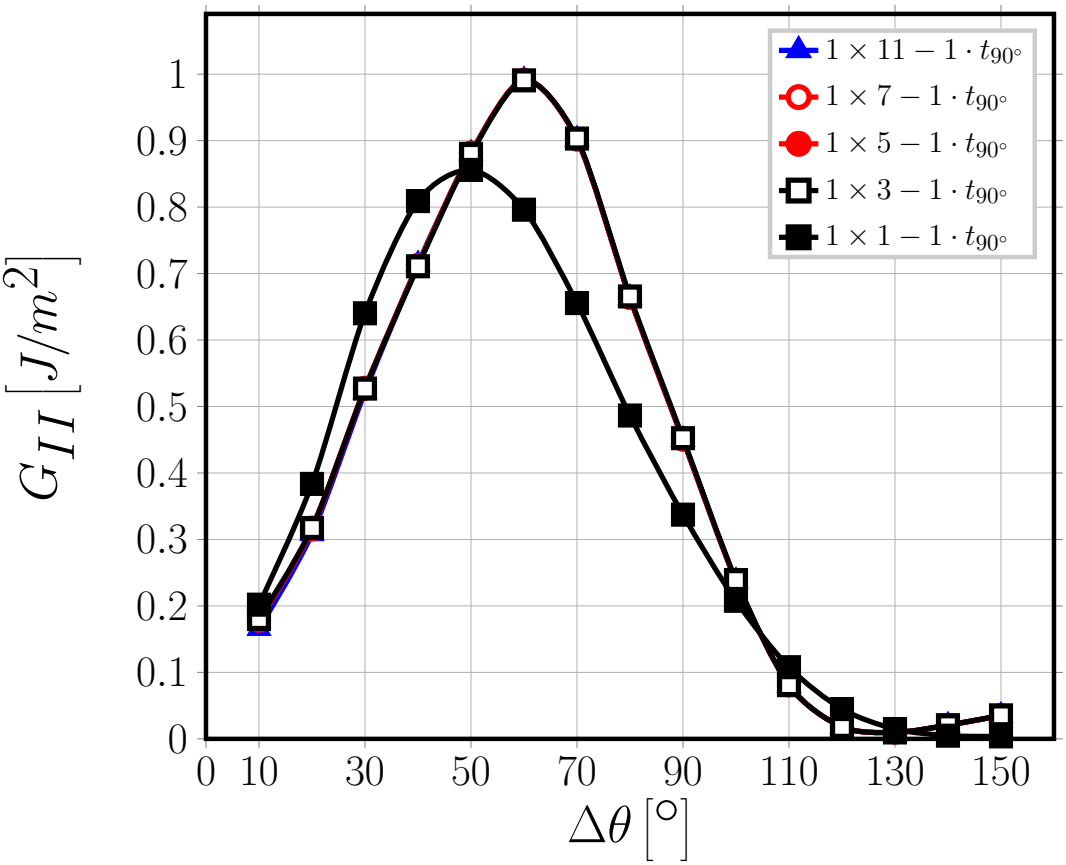

Figure 9: Effect of the presence of undamaged fiber rows in the 90° *layer on debond-*0°/90° *interface interaction for Mode II ERR: models* $1 \times k - 1 \cdot t_{90^\circ}$. $V_f = 60\%$, $\bar{\varepsilon}_x = 1\%$.

of fiber rows present through its thickness, the results presented here point to another conclusion: the ply-thickness effect does not seem to apply to debond growth, unless an *ultra-thin* ply constituted by only one fiber row ($k = 1$) is considered.

Analogous results can be found in [36, 37], where the authors investigate the ply-thickness effect on debond growth in cross-ply laminates using: first, a single centrally-placed partially debonded fiber with surrounding matrix corresponding to $V_f = 55\%$, embedded from all sides in a homogenized 90° ply bounded by homogenized 0° layers; second, one partially debonded fiber placed in the center and a second partially debonded fiber placed at an angle θ_2 with respect to the horizontal direction with surrounding matrix corresponding to $V_f = 55\%$, embedded from all sides in a homogenized 90° ply bounded by homogenized 0° layers. The thickness of the 0° layer is chosen as reference and a $\left[0^\circ_p, 90^\circ_{r \cdot p}\right]_S$ laminate is considered. Carbon-epoxy and glass-epoxy systems are both studied. The thickness of the 90° ply, $t_{90^\circ} = r \cdot t_{0^\circ}$, varies from $r = 3$ (thick 90° ply, > 100 fiber diameters) to $r = 0.1$ (thin 90° ply, $\sim 4 - 5$ fiber diameters). No measurable ply-thickness effect was observed. Experimental support to the claim that the ply-thickness effect has no influence on debond growth can be also found in the literature, in [6]. The

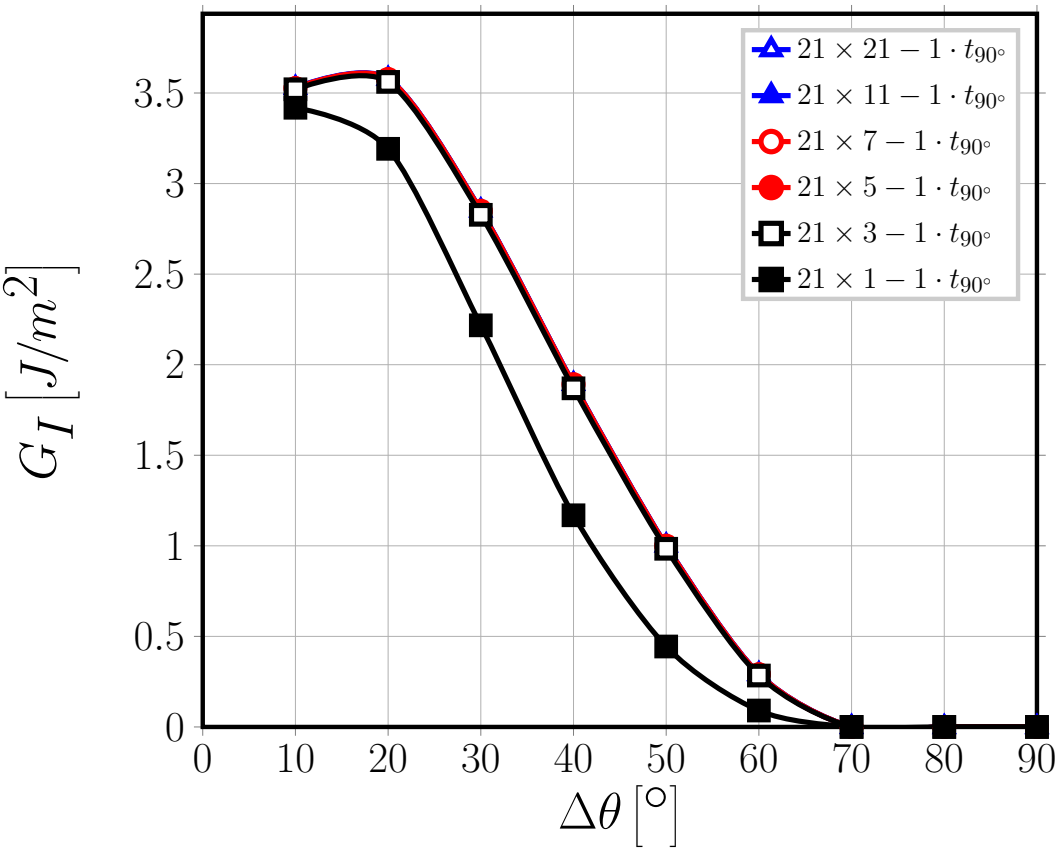

Figure 10: Effect of the presence of undamaged fiber rows in the 90° *layer on debond-*0°/90° *interface interaction for Mode I ERR: models* $n \times k - 1 \cdot t_{90^\circ}$. $V_f = 60\%$, $\bar{\varepsilon}_x = 1\%$.

authors conducted *in-situ* observations of edge micro-cracks with an optical microscope on $[0^\circ_2, 90^\circ_n, 0^\circ_2]$ carbon fiber-epoxy laminates with $n = 1, 2, 4$, corresponding to a 90° ply thickness of respectively 40 $[\mu m]$ ($\sim 6 - 8$ fiber diameters), 80 $[\mu m]$ ($\sim 12 - 16$ fiber diameters) and 160 $[\mu m]$ ($\sim 24 - 32$ fiber diameters). For $n = 1$, i.e. the case of a very thin 90° ply, isolated debonds appear at a lower value of the applied strain than in thicker plies (at 0.4% vs 0.7%) while growth and coalescence of debonds is suppressed and no transverse crack can be observed even at a strain of 1.5%. The ply-thickness effect was thus observed in [6] for transverse cracks, i.e. coalescence of debonds was delayed to higher strains and even suppressed, but not for debond growth. The analysis presented in this article brings new arguments to the claim that the ply-thickness effect does not influence the growth of debonds.

D Conclusions

Different models of Repeating Unit Cell, representing different cross-ply laminates, have been studied in order to investigate the effect of the presence of the 0° layer and of its thickness on debond Energy Release Rate for interactive and non-interactive debonds. A

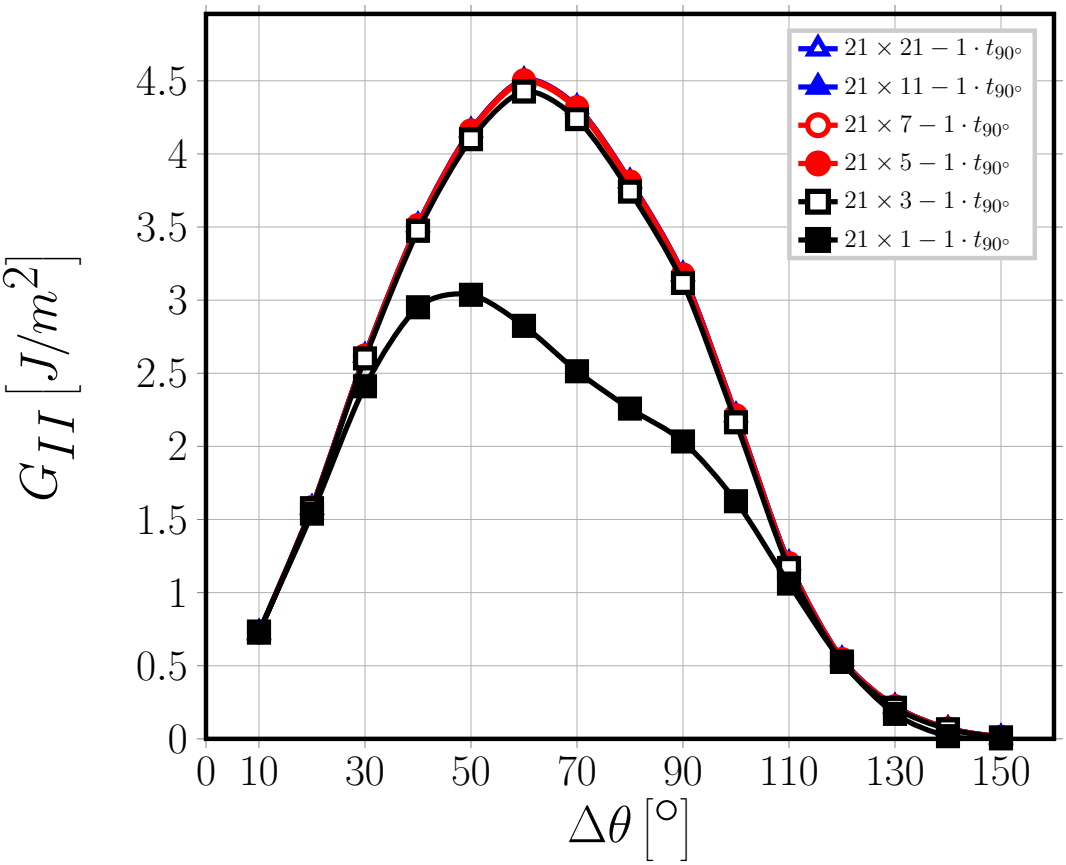

Figure 11: Effect of the presence of undamaged fiber rows in the 90° *layer on debond-*0°/90° *interface interaction for Mode II ERR: models* $n \times k - 1 \cdot t_{90°}$. $V_f = 60\%$, $\bar{\varepsilon}_x = 1\%$.

particular damage state is studied, in which only the central row of fibers of the 90° ply possesses debonds. The thickness of the 90° ply is measured in terms of the number of fiber rows in the layer; the 0° layer is on the other hand modelled as a homogenized material, the thickness of which is a multiple of the 90° ply thickness. In order to investigate the mechanisms of the debond-0°/90° interface interaction, Mode I and Mode II ERR of cross-ply RUCs are compared with those of RUCs with equivalent boundary conditions on the upper boundary: free surface; coupling conditions on the vertical displacements; an applied linear distribution of the horizontal displacement; coupling conditions on the vertical displacements superimposed to an applied linear distribution of the horizontal displacement (this last combination represents the most extreme effect of the 0° layer on debond growth). It has been found that:

- by forcing the 0°/90° interface to remain approximately straight and controlling the uniformity of the horizontal displacements in the composite (and thus in the 90° ply), the presence of the 0° layer causes more homogeneous local (i.e. in the debond neighborhood) strains, reducing the ERR at the debond crack tip;
- when increasing the thickness of the 0° layer, the effect of the presence of the 0°

layer on debond ERR remains the same as in the case $t_{0^\circ} = t_{90^\circ}$;

- no effect of the 90° layer thickness, measured in terms of number of fiber rows, is observed; a reduction in ERR takes place only when the thickness is reduced to only one fiber row.

The results reported in this article strengthen the claim that the ply-thickness effect does not influence the growth of individual debonds, as previously suggested in the literature [6, 18, 36, 37].

Acknowledgements

Luca Di Stasio gratefully acknowledges the support of the European School of Materials (EUSMAT) through the DocMASE Doctoral Programme and the European Commission through the Erasmus Mundus Programme.

References

[1] Kazumasa Kawabe. "New Spreading Technology for Carbon Fiber Tow and Its Application to Composite Materials". Japanese. In: *Sen'i Gakkaishi* 64.8 (2008), pp. 262–267. DOI: 10.2115/fiber.64.p_262.

[2] K. Yamaguchi and H.T. Hahn. "The improved ply cracking resistance of thin-ply laminates". In: *Proceedings of the* 15^{th} *International Conference on Composite Materials (ICCM-15)*. (Durban, South Africa, June 27–July 2, 2005). 2005.

[3] S. Sihn et al. "Experimental studies of thin-ply laminated composites". In: *Composites Science and Technology* 67.6 (May 2007), pp. 996–1008. DOI: 10.1016/j.compscitech.2006.06.008.

[4] Tomohiro Yokozeki, Yuichiro Aoki, and Toshio Ogasawara. "Experimental characterization of strength and damage resistance properties of thin-ply carbon fiber/toughened epoxy laminates". In: *Composite Structures* 82.3 (Feb. 2008), pp. 382–389. DOI: 10.1016/j.compstruct.2007.01.015.

[5] Tomohiro Yokozeki et al. "Damage characterization in thin-ply composite laminates under out-of-plane transverse loadings". In: *Composite Structures* 93.1 (Dec. 2010), pp. 49–57. DOI: 10.1016/j.compstruct.2010.06.016.

[6] Hiroshi Saito, Hiroki Takeuchi, and Isao Kimpara. "Experimental Evaluation of the Damage Growth Restraining in 90° Layer of Thin-ply CFRP Cross-ply Laminates". In: *Advanced Composite Materials* 21.1 (2012), pp. 57–66. DOI: 10.1163/156855112X629522.

[7] A. Arteiro et al. "Notched response of non-crimp fabric thin-ply laminates". In: *Composites Science and Technology* 79 (Apr. 2013), pp. 97–114. DOI: 10.1016/j.compscitech.2013.02.001.

[8] A. Arteiro et al. "Large damage capability of non-crimp fabric thin-ply laminates". In: *Composites Part A: Applied Science and Manufacturing* 63 (Aug. 2014), pp. 110–122. DOI: 10.1016/j.compositesa.2014.04.002.

[9] R. Amacher et al. "Thin ply composites: Experimental characterization and modeling of size-effects". In: *Composites Science and Technology* 101 (Sept. 2014), pp. 121–132. DOI: 10.1016/j.compscitech.2014.06.027.

[10] G. Guillamet et al. "Damage occurrence at edges of non-crimp-fabric thin-ply laminates under off-axis uniaxial loading". In: *Composites Science and Technology* 98 (June 2014), pp. 44–50. DOI: 10.1016/j.compscitech.2014.04.014.

[11] J. Cugnoni et al. "Towards aerospace grade thin-ply composites: Effect of ply thickness, fibre, matrix and interlayer toughening on strength and damage tolerance". In: *Composites Science and Technology* 168 (Nov. 2018), pp. 467–477. DOI: 10.1016/j.compscitech.2018.08.037.

[12] Alexander Kopp et al. "The Aurora space launcher concept". In: *CEAS Space Journal* 10.2 (Nov. 2017), pp. 167–187. DOI: 10.1007/s12567-017-0184-2.

[13] J. E. Bailey and A. Parvizi. "On fibre debonding effects and the mechanism of transverse-ply failure in cross-ply laminates of glass fibre/thermoset composites". In: *Journal of Materials Science* 16.3 (Mar. 1981), pp. 649–659. DOI: 10.1007/bf02402782.

[14] R. Krueger, K. N. Shivakumar, and I. S. Raju. "Fracture Mechanics Analyses for Interface Crack Problems - A Review". In: *54th AIAA, ASME, ASCE, AHS, ASC Structures, Structural Dynamics, and Materials Conference*. American Institute of Aeronautics and Astronautics, Apr. 2013. DOI: 10.2514/6.2013-1476.

[15] V.I. Kushch et al. "Numerical simulation of progressive debonding in fiber reinforced composite under transverse loading". In: *International Journal of Engineering Science* 49.1 (Jan. 2011), pp. 17–29. DOI: 10.1016/j.ijengsci.2010.06.020.

[16] Luis Pablo Canal et al. "Intraply fracture of fiber-reinforced composites: Microscopic mechanisms and modeling". In: *Composites Science and Technology* 72.11 (June 2012), pp. 1223–1232. DOI: 10.1016/j.compscitech.2012.04.008.

[17] Lyazid Bouhala et al. "Modelling of failure in long fibres reinforced composites by X-FEM and cohesive zone model". In: *Composites Part B: Engineering* 55 (Dec. 2013), pp. 352–361. DOI: 10.1016/j.compositesb.2012.12.013.

[18] Miguel Herráez et al. "Transverse cracking of cross-ply laminates: A computational micromechanics perspective". In: *Composites Science and Technology* 110 (Apr. 2015), pp. 196–204. DOI: 10.1016/j.compscitech.2015.02.008.

[19] V. Mantič. "Interface crack onset at a circular cylindrical inclusion under a remote transverse tension. Application of a coupled stress and energy criterion". In: *International Journal of Solids and Structures* 46.6 (Mar. 2009), pp. 1287–1304. DOI: 10.1016/j.ijsolstr.2008.10.036.

[20] Yuval Freed and Leslie Banks-Sills. "A new cohesive zone model for mixed mode interface fracture in bimaterials". In: *Engineering Fracture Mechanics* 75.15 (Oct. 2008), pp. 4583–4593. DOI: 10.1016/j.engfracmech.2008.04.013.

[21] Z.-H. Jin and C.T. Sun. "Cohesive zone modeling of interface fracture in elastic bi-materials". In: *Engineering Fracture Mechanics* 72.12 (Aug. 2005), pp. 1805–1817. DOI: 10.1016/j.engfracmech.2004.09.011.

[22] Leif E. Asp, Lars A. Berglund, and Peter Gudmundson. "Effects of a composite-like stress state on the fracture of epoxies". In: *Composites Science and Technology* 53.1 (Jan. 1995), pp. 27–37. DOI: 10.1016/0266-3538(94)00075-1.

[23] Andrzej Pawlak, Andrzej Galeski, and Artur Rozanski. "Cavitation during deformation of semicrystalline polymers". In: *Progress in Polymer Science* 39.5 (May 2014), pp. 921–958. DOI: 10.1016/j.progpolymsci.2013.10.007.

[24] Ronald Krueger. "Virtual crack closure technique: History, approach, and applications". In: *Applied Mechanics Reviews* 57.2 (2004), p. 109. DOI: 10.1115/1.1595677.

[25] J. R. Rice. "A Path Independent Integral and the Approximate Analysis of Strain Concentration by Notches and Cracks". In: *Journal of Applied Mechanics* 35.2 (1968), p. 379. DOI: 10.1115/1.3601206.

[26] M. Toya. "A crack along the interface of a circular inclusion embedded in an infinite solid". In: *Journal of the Mechanics and Physics of Solids* 22.5 (Oct. 1974), pp. 325–348. DOI: 10.1016/0022-5096(74)90002-7.

[27] F. París, J. C. Caño, and J. Varna. "The fiber-matrix interface crack — A numerical analysis using Boundary Elements". In: *International Journal of Fracture* 82.1 (May 1996), pp. 11–29. DOI: 10.1007/bf00017861.

[28] Linqi Zhuang et al. "Effects of inter-fiber spacing on fiber-matrix debond crack growth in unidirectional composites under transverse loading". In: *Composites Part A: Applied Science and Manufacturing* 109 (June 2018), pp. 463–471. DOI: 10.1016/j.compositesa.2018.03.031.

[29] M. Muñoz-Reja et al. "Crack onset and propagation at fibre–matrix elastic interfaces under biaxial loading using finite fracture mechanics". In: *Composites Part A: Applied Science and Manufacturing* 82 (Mar. 2016), pp. 267–278. DOI: 10.1016/j.compositesa.2015.09.023.

[30] E. Correa, V. Mantič, and F. París. "Effect of thermal residual stresses on matrix failure under transverse tension at micromechanical level: A numerical and experimental analysis". In: *Composites Science and Technology* 71.5 (Mar. 2011), pp. 622–629. DOI: 10.1016/j.compscitech.2010.12.027.

[31] E. Correa, F. París, and V. Mantič. "Effect of the presence of a secondary transverse load on the inter-fibre failure under tension". In: *Engineering Fracture Mechanics* 103 (May 2013), pp. 174–189. DOI: 10.1016/j.engfracmech.2013.02.026.

[32] E. Correa, F. París, and V. Mantič. "Effect of a secondary transverse load on the inter-fibre failure under compression". In: *Composites Part B: Engineering* 65 (Oct. 2014), pp. 57–68. DOI: 10.1016/j.compositesb.2014.01.005.

[33] C. Sandino, E. Correa, and F. París. "Numerical analysis of the influence of a nearby fibre on the interface crack growth in composites under transverse tensile load". In: *Engineering Fracture Mechanics* 168 (Dec. 2016), pp. 58–75. DOI: 10.1016/j.engfracmech.2016.01.022.

[34] C. Sandino, E. Correa, and F. París. "Interface crack growth under transverse compression: nearby fibre effect". In: *Proceeding of the* 18^{th} *European Conference on Composite Materials (ECCM-18).* (Athens, Greece, June 24–28, 2018). 2018.

[35] Janis Varna et al. "Growth and Interaction of Debonds in Local Clusters of Fibers in Unidirectional Composites during Transverse Loading". In: *Key Engineering Materials* 754 (Sept. 2017), pp. 63–66. DOI: 10.4028/www.scientific.net/kem.754.63.

[36] M.L. Velasco et al. "BEM multiscale modelling involving micromechanical damage in fibrous composites". In: *Engineering Analysis with Boundary Elements* 93 (Aug. 2018), pp. 1–9. DOI: 10.1016/j.enganabound.2018.03.012.

[37] Federico París, María Luisa Velasco, and Elena Correa. "Micromechanical study on the influence of scale effect in the first stage of damage in composites". In: *Composites Science and Technology* 160 (May 2018), pp. 1–8. DOI: 10.1016/j.compscitech.2018.03.004.

[38] *ABAQUS/Standard User's Manual, Version 6.12.* Simulia. Providence, RI, USA, 2012.

[39] H. Zhang et al. "Transverse single-fibre test for interfacial debonding in composites: 1. Experimental observations". In: *Composites Part A: Applied Science and Manufacturing* 28.4 (Jan. 1997), pp. 309–315. DOI: 10.1016/s1359-835x(96)00123-6.

[40] Luca Di Stasio, Janis Varna, and Zoubir Ayadi. "Energy release rate of the fiber/matrix interface crack in UD composites under transverse loading: effect of the fiber volume fraction and of the distance to the free surface and to non-adjacent debonds". In: *Theoretical and Applied Fracture Mechanics* (June 2019), p. 102251. DOI: 10.1016/j.tafmec.2019.102251.

[41] R.F. Teixeira, S.T. Pinho, and P. Robinson. "Thickness-dependence of the translaminar fracture toughness: Experimental study using thin-ply composites". In: *Composites Part A: Applied Science and Manufacturing* 90 (Nov. 2016), pp. 33–44. DOI: 10.1016/j.compositesa.2016.05.031.

[42] J.A. Garrido, A. Foces, and F. Paris. "B.E.M. applied to receding contact problems with friction". In: *Mathematical and Computer Modelling* 15.3-5 (1991), pp. 143–153. DOI: 10.1016/0895-7177(91)90060-k.

[43] L. M. Keer, J. Dundurs, and K. C. Tsai. “Problems Involving a Receding Contact Between a Layer and a Half Space”. In: *Journal of Applied Mechanics* 39.4 (1972), p. 1115. DOI: 10.1115/1.3422839.

[44] K. C. Tsai, J. Dundurs, and L. M. Keer. “Elastic Layer Pressed Against a Half Space”. In: *Journal of Applied Mechanics* 41.3 (1974), p. 703. DOI: 10.1115/1.3423375.

[45] Z. Hashin. “Analysis of Composite Materials—A Survey”. In: *Journal of Applied Mechanics* 50.3 (1983), p. 481. DOI: 10.1115/1.3167081.

[46] R.M. Christensen and K.H. Lo. “Solutions for effective shear properties in three phase sphere and cylinder models”. In: *Journal of the Mechanics and Physics of Solids* 27.4 (Aug. 1979), pp. 315–330. DOI: 10.1016/0022-5096(79)90032-2.

[47] Federico París, Elena Correa, and Vladislav Mantič. “Kinking of Transversal Interface Cracks Between Fiber and Matrix”. In: *Journal of Applied Mechanics* 74.4 (2007), p. 703. DOI: 10.1115/1.2711220.

Paper D

Growth of interface cracks on consecutive fibers: on the same or on the opposite sides?

Authors:
Luca Di Stasio, Janis Varna and Zoubir Ayadi

Reformatted version of paper submitted to:
Proceedings of the 12^{th} International Conference on Composite Science and Technology (ICCST 12), Materials Today: Proceedings, 2019.

© 2019, The Authors.

Growth of interface cracks on consecutive fibers: on the same or on the opposite sides?

Luca Di Stasio[1,2], Janis Varna[1] and Zoubir Ayadi[2]

[1]Luleå University of Technology, University Campus, SE-97187 Luleå, Sweden
[2]Université de Lorraine, EEIGM, IJL, 6 Rue Bastien Lepage, F-54010 Nancy, France

*Corresponding author: luca.di.stasio@ltu.se

Abstract

The growth of fiber/matrix interface cracks (debonds) located on consecutive fibers along the through-the-thickness (vertical) direction is studied in glass fiber-epoxy UD composites. Debonds could appear, along the vertical direction, on the same or on opposite sides of their respective fibers. Determining which configuration is the most energetically favorable to debond growth is the objective of this paper. To this end, two different families of Representative Volume Elements (RVEs) are developed: the first implements the classic condition of coupling of the vertical displacements to model a unit cell repeating symmetrically along the vertical direction; the second uses a novel set of boundary conditions, proposed here by the authors, to represent a unit cell repeating anti-symmetrically along the vertical direction. The model is analyzed in the context of Linear Elastic Fracture Mechanics (LEFM) and the Mode I and Mode II Energy Release Rate are evaluated to investigate crack growth. The calculation is performed using the Virtual Crack Closure Technique (VCCT) in the framework of the Finite Element Method (FEM). It is found that Mode I dominated propagation is favored when debonds are located on the same sides of their respective fibers; while for larger (Mode II-dominated) debonds, Mode II ERR is higher when they lie on the opposite sides. No interaction effect is present when at least two fully bonded fibers are located between the partially debonded ones.

Keywords: Polymer Matrix Composite (PMC), Fracture mechanics, Debonding, Debond Interaction

A Introduction

Organized over the last three decades, the three World Wide Failure Exercises (WWFEs) [1, 2, 3] represent one of the most comprehensive attempts to date to evaluate the maturity of failure criteria and predictive theories of damage of Fiber-Reinforced Polymer Composites (FRPC). The third and last one (WWFE-III) aims at providing a benchmark for

models of sub-critical damage, namely matrix cracking, delamination and fiber failure, by comparing the independent predictions of 12 different approaches (each one from a different individual, group or institution) over 13 test cases [3]. The comparison of predictions by the different theories shows a wide scatter of results, symptomatic of the immaturity of the field [4]. Furthermore, it uncovers the existence of gaps in the knowledge shared by all models. Among these, a clear understanding is still elusive regarding the mechanisms of initiation of an individual transverse crack.

Onset of transverse cracks is determined at the microscopic level by initiation and propagation of fiber-matrix interface cracks [5, 6], or debonds. Debonds first grow along the arc direction of the fiber; at a certain critical size they kink out of the interface and lead to the onset of matrix micro-cracks; micro-cracks coalesce together forming a through-the-thickness crack [7]; when a critical size is reached, this crack propagates along the fiber direction, i.e. "tunneling" across the width of the laminate, and creating a transverse crack. Thus, understanding the mechanism of debond growth and predicting debond critical arc size (at which kinking starts) represent an important step in the development of precise predictive models of transverse cracking.

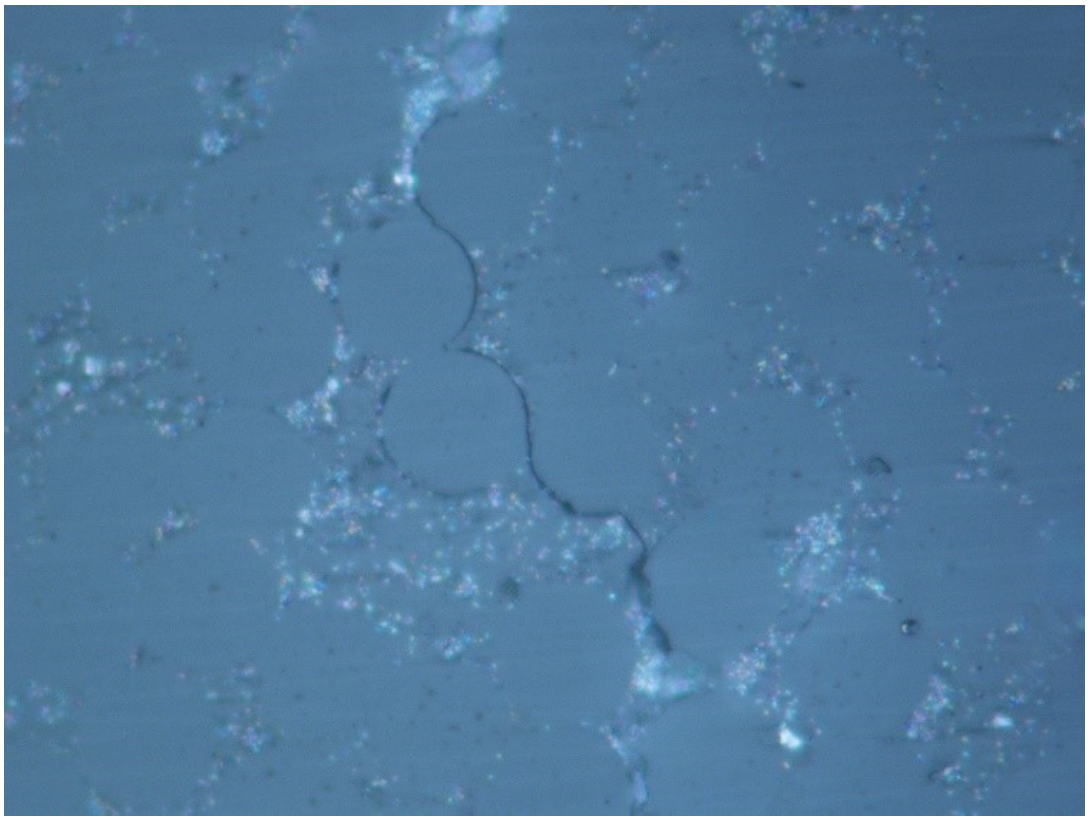

Figure 1: Debonds in the 90° *layer of a* $[0^\circ/90^\circ]_S$ *laminate after being subjected to tensile strain in the horizontal direction.*

Initial attempts to analyze the mechanics of debonding were based on the linear elastic solution of a single partially debonded fiber in an infinite matrix with an applied tensile stress at infinity, evaluated analytically by using complex potentials [8, 9, 10]. It was found that stress and displacement fields have an oscillating singularity at the crack tip, which prevents the use of Stress Intensity Factors (SIFs) as they are not defined at the debond tip. Similarly, Mode I and Mode II Energy Release Rate (ERR) do not converge and mode-based partition of the ERR is not possible. However, the ERR can be interpreted as the work needed to open the crack by an infinitesimal amount da or equivalently, in the case of Linear Elastic Fracture Mechanics, to close the crack by the same infinitesimal amount da. By considering a small but finite crack increase Δa instead of the infinitesimal increase da, the lack of convergence due to the oscillatory singularity can be circumvented and an approximation of Mode I and Mode II ERR can be provided. The recourse to this strategy makes the problem suitable for a resolution technique based on domain discretization such as the Finite Element Method (FEM) or the Boundary Element Method (BEM). In subsequent works [11, 12], it was shown that Toya's analytical solution [10] implies a non-physical interpenetration zone in the crack tip neighborhood. This led to the introduction of a no-interpenetration contact interaction which, solved with the Boundary Element Method (BEM), showed the existence of a contact zone (a finite size region in which crack faces are in contact) for debonds larger than a critical value [12]. In [13], the authors compared the one-debond with respect to the two-symmetric-debonds configuration and found that the former is energetically the most favorable to crack growth. The effect of several load combinations on ERR of a single partially debonded fiber in an effectively infinite matrix was later studied [14, 15, 16], as well as the effect of a neighboring fully bonded fiber [17, 18]. Researchers in [19] studied the effect on debond ERR of the presence of a second partially debonded fiber, with the two debonds placed facing each other (i.e. no fiber in between).
Microscopic observations of debond growth, such as the one reported in Fig. 1, show debonds developed on the same as well as the opposite sides of consecutive fibers on average aligned along the vertical, i.e. through-the thickness, direction. It is thus interesting to investigate the effect on debond ERR of the position of the next debond on the neighboring partially debonded fiber along the vertical direction. To this end, we develop Representative Volume Elements (RVEs) which, by application of displacement-coupling boundary conditions along the right and left sides, are repeating in a mirror-like fashion horizontally. The use of coupling conditions on the vertical displacement along the upper boundary models the presence of another partially debonded fiber with a debond of equal size and on the same side. In order to model the case of a fiber with a debond of equal size but appearing on the opposite side, we propose a set of anti-symmetric coupling conditions that are applied to the upper boundary. Details regarding coupling conditions, RVEs and Finite Element (FE) discretization are presented in Sec. B and Sec. 3, while results are presented and discussed in Sec. 4.

B Representative Volume Elements (RVEs)

Two families of RVE are studied in the present work. RVEs from both families:

- represent a Uni-Directional (UD) composite, infinite in all 3 directions (length, width and thickness);
- are solved using plain strain conditions, and thus represent a debond whose length along the fiber is much greater than its arc size;
- consider two linear, homogeneous, isotropic elastic phases, i.e. glass fiber and epoxy matrix, whose properties are reported in Table 1;
- possess a centrally placed partially debonded fiber and have a total of n fibers along the horizontal direction (loading direction, transverse to composite 0° direction) and k in the vertical (i.e. through-the-thickness) direction;
- repeat infinitely along the horizontal direction in a mirror-like way (the next RVE to the right is the mirror image with respect to the right-side boundary) thanks to the application of coupling conditions on the horizontal displacement along the right and left sides of the element;
- are symmetric with respect to the horizontal axis, which allows the discretization of only half RVE through the application of symmetry boundary conditions on the lower side;
- are subject to tensile loading in the form of applied displacement corresponding to a x-strain level of 1%.

The distinction between the two families of RVE lies in the boundary conditions applied along the upper side.

Table 1: Material properties of glass fiber and epoxy adopted in the present study.

Material	$E\,[GPa]$	$\mu\,[GPa]$	$\nu\,[-]$
Glass fiber	70.0	29.2	0.2
Epoxy	3.5	1.25	0.4

Given a global reference frame with axes x, y and z, the composite is modeled as a plate with its mid-plane lying in the $x-y$ plane, such that y represents the UD composite 0° direction, x the in-plane transverse direction and z the through-the-thickness direction. The RVEs are defined in the $x-z$ plane (see Fig. 2 and Fig. 3).

The first family has coupling conditions applied to the vertical displacement of the points belonging to the upper side, such that

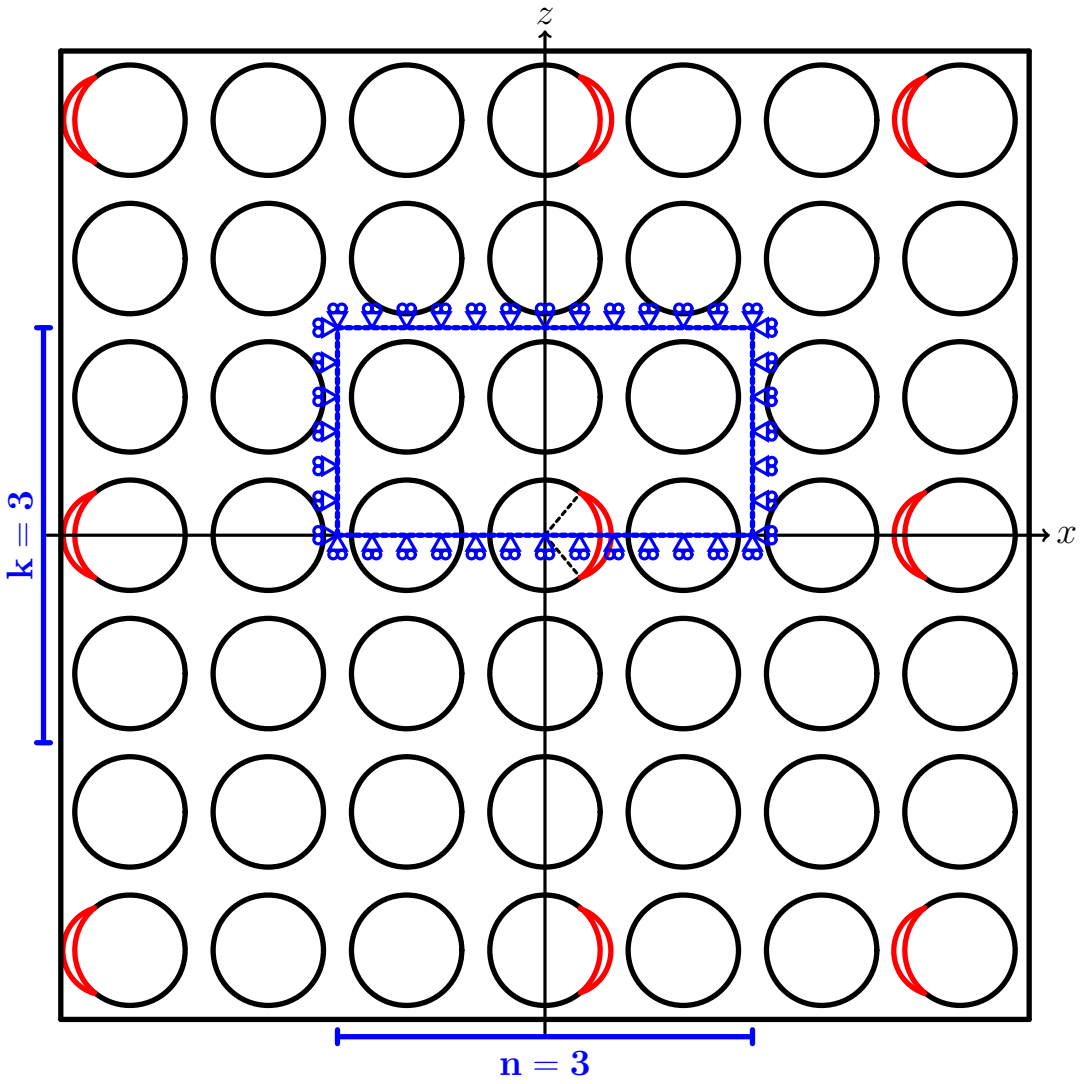

Figure 2: Representative Volume Element $n \times k - symm$ of a UD composite with debonds appearing after $n-1$ and after $k-1$ undamaged fibers respectively in the horizontal and vertical direction. In the vertical direction, on fibers belonging to the same Â´Â´column", debonds are located always on the same side.

$$u_z(x,h) = u_z^{\nu}, \tag{B.1}$$

where h is the height of the RVE and u_z^{ν} is the unknown constant vertical displacement of the upper boundary due to Poisson's effect, which is evaluated as part of the elastic solution. This condition implies that the element is repeating along the vertical direction, symmetrically with respect to the upper boundary line. It means, in turn, that the next debonded fiber will have a debond on the same side as the preceding one (see Fig. 2). We will refer to this set of RVEs as $n \times k - symm$, where n and k are the number of fibers respectively in the RVE's horizontal and vertical direction.

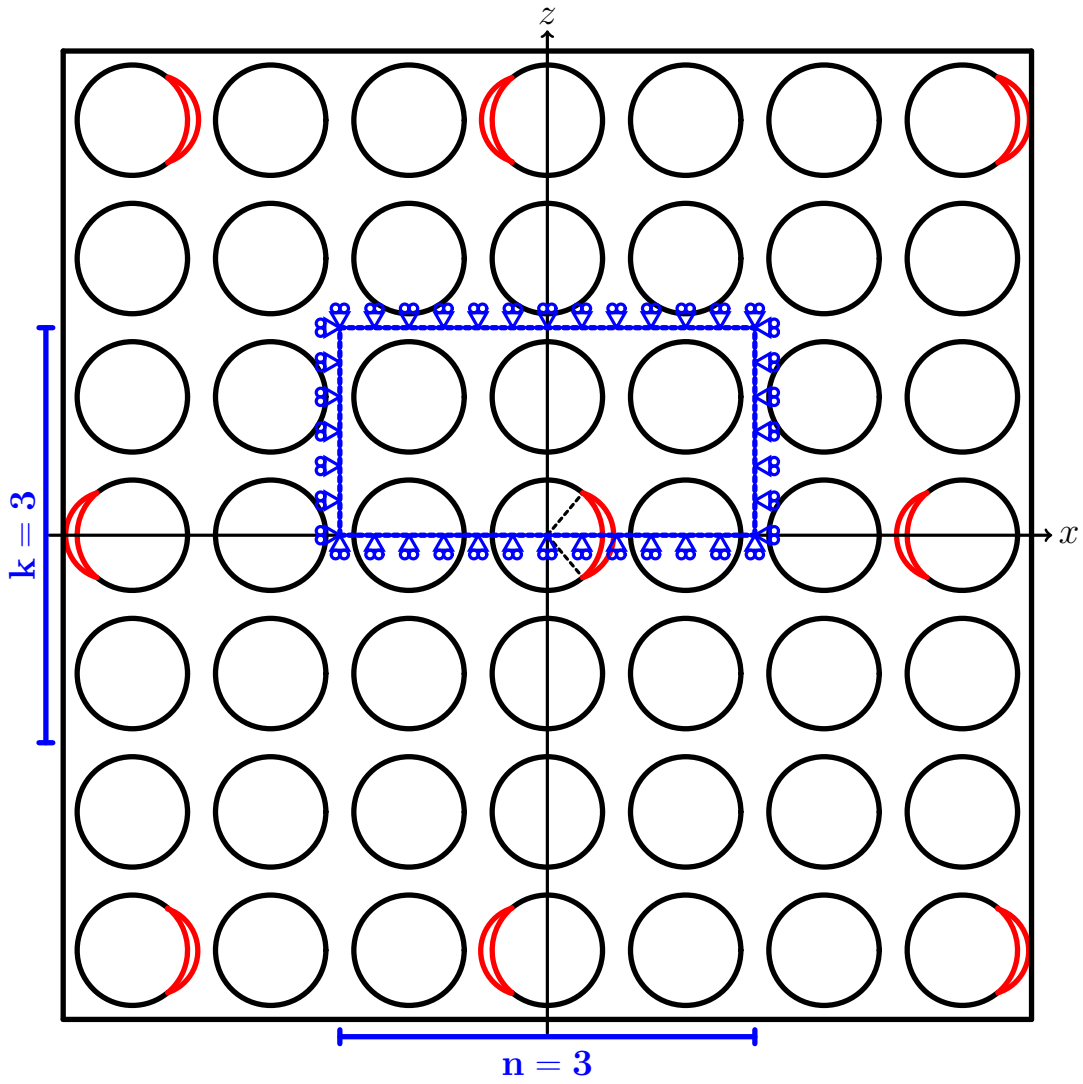

Figure 3: Representative Volume Element $n \times k -$ asymm of a UD composite with debonds appearing after $n-1$ and after $k-1$ undamaged fibers respectively in the horizontal and vertical direction. In the vertical direction, on fibers belonging to the same Â´Â´column", debonds are located on the opposite sides of consecutive fibers.

The second type of RVE has a set of boundary conditions applied to the upper side of the form (see Fig. 3):

$$u_z(x,h) - u_z(0,h) = -\left(u_z(-x,h) - u_z(0,h)\right), \tag{B.2}$$

$$u_x(x,h) = -u_x(-x,h), \tag{B.3}$$

where h is the height of the RVE and $u_z(0,h)$ is the unknown vertical displacement of the upper boundary's mid-point due to Poisson's effect, which is evaluated as part of the elastic solution. This condition, an anti-symmetric coupling condition, implies that

the element is repeating along the vertical direction, anti-symmetrically with respect to the upper boundary line, i.e. the next debonded fiber will have a debond on the opposite side with respect to the preceding one (see Fig. 3). To the authors' knowledge, this is the first time that this kind of coupling condition is proposed to model the growth of multiple debonds on alternating sides of consecutive fibers along the through-the-thickness direction. We will refer to this set of RVEs as $n \times k - asymm$, where n and k are the number of fibers respectively in the RVE's horizontal and vertical direction.

C Finite Element solution

The length and height of the generic $n \times k - symm$ and $n \times k - asymm$ RVE are respectively defined as

$$l = n \cdot 2L \quad h = k \cdot 2L, \tag{C.4}$$

where $2L \cdot 2L$ is the size of a 1-fiber unit cell (see Fig. 4) and L is determined by

$$L = \frac{R_f}{2}\sqrt{\frac{\pi}{V_f}}, \tag{C.5}$$

where R_f and V_f are respectively the fiber radius and volume fraction. The fiber radius is assumed to be always equal to 1 μm: within the scope of Linear Elastic Fracture Mechanics (LEFM), the ERR is linearly proportional to the fiber radius, which is representative of the crack size. Thus, the fiber radius represents a scale parameter and a simple multiplication is needed to obtain the ERR for a different value of the fiber radius. The volume fraction is assumed to be homogeneous and equal to 60%.

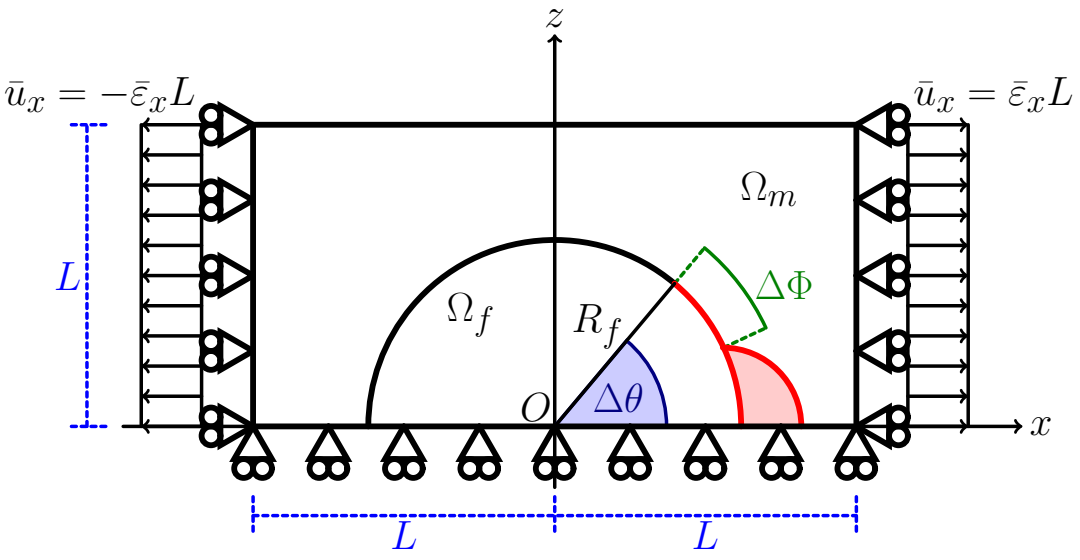

Figure 4: Schematic of the model with its main parameters.

The debond size is equal to $2\Delta\theta$, while the contact zone size is denoted by $\Delta\Phi$. The crack faces interaction in the contact zone is assumed to be frictionless. Consequently, crack faces are modeled as surfaces whose interaction is defined by conditions of no-interpenetration and frictionless sliding.
The model is discretized and solved using the Finite Element Method (FEM) in the Abaqus environment [20]. The Mode I and Mode II ERR are computed using the Virtual Crack Closure Technique (VCCT) [21] implemented in a custom Python routine, while the total ERR is evaluated by means of the Abaqus built-in J-Integral method [22]. The mesh is composed by 8-nodes quadrilaterals and 6-nodes triangles with quadratic shape functions. It is worth to recall here that the linear elastic solution of the fiber/interface crack possesses an oscillating singularity in the stress and displacement at the crack tip [8, 9, 10]. The oscillating nature of the singularity prevents the convergence of Mode I and Mode II ERR at least when, according to their definition, computed for an infinitesimal increment of the crack length. The computational issue can be circumvented by evaluating the mode decomposition of the ERR over a finite size. This leads naturally to the use of numerical techniques based on domain discretization (such as FEM or BEM) in conjunction with the VCCT. In order to ensure the convergence of the Energy Release Rate, a regular mesh of quadrilaterals with almost unitary aspect ratio is used in the crack tip neighborhood in every RVE analyzed. The size of the elements in this region is characterized by their angular size δ, which is always equal to 0.05° in all our analyses. This ensures that the results from different models are consistent with each other and comparisons between them are meaningful. The convergence of the model has been verified on the 1-fiber RVE with an infinite matrix ($V_f \to 0$) with respect to the BEM results presented in [17]. By comparing FEM and BEM results, it is possible to estimate the relative accuracy of our results at around 5%. It implies that differences in the ERR smaller than this value cannot be considered significant.

D Results & discussion

We first devote our attention to the $n \times 1 - symm$ and $n \times 1 - asymm$ Representative Volume Elements. They both represent an infinite UD in which a column (i.e. a vertical line) made of only partially debonded fibers, with debonds of equal size, is repeating along the horizontal (loading, transverse to laminate 0°) direction every $n - 1$ columns of fully bonded fibers.
In the $n \times 1 - symm$ RVE, debonds appear always on the same side of consecutive fibers belonging to the same column, i.e. the debond mid-point is always at 0° inside the same column of partially debonded fibers (see Figure 2). In the $n \times 1 - asymm$ RVE instead, debonds are placed on alternating sides of consecutive fibers belonging to the same column of damaged fibers, i.e. the debond mid-point is located alternatively at 0° and 180° inside the same column (see Figure 3). Observing Fig. 5 and Fig. 6, it is possible to notice that, for both types of RVE, Mode I and Mode II ERR increase when the spacing between columns of damaged fibers (measured in terms of number of columns of fully bonded fibers) increases.

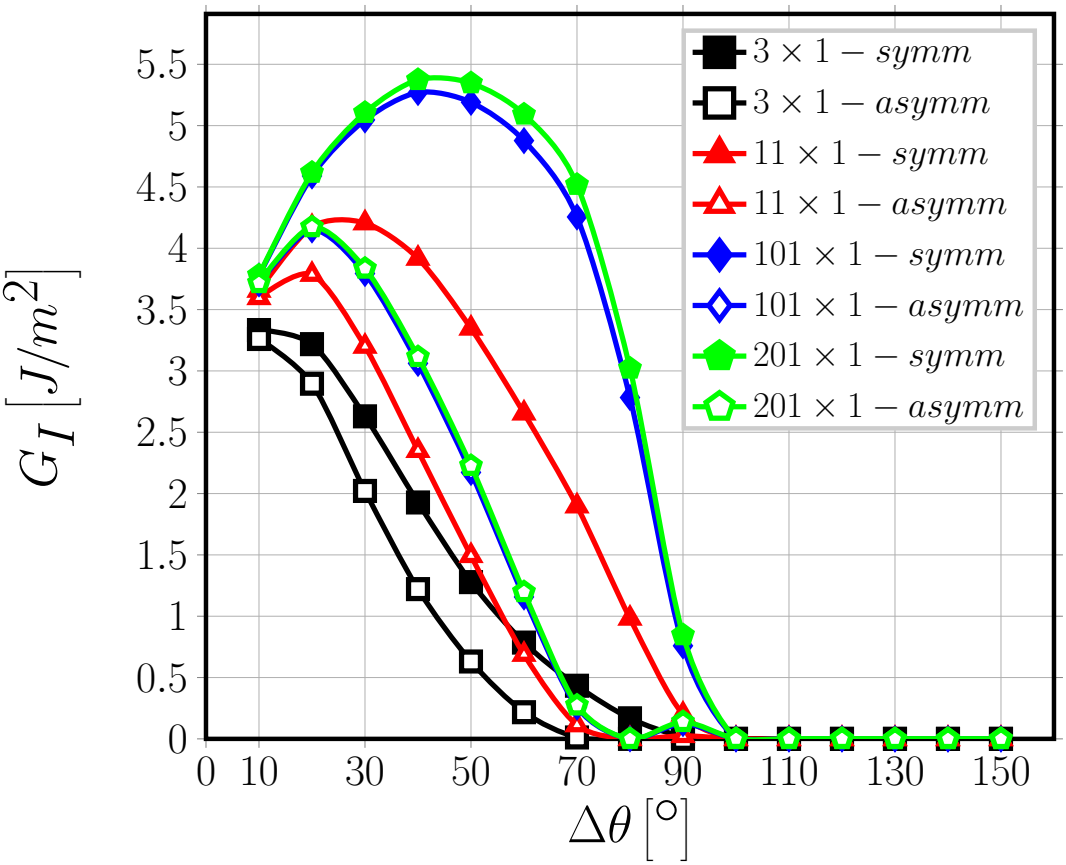

Figure 5: Comparison of Mode I ERR between $n\times1-symm$ and $n\times1-asymm$ RVEs, $V_f=60\%$, $\varepsilon_x=1\%$.

This is due to the x-strain magnification effect: the presence of an increasing number of unit cells with a fully bonded fiber between consecutive unit cells containing a debond in the horizontal direction causes, for the same applied macroscopic strain, an increase of the x-strain applied to the unit cell with the debonded fiber and thus of the larger local x-strain in the debond tip neighborhood. Given that the ERR is equal to the integral of the product of stresses and displacements at the debond tip, a magnification of the strain, and thus of the displacement, leads to an increase in the value of ERR.
In reverse, this effect can be interpreted as a consequence of crack shielding: increasing the number of columns of partially debonded fibers in the UD decreases the local magnitude of the strain at the debond tip, as a discontinuity appears in the displacement field for each additional debond present. In turn, decreasing the magnitude of the displacements in the debond neighborhood decreases the ERR.

An increasing number of fully bonded fibers between partially debonded ones causes also a delay in the contact zone onset (corresponding to $G_I=0$) by $\sim10^\circ$ in both sets of RVEs: from 70° to 80° for $n\times1-asymm$, from 90° to 100° for $n\times1-symm$ (see Fig. 5). Furthermore, it causes the maximum of G_{II} to occur at larger debond sizes: from 80° to 100° for $n\times1-asymm$, from 60° to 90° for $n\times1-symm$ (see Fig. 6).

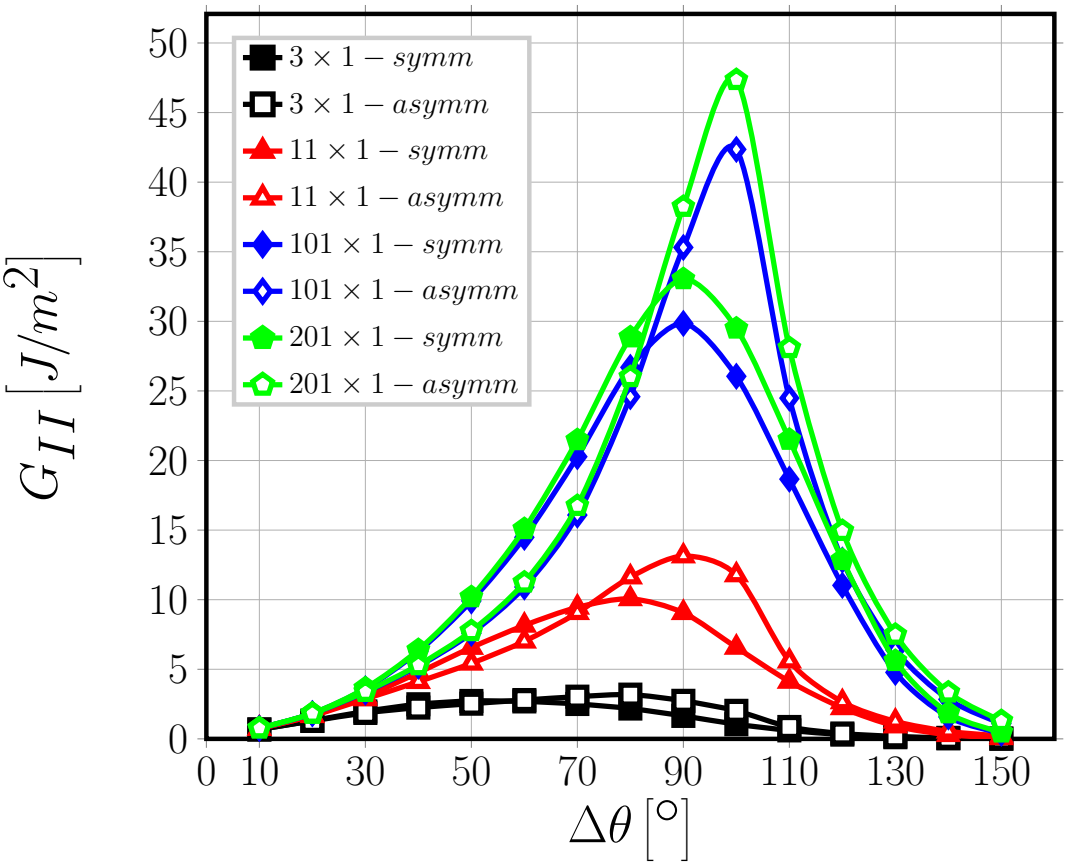

Figure 6: Comparison of Mode II ERR between $n \times 1 - symm$ and $n \times 1 - asymm$ RVEs, $V_f = 60\%$, $\varepsilon_x = 1\%$.

Comparing the two families of RVE, it is possible to see in Fig. 5 that G_I is consistently higher for $n \times 1 - symm$. Similarly, the onset of the contact zone in $n \times 1 - symm$ (at $90^\circ - 100^\circ$) is significantly delayed with respect to $n \times 1 - asymm$ (at $70^\circ - 80^\circ$).

In the $n \times 1 - symm$ RVE, in the case of smaller Mode I dominated debonds, the presence of a debond on the same side of the consecutive fiber provides a local free surface which causes the matrix to shrink away from the surface of the two fibers. This mechanism favors the opening of crack faces, and thus an increase in Mode I ERR. In $n \times 1 - asymm$ RVE, on the other hand, the matrix in the debond tip neighborhood is constrained by the next fiber (debonded on the opposite side) which reduces the x-displacement.

Comparing Mode II ERR for the two types of RVE in Fig. 6, G_{II} appears to be higher for $n \times 1 - asymm$ RVEs than for $n \times 1 - symm$ in the $80^\circ - 100^\circ$ range while slightly lower for smaller debonds ($< 80^\circ$). Mode II peak value is delayed in $n \times 1 - asymm$ to larger debond sizes ($80^\circ - 100^\circ$) than in $n \times 1 - symm$ ($60^\circ - 90^\circ$). For larger values of $\Delta\theta$ ($\sim 80^\circ - 100^\circ$), the presence of a local free surface due to a debond on the same side of the consecutive fiber causes a decrease in the x-displacement at the crack tip, which now contributes mainly to Mode II. When debonds are located on opposite sides of consecutive

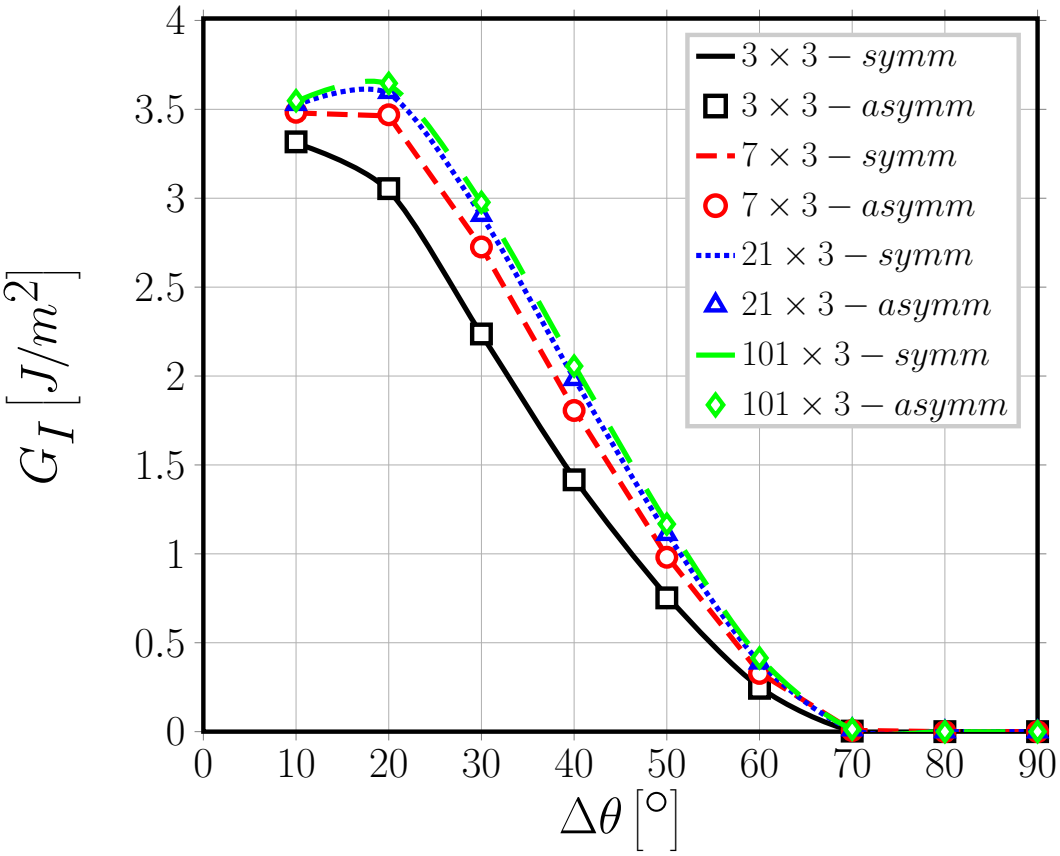

Figure 7: Comparison of Mode I ERR between $n \times 3 - symm$ and $n \times 1 - asymm$ RVEs, $V_f = 60\%$, $\varepsilon_x = 1\%$.

fibers, the presence of a fully bonded interface leads instead to a magnification of the x-displacement at the crack tip, and thus an increase in G_{II}. When debonds on consecutive fibers reach a size of $\sim 110°$, they are creating two free surfaces close to each other, which cause a relaxation in the elastic fields in both types of RVE. This leads to a quick decrease in the value of Mode II ERR and makes the results of the two different RVEs practically indistinguishable.

It is at this point interesting to investigate the effect of the presence of fully bonded fibers between two consecutive partially debonded fibers in the through-the-thickness direction. A comparison of Mode I and of Mode II ERR between $n \times 3 - symm$ and $n \times 3 - asymm$ are reported respectively in Fig. 7 and in Fig. 8: the presence of two bonded fiber rows between rows containing debonded fibers already makes the results of the two different RVEs practically identical. The effect of the relative position (same or opposite sides of the fibers) of two consecutive debonds in the through-the-thickness direction is thus an extremely localized problem: the presence of just two fully bonded fibers in between makes the two configurations indistinguishable, at least from an energy point of view.

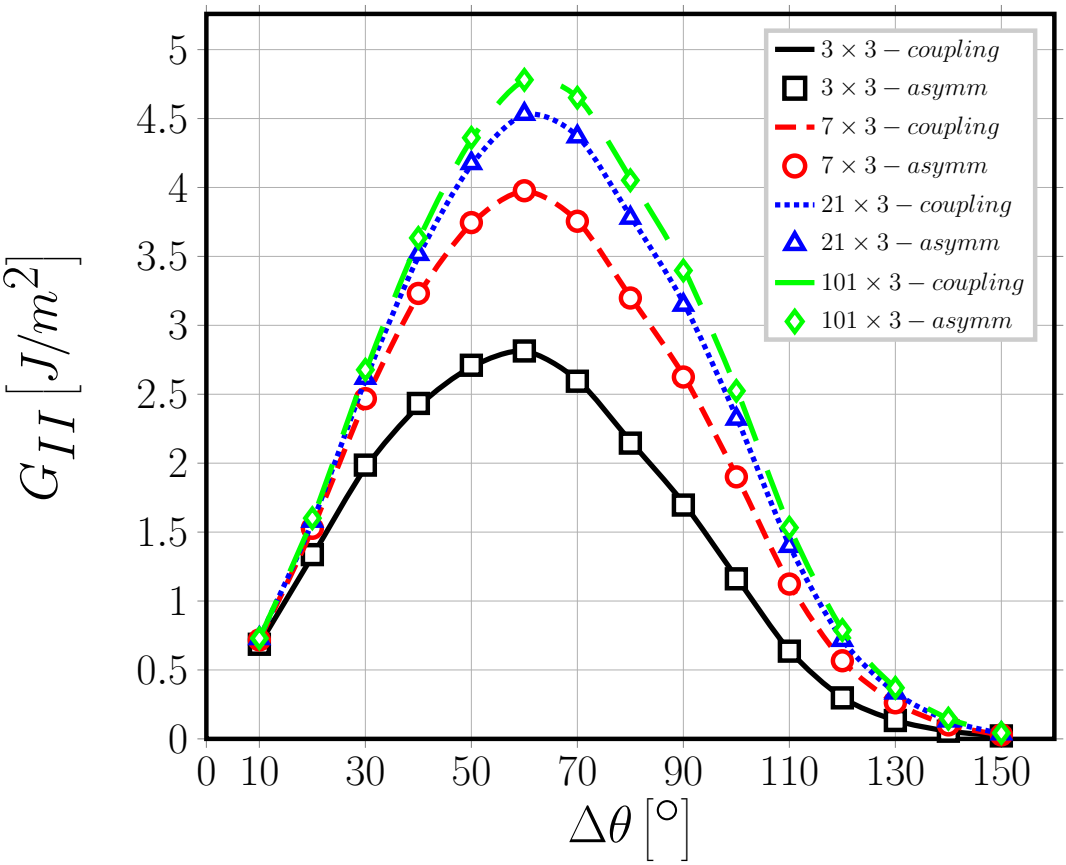

Figure 8: Comparison of Mode II ERR between $n\times3-symm$ and $n\times1-asymm$ RVEs, $V_f=60\%$, $\varepsilon_x=1\%$.

E Conclusions

An increasing number of fiber/matrix interface cracks (debonds) appear in the cross-section of a UD composite localized in the regions where transverse failure (transverse cracks) will occur. In each of these regions of debond localization, debonds can be on the same sides of fibers or on alternating sides. The Energy Release Rate (ERR) in these two cases depends on the density of debonded fibers, which are separated by fully bonded fibers, and on the distance to the next debond localization region in the cross-section. Two different types of Representative Volume Element have been developed to study the effect of the relative position (same or opposite sides of the fibers) of consecutive debonds in the through-the thickness direction. The RVEs are repeating in the horizontal direction thanks to the application of coupling conditions on the horizontal displacements on their right and left sides. The case with debonds located on the same side of their respective fibers is modeled using conditions of coupling of the vertical displacements on the top boundary, which corresponds to the element repeating in the vertical (through-the-thickness) direction in a symmetric way. In order to model the second configuration, with debonds placed on opposite sides of consecutive fibers, a novel set of coupling

conditions is introduced, which models an element repeating in the vertical direction anti-symmetrically.
Debond growth is characterized through the evaluation of Mode I and Mode II Energy Release Rate by means of the Virtual Crack Closure Technique. The comparison between the ERR of the two families of RVE provides insights into the effect of the relative position of debonds (same or opposite sides of the respective fiber) belonging to fibers aligned in the vertical or through-the-thickness direction, i.e. located in the same "column" of fibers. It has been found that:

1. the relative position of debonds influences the ERR only if debonds are located on consecutive fibers: the presence of just two fully bonded fiber rows between rows containing debonds makes the ERR unaffected by debonds' relative position;

2. when debonds are located on consecutive vertically aligned fibers, G_I is higher and contact zone onset is delayed if debonds are on the same side of their respective fibers;

3. no significant difference in G_{II} between the two RVE families can be observed except in the range $\Delta\theta = 80° - 100°$, in which the largest values of G_{II} are reached and G_{II} is higher when debonds are located on opposite sides of consecutive vertically aligned fibers.

Given that debond growth is likelier when the Mode Ratio is Mode I dominated, it is reasonable to expect that the growth of consecutive vertically aligned debonds with no fully bonded fiber in between is favored when they are located on the same side of their respective fibers. However, assuming that the applied strain is high enough to cause debond growth in Mode II with the onset of a contact zone, larger debond sizes are reached when debonds are on opposite sides. When instead vertically-aligned debonds are separated by fully bonded fibers, neither configuration (debonds on the same or opposite sides of the debonded fibers) is favored from an energy point of view.

Acknowledgements

Luca Di Stasio gratefully acknowledges the support of the European School of Materials (EUSMAT) through the DocMASE Doctoral Programme and the European Commission through the Erasmus Mundus Program.

References

[1] M.J. Hinton, A.S. Kaddour, and P.D. Soden. "The world-wide failure exercise". In: *Failure Criteria in Fibre-Reinforced-Polymer Composites*. Elsevier, 2004, pp. 2–28. DOI: 10.1016/b978-008044475-8/50002-0.

[2] MJ Hinton and AS Kaddour. "The background to the Second World-Wide Failure Exercise". In: *Journal of Composite Materials* 46.19-20 (June 2012), pp. 2283–2294. DOI: 10.1177/0021998312449885.

[3] AS Kaddour et al. "The background to the third world-wide failure exercise". In: *Journal of Composite Materials* 47.20-21 (Sept. 2013), pp. 2417–2426. DOI: 10.1177/0021998313499475.

[4] AS Kaddour et al. "A comparison between the predictive capability of matrix cracking, damage and failure criteria for fibre reinforced composite laminates: Part A of the third world-wide failure exercise". In: *Journal of Composite Materials* 47.20-21 (Sept. 2013), pp. 2749–2779. DOI: 10.1177/0021998313499476.

[5] J. E. Bailey and A. Parvizi. "On fibre debonding effects and the mechanism of transverse-ply failure in cross-ply laminates of glass fibre/thermoset composites". In: *Journal of Materials Science* 16.3 (Mar. 1981), pp. 649–659. DOI: 10.1007/bf02402782.

[6] J. E. Bailey, P. T. Curtis, and A. Parvizi. "On the Transverse Cracking and Longitudinal Splitting Behaviour of Glass and Carbon Fibre Reinforced Epoxy Cross Ply Laminates and the Effect of Poisson and Thermally Generated Strain". In: *Proceedings of the Royal Society A: Mathematical, Physical and Engineering Sciences* 366.1727 (July 1979), pp. 599–623. DOI: 10.1098/rspa.1979.0071.

[7] H. Zhang et al. "Transverse single-fibre test for interfacial debonding in composites: 1. Experimental observations". In: *Composites Part A: Applied Science and Manufacturing* 28.4 (Jan. 1997), pp. 309–315. DOI: 10.1016/s1359-835x(96)00123-6.

[8] A. H. England. "An Arc Crack Around a Circular Elastic Inclusion". In: *Journal of Applied Mechanics* 33.3 (1966), p. 637. DOI: 10.1115/1.3625132.

[9] A.B. Perlman and G.C. Sih. "Elastostatic problems of curvilinear cracks in bonded dissimilar materials". In: *International Journal of Engineering Science* 5.11 (Nov. 1967), pp. 845–867. DOI: 10.1016/0020-7225(67)90009-2.

[10] M. Toya. "A crack along the interface of a circular inclusion embedded in an infinite solid". In: *Journal of the Mechanics and Physics of Solids* 22.5 (Oct. 1974), pp. 325–348. DOI: 10.1016/0022-5096(74)90002-7.

[11] F. París, J. C. Caño, and J. Varna. "The fiber-matrix interface crack — A numerical analysis using Boundary Elements". In: *International Journal of Fracture* 82.1 (May 1996), pp. 11–29. DOI: 10.1007/bf00017861.

[12] J. Varna, Federico París, and J. C.Caño. "The effect of crack-face contact on fiber/matrix debonding in transverse tensile loading". In: *Composites Science and Technology* 57.5 (1997), pp. 523–532. DOI: 10.1016/s0266-3538(96)00175-3.

[13] I.G. García, V. Mantič, and E. Graciani. "Debonding at the fibre–matrix interface under remote transverse tension. One debond or two symmetric debonds?" In: *European Journal of Mechanics - A/Solids* 53 (Sept. 2015), pp. 75–88. DOI: 10.1016/j.euromechsol.2015.02.007.

[14] E. Correa et al. "Effects of the presence of compression in transverse cyclic loading on fibre–matrix debonding in unidirectional composite plies". In: *Composites Part A: Applied Science and Manufacturing* 38.11 (Nov. 2007), pp. 2260–2269. DOI: 10.1016/j.compositesa.2006.11.002.

[15] E. Correa, F. París, and V. Mantič. "Effect of the presence of a secondary transverse load on the inter-fibre failure under tension". In: *Engineering Fracture Mechanics* 103 (May 2013), pp. 174–189. DOI: 10.1016/j.engfracmech.2013.02.026.

[16] E. Correa, F. París, and V. Mantič. "Effect of a secondary transverse load on the inter-fibre failure under compression". In: *Composites Part B: Engineering* 65 (Oct. 2014), pp. 57–68. DOI: 10.1016/j.compositesb.2014.01.005.

[17] C. Sandino, E. Correa, and F. París. "Numerical analysis of the influence of a nearby fibre on the interface crack growth in composites under transverse tensile load". In: *Engineering Fracture Mechanics* 168 (Dec. 2016), pp. 58–75. DOI: 10.1016/j.engfracmech.2016.01.022.

[18] Linqi Zhuang et al. "Effects of inter-fiber spacing on fiber-matrix debond crack growth in unidirectional composites under transverse loading". In: *Composites Part A: Applied Science and Manufacturing* 109 (June 2018), pp. 463–471. DOI: 10.1016/j.compositesa.2018.03.031.

[19] Janis Varna et al. "Growth and Interaction of Debonds in Local Clusters of Fibers in Unidirectional Composites during Transverse Loading". In: *Key Engineering Materials* 754 (Sept. 2017), pp. 63–66. DOI: 10.4028/www.scientific.net/kem.754.63.

[20] *ABAQUS/Standard User's Manual, Version 6.12*. Simulia. Providence, RI, USA, 2012.

[21] Ronald Krueger. "Virtual crack closure technique: History, approach, and applications". In: *Applied Mechanics Reviews* 57.2 (2004), p. 109. DOI: 10.1115/1.1595677.

[22] J. R. Rice. "A Path Independent Integral and the Approximate Analysis of Strain Concentration by Notches and Cracks". In: *Journal of Applied Mechanics* 35.2 (1968), p. 379. DOI: 10.1115/1.3601206.

Paper E

Estimating the average size of fiber/matrix interface cracks in UD and cross-ply laminates

Authors:
Luca Di Stasio, Janis Varna and Zoubir Ayadi

Reformatted version of paper originally published in:
Proceedings of the 7^{th} ECCOMAS Thematic Conference on the Mechanical Response of Composites, 2019.

© 2019, The Publisher, Reprinted with permission.

Estimating the average size of fiber/matrix interface cracks in UD and cross-ply laminates

Luca Di Stasio[1,2], Janis Varna[1] and Zoubir Ayadi[2]

[1]Luleå University of Technology, University Campus, SE-97187 Luleå, Sweden
[2]Université de Lorraine, EEIGM, IJL, 6 Rue Bastien Lepage, F-54010 Nancy, France

*Corresponding author: luca.di.stasio@ltu.se

Abstract

Initiation and propagation of fiber/matrix interface cracks are analyzed in Representative Volume Elements (RVEs) of UD and cross-ply laminates. By studying the distribution of stresses at the fiber/matrix interface in the undamaged case, an estimate of the initial flaw size is derived. By adopting a 2-parameters energy-based criterion for propagation [1], we then proceed to the estimation of the expected debond size in different microstructural arrangements. Finally, the results are compared with microscopic observations available in the literature [2].

Keywords: Fiber Reinforced Polymer (FRP), Debonding, Linear Elastic Fracture Mechanics (LEFM).

A Introduction

Characterization of initiation and growth of fiber/matrix interface cracks (or debonds) in Fiber Reinforced Polymer (FRP) composites has proven elusive, particularly the determination of initial flaw size and maximum debond extension. Different methodological approaches exist in the literature to study debond growth, namely Linear Elastic Fracture Mechanics (LEFM) [3], Finite Fracture Mechanics (FFM) [4], Cohesive Zone Modeling (CSM) [5], as well as several initiation physics-based criteria, such as tensile failure of the interface [3], local cavitation-induced brittle matrix failure [6, 7], local matrix plasticization [5], local nucleation plane [8]. We propose here an attempt to evaluate initiation and propagation of debonds by taking into account the uncertainty in failure criteria and mechanisms evident from the literature. We thus aim to estimate a range of plausible values of initial flaw size and maximum debond size by: first, analyzing the stress distribution at the fiber/matrix interface in the absence of damage in Representative Volume Elements (RVEs) of UD and cross-ply laminates; second, determining the angular size of the regions where $\sigma \geq 99\%\sigma_{max}$, $\sigma \geq 95\%\sigma_{max}$ and $\sigma \geq 90\%\sigma_{max}$ with σ_{max} the peak stress value, which provides an estimate of the expected initial debond size; third,

estimating G_{Ic} (Mode I critical Energy Release Rate, one of the two parameters in the adopted propagation criterion [1]), by assuming unstable propagation starting from such initial debond size; fourth, identifying the expected maximum debond size in different RUCs and for different values of the material parameters in the propagation criterion [1]. Finally, the estimated range of maximum debond size is compared with the results of microscopical observations of cross-ply specimens reported in [2].

B RVE models and FE discretization

In this contribution, we analyze debond initiation and propagation in Representative Volume Elements (RVEs) of Uni-Directional (UD) composites and $[0^\circ_{m\cdot k\cdot 2L}, 90^\circ_{k\cdot 2L}, 0^\circ_{m\cdot k\cdot 2L}]$ laminates. Given a global reference frame with axis x, y and z, both types of composites are modeled as plates lying in the $x-y$ plane, with the through-the-thickness direction thus aligned with the z axis. The UD composite 0° direction is parallel to the y axis, while the cross-ply 0° direction is parallel to the x axis. Both composites are loaded in tension along the x axis, which thus corresponds to: transverse loading of the UD specimen; axial loading of the cross-ply specimen. In both composites, damage is present only in the form of fiber/matrix interface cracks, or debonds. In cross-plies, debonds are assumed to be present only in the central 90° ply. Given that: first, in the presence of a load in the x-direction, in both lay-ups the y-strain due to Poisson's effect is very small; second, debond size is assumed to be considerably larger in the fiber than in the arc direction [9]; third, we are interested in studying debond growth along the arc direction; we can consider $2D$ models under plane strain conditions defined in the $x-z$ plane. Although generalized plane strain conditions would represent a more appropriate modeling choice, it would limit the ability to compare with previous results. Simple plane strain conditions are thus preferred. UD composites and 90° plies are characterized by a regular microstructure following a square-packing configuration of fibers, built through the repetition of a one-fiber unit cell along the horizontal and the vertical direction. This unit cell is a square with the center occupied by one fiber of radius $R_f = 1\ \mu m$ and the rest of the element constituted by matrix. The size of the one-fiber unit cell is $2L \times 2L$, such that:

$$L = \frac{R_f}{2}\sqrt{\frac{\pi}{V_f}}, \tag{B.1}$$

where V_f is the fiber volume fraction, here assumed to be 60%. It is worth to specify at this point that the choice $R_f = 1\ \mu m$ is arbitrary and stems from the fact that ERR, in the contest of a linear elastic solution as the one considered in this article, is proportional to the geometrical dimensions of the model. Simplicity is thus the main reason for this choice. Also, V_f is always the same in the one-fiber unit cell and the entire RVE, i.e. no fiber clustering is analyzed in this work. In the case of cross-ply laminates, the 0° layer is homogenized with properties evaluated according to the Concentric Cylinders Assembly with Self-Consistent Shear (CCA-SCS) model [10, 11]. A glass fiber-epoxy system is

considered for both UDs and cross-ply laminates. Material properties are reported in Table 1.

Table 1: Summary of mechanical properties of fiber, matrix and UD layer.

Material	$V_f\,[\%]$	$E_L\,[GPa]$	$E_T\,[GPa]$	$G_{LT}\,[GPa]$	$\nu_{LT}\,[-]$	$\nu_{TT}\,[-]$
Glass fiber	-	70.0	70.0	29.2	0.2	0.2
Epoxy	-	3.5	3.5	1.25	0.4	0.4
UD	60.0	43.442	13.714	4.315	0.273	0.465

The use of coupling conditions allows the study of a Repeating Unit Cells (RUC) of reduced size with respect to the corresponding RVE, which translates in a gain in terms of computational time and memory usage during the evaluation of Finite Element (FE) solution. The RVEs studied in this article are reported in Figure 1 with the corresponding RUC highlighted by dashed line (in blue in the online color version) and with symmetry and coupling conditions represented by rollers (🛆). Details about the central one-fiber unit cell are shown in Figure 2. Notice that the analysis, in terms of stresses and Energy Release Rate (ERR), is conducted on this central one-fiber unit cell, both in the case of an undamaged and of a partially debonded fiber.
Nomenclature and main features of the RVEs studied are described in the following.

$\mathbf{n \times k}$ – free, Figure 1a: UD composite with thickness $t_{UD} = k \cdot 2L$, where k is the number of fiber "rows" in the vertical (through-the-thickness) direction and $2L$ the side length of the one-fiber unit cell as defined in Equation B.1. Debonds appear only in the central fiber "row" with $n-1$ fully bonded fibers in between, where n is the number of fibers present in the RUC along the horizontal direction.

$\mathbf{n \times k}$ – coupling, Figure 1b: UD composite with multiple fiber "rows" containing debonds with $n-1$ fully bonded fibers in between, where n is the number of fibers present in the RUC along the horizontal direction. Fiber "rows" containing debonds are separated along the vertical (through-the-thickness) direction by $k-1$ "rows" of fully bonded fibers, where k is the number of fiber "rows" present in the RUC along the vertical direction. Debonds that are vertically aligned are placed on the same side of their respective fiber. To model this configuration, conditions of coupling of the vertical displacement are applied on the top side.

$\mathbf{n \times k}$ – asymm, Figure 1c: same as in $n \times k -$ *coupling*, but debonds that are vertically aligned are placed on opposite sides of their respective fiber. To model this configuration, the following set of conditions is applied to the upper boundary:

$$\begin{aligned} u_z\left(x, kL\right) - u_z\left(0, kL\right) &= -\left(u_z\left(-x, kL\right) - u_z\left(0, kL\right)\right) \\ u_x\left(x, kL\right) &= -u_x\left(-x, kL\right) \end{aligned} \tag{B.2}$$

which represent conditions of anti-symmetric coupling [12].

$\mathbf{n \times k - m \times t_{90^\circ}}$, Figure 1d: Cross-ply laminate with 90° layer thickness $t_{90^\circ} = k \cdot 2L$ and 0° layer thickness $t_{0^\circ} = m \cdot t_{90^\circ}$. k is the number of fiber "rows" in the vertical (through-the-thickness) direction of the 90° layer and $2L$ the side length of the one-fiber unit cell as defined in Equation B.1. Debonds are present only in the central fiber "row" of the 90° layer with $n - 1$ fully bonded fibers in between, where n is the number of fibers present in the RUC along the horizontal direction.

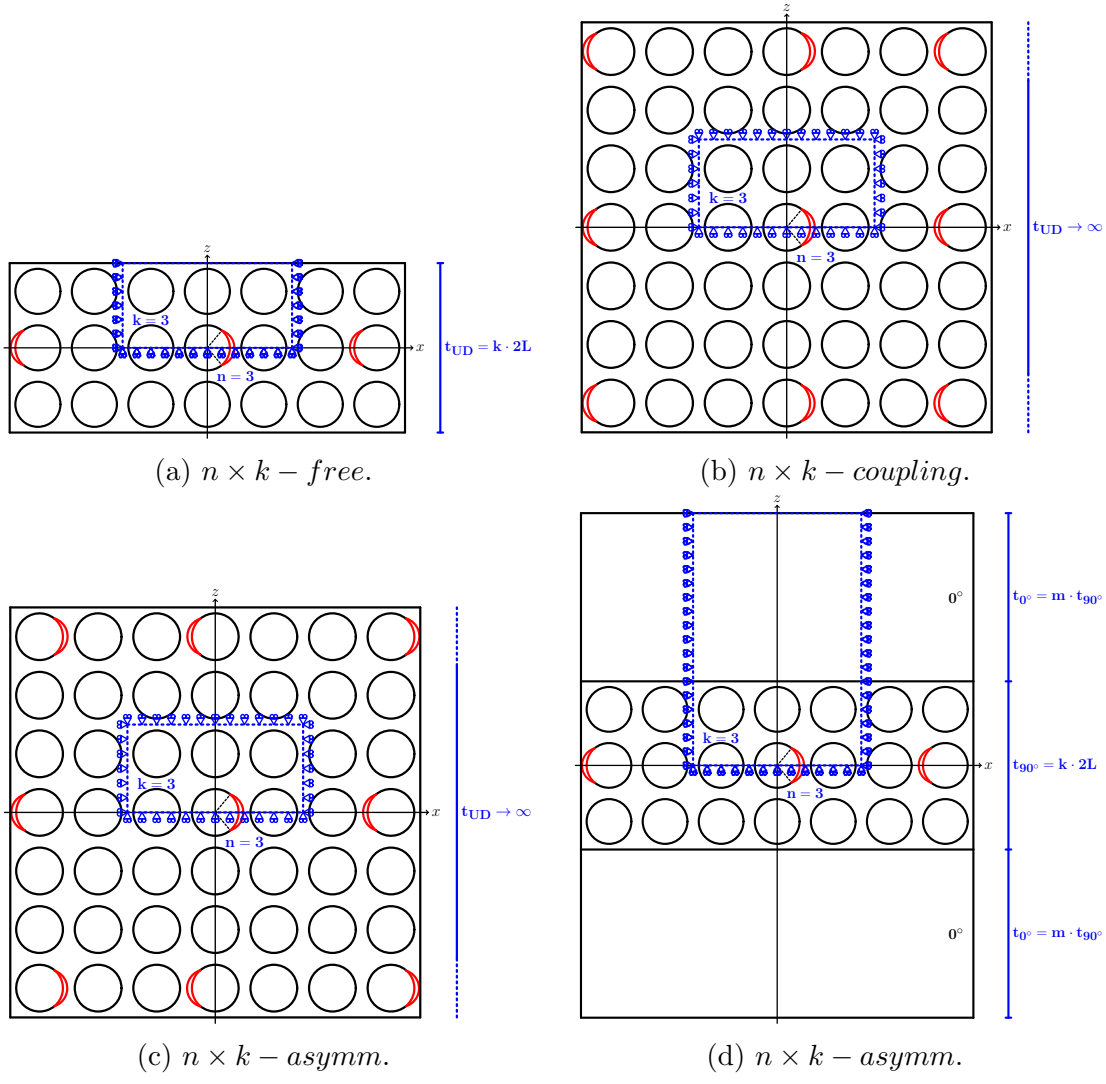

(a) $n \times k - free.$ (b) $n \times k - coupling.$

(c) $n \times k - asymm.$ (d) $n \times k - asymm.$

Figure 1: Composite RVEs and corresponding RUCs analyzed.

Every RUC is symmetric with respect to the horizontal (x) direction, thus only half of it is modeled in the FE solution through the use of symmetry boundary conditions on

the bottom side. Conditions of coupling of the horizontal displacement are applied on the left and right side, to model the repetition of the RUC along the horizontal direction. A tensile load is applied on the right and left side in the form of displacement $\bar{u}_x = \pm\bar{\varepsilon}_x nL$ with $\bar{\varepsilon}_x = 1\%$. The debond has a size of $2\Delta\theta$ (see Figure 2), with $\Delta\theta \geq 0$ ($\Delta\theta = 0$ is the case of no damage at all). For large debonds ($\Delta\theta \geq 60° - 80°$), a region called *contact zone*, of size $\Delta\Phi$ to be determined by the solution itself, appears at the crack tip. Correct resolution of this behavior requires the imposition of conditions of non-interpenetration of the crack faces. Crack face contact is assumed to be frictionless.

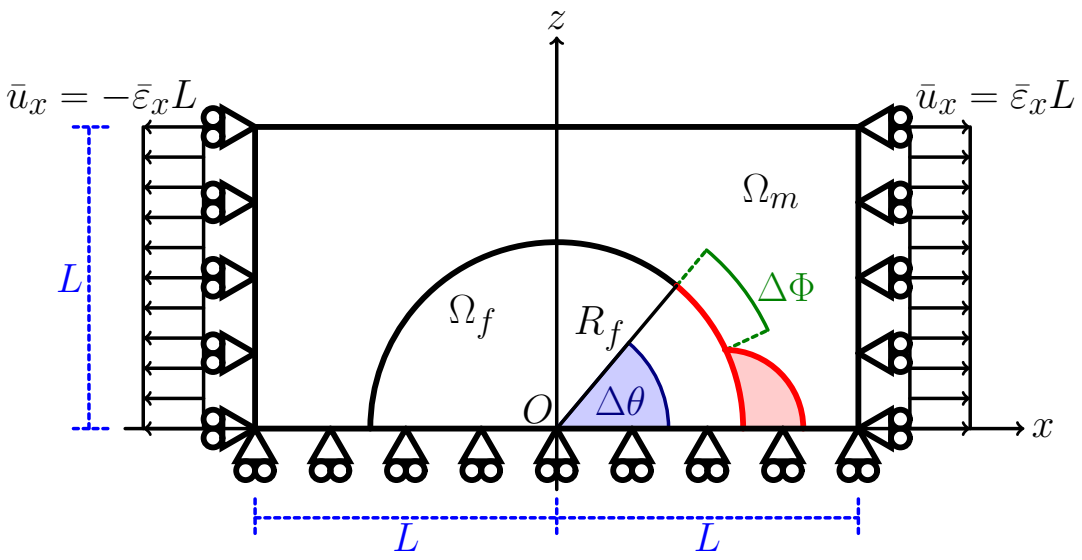

Figure 2: One-fiber unit cell and main parameters characterizing the debonding process.

The FE solution is obtained using Abaqus [13] using second order, 2D, plane strain triangular (CPE6) and rectangular (CPE8) elements. To accurately resolve the singularity at the crack tip, a regular mesh of only rectangular elements is used with almost unitary aspect ratio and angular size $\delta = 0.05°$. The crack faces are represented as element-based surfaces with frictionless small-sliding contact pair interaction.
Total ERR is underestimated, due to the high $\frac{\delta}{\Delta\theta}$ ratio, with the Virtual Crack Closure Technique (VCCT) [14] for very small debonds (see Figure 3), where it is dominated by Mode I. Thus, for $\Delta\theta < 10°$, G_{TOT} is evaluated using the J-integral [15], G_{II} with the VCCT and $G_I = G_{TOT} - G_{II}$; for $\Delta\theta \geq 10°$ only the VCCT is used. Validation of the model is performed with respect to BEM results of [3, 16]; the order of accuracy of the results is discussed in [17].

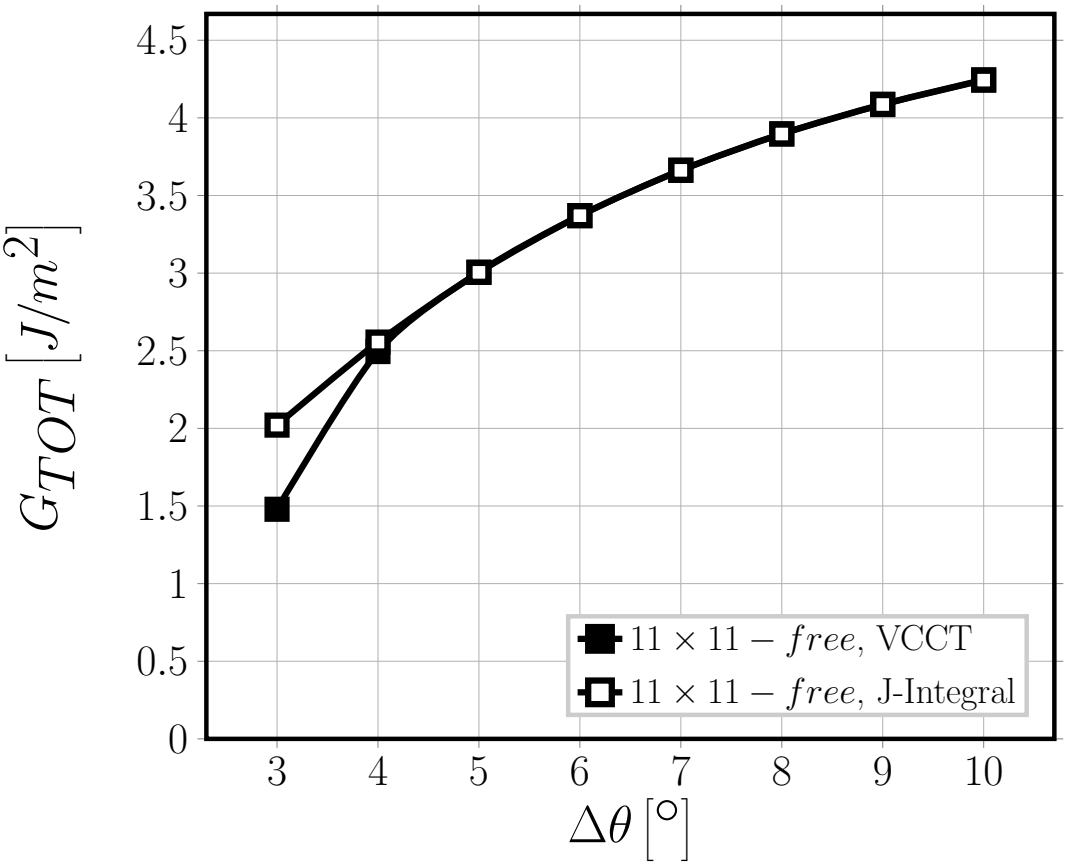

Figure 3: Total ERR of $11\times11-free$ *evaluated respectively with the VCCT and the J-integral.*

C Stress-based analysis of debond initiation ($\Delta\theta = 0^\circ$)

In this section, we assume stress-based debond initiation at the undamaged fiber/matrix interface. Thus, we analyze the distribution of stresses at the fiber/matrix interface in models $1\times k-free$ and $1\times k-1\cdot t_{90^\circ}$ with $k=1,3,11,201$, $\Delta\theta=0^\circ$ (i.e. the undamaged case) and $\bar{\varepsilon}_x=1\%$. Some selected stress components are presented, based on their relevance in previous studies on debond initiation and growth: the radial σ_{rr} and shear $\tau_{r\psi}$ stress [4] (Fig. 4a and Fig. 4b), the Local Hydrostatic Stress (LHS, following the notation of [18]) σ_{LHS} [6, 7] (Fig. 4c and Fig. 4d), the local von Mises stress σ_{vM} [5] (Fig. 4e and Fig. 4f), the Local Maximum Principal Stress (LMPS, following the notation of [18]) σ_{LMPS} [8] (Fig. 4g and Fig. 4h). In plane strain conditions imply that there exists an out-of-plane axial component of the stress (σ_{yy} in our notation): in order to study the importance of this out-of-plane component (tri-axial stress state, see [19]), σ_{LHS}, σ_{vM} and σ_{LMPS} are evaluated both neglecting (index $2D$) and considering it (index $3D$).
It is possible to observe that:

1. for all stresses reported in Fig. 4, no significant difference is present between the

different RUCs for $\psi \leq 10°$;

2. for all stresses reported in Fig. 4, no difference can be observed by increasing k when $k \geq 3$;
3. for all stresses reported in Fig. 4, no difference can be observed between $1 \times k - free$ and $1 \times k - 1 \cdot t_{90°}$ for $k \geq 3$;
4. at $\psi = 0°$ (i.e. the intersection between fiber/matrix interface and horizontal axis); the shear stress $\tau_{r\psi}$ (Fig. 4b) is 0 while the radial stress σ_{rr} (Fig. 4a) is at its maximum;
5. comparison of Fig. 4c with Fig. 4d shows that the out-of-plane stress σ_{yy} has only a marginal effect on the local hydrostatic stress σ_{LHS}: the distribution remains the same, while the peak value is reduced from 270 $[MPa]$ in Fig. 4c to 250 $[MPa]$ in Fig. 4d by considering σ_{yy};
6. comparison of Fig. 4e with Fig. 4f shows a remarkable effect of the out-of-plane stress σ_{yy} on the von Mises stress: if σ_{yy} is neglected, σ_{vM} presents a maximum of 287 $[MPa]$ at $\psi = 0°$, slightly higher than the value of σ_{LHS} (neglecting σ_{yy}) of 270 $[MPa]$ at $\psi = 0°$; if σ_{yy} is considered, the peak value of σ_{vM} is shifted to $\psi \sim 20°$ and reduced to 186 $[MPa]$ while at $\psi = 0°$ σ_{vM} is reduced to ~ 110 $[MPa]$, significantly lower than $\sigma_{LHS} = 250$ $[MPa]$ at $\psi = 0°$ (considering σ_{yy});
7. comparison of Fig. 4g with Fig. 4g shows that the Local Maximum Principal Stress is practically unaffected by the out-of-plane stress σ_{yy};
8. σ_{rr}, $\sigma_{LHS,2D}$, $\sigma_{LHS,3D}$, $\sigma_{vM,2D}$, $\sigma_{LMPS,2D}$ and $\sigma_{LMPS,3D}$ all reach their peak value at 0° and 180° and decrease to 99% the peak value between 2° and 8°, to 95% the peak value between 6° and 12° and to 90% the peak value between 8° and 15° from the occurrence of the maximum.

Based on the previous considerations, it is reasonable to assume that a stress-based criterion would predict, irrespectively of the specific criterion chosen, the onset of an interface crack at 0° or 180° with an initial size at least comprised in the range $2° - 8°$ (1% margin) and likely in the range $6° - 12°$ (5% margin). It is worth to point out that, in the case of a linear elastic solution as the one presented here, the stresses at the fiber/matrix interface for a different value of the applied strain $\bar{\varepsilon}_x$ will change in magnitude but will keep the same functional form and relative magnitude with respect to each other. Thus, the considerations made so far, based on the relative magnitude of stresses and their rate of decrease from the peak value, will apply at any other strain level.

D Energy-based analysis of debond propagation

In the previous section, we assumed stress-based debond initiation. We now assume that (as in [20]), once an initial debond of a size in the range predicted in the previous section ($\Delta\theta_0 \sim 2° - 12°$) is formed, the debond will grow unstably (at the same level of global applied strain $\bar{\varepsilon}_x$) according to an energy-based criterion of the form [1, 4]:

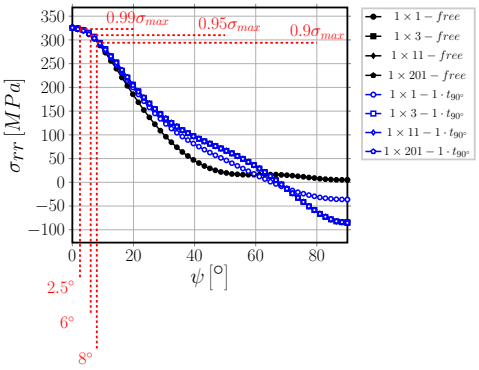

(a) Radial stress σ_{rr}.

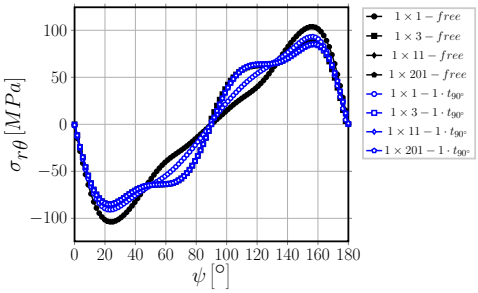

(b) Shear stress $\tau_{r\psi}$.

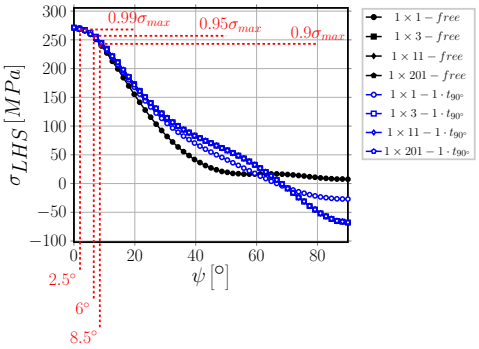

(c) Local Hydrostatic Stress (LHS), neglecting σ_{yy}, $\sigma_{LHS,2D}$.

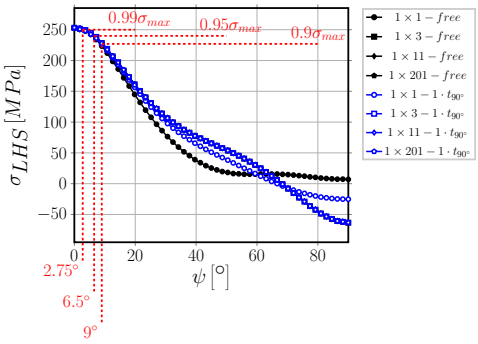

(d) Local Hydrostatic Stress (LHS), considering σ_{yy}, $\sigma_{LHS,3D}$.

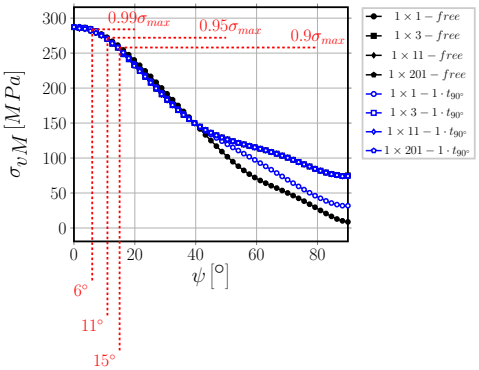

(e) Local von Mises stress, neglecting σ_{yy}, $\sigma_{vM,2D}$.

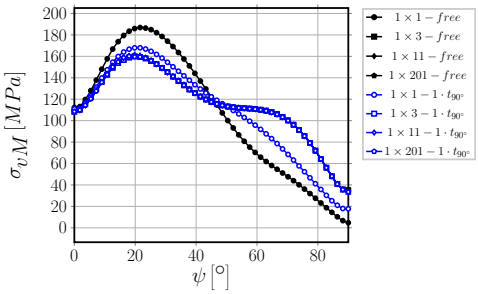

(f) Local von Mises stress, considering σ_{yy}, $\sigma_{vM,3D}$.

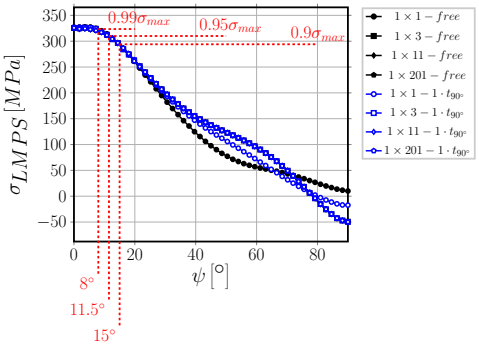

(g) Local Maximum Principal Stress (LMPS), neglecting σ_{yy}, $\sigma_{LMPS,2D}$.

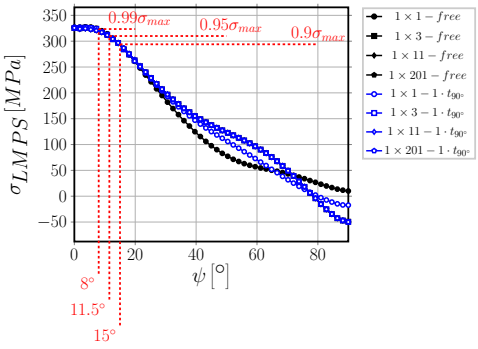

(h) Local Maximum Principal Stress (LMPS), considering σ_{yy}, $\sigma_{LMPS,3D}$.

Figure 4: Stress distribution at the fiber/matrix interface in the absence of damage with respect to angular coordinate ψ; applied strain $\bar{\varepsilon}_x = 1\%$.

$$G_{TOT} \geq G_c = G_{Ic}\left(1 + \tan^2\left(\left(1-\lambda\right)\Psi_G\right)\right), \quad \Psi_G = tan^{-1}\left(\sqrt{\frac{G_{II}}{G_I}}\right), \tag{D.3}$$

where Ψ_G is the energy-based phase angle, G_{TOT} is the total ERR, G_c is the critical ERR, G_{Ic} is the Mode I critical ERR (material property) and λ the mode mixity sensitivity parameter (material property, usually $0.2 \leq \lambda \leq 0.35$)[1]. Given that debond propagation starts as soon as an initial debond is formed (in our model), the propagation criterion in Eq. D.3 is satisfied for the initial debond size $\Delta\theta_0$. Thus, by calculating G_I, G_{II} and G_{TOT} and equating G_c to G_{TOT} in Eq. D.3, it is possible to estimate G_{Ic} for different values of the initial debond size $\Delta\theta_0$ and of the parameter λ (Figure 5). The estimation is performed using a restricted set of RUCs: $11 \times 1 - free$, $11 \times 11 - free$, $11 \times 1 - 1 \cdot t_{90^\circ}$ and $11 \times 11 - 1 \cdot t_{90^\circ}$, with $\bar{\varepsilon}_x = 1\%$.

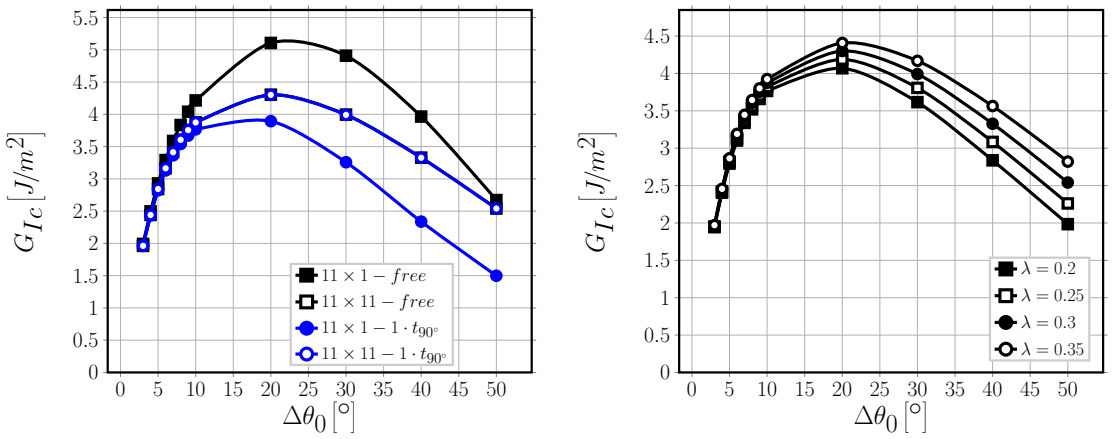

(a) $\lambda = 0.3$.

(b) $11 \times 11 - 1 \cdot t_{90^\circ}$.

Figure 5: Estimated values of G_{Ic} assuming different values of initial debond size, for different RUCs and varying λ, with global applied strain $\bar{\varepsilon}_x$ equal to 1%.

Neither RUC configuration nor λ affects G_{Ic} significantly for small initial debond sizes, i.e $\Delta\theta_0 < 10^\circ$ (Figure 5), corresponding to the range of initial debond size determined in Section C. Observing Figure 5, we can assume a value of G_{Ic} in the range $2 - 4.5\ \left[\frac{J}{m^2}\right]$, with $0.2 \leq \lambda \leq 0.35$. Notice that this estimate is based on calculations with $\bar{\varepsilon}_x = 1\%$ and the value of G_{Ic} will scale with $\bar{\varepsilon}_x$ according to $\frac{G_{Ic,\bar{\varepsilon}_{x,1}}}{G_{Ic,\bar{\varepsilon}_{x,2}}} = \left(\frac{\bar{\varepsilon}_{x,1}}{\bar{\varepsilon}_{x,2}}\right)^2$. Given that no dependence of G_{Ic} on RUC type is observed for $\Delta\theta_0 < 10^\circ$, we can use $G_{Ic} \sim 2 - 4.5\ \left[\frac{J}{m^2}\right]$ to estimate the expected maximum size of debonds in several other RUCs (Figure 6), by

[1] λ governs the influence of mode ratio $\frac{G_{II}}{G_I}$ on G_c such that: for $\lambda = 1$, $G_c = G_{Ic}$; for $\lambda = 0$, $G_c = G_{Ic}\left(1 + \frac{G_{II}}{G_I}\right)$.

evaluating G_c according to Equation D.3. The expected maximum debond size $\Delta\theta_{max}$ is the value of $\Delta\theta$ such that

$$G_{TOT}\left(\Delta\theta \geq \Delta\theta_{max}\right) \leq G_c\left(\Delta\theta \geq \Delta\theta_{max}\right). \tag{D.4}$$

Notice that, although evaluated using G_I, G_{II} and G_{TOT} computed with $\bar{\varepsilon}_x = 1\%$, the values of $\Delta\theta_{max}$ do not depend on $\bar{\varepsilon}_x$ as both sides in Equation D.4 scale with the applied strain by a factor $\left(\frac{\bar{\varepsilon}_{x,1}}{\bar{\varepsilon}_{x,2}}\right)^2$. If the procedure described in this section is applied using values of G_I, G_{II} and G_{TOT} computed with a different value of $\bar{\varepsilon}_x$, the estimated values of $\Delta\theta_{max}$ will be the same.

Comparison of Fig. 6a with Fig. 6b shows that the effect of the presence of the 0° layer is to reduce the maximum size of debonds: from $\sim 105°$ in $21 \times 1 - free$ to $\sim 45°$ in $21 \times 1 - 1 \cdot t_{90°}$, for $G_{Ic} = 2\ \left[\frac{J}{m^2}\right]$, $\lambda = 0.35$. However, the presence of just 1 "row" of undamaged fibers between the debond and the free surface or the 0°/90° interface (in RVEs respectively of UD composites and cross-ply laminates) makes the estimate of the maximum debond size unaffected by the number k of fiber rows (Figures 6c, 6d, 6e and 6f). Moreover, for any given combination of G_{Ic} and λ, the estimated debond size is the same for $n \times k - free$ and $n \times k - 1 \cdot t_{90°}$ for $k \geq 3$. The presence of a debond on the neighboring fiber in the vertical direction (RUCs $21 \times 1 - coupling$ and $21 \times 1 - asymm$) favors instead the growth of larger debonds (Figures 6g and 6h), with the largest size achieved when debonds are on opposite sides of consecutive fibers: $\sim 115°$ in $21 \times 1 - asymm$ and $\sim 110°$ in $21 \times 1 - coupling$, for $G_{Ic} = 2\ \left[\frac{J}{m^2}\right]$, $\lambda = 0.35$. Considering the different combinations of G_{Ic} and λ, it is possible to identify the range of maximum debond propagation: for a 1-fiber row UD composite ($21 \times 1 - free$), between 30° ($G_{Ic} = 4.5\ \left[\frac{J}{m^2}\right]$, $\lambda = 0.0.2$) and 105° ($G_{Ic} = 2\ \left[\frac{J}{m^2}\right]$, $\lambda = 0.35$); for a 1-fiber row 90° ply in a cross-ply laminate ($21 \times 1 - 1 \cdot t_{90°}$), between 30° ($G_{Ic} = 3\ \left[\frac{J}{m^2}\right]$, $\lambda = 0.2$) and 45° ($G_{Ic} = 2\ \left[\frac{J}{m^2}\right]$, $\lambda = 0.35$); for a k-fiber rows UD composite and a k-fiber rows 90° ply in a cross-ply laminate with $k \geq 3$ ($21 \times k - free$ and $21 \times k - 1 \cdot t_{90°}$), between 40° ($G_{Ic} = 3\ \left[\frac{J}{m^2}\right]$, $\lambda = 0.2$) and 60° ($G_{Ic} = 2\ \left[\frac{J}{m^2}\right]$, $\lambda = 0.35$); for consecutive debonds along the vertical direction in a UD composite ($21 \times 1 - coupling$ and $21 \times 1 - asymm$), between 80° ($G_{Ic} = 4.5\ \left[\frac{J}{m^2}\right]$, $\lambda = 0.2$) and 110° ($G_{Ic} = 2\ \left[\frac{J}{m^2}\right]$, $\lambda = 0.35$) when debonds are on the same sides and between 60° ($G_{Ic} = 3\ \left[\frac{J}{m^2}\right]$, $\lambda = 0.2$) and 115° ($G_{Ic} = 2\ \left[\frac{J}{m^2}\right]$, $\lambda = 0.35$) when on opposite sides. These theoretical predictions are in agreement with the microscopical observations performed in [2] on $[0^\circ_3, 90^\circ_3]_S$ carbon fiber (AS4) - epoxy (8552) specimens subjected to tensile loading (corresponding to RUCs $n \times k - 1 \cdot t_{90°}$ in this article, for which we estimated the range of maximum debond size to be $40° - 60°$). They report debond sizes in the range $21.4° - 89.2°$ with average value of 49.3° and standard deviation of 11.7°, with 63% of the measurements in the range $40° - 60°$.

E Conclusions

Onset and propagation of fiber/matrix interface cracks has been studied in Representative Volume Elements (RVEs) of UD composites and $[0^\circ_{m \cdot k \cdot 2L}, 90^\circ_{k \cdot 2L}, 0^\circ_{m \cdot k \cdot 2L}]$ laminates

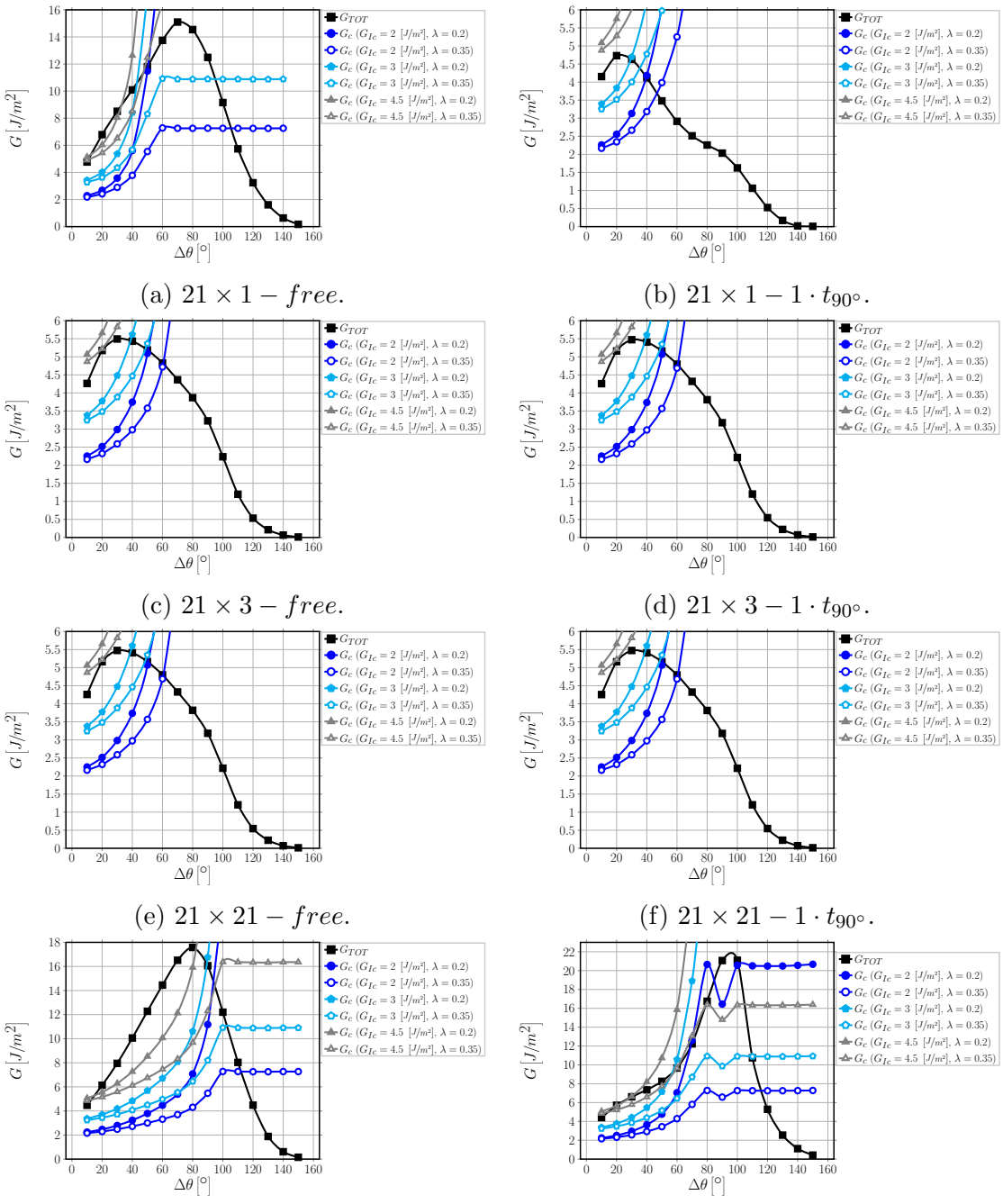

(a) $21 \times 1 - free.$ (b) $21 \times 1 - 1 \cdot t_{90^\circ}.$

(c) $21 \times 3 - free.$ (d) $21 \times 3 - 1 \cdot t_{90^\circ}.$

(e) $21 \times 21 - free.$ (f) $21 \times 21 - 1 \cdot t_{90^\circ}.$

(g) $21 \times 1 - coupling.$ (h) $21 \times 1 - asymm.$

Figure 6: G_{TOT} and G_c for several RUCs and different values of G_{Ic} and λ, computed for $\bar{\varepsilon}_x = 1\%$. Each intersection point of G_{TOT} and G_c curves such that $G_{TOT}\,(\Delta\theta \geq \Delta\theta_{intersection}) \leq G_c\,(\Delta\theta \geq \Delta\theta_{intersection})$ determines an estimate of $\Delta\theta_{max}$.

by means of Repeating Unit Cells (RUCs). Analysis of the stress distribution at the fiber/matrix interface in the absence of damage has shown that a stress criterion for initiation would predict, irrespectively of which criterion from those proposed in the literature is chosen, the onset of a debond at 0° or 180° with a semi-aperture $\Delta\theta_0$ in the range $2° - 12°$, corresponding to a margin of 5% on the satisfaction of the criterion. Assuming that debond propagation occurs unstably immediately after debond onset at the same level of global applied strain $\bar{\varepsilon}_x$ (as in [20]), it is possible to evaluate the parameter G_{Ic} in the expression of the critical ERR [1] and with it to estimate the range of expected maximum debond size. The latter finally provides the following ranges: for a 1-fiber row UD composite, $30° - 105°$; for a 1-fiber row 90° ply in a cross-ply laminate, $30° - 45°$; for a multiple fiber-rows UD composite and a multiple fiber-rows 90° ply in a cross-ply laminate , $40° - 60°$; for consecutive debonds along the vertical direction in a UD composite, $80° - 110°$ when debonds are on the same sides and $60° - 115°$ when on opposite sides. The prediction for a cross-ply laminate (models $n \times k - 1 \cdot t_{90°}$, $k \geq 3$) agrees well with the debond size distribution estimated in [2] through microscopic observations of $[0_3^\circ, 90_3^\circ]_S$ specimens loaded in tension.

Acknowledgements

Luca Di Stasio gratefully acknowledges the support of the European School of Materials (EUSMAT) through the DocMASE Doctoral Programme and the European Commission through the Erasmus Mundus Programme.

References

[1] J.W. Hutchinson and Z. Suo. "Mixed Mode Cracking in Layered Materials". In: *Advances in Applied Mechanics*. Elsevier, 1991, pp. 63–191. DOI: 10.1016/s0065-2156(08)70164-9.

[2] Elena Correa et al. "Microscopical observations of inter-fibre failure under tension". In: *Composites Science and Technology* 155 (Feb. 2018), pp. 213–220. DOI: 10.1016/j.compscitech.2017.12.009.

[3] Federico París, Elena Correa, and Vladislav Mantič. "Kinking of Transversal Interface Cracks Between Fiber and Matrix". In: *Journal of Applied Mechanics* 74.4 (2007), p. 703. DOI: 10.1115/1.2711220.

[4] V. Mantič. "Interface crack onset at a circular cylindrical inclusion under a remote transverse tension. Application of a coupled stress and energy criterion". In: *International Journal of Solids and Structures* 46.6 (Mar. 2009), pp. 1287–1304. DOI: 10.1016/j.ijsolstr.2008.10.036.

[5] Luis Pablo Canal et al. "Intraply fracture of fiber-reinforced composites: Microscopic mechanisms and modeling". In: *Composites Science and Technology* 72.11 (June 2012), pp. 1223–1232. DOI: 10.1016/j.compscitech.2012.04.008.

[6] L.E. Asp, L.A. Berglund, and R. Talreja. "A criterion for crack initiation in glassy polymers subjected to a composite-like stress state". In: *Composites Science and Technology* 56.11 (Jan. 1996), pp. 1291–1301. DOI: 10.1016/s0266-3538(96)00090-5.

[7] L.E. Asp, L.A. Berglund, and R. Talreja. "Prediction of matrix-initiated transverse failure in polymer composites". In: *Composites Science and Technology* 56.9 (Jan. 1996), pp. 1089–1097. DOI: 10.1016/0266-3538(96)00074-7.

[8] P.A. Carraro and M. Quaresimin. "A damage based model for crack initiation in unidirectional composites under multiaxial cyclic loading". In: *Composites Science and Technology* 99 (July 2014), pp. 154–163. DOI: 10.1016/j.compscitech.2014.05.012.

[9] H. Zhang et al. "Transverse single-fibre test for interfacial debonding in composites: 1. Experimental observations". In: *Composites Part A: Applied Science and Manufacturing* 28.4 (Jan. 1997), pp. 309–315. DOI: 10.1016/s1359-835x(96)00123-6.

[10] Z. Hashin. "Analysis of Composite Materials—A Survey". In: *Journal of Applied Mechanics* 50.3 (1983), p. 481. DOI: 10.1115/1.3167081.

[11] R.M. Christensen and K.H. Lo. "Solutions for effective shear properties in three phase sphere and cylinder models". In: *Journal of the Mechanics and Physics of Solids* 27.4 (Aug. 1979), pp. 315–330. DOI: 10.1016/0022-5096(79)90032-2.

[12] Luca Di Stasio, Janis Varna, and Zoubir Ayadi. "Growth of interface cracks on consecutive fibers: on the same or on the opposite sides?" In: *Materials Today: Proceedings* In Press ().

[13] *ABAQUS/Standard User's Manual, Version 6.12*. Simulia. Providence, RI, USA, 2012.

[14] Ronald Krueger. "Virtual crack closure technique: History, approach, and applications". In: *Applied Mechanics Reviews* 57.2 (2004), p. 109. DOI: 10.1115/1.1595677.

[15] J. R. Rice. "A Path Independent Integral and the Approximate Analysis of Strain Concentration by Notches and Cracks". In: *Journal of Applied Mechanics* 35.2 (1968), p. 379. DOI: 10.1115/1.3601206.

[16] C. Sandino, E. Correa, and F. París. "Numerical analysis of the influence of a nearby fibre on the interface crack growth in composites under transverse tensile load". In: *Engineering Fracture Mechanics* 168 (Dec. 2016), pp. 58–75. DOI: 10.1016/j.engfracmech.2016.01.022.

[17] Luca Di Stasio, Janis Varna, and Zoubir Ayadi. "Energy release rate of the fiber/matrix interface crack in UD composites under transverse loading: effect of the fiber volume fraction and of the distance to the free surface and to non-adjacent debonds". In: *Theoretical and Applied Fracture Mechanics* (June 2019), p. 102251. DOI: 10.1016/j.tafmec.2019.102251.

[18] P.A. Carraro and M. Quaresimin. "Modeling the crack initiation in unidirectional laminates under multiaxial fatigue loading1". In: *Modeling Damage, Fatigue and Failure of Composite Materials*. Elsevier, 2016, pp. 357–375. DOI: 10.1016/b978-1-78242-286-0.00016-9.

[19] Leif E. Asp, Lars A. Berglund, and Peter Gudmundson. "Effects of a composite-like stress state on the fracture of epoxies". In: *Composites Science and Technology* 53.1 (Jan. 1995), pp. 27–37. DOI: 10.1016/0266-3538(94)00075-1.

[20] E. Correa, F. París, and V. Mantič. "Fiber–matrix debonding in composite materials: transverse loading". In: *Modeling Damage, Fatigue and Failure of Composite Materials*. Elsevier, 2016, pp. 97–116. DOI: 10.1016/b978-1-78242-286-0.00006-6.